



저작자표시-비영리-변경금지 2.0 대한민국

이용자는 아래의 조건을 따르는 경우에 한하여 자유롭게

- 이 저작물을 복제, 배포, 전송, 전시, 공연 및 방송할 수 있습니다.

다음과 같은 조건을 따라야 합니다:



저작자표시. 귀하는 원저작자를 표시하여야 합니다.



비영리. 귀하는 이 저작물을 영리 목적으로 이용할 수 없습니다.



변경금지. 귀하는 이 저작물을 개작, 변형 또는 가공할 수 없습니다.

- 귀하는, 이 저작물의 재이용이나 배포의 경우, 이 저작물에 적용된 이용허락조건을 명확하게 나타내어야 합니다.
- 저작권자로부터 별도의 허가를 받으면 이러한 조건들은 적용되지 않습니다.

저작권법에 따른 이용자의 권리는 위의 내용에 의하여 영향을 받지 않습니다.

이것은 [이용허락규약\(Legal Code\)](#)을 이해하기 쉽게 요약한 것입니다.

[Disclaimer](#)

이학박사 학위논문

Dynamical Evolution of
Giant Molecular Clouds Driven by
UV Radiation Feedback
from Massive Stars

무거운 별의 자외선 복사 되먹임에 기인한
거대 분자운의 역학적 진화

2018 년 8 월

서울대학교 대학원
물리 천문학부 천문학 전공
김 정 규

Abstract

Giant molecular clouds (GMCs) are primary sites of star formation in the present-day universe. Although scarce in numbers, newborn massive stars exert a disproportionate influence on the chemistry, dynamics, and structure of natal clouds and the surrounding interstellar medium (ISM). In particular, copious ultraviolet (UV) photons emitted by massive stars create regions of warm ionized gas, H II regions, which expel and erode cold molecular gas available for star formation. While the destructive effects of UV radiation feedback on birth clouds have long been recognized by theorists, quantitative understanding of how cloud dispersal actually occurs remains incomplete. To assess the impact of UV feedback on the evolution of GMCs and star formation therein, this thesis explores the dynamics of H II regions and dispersal of GMCs in diverse star-forming environments using analytic calculations as well as numerical simulations.

In Chapter 2, we investigate the nature of small-scale dynamical instabilities that may occur at ionization fronts (IFs), sharp boundaries of H II regions separating a warm ionized gas from a cold neutral gas. We carry out a linear stability analysis of a plane-parallel IF threaded by magnetic fields parallel to the front. We find that the growth rate of the IF instability is linearly proportional to the wavenumber of perturbation as well as the velocity of the upstream cold gas with respect to the IF, completely analogous to the Darrieus-Landau instability of deflagration fronts in terrestrial combustion and thermonuclear supernovae. Magnetic fields play a stabilizing role by reducing the density contrast across the IF and by exerting magnetic pressure and tension forces. In strongly magnetized IFs, perturbations propagating parallel to the IF are completely suppressed by magnetic tension. The IF instability works together with the Rayleigh-Taylor instability for IFs accel-

erating away from an ionizing source.

In Chapter 3, we study spherical expansion of dusty H II regions and related cloud disruption. We develop a semi-analytic model for expansion of dusty H II regions due to thermal pressure of ionized gas and radiation pressure on dust grains, accounting for non-uniform internal structure as well as the inward gravity from gas and central star cluster. We confirm the semi-analytic shell expansion solutions by comparing with numerical simulations. We calculate the minimum star formation efficiency (SFE) required for an expanding H II region around a star cluster to disrupt the parent cloud. We find that while typical GMCs in normal disk galaxies are disrupted by gas-pressure-driven expansion with SFE of less than about 10%, denser, more massive clouds in extreme environments are disrupted by radiation-pressure-driven expansion with higher SFE. The disruption timescale is on the order of a free-fall timescale, suggesting that cloud disruption is rapid once sufficiently luminous H II region is formed.

In Chapter 4, we turn to computational modeling of star cluster formation in turbulent GMCs. We implement a highly efficient and accurate adaptive ray tracing (ART) method for describing propagation of UV radiation produced by multiple point sources in the magnetohydrodynamics code *Athena*. We adopt a recently proposed parallel algorithm for communication of ray information between processors with additional new features that further improve parallel performance. We validate our implementation against a variety of test problems of expanding H II regions. The results of scaling tests show that the ART module has excellent strong and weak scaling up to $\sim 10^3$ processors. To demonstrate application of our ART implementation, we conduct a simulation of star cluster formation allowing for self-consistent star formation as well as density inhomogeneities resulting from supersonic turbulence. We also make direct comparison of radiation fields computed from the ART and the widely-used M_1 closure scheme, and find that the latter is unable to accurately describe radiation field near individual point sources.

Finally, in Chapter 5, we present the results of radiation hydrodynamic

simulations of star cluster formation and ensuing cloud dispersal by photoionization and radiation pressure for a range of cloud parameters. Our parameter study shows that the net SFE increases primarily with the initial surface density of the cloud and that clouds are destroyed within $\sim 2\text{--}10\text{Myr}$ after the onset of radiation feedback. The importance of radiation pressure (relative to photoionization) increases with the initial surface density. The dominant mass loss mechanism is photoevaporation, although dynamical ejection also contributes significantly in low-mass and/or high surface density clouds. We show that the photoevaporation rate depends only on the ionizing photon rate and cloud size with a scaling relation consistent with theoretical expectations. However, the radial outflow momentum generated by thermal and radiation pressure forces is nearly an order of magnitude lower than the prediction based on spherical expansion of an embedded H II region, due to escape of radiation and momentum cancellation.

Keywords: H II regions — instabilities — ISM: clouds — ISM: kinematics and dynamics — methods: analytical — methods: numerical — radiation: dynamics — radiative transfer — stars: formation

Student Number: 2012-30111

This thesis contains four original papers published in peer reviewed journals.

Chapter 2: “Instability of Magnetized Ionization Fronts Surrounding H II Regions”, Kim, J.-G. & Kim, W.-T. 2014, *The Astrophysical Journal*, 797, 135

Chapter 3: “Disruption of Molecular Clouds by Expansion of Dusty H II Regions”, Kim, J.-G., Kim, W.-T., & Ostriker, E. C. 2016, *The Astrophysical Journal*, 819, 137

Chapter 4: “Modeling UV Radiation from Massive Stars. I. Implementation of Adaptive Ray-tracing Method and Tests,” Kim, J.-G., Kim, W.-T., Ostriker, E. C., & Skinner, M. A. 2017, *The Astrophysical Journal*, 851, 93

Chapter 5: “Modeling UV Radiation from Massive Stars. II. Dispersal of Star-Forming Giant Molecular Clouds by Photoionization and Radiation Pressure,” Kim, J.-G., Kim, W.-T., & Ostriker, E. C. 2018, *The Astrophysical Journal*, 859, 68

Contents

Abstract	i
1 Introduction	1
1.1 Giant Molecular Clouds	3
1.1.1 Physical Properties	3
1.1.2 Slow and Inefficient Star Formation	8
1.1.3 Lifetime of GMCs	10
1.2 UV Radiation Feedback	11
1.2.1 Structure and Dynamics of H II Regions	11
1.2.2 Theoretical Models on Cloud Disruption	14
1.3 Outline of the Thesis	16
2 Instability of Magnetized Ionization Fronts Surrounding H II Regions	18
2.1 Introduction	19
2.2 Steady Ionization Fronts	24
2.2.1 Basic Equations	24
2.2.2 Steady-State Configurations	25
2.3 Perturbation Equations	33
2.3.1 Canonical Modes	34

2.3.2	Perturbed Jump Conditions	36
2.4	Instability of Unmagnetized IFs	39
2.5	Instability of Magnetized IFs	44
2.5.1	Cases with $k_x = 0$ and $k_y \neq 0$	45
2.5.2	Cases with $k_x \neq 0$ and $k_y = 0$	46
2.6	Summary and Discussion	53
2.6.1	Summary	53
2.6.2	Discussion	56
Appendix	61
2.A	Derivation of Equation (2.76)	61
2.B	Perturbation Equations for $k_x \neq 0$ and $k_y = 0$	62
3	Disruption of Molecular Clouds by Expansion of Dusty H II	
	Regions	64
3.1	Introduction	65
3.2	Internal Structure of Dusty H II Regions	71
3.3	Expansion of Dusty H II Regions	77
3.3.1	Model	77
3.3.2	Non-gravitating Similarity solutions	82
3.3.3	Valid Range of k_ρ	83
3.3.4	Shell Expansion	83
3.3.5	Comparison with Numerical Simulations	86
3.4	Minimum Efficiency of Star Formation for Cloud Disruption	90
3.4.1	Fiducial Case	91
3.4.2	Analytic Estimates	98
3.4.3	Effects of k_ρ and Trapped Infrared Radiation	101
3.5	Summary and Discussion	104
3.5.1	Summary	104
3.5.2	Discussion	108

Appendix	116
3.A Light-to-mass ratio of Star Clusters	116
3.B Method of Numerical Simulations	118
4 Implementation of Adaptive Ray Tracing Method and Tests	123
4.1 Introduction	124
4.2 Numerical Method	129
4.2.1 Adaptive Ray Tracing	130
4.2.2 Parallelization	133
4.2.3 Update of Radiation Source Terms	140
4.3 Results of Code Tests	144
4.3.1 Scaling Tests	144
4.3.2 Radiation in a Vacuum	147
4.3.3 Expansion of H II Regions	149
4.4 Application to Star Cluster Formation in Turbulent Clouds .	158
4.4.1 Numerical Setup	158
4.4.2 Overall Evolution & Scaling Test	162
4.4.3 Comparison of Radiation Field Computed from M_1 - Closure and ART	163
4.5 Summary	171
Appendix	175
4.A One-Cell Test of Photoionization Update	175
5 Dispersal of Star-Forming Giant Molecular Clouds by Pho-	178
toionization and Radiation Pressure	
5.1 Introduction	179
5.2 Numerical Methods	186
5.2.1 Radiation Hydrodynamics Scheme	186
5.2.2 Initial and Boundary Conditions	190

5.2.3	Models	190
5.3	Simulation Results	194
5.3.1	Overall Evolution: Fiducial Model	194
5.3.2	Star Formation and Mass Loss Efficiencies	201
5.3.3	Timescales for Star Formation and Cloud Destruction	206
5.3.4	Outflow Velocity	209
5.4	Mass Loss Processes	210
5.4.1	Mass Loss by Photoevaporation	212
5.4.2	Momentum Injection	219
5.5	Models for Cloud Dispersal and SFE	226
5.5.1	Destruction by Photoevaporation	226
5.5.2	Destruction by Dynamical Mass Ejection	228
5.6	Summary and Discussion	229
5.6.1	Summary	230
5.6.2	Discussion	233
	Appendix	238
5.A	Resolution Study of the Fiducial Model	238
5.B	Net Star Formation Efficiency Regulated by Radiation-Pressure Feedback	241
6	Summary and Outlook	245
6.1	Summary	245
6.2	Outlook	248
	Bibliography	252
	요약	266

List of Tables

4.1	Global properties of the radiation fields from the ART and M_1 schemes	171
5.1	Model Cloud Parameters	192
5.2	Simulation Results	207

List of Figures

2.1	(a) Dependence on the upstream plasma beta β_1 of the critical Mach numbers \mathcal{M}_D and \mathcal{M}_R and the critical expansion factors α_D and α_R for the temperature ratio between the ionized and neutral phases $\theta = 200$. (b) Expansion factors α of magnetic IFs with $\theta = 200$ for various β_1	30
2.2	Dependence of (a) the upstream magnetosonic Mach number \mathcal{M}_{M1} and (b) the expansion factor α on the downstream magnetosonic Mach number \mathcal{M}_{M2} for weak D-type IFs with $\theta = 200$.	32
2.3	(a) Dimensionless growth rate σ of the instability of unmagnetized IFs. (b) Dependence of σ on acceleration parameter G	44
2.4	Growth rate of the instability of magnetized IFs with $\theta = 200$ and differing β_1 as a function of \mathcal{M}_{M2} , when the perturbations propagate perpendicular to the initial magnetic fields ($k_x = 0$).	47
2.5	Incompressible growth rate σ of the instability of magnetized IFs as a function of the upstream Alfvénic Mach number \mathcal{M}_{A1} , for in-plane perturbations with $k_y = 0$	50

2.6	(a) Compressible growth rate σ of the instability of magnetized IFs as a function of \mathcal{M}_{M2} and (b) the contour of σ in the β_1 - \mathcal{M}_{M2} plane.	54
3.1	Radial distributions of density, radiation pressure, and force per unit volume in dusty H II regions in static equilibrium. . .	74
3.2	Dependence on $Q_{i,49}n_{\text{rms}}$ of the ratios of the edge-to-rms densities, the rms-to-mean densities, the dust optical depth to the ionization front, and the fraction of ionizing photons attenuated by photoionization prior to reaching the shell.	76
3.3	Outward gas and radiation pressure forces on the shell surrounding the H II region as a function of the shell radius. . .	80
3.4	Temporal evolution of the shell radius and the shell velocity for $Q_i = 10^{50} \text{ s}^{-1}$ and $Q_i = 10^{52} \text{ s}^{-1}$	84
3.5	Evolution of the radial density distributions in numerical simulations of expanding H II regions in a power-law density background with $k_\rho = 1$ and $r_0 = 1 \text{ pc}$	87
3.6	Temporal evolution of the shell radius in the simulations (solid lines) compared to the solutions of semi-analytic model. . . .	89
3.7	Minimum star formation efficiency ε_{min} for cloud disruption by H II region expansion based on four different criteria. . . .	92
3.8	Contours of the minimum SFE ε_{min} for cloud disruption by H II region expansion.	93
3.9	Contours of the rate of ionizing photons Q_i and the mean gas density n_{mean} for clouds with $\varepsilon_* = \varepsilon_{\text{min}}$	95
3.10	Contours of the expansion time $t(R_{\text{cl}})$ for clouds with $\varepsilon_* = \varepsilon_{\text{min}}$	98
3.11	Effects of the power-law index k_ρ on ε_{min} for the disruption criterion $v_{\text{sh}}(R_{\text{cl}}) = v_{\text{bind}}$	102

3.12	Effects of trapped infrared radiation on ε_{\min} for the disruption criteria $v_{\text{sh}}(R_{\text{cl}}) = v_{\text{bind}}$ and $v_{\text{sh}}(R_{\text{cl}}) = \sigma$	103
3.13	Probability distributions of (a) the maximum stellar mass $m_{*,\text{max}}$, (b) the ionizing luminosity per stellar mass Ξ , (c) the spectral parameter β , and (d) the mean ionizing photon energy $h\nu_i$ from 10^3 realizations of a star cluster with mass $M_* = 10^2 M_\odot$, $10^3 M_\odot$, and $10^4 M_\odot$ using SLUG.	117
3.14	Dependence on the cluster mass of the median values of (a) the light-to-mass ratio Ψ , (b) the ionizing photon rate per unit mass Ξ , (c) the spectral parameter β , and (d) the mean ionizing photon energy $h\nu_i$	119
4.1	Flowchart of the ART algorithm.	136
4.2	Strong and weak scaling tests for the ART and hydrodynamics solver.	145
4.3	Test of the ART on the radiation field around a single point source in vacuum.	148
4.4	Test of the expansion of an R-type ionization front in a uniform medium with different update schemes.	151
4.5	Test of the expansion of an R-type ionization front in a uniform medium with varying spatial resolution.	152
4.6	Test of the expansion of a D-type ionization front in a uniform medium.	154
4.7	Test of the expansion of a dusty H II region with $Q_i = 10^{51} \text{ s}^{-1}$ and $n_{\text{H}} = 10^3 \text{ cm}^{-3}$	156
4.8	Temporal evolution of shell radius and ionization front radius for an expanding dusty H II region with $Q_i = 10^{51} \text{ s}^{-1}$ and $n_{\text{H}} = 10^3 \text{ cm}^{-3}$	157

4.9	Snapshots of gas surface density and emission measure of ionized gas for the test simulations of a star-forming giant molecular cloud with radiation feedback.	161
4.10	Strong scaling test of a star cluster simulation with $N_{\text{cell}} = 256^3$.	163
4.11	Snapshots of the control model with radiation pressure alone in the plane (a) with $y = -0.4 \text{ pc}$ at $t_{10\%} = 0.7t_{\text{ff},0}$ and (b) with $y = 0.3 \text{ pc}$ at $t_{90\%} = 1.75t_{\text{ff},0}$	166
4.12	Comparison of radial component of the radiation force computed by the ART and M_1 schemes at times $t_{10\%}$ and $t_{90\%}$	167
4.13	Angle-averaged radial radiation force computed by ART and M_1 centered (a) at a sink particle at $t = t_{10\%}$, and (b) at the center of mass of all sinks at $t = t_{90\%}$	169
4.14	(a) Neutral fraction x_n vs. time obtained using the different update schemes for x_n with various C . (b) Difference of x_n relative to the results with $C = 0.001$	177
5.1	Locations of model clouds and observed clouds in the M - Σ plane.	191
5.2	Evolutionary histories of the fiducial model with $M_0 = 10^5 M_\odot$ and $R_0 = 20 \text{ pc}$	195
5.3	Snapshots of the fiducial model in the x - y plane.	197
5.4	Volume rendering of the neutral hydrogen number density n_{H^0} and the electron number density n_e of the fiducial model.	198
5.5	Snapshots projected on the x - y plane of the emission measure of the fiducial model.	200
5.6	(a) Net star formation efficiency ε_* , (b) ejection efficiency ε_{ej} , (c) photoevaporation efficiency ε_{ion} , and (d) neutral ejection efficiency $\varepsilon_{\text{ej,neu}}$ for the PH+RP runs (star symbols) as functions of the initial gas surface density Σ_0	202

5.7	Net SFE ε_* as a function of initial surface density Σ_0 for the models with photoionization only (PH-only), models with radiation-pressure only (RP-only), and models with both photoionization and radiation pressure included (PH+RP). . . .	203
5.8	Timescales for star formation (t_{SF}), cloud destruction (t_{dest}), and effective gas depletion (t_{dep}) for all PH+RP models. . .	206
5.9	Mean radial velocity of the outflowing neutral gas and ionized gas for all PH+RP models.	208
5.10	(a) Mass loss rate $\mu_{\text{H}}\dot{N}_{\text{e}}$ via photoevaporation normalized by the initial cloud mass M_0 , (b) total photoionization rate $Q_{\text{i,eff}}$, (c) fraction of ionizing photons absorbed by neutral hydrogen $f_{\text{ion}} = Q_{\text{i,eff}}/Q_{\text{i}}$, and (d) shielding factor $q = Q_{\text{i,eff}}/\dot{N}_{\text{e}}$ as functions of time.	211
5.11	Dependence on Σ_0 of (a) the dimensionless ionization rate ϕ_{ion} , (b) the dimensionless photoevaporation timescale ϕ_t for clouds, and (c) the product $\phi_{\text{ion}}\phi_t$ for all PH+RP models. . .	217
5.12	Total radial momentum yields $p_{\text{ej,final}}/M_{*,\text{final}}$ in the PH-only, RP-only, and PH+RP runs, as a function of the cloud surface density Σ_0	220
5.13	Average rates of the radial momentum injection due to gas pressure normalized by $\mu_{\text{H}}c_{\text{i}}^2 (12\pi Q_{\text{i}}R_0/\alpha_{\text{B}})^{1/2}$ and by $\dot{M}_{\text{ion}}c_{\text{i}}$, due to radiation pressure normalized by L/c and $(1 - f_{\text{esc}})L/c$ for all the PH+RP models	224
5.14	Injected radial momentum due to gas pressure and radiation pressure forces normalized by the final stellar mass $M_{*,\text{final}}$ for all the PH+RP models.	225
5.15	Ejected ion efficiency (EIE) and (b) ejected neutral efficiency (ENE) at times $t_{*,0} + t_{\text{SN}}$, $t_{*,0} + t_{\text{UV}}$, and t_{final}	234

5.16	Evolutionary histories of key quantities for the fiducial cloud model ($M_0 = 10^5 M_\odot$ and $R_0 = 20$ pc) at varying resolution. .	239
5.17	Snapshots of the gas surface density and emission measure in the fiducial model at varying resolution.	240
5.18	Comparison of the net SFE from the RP-only simulations with those from the theoretical predictions.	242

Chapter 1

Introduction

Giant molecular clouds (GMCs) are a cold condensation of molecular gas in the interstellar medium (ISM). The formation of GMCs is initiated by large-scale converging flows due to gravitational instabilities and/or spiral shocks in disk galaxies (Dobbs et al. 2014). The structure of GMCs is highly irregular over a range of scales, consisting of filaments, sheets, and clumps resulting from interactions between shock waves, a common characteristic of supersonic turbulence (Elmegreen & Scalo 2004). GMCs are permeated by dynamically important magnetic fields, although observations indicate that they are not as important as turbulence in providing support against gravitational collapse (Crutcher 2012).

GMCs are star factories in the universe. There is a good correspondance between tracers of star formation activity and tracers of dense molecular gas over a wide range of scales and environments (Kennicutt & Evans 2012). Most stars form in clusters rather than in isolation, and cluster formation predominantly takes place in dense, gravitationally bound subregions embedded within GMCs (Lada & Lada 2003).

Star formation inevitably involves the release of energy produced through gravitational collapse and nuclear burning, and this occurs in the form of outflows, winds, radiation, and supernovae. These processes are collectively referred to as *stellar feedback*. Although massive stars with $M_* \gtrsim 10 M_\odot$ make up only $\sim 0.2\%$ of all stars formed in numbers (Krumholz 2015), their feedback dominates the energy and momentum deposited into the ISM. The importance of stellar feedback in shaping the structure of the ISM and in regulating star formation in galaxies cannot be overemphasized; the amount of injected energy and momentum by winds, radiation, and supernovae feedback from newborn star clusters is large enough to unbind natal clouds, to drive interstellar turbulence, and potentially to produce galaxy-scale outflows. Therefore, massive star feedback is a key ingredient in many areas of theoretical astrophysics such as formation of star clusters and cloud evolution (Krumholz et al. 2014), galaxy formation and evolution (Naab & Ostriker 2017), formation of first stars (Bromm & Yoshida 2011), and reionization of the universe (Barkana & Loeb 2001).

UV radiation feedback is arguably the most important contributor to the destruction of natal clouds. Hot, massive stars produce strong ultraviolet (UV) radiation fields and create H II regions around them. The overpressurized H II regions expand into the ambient ISM due to thermal pressure of ionized gas as well as radiation pressure on dust grains, returning gas that would otherwise collapse to form stars to the diffuse ISM. Although the topic of molecular cloud dispersal by H II region feedback has been the subject of many classic studies in the field of star formation (e.g., Tenorio-Tagle 1979; Whitworth 1979; Franco et al. 1994; Williams & McKee 1997; Matzner 2002; Krumholz et al. 2006; Dale et al. 2012), quantitative understanding of radiation feedback in turbulent GMC and how star formation efficiency and timescale of destruction depend on star-forming environment is still lacking.

The central theme of this thesis is the dynamics of H II regions and their

destructive effects on the evolution of cluster birth clouds. Using analytic calculation, we study small-scale dynamical instabilities of magnetized ionization fronts and spherical expansion of dusty H II regions by thermal pressure of ionized gas and radiation pressure. We also perform three-dimensional radiation hydrodynamic simulations of star cluster formation, following the evolution of turbulent molecular clouds from self-gravitational collapse in filaments to eventual dispersal by radiation feedback.

The remainder of this chapter is organized as follows. In Section 1.1, we give an overview of the physical properties of GMCs, focusing on those found in nearby galaxies and the Milky Way for which detailed observational data are available. We enumerate some of the major open questions in star formation, namely the problem of slow and inefficient star formation and cloud lifetime. In Section 1.2, we briefly review the dynamics and structure of H II regions and its impact on cloud dispersal. In Section 1.3, we give outline of the remainder of this thesis.

1.1 Giant Molecular Clouds

1.1.1 Physical Properties

The main constituent of molecular clouds¹ is a molecular hydrogen H_2 . H_2 is mainly formed on the surfaces of dust grains and survives in regions that are well shielded from dissociating far-UV radiation by column of dust and molecules. H_2 is a homonuclear molecule that does not possess a permanent dipole moment. Even the lowest-lying rotational quadrupole transition ($J = 2 \rightarrow 0$) has an excitation energy of $h\nu/k_{\text{B}} = 510 \text{ K}$, making H_2 extremely difficult to be detected directly in line emission under typical conditions of

¹There is no standard for the mass threshold above which molecular clouds are regarded as “giant” in the literature. Although we do not make a sharp distinction, we will regard clouds with mass in excess of $\sim 10^4 M_{\odot}$ as GMCs, capable of forming a star cluster of at least over a few hundred solar masses.

cold molecular clouds ($T \sim 10$ K).

Instead, carbon monoxide (CO) molecule and its isotopologue are widely used as a proxy for molecular gas content, assuming coexistence of CO with H₂. CO is the most abundant molecule in the cold ISM besides H₂. In addition, the lowest-level rotational transition ¹²CO $J = 1 \rightarrow 0$ has an energy of $h\nu/k_B = 5.53$ K and a high value of the Einstein coefficient $A = 7.11 \times 10^{-8} \text{ s}^{-1}$ for spontaneous emission, so they can be easily detected even in cold molecular clouds. Even though the emission from ¹²CO($J = 1 \rightarrow 0$) is in general optically thick, there is a good empirical correlation between the frequency-integrated line intensity W_{CO} (or CO luminosity L_{CO}) and column density (or molecular gas mass M_{mol}) of molecular hydrogen N_{H_2} . Calibrations against independent measurements of gas column density such as γ -ray emission (e.g., Strong & Mattox 1996) and dust emission (e.g., Dame et al. 2001) provide a fairly robust conversion factor on the scale of molecular cloud, for example, $X_{\text{CO}} \equiv N_{\text{H}_2}/W_{\text{CO}} \approx 2.0 \times 10^{20} \text{ cm}^{-2} (\text{K km s}^{-1})^{-1}$ (or $\alpha_{\text{CO}} \equiv M_{\text{mol}}/L_{\text{CO}} = 4.3 M_{\odot} (\text{K km s}^{-1} \text{ pc}^2)^{-1}$ for conditions appropriate for the inner part of the Galaxy (see Bolatto et al. 2013 for a recent review).

Since the first detection of H₂ (Carruthers 1970) and CO (Wilson et al. 1970) in the 1970's, a flurry of observational campaigns have been carried out to characterize the physical properties of molecular gas (Dame et al. 1987; Solomon et al. 1987; Scoville et al. 1987; see also Fukui & Kawamura 2010 and Heyer & Dame 2015 for recent reviews). The early CO surveys of the Milky Way revealed that molecular clouds have a range of masses. The mass spectrum of molecular clouds is characterized by a simple or truncated power-law function $dN/d \ln M \propto (M/M_u)^{-\alpha_M}$, where α_M is the power-law index and M_u is the cutoff mass. For the inner Galaxy, the best-fit value of α_M ranges from 1.5 to 1.8 (e.g., Solomon et al. 1987; Williams & McKee 1997; Roman-Duval et al. 2010) with $M_u = 6 \times 10^6 M_{\odot}$ (e.g., Williams & McKee 1997), although the mass spectra in the outer Galaxy and flocculent spirals

appear to have a steeper slope (e.g., Rosolowsky 2005; Gratier et al. 2012). Because each logarithmic mass interval contains the same amount of mass when $\alpha_M = 2$, and because the inner Galaxy dominates the overall molecular gas mass budget (see below), these results indicate that while low-mass clouds greatly exceeds massive clouds in numbers, the bulk of molecular gas mass is contained in most massive clouds. The fraction of molecular gas relative to the atomic hydrogen (H I) tends to decrease with increasing galactocentric radius; inside ~ 3 kpc radius, most of gas is in molecular phase while at solar neighborhood the molecular mass fraction is only $\sim 10\%$. The total mass of H₂ in our galaxy is $(1.0 \pm 0.3) \times 10^9 M_\odot$ (Heyer & Dame 2015).

Gas motions in molecular clouds are highly turbulent and supersonic (e.g., Elmegreen & Scalo 2004). A simple back-of-the-envelope calculation shows that the Reynolds number, the ratio between the molecular diffusion time and the advective time scale, is extremely large in the cold ISM.² Larson (1981) compiled the observations of molecular line emission and identified a power-law relationship between the sizes $L(\text{pc})$ and the velocity dispersions $\Delta v(\text{km s}^{-1})$ of molecular clouds, $\Delta v = CL^\Gamma$, where $C = 1.1$ and $\Gamma = 0.38$. Later studies found similar values of C , albeit with a slightly steeper scaling exponent $\Gamma \approx 0.5$ (e.g., Solomon et al. 1987; Scoville et al. 1987; Heyer & Brunt 2004), which is consistent with the scaling of the velocity power spectrum in Burgers shock-dominated turbulence (e.g., McKee & Ostriker 2007). Note that the measured linewidth on the scale of molecular clouds is much larger than that expected for Doppler broadening resulting from pure thermal motions ($\sim 0.2 \text{ km s}^{-1}$).

The importance of gravitational binding energy relative to turbulent pres-

²For example, taking the molecular viscosity $\nu \sim \lambda_{\text{mfp}} c_s \sim c_s / (n\sigma) \sim 10^4 \text{ cm s}^{-1} / (100 \text{ cm}^{-3} (10^{-7} \text{ cm})^2) = 10^{16} \text{ cm}^2 \text{ s}^{-1}$ and characteristic length and velocity scales of molecular clouds $L \sim 10^{19} \text{ cm}$ and $U \sim 10^5 \text{ cm s}^{-1}$, gives $\text{Re} = LU/\nu \sim 10^8 \gg 1$.

sure support is parametrized by a dimensionless virial parameter

$$\alpha_{\text{vir}} \equiv \frac{5\sigma_v^2 R}{3GM}, \quad (1.1)$$

where G is the gravitational constant, σ_v is the three-dimensional mass-weighted velocity dispersion, and R is the cloud radius (e.g., Bertoldi & McKee 1992; Tan et al. 2014). A cloud that is marginally gravitationally bound has $\alpha_{\text{vir}} = 2$, while a cloud in virial equilibrium corresponds to $\alpha_{\text{vir}} = 1$. The values of α_{vir} for the observed GMCs range from ~ 0.1 to 10, but typical values are $\alpha_{\text{vir}} \sim 1\text{--}3$ (e.g., Roman-Duval et al. 2010; Miville-Deschênes et al. 2017), suggesting that self-gravity plays an important role in controlling the dynamics of molecular clouds. However, the question remains as to whether the observed equipartition between gravitational binding energy and turbulent kinetic energy ($\alpha_{\text{vir}} \sim 1$) is a consequence of clouds being in virial equilibrium (e.g., Heyer et al. 2009) or in global free-fall collapse (e.g., Ballesteros-Paredes et al. 2011). With the cloud surface density defined as $\Sigma \equiv M/(\pi R^2)$, Equation (1.1) allows us to write the velocity dispersion as $\sigma_v = (3\alpha_{\text{vir}}\pi G/5)^{1/2}\Sigma^{1/2}R^{1/2} \propto \Sigma^{1/2}R^{1/2}$. This suggests that the velocity dispersion of a given depends not only on the radius but also on the surface density. Indeed, Heyer et al. (2009) re-examined the Larson’s scaling relationship and found that the velocity coefficient C varies with the square root of the cloud surface density.

While typical GMCs in the Milky Way contain $\sim 10^2 \text{ H}_2 \text{ cm}^{-3}$ on average, the distribution of gas density is far from uniform; in supersonic turbulence a network of interacting shock waves and rarefaction waves create a highly irregular structure over a range of scales. Numerical simulations show that the volume/mass probability density distribution function (PDF) for (both magnetized and unmagnetized) isothermal supersonic turbulence is close to

a lognormal function

$$p_{V/M}(x) = \frac{1}{\sqrt{2\pi}\sigma_x} \exp \left[-(x - \mu_{V/M})^2 / (2\sigma_x^2) \right], \quad (1.2)$$

where $x = \ln(\rho/\bar{\rho})$ with $\bar{\rho}$ being the volume-averaged density. The mean $\mu_{V/M}$ and width σ_x of the lognormal are not independent and related by $\mu_{V/M} = \mp\sigma_x^2/2$. Therefore, while the most of volume is occupied by low-density gas, the bulk of mass is localized in high-density filaments and clumps. Numerical simulations found that the width of the lognormal PDF increases with turbulence velocity dispersion σ_v as $\sigma_x \approx \ln(1 + b^2\mathcal{M}^2\beta/(\beta + 1))$, where $\mathcal{M} = \sigma_v/c_s$ is the turbulent Mach number, $1/3 < b < 1$ is the parameter that depends on the nature of turbulence driving, and the plasma beta β is the ratio between thermal and magnetic pressure (e.g., Ostriker et al. 2001; Federrath et al. 2010; Molina et al. 2012). The density PDF develops a power-law tail at high density regions where self-gravity takes over (e.g., Cho & Kim 2011; Kritsuk et al. 2011; Burkhart et al. 2017). Similar behavior has also been observed in the column density PDFs of star-forming clouds (e.g., Kainulainen et al. 2009; Schneider et al. 2015).

The gas temperature in molecular regions is determined by the balance between heating and cooling processes. Except for densest regions ($n \gtrsim 10^4$ – 10^5 cm^{-3}) where gas is tightly coupled with thermally emitting dust grains, the primary heating source is photoelectrons ejected from small dust grains and PAHs (in outer regions) and electrons created by cosmic ray-induced ionizations (inner regions), while cooling is mainly from the emission of rotational lines of CO molecules.³ Because the line emission is not in general optically thin nor thermally excited, the cooling rate depends sensitively on the gas temperature and escape of emitted photon. Therefore, modeling of ther-

³It is interesting to note that molecular cooling is not a necessary condition for cloud to become cool and hence to form stars; Glover & Clark (2012) found that fine structure emission from C^+ alone can reduce the temperature of atomic gas down to $\sim 20 \text{ K}$.

hydrodynamic processes in molecular clouds requires numerical approach and sophisticated analytic treatment involving chemistry and radiative transfer (Krumholz 2015). Nevertheless, numerical calculations show that molecular gas is in rough thermal equilibrium with temperature $\sim 10\text{--}40$ K (e.g., Glover & Clark 2012; Gong et al. 2017). This result is also roughly consistent with the range of gas temperature in molecular clouds estimated by CO line ratios (Yoda et al. 2010).

1.1.2 Slow and Inefficient Star Formation

The study of the correlation between the molecular gas content in the ISM and star-forming activity provides key information for understanding how efficiently galaxies build up their stellar mass from the cold ISM. Observers combine information on the properties of molecular clouds with the stellar content of the star-forming region. A multitude of different tracers and their combinations are used to infer the star formation rate of a molecular cloud: counting the number of young stellar objects of a certain age (only for nearby clouds), broadband far-UV luminosity flux, narrowband $H\alpha$ luminosity, single band or total infrared flux from thermal dust emission, free-free emission from H II regions, to name but a few (Kennicutt & Evans 2012). The basic idea is that the observed luminosity of a given star-forming tracer can be inverted to stellar mass, assuming the initial mass function (IMF) of stars and light-to-mass conversion factor, the latter of which is computed from stellar evolution and atmospheric models. Different star formation tracers probe star formation activity averaged over certain timescales because of the difference in the age of stellar population contributing to emission.

It is well established that the rate at which gas is converted into stars is much slower than what one would expect from a pure free-fall collapse (e.g., Zuckerman & Palmer 1974; Zuckerman & Evans 1974; Kennicutt & Evans 2012). For example, the total star formation rate in the Milky Way

inferred from the total luminosity of ionizing photons ($Q_i \sim 3 \times 10^{53} \text{ s}^{-1}$) is $\dot{M}_* \sim 1 M_\odot \text{ yr}^{-1}$ (Williams & McKee 1997; Murray & Rahman 2010), while the total molecular gas mass is $M_{\text{gas}} \sim 10^9 M_\odot$ (Heyer & Dame 2015; Miville-Deschênes et al. 2017). The gas depletion timescale, the time required for all the current molecular gas to be converted into stars at the current star formation rate, is then $t_{\text{dep}} = M_{\text{gas}}/\dot{M}_* \sim 10^9 \text{ yr}$. An empirical relationship between the surface density of molecular gas and the surface density of star formation rate in nearby galaxies also indicates that the average depletion time for molecular gas is roughly constant with $\sim 2 \times 10^9 \text{ yr}$ (e.g., Bigiel et al. 2008; Leroy et al. 2013), orders of magnitude larger than the typical free-fall timescale of GMCs $\sim 3\text{--}10 \text{ Myr}$.

Another widely-used, equivalent way of expressing the slowness of star formation is to define the star formation efficiency per free-fall time $\varepsilon_{\text{ff}} \equiv \dot{M}_*/(M_{\text{gas}}/t_{\text{ff}})$, which is simply the fraction of cloud’s gas mass turned into stars per local free-fall time. A number of studies suggest that star formation rate is much smaller than the free-fall rate with $\varepsilon_{\text{ff}} \sim 10^{-2}$ on both galactic scales and scales of individual star-forming clouds (Kennicutt 1998; Krumholz & Tan 2007; Krumholz et al. 2012; Da Rio et al. 2014).

In addition to slow star formation, star formation in molecular clouds is inefficient, in the sense that only a small fraction of available gas mass is converted into stars before the cloud is dispersed. A number of observations that cross-correlate molecular gas mass with stellar mass (traced by $\text{H}\alpha$ emission or free-free emission from ionized gas or mid-infrared emission from UV-heated dust grains) found a wide scatter in the distribution of “instantaneous” star formation efficiency $\text{SFE} = M_*/(M_{\text{gas}} + M_*)$, but the average value is only a few percent (e.g., Myers et al. 1986; Williams & McKee 1997; Carpenter 2000; Evans et al. 2009; García et al. 2014; Lee et al. 2016).

Although we have focused on star formation of molecular clouds in the Milky Way and those found in nearby normal disk galaxies, the slowness and

efficiency of star formation appear to depend on physical scales as well as star-forming environments. The estimated star formation efficiency of compact, cluster-forming clumps (embedded within GMCs) is $\sim 0.1\text{--}0.5$, higher than the typical value on cloud scales (Lada & Lada 2003; Da Rio et al. 2014). The gas depletion time of dense gas in nearby star-forming clouds is ~ 40 Myr on average (Evans et al. 2009). The gas depletion time of dense molecular gas at the center of nuclear starburst spiral galaxies is $\sim 10^8$ yr, orders of magnitude shorter than the typical disk value of $\sim 10^9$ yr (e.g., Leroy et al. 2015; Usero et al. 2015; Gallagher et al. 2018). High surface density, high-pressure clouds in starburst galaxies appear to convert gas into stars more rapidly and efficiently. For example, massive clouds in a local starburst dwarf galaxy, NGC 5253, has estimated star formation efficiency as high as $\sim 50\%$, and is likely to become a super star cluster (e.g., Turner et al. 2015; see also Consiglio et al. 2016).

1.1.3 Lifetime of GMCs

The cloud lifetime is closely related to the slowness and efficiency of star formation. To illustrate this idea, consider an isolated cloud of initial mass M_0 and free-fall time $t_{\text{ff},0}$ forming stars at a steady rate $\dot{M}_{*,0} = \varepsilon_{\text{ff},0} M_0 / t_{\text{ff},0}$. If we define the net star formation efficiency ε_* as the fraction of initial cloud gas mass that would ever become stellar before the cloud is destroyed, the cloud lifetime t_{cloud} is related to ε_* and $\varepsilon_{\text{ff},0}$ by $\varepsilon_* = \varepsilon_{\text{ff},0} t_{\text{cloud}} / t_{\text{ff},0}$. That is, efficiency (ε_*) is the product of slowness ($\varepsilon_{\text{ff},0}$) and cloud lifetime t_{cl} (measured in units of free-fall time).

The lifetime of GMCs has been a hotly debated topic for decades. Based on the measured age spreads ($\lesssim 3$ Myr) of embedded star clusters in nearby star-forming clouds, Hartmann (2001) and Ballesteros-Paredes & Hartmann (2007) argued that lifetime of molecular clouds cannot exceed ~ 5 Myr. Elmegreen (2000) found a correlation between age difference and distance

separation for star clusters in the Large Magellanic Cloud and claimed that GMCs are transient objects that form stars within a single dynamical timescale and are dissipated rapidly by stellar feedback. Kawamura et al. (2009) took statistical approach to estimate the lifetime of GMCs in the Large Magellanic Cloud. They classified observed GMCs into three different types according to their spatial association with H II regions and young star clusters, which indicate the activity of massive star formation. Above the completeness limit of $5 \times 10^4 M_{\odot}$, they found that the number of three different types of GMCs, i.e., GMCs with no SF, with relatively small H II regions, and with both H II regions and star cluster(s), are 72, 142, and 58, respectively. Assuming that the galaxy-wide star formation is steady and that the characteristic lifetime of young star clusters is ~ 10 Myr, the estimated the cloud lifetime is a few dynamical times of ~ 20 – 30 Myr. On the other hand, Scoville (2013) argued that GMCs have long lifetimes because the continuity of ISM mass between H I and H II gives the characteristic lifetime of H₂ is $\tau_{\text{H}_2} \sim \tau_{\text{HI}} M_{\text{H}_2} / M_{\text{HI}}$, which implies τ_{H_2} is at least several 10^8 yr in the molecule-dominated galactic disk.

1.2 UV Radiation Feedback

1.2.1 Structure and Dynamics of H II Regions

Once formed, massive stars produce intense UV photons, creating warm ionized bubbles, or H II regions, around them. Photons with energies above $h\nu_{\text{L}} = 13.6$ eV can ionize atomic hydrogen, and the excess kinetic energy above the ionization potential carried away by the ejected electron is rapidly thermalized via collisions with other free electrons. This photoheating is balanced mainly by the radiative cooling from collisionally excited lines of heavy elements, maintaining the temperature of the ionized gas at a roughly con-

stant value $T_{\text{ion}} \sim 10^4 \text{ K}$.⁴

In addition to thermal equilibrium, the ionized gas in H II regions is in photoionization and recombination equilibrium. The local photoionization rate per unit volume \mathcal{I} and recombination rate per unit volume \mathcal{R} are given by

$$\mathcal{I} = n_{\text{H}^0} \int_{\nu_{\text{L}}}^{\infty} \frac{c\mathcal{E}_{\nu}}{h\nu} \sigma_{\text{H}}(\nu) d\nu \equiv n_{\text{H}^0} \Gamma_{\text{ph}}, \quad (1.3)$$

$$\mathcal{R} = \alpha_{\text{B}} n_{\text{H}^+} n_{\text{e}}, \quad (1.4)$$

where n_{H^0} , n_{H^+} , and n_{e} are the number density of neutral hydrogen, ionized hydrogen, and free electrons, respectively, \mathcal{E}_{ν} is the radiation energy density per unit frequency, $\sigma_{\text{H}}(\nu) \approx 6.3 \times 10^{-18} \text{ cm}^{-2} \text{ H}^{-1} (\nu/\nu_{\text{L}})^{-3}$ is the photoionization cross section, $\alpha_{\text{B}} = 3.03 \times 10^{-13} (T/8000 \text{ K})^{-0.7} \text{ cm}^3 \text{ s}^{-1}$ is the case B recombination coefficient under the ‘‘on-the-spot’’ approximation (assuming that the medium is opaque to all the Lyman series photons), and c is the speed of light. The local photoionization rate Γ_{ph} is the measure of the probability of photoionization per unit time for a neutral hydrogen, while $\alpha_{\text{B}} n_{\text{e}}$ is the measure of the probability of recombination per unit time for a ionized hydrogen. Equating Equations (1.3) and (1.4) gives $x_{\text{n}}/(1-x_{\text{n}})^2 = \Gamma_{\text{ph}} \ll 1/\alpha_{\text{B}} n_{\text{H}}$, where $x_{\text{n}} = n_{\text{H}^0}/n_{\text{H}}$ is the neutral fraction. Under conditions prevalent in typical H II regions, $x_{\text{n}} \approx \Gamma_{\text{ph}}/(\alpha_{\text{B}} n_{\text{H}}) \ll 1$. Therefore, a typical hydrogen atom spends most of its time in an ionized state.

The size of an H II region can be calculated by considering the global photoionization-recombination balance. Consider a single star placed in a static, neutral medium of constant hydrogen number density $n_{\text{H}} = n_2 10^2 \text{ cm}^{-3}$. Let the ionizing photon emission rate be $Q_{\text{i}} = 10^{49} Q_{\text{i},49} \text{ s}$. Initially, an ionization front separating the neutral and ionized regions propagates at speeds

⁴The equilibrium temperature of H II region is expected to be somewhat higher in low-metallicity and/or less dense environments where cooling by line emission is less efficient (Draine 2011a).

much greater than the sound speed of ionized gas, causing little dynamical disturbance to the gas. The expansion speed slows down with time as ionizing photon flux reaching the IF decreases because of geometric dilution as well as attenuation by recombining atoms. When the total case B recombinations inside the H II region (almost) equal to Q_i , the radius of ionization front is $R_{\text{St},0} = (3Q_i/(4\pi\alpha_B n^2))^{1/3} = 3.0Q_{i,49}^{1/3}n_2^{-2/3}$ pc, with the speed of propagation comparable to the sound speed of ionized gas. This radius is called the initial Strömgren radius.

After the rapid formation phase, the expansion of the H II region is driven by thermal pressure of ionized gas and the ionization front is preceded by a strong shock wave. Expansion of an H II region is a classic problem in theoretical astrophysics. Since the shocked neutral shell is geometrically thin and dominates the mass of ionized gas, the equation of motion for the expanding shell can be written as $d/dt(M_{\text{sh}}v_{\text{sh}}) \approx 4\pi r_{\text{sh}}^2 \times 2n k_B T_{\text{ion}}$, where $M_{\text{sh}} \approx \frac{4\pi}{3}(1.4m_{\text{H}}n)r_{\text{sh}}^3$ is the mass of the shell, $v_{\text{sh}} = dr_{\text{sh}}/dt$ is the velocity of the shell, and n_{ion} is the number density of the ionized gas inside the H II region. Assuming the power-law solution of the form $r_{\text{sh}} \propto t^\eta$ and using the scaling from the ionization-recombination balance $n_{\text{ion}} \propto Q_i^{1/2}r_{\text{sh}}^{-3/2} \propto t^{-3\eta/2}$, one obtains $\eta = 4/7$. The expansion stalls when the ionized gas pressure is in equilibrium with the pressure of neutral gas (see Spitzer 1978; Shu 1992; Bisbas et al. 2015; Williams et al. 2018 for full details of the derivation steps).

Dust grains in H II regions absorb both ionizing and non-ionizing UV photons efficiently and impart photon momentum to the gas through collisional and Coulomb drag forces. The size of a dusty H II region is smaller than the dustless case because the number of photons absorbed by gas is reduced (Petrosian et al. 1972). Draine (2011b) found that the density profile inside a dusty H II region is non-uniform when radiation pressure acting on dust grains are considered. He found a family of similarity solutions for static, dusty H II regions. The importance of radiation pressure is

parametrized by the dust optical depth through a dustless Strömgen radius $\tau_{d0} = n_{\text{rms}}\sigma_d R_{\text{St},0} \propto (Q_i n_{\text{rms}})^{1/3}$, where $n_{\text{rms}} = (\int n^2 dV / \int dV)^{1/2}$ is the rms number density of ionized gas inside the H II region, $\sigma_d \sim 10^{-21} \text{ cm}^2 \text{ H}^{-1}$ is the dust absorption cross section per hydrogen atom, and $R_{\text{St},0} = (3Q_i / (4\pi\alpha_B n_{\text{rms}}^2))^{1/3}$. He found that, for $Q_i n_{\text{rms}} \gtrsim 10^{52} \text{ cm}^{-3} \text{ s}^{-1}$, the density profile exhibits a pronounced central cavity surrounded by dense layer of ionized gas.

1.2.2 Theoretical Models on Cloud Disruption

Traditionally, models for cloud disruption focused on the effects of photoionization, arguing that photoevaporation (conversion of neutral gas to ionized gas by ionizing radiation) and dynamical disruption (momentum deposition by gas-pressure-driven expansion of H II regions) can explain the low observed star formation efficiency of Galactic molecular clouds (e.g., Williams & McKee 1997; Krumholz et al. 2006). While this is generally true for low-column clouds ($\Sigma \lesssim 10^2 M_\odot \text{ pc}^{-2}$), thermal pressure alone cannot drive shell expansion against gravity for dense and massive clouds for which the escape velocity exceeds the sound speed of the ionized gas $c_{\text{s,ion}} \sim 10 \text{ km s}^{-1}$. Krumholz & Matzner (2009) examined the importance of radiation pressure exerted by photons in the dynamics of H II regions. They showed that the relative importance of radiation pressure increases with the product of ionized gas density n_{rms} and total ionizing photon rate Q_i , and concluded that radiation pressure dominates the dynamics of H II regions powered by young massive star clusters. Based on the results of Krumholz & Matzner (2009), Fall et al. (2010) developed a simple model for disruption of massive cluster-forming clouds by radiation-driven shell expansion. They found that the efficiency of star formation required for the residual gas to be expelled from the system increases with the mean surface density of the cloud. Murray et al. (2010) developed spherical models for disruption of GMCs found in various star-forming environments, ranging from normal spirals like the Milky

Way to starburst galaxies. They studied shell expansion due to a combination of protostellar outflows, pressure of the photoionized gas, and pressure from direct and dust-reprocessed radiation, for some specific cases of observed clouds.

While these models provide valuable insights, they simplified the situations greatly to make the problem analytically tractable. Real turbulent molecular clouds abound with structures, and this leads to a more complex dynamical model for cloud disruption. For example, the distribution of gravitational and radiation forces is quite different for a turbulent medium than for a uniform medium, because of the log-normal distribution of densities, and this can strongly affect mass loss. Therefore, it is necessary to take allowance for density and velocity inhomogeneities arising from interstellar turbulence, which requires fully three-dimensional numerical simulations.

Numerical simulations of Dale et al. (2012, 2013a) studied the effect of ionizing radiation on disruption of turbulent molecular clouds. They showed that for clouds with an escape speed $v_{\text{esc}} \gtrsim 10 \text{ km s}^{-1}$, the dynamical evolution is largely unaffected by expansion of H II regions. However, these works did not include the effect of radiation pressure on dust grains. More recently, Raskutti et al. (2016) performed three-dimensional radiation hydrodynamic simulations of turbulent molecular clouds focusing exclusively on the effect of nonionizing radiation from stars. They showed that the net star formation efficiency increases with the surface density of clouds and that the net efficiency is larger than that calculated from one-dimensional models. The latter result is expected because there is a broad range of distribution of column densities to the sources, and the outward force from radiation pressure would preferentially eject low-surface density, super-Eddington gas in a gradual fashion.

1.3 Outline of the Thesis

The central questions this thesis addresses are:

- Can small-scale instabilities occurring at ionization fronts explain observed irregular structures at the peripheries of H II regions? Do magnetic fields stabilize or enhance the ionization front instability?
- Can UV radiation feedback alone regulate the efficiency of star formation in GMCs? How does the net star formation efficiency vary with cloud parameters?
- How does the timescales (both in physical units and in units of free-fall time) for star formation and cloud destruction by radiation feedback vary with star-forming environments?
- How efficiently radiation deposit momentum into their environments compared to the predictions based on expansion of a spherical, embedded H II region?
- How does the relative importance of photoionization, radiation pressure feedback vary with cloud parameters?

The rest of this thesis is structured as follows. In Chapter 2, we investigate small-scale dynamical instabilities in ionization fronts by performing a linear stability analysis of ionization fronts threaded by magnetic fields parallel to them. In Chapter 3, we focus on cloud-scale dynamics, and present a model for cloud disruption by expanding dusty H II regionn under spherical symmetry. In Chapter 4, we describe an implementation of adaptive ray tracing module for *Athena* magnetohydrodynamics code. We present details of parallellization strategy for ray tracing module for describing propagation of radiation from point sources, and present the results of various tests to assess the performance and accuracy of our implementation. We also give a detailed

description of simulation setup for star-forming cloud simulations. In Chapter 5, we present the results of simulations of cluster formation and resulting cloud dispersal by radiation feedback. We study dependence of net SFE, lifetime, momentum injection. We also perform detailed analysis of mass loss by photoevaporation and momentum injection, and present semi-analytic model for cloud dispersal. In Chapter 6, we summarize and discuss possible future work.

Chapter 2

Instability of Magnetized Ionization Fronts Surrounding H II Regions¹

Abstract

An ionization front (IF) surrounding an H II region is a sharp interface where a cold neutral gas makes transition to a warm ionized phase by absorbing UV photons from central stars. We investigate the instability of a plane-parallel D-type IF threaded by parallel magnetic fields, by neglecting the effects of recombination within the ionized gas. We find that weak D-type IFs always have the post-IF magnetosonic Mach number $\mathcal{M}_{M2} \leq 1$. For such fronts, magnetic fields increase the maximum propagation speed of the IFs, while reducing the expansion factor α by a factor of $1 + 1/(2\beta_1)$ compared to the unmagnetized case, with β_1 denoting the plasma beta in the pre-IF region. IFs become unstable to distortional perturbations due to gas expansion across the fronts, exactly analogous to the Darrieus-Landau instability

¹A version of this chapter has been published as “Instability of Magnetized Ionization Fronts Surrounding H II Regions,” Kim, J.-G. & Kim, W.-T. 2014, *The Astrophysical Journal*, 797, 135.

of ablation fronts in terrestrial flames. The growth rate of the IF instability is proportional linearly to the perturbation wavenumber as well as the upstream flow speed, and approximately to $\alpha^{1/2}$. The IF instability is stabilized by gas compressibility and becomes completely quenched when the front is D-critical. The instability is also stabilized by magnetic pressure when the perturbations propagate in the direction perpendicular to the fields. When the perturbations propagate in the direction parallel to the fields, on the other hand, it is magnetic tension that reduces the growth rate, completely suppressing the instability when $\mathcal{M}_{M2}^2 < 2/(\beta_1 - 1)$. When the front experiences an acceleration, the IF instability cooperates with the Rayleigh-Taylor instability to make the front more unstable.

2.1 Introduction

H II regions are volumes of ionized gas formed by absorbing UV photons emitted by newborn massive stars. Since the ionized gas is overpressurized by about two orders of magnitude compared to the surrounding neutral medium, it naturally expands to affect the structure and dynamics of a surrounding interstellar medium (ISM). Photoionization appears to play a dual role in regulating star formation in the ISM. On one hand, it can evaporate and disrupt parental molecular clouds, limiting the efficiency of star formation to about a few percents (Matzner 2002; Krumholz et al. 2006; Walch et al. 2012; Dale et al. 2012). On the other hand, the expansion of H II regions may sustain turbulence in clouds (Mellema et al. 2006a; Krumholz et al. 2006; Gritschneider et al. 2010; Dale et al. 2012), and trigger gravitational collapse of compressed shells (Elmegreen & Lada 1977; Hosokawa & Inutsuka 2006; Dale et al. 2009; Iwasaki et al. 2011a) as well as pre-existing clumps in the surrounding medium (e.g., Sandford et al. 1982; Bertoldi 1989; Bisbas et al. 2011), tending to promote further star formation. Understanding how

H II regions evolve may thus be the first step to understand the effect of the star formation feedback on the ISM (see Krumholz et al. 2014, for a recent review).

A number of pioneering studies have explored the dynamical expansion of an H II region (Strömgren 1939; Kahn 1954; Goldsworthy 1958; Axford 1961; Mathews 1965; see also Yorke 1986; Shu 1992). Soon after a central ionizing source is turned on, an ionization front (IF) develops to separate a warm ionized gas with temperature $T \sim 10^4$ K from a cold neutral gas with $T \sim 10^2$ K, with thickness of order of only a few photon mean free paths. At early times, the ionizing photon flux is very large and the IF advances into the neutral medium supersonically, without inducing gas motions. In this early phase, the IF is termed “weak R-type” (Kahn 1954). After roughly a few recombination times (typically $\sim 10^3$ yrs), the initial Strömgren sphere is established within which the recombination rate balances the ionizing rate. At this point, the IF stops propagating and turns to a “R-critical” front. Since the ionized gas behind the IF moves at the sonic speed with respect to the IF, it is able to launch shock waves into the regions ahead of the IF, which in turn makes the R-critical front switch to a “D-critical” front. After this transition, the expansion of the IF is driven by the pressure difference between the ionized and neutral gas. The IF becomes “weak D-type” and moves subsonically with respect to the neutral gas. Given that the main-sequence lifetime of O/B stars is typically $\sim 10^6 - 10^7$ yrs, H II regions spend most of their lives in the weak D-type phase.

While the early efforts based on one-dimensional models under spherical symmetry provide valuable insights on the overall evolution, H II regions are abound with various substructures such as globules, filaments, gaseous pillars (or “elephant trunks”), etc. that cannot be explained by the one-dimensional models (e.g., Sugitani et al. 1991; Hester et al. 1996; Churchwell et al. 2006). One promising explanation may be that these non-spherical structures re-

sult from pre-existing density inhomogeneities and/or turbulent motions in the background medium. Numerical simulations indeed showed that ionizing radiation illuminating on a turbulent, inhomogeneous medium forms non-axisymmetric structures, elongated away from the ionizing source, which may undergo gravitational collapse (e.g., Gritschneider et al. 2010; Arthur et al. 2011; Tremblin et al. 2012).

Although less well-recognized, instability of IFs can be another route to the formation of non-spherical structures. Frieman (1954) and Spitzer (1954) suggested that IFs are susceptible to the Rayleigh-Taylor instability (RTI) when the front is accelerating away from the central source, which may occur due to a steep gradient of the background density or time-varying radiation intensity. Vandervoort (1962) performed a linear stability analysis of an unmagnetized, planar weak D-type IF by including a steady motion of gas relative to the front. He found that such steady-state IFs even without acceleration are unstable at all wavelengths, with the growth rate inversely proportional to the perturbation wavelength. Axford (1964) subsequently showed that the long-wavelength modes are stabilized by the attenuation of radiation due to hydrogen recombination in the perturbed ionized gas if the radiation is normal to the front. Allowing for finite temperature ratio between the neutral and ionized phases, Saaf (1966) obtained an approximate, closed-form expression for the growth rate of the IF instability. Later, Sysoev (1997) discovered the existence of long-wavelength unstable modes even in the presence of recombination. Williams (2002) further extended the previous studies by including oblique incident angles of the ionizing radiation relative to the front, and carried out local isothermal simulations of the instability to study its nonlinear development. By running simulations of expanding H II regions, Garcia-Segura & Franco (1996) and Whalen & Norman (2008) suggested that a shocked shell undergoes a thin-shell instability (Vishniac 1983) to grow into sword-like structures. Ricotti (2014) performed a stability anal-

ysis of accelerating IFs in the limit of incompressible fluids and showed that the recombination stabilizes RTI of IFs (see also Mizuta et al. 2005; Park et al. 2014).

Despite these efforts on the IF instability, however, there are still two main issues that remain to be answered. First, what is the physical nature of the instability? Vandervoort (1962) argued that the IF instability results from a mechanism similar to the “rocket effect” of gradually evaporating clouds (Kahn 1954; Oort & Spitzer 1955). However, the rocket effect acting on the IF can always make the IF move away from the central source and is thus unable to explain the wavy movement of the perturbed IF toward the source, which is the key in the operation of the IF instability, as we will show below. The second issue concerns the effect of magnetic fields on the IF instability. Observations indicate that the ISM around H II regions are permeated by magnetic fields. The typical values for the ratio of magnetic to thermal pressure are ~ 0.3 and ~ 0.04 in cold neutral and molecular clouds, respectively (Crutcher 1999; Heiles & Crutcher 2005). The line-of-sight component of magnetic fields *inside* five Galactic H II regions based on Faraday rotation diagnostics is estimated to be in the range of $B_{\text{los}} \sim 2\text{--}6 \mu\text{G}$, corresponding to subthermal magnetic pressure (Harvey-Smith et al. 2011; see also Heiles & Chu 1980; Heiles et al. 1981; Rodríguez et al. 2012). On the other hand, Zeeman observations of H I and OH absorption lines reveal that the interfaces between the ionized and molecular gases are strongly magnetized with $B_{\text{los}} \sim 50\text{--}300 \mu\text{G}$ and $\sim 250\text{--}750 \mu\text{G}$ for Orion’s Bar and M17, respectively (Brogan et al. 1999; Brogan & Troland 2001; Brogan et al. 2005). Using hydrostatic models, Pellegrini et al. (2007, 2009) confirmed that these clouds are indeed dominated by magnetic pressure.

Importance of magnetic fields associated with IFs has been emphasized by several authors. For instance, Lasker (1966) showed that D-type IFs may contain strong magnetic fields when preceded by an isothermal shock. Red-

man et al. (1998) calculated the jump conditions for IFs with magnetic fields parallel to the fronts. Williams et al. (2000) show that an IF with oblique magnetic fields drives fast- and slow-mode shocks separately as it slows down, suggesting IFs should be subclassified according to the propagation speed. Numerical simulations showed that H II regions threaded by uniform magnetic fields expand aspherically and that both shock strength and density contrast across the IF are reduced in regions where the magnetic fields are parallel to the front (Krumholz et al. 2007a; Mackey & Lim 2011). Although these simulations also reported the deformation of IFs during nonlinear evolution, they lacked spatial resolution to capture the instability of IFs.

In this chapter we address the two issues mentioned above by performing a linear stability analysis of weak D-type IFs with and without magnetic fields. We also include the acceleration/deceleration term in the momentum equation in order to study the combined effects of the RTI and IF instability. We will show that the operating mechanism behind the IF instability is the same as that of the Darrieus-Landau instability (DLI) found in terrestrial flames (e.g. Landau & Lifshitz 1959; Zeldovich et al. 1985). The DLI is inherent to any evaporative interfacial layer through which a cold dense gas expands to become a warm rarefied gas by absorbing heat. Examples include carbon deflagration fronts in Type Ia supernovae (Bell et al. 2004; Dursi 2004), evaporation fronts in the multi-phase ISM (Inoue et al. 2006; Stone & Zweibel 2009; Kim & Kim 2013), and ablation fronts in inertial confinement fusion (Bychkov et al. 2008; Modestov et al. 2009). We will also show that magnetic fields stabilize the IF, although the roles of magnetic pressure and tension are different depending on the propagation direction of perturbations. We will further show that the RTI can enhance the IF instability when the IF is accelerating away from the ionizing source, while buoyancy stabilizes large-scale modes for decelerating IFs.

The rest of this chapter is organized as follows. In Section 2.2, we present

the steady-state equilibrium solutions of IFs, and provide approximate expressions for the density jumps for weak D-type, D-critical, and R-critical fronts. In Section 2.3, we describe our method of a linear stability analysis by classifying the basis modes of perturbations and presenting the perturbed jump conditions across an IF. In Section 2.4, we revisit the case of unmagnetized IFs and clarify the physical nature of the IF instability. In Section 2.5, we analyze the stability of magnetized IFs for perturbations that propagate along the direction either perpendicular (Section 2.5.1) or parallel (Section 2.5.2) to the magnetic fields. The growth rate of the instability is presented for both incompressible and compressible cases. In Section 2.6, we summarize our findings and discuss their astrophysical implications.

2.2 Steady Ionization Fronts

2.2.1 Basic Equations

In this chapter we investigate a linear stability of a magnetized D-type IF subject to an effective external gravity. We treat the IF as a plane-parallel surface of discontinuity and do not include the effects of heat conduction, magnetic diffusion, and gaseous self-gravity. The basic equations of ideal magnetohydrodynamics (MHD) are

$$\frac{\partial \rho}{\partial t} + \nabla \cdot (\rho \mathbf{v}) = 0, \quad (2.1)$$

$$\frac{\partial \mathbf{v}}{\partial t} + (\mathbf{v} \cdot \nabla) \mathbf{v} = -\frac{1}{\rho} \nabla \left(P + \frac{|\mathbf{B}|^2}{8\pi} \right) - \frac{1}{4\pi\rho} (\mathbf{B} \cdot \nabla) \mathbf{B} + \mathbf{g}, \quad (2.2)$$

$$\frac{\partial \mathbf{B}}{\partial t} = \nabla \times (\mathbf{v} \times \mathbf{B}), \quad (2.3)$$

and

$$\nabla \cdot \mathbf{B} = 0, \quad (2.4)$$

where ρ , P , \mathbf{v} , and \mathbf{B} denote the gas density, thermal pressure, velocity, and magnetic fields, respectively. The constant acceleration \mathbf{g} in Equation (2.2) is

to represent a situation where the IF propagation away from a central source speeds up or slows down, which may occur due to a nonuniform background density and/or the geometrical dilution of UV radiation intensity. Since the thermal time scale is usually very short compared to the dynamical time scale of H II regions, we adopt an isothermal equation of state

$$P = c_s^2 \rho, \quad (2.5)$$

where c_s is the speed of sound that takes different values in the regions ahead and behind of an IF separating ionized and neutral gases.

The mass flux across an IF is determined by the amount of UV photons irradiated to it. Let $\mathbf{J}(\boldsymbol{\omega})$ denote the photon number intensity at the front in the direction $\boldsymbol{\omega} \equiv \mathbf{J}/|\mathbf{J}|$ (Vandervoort 1962). Then, the photon flux at the front is equal to $F_{\text{ph}} \equiv -\int \hat{\mathbf{n}} \cdot \mathbf{J} d\omega$, where $\hat{\mathbf{n}}$ is the unit vector normal to the front and the integration is taken over the solid angle of the hemisphere directed toward the ionizing source. In this work, we consider only the case in which the incident ionizing radiation is the normal to the front, i.e., $J(\boldsymbol{\omega}) = F_{\text{ph}} \delta(\boldsymbol{\omega} + \hat{\mathbf{n}})$, with δ being the Dirac delta function.² The condition that all arriving photons are consumed at the IF can then be expressed as

$$\rho \mathbf{v} \cdot \hat{\mathbf{n}} = m_{\text{H}} F_{\text{ph}}, \quad (2.6)$$

where m_{H} is the mass per particle in the neutral atomic medium.

2.2.2 Steady-State Configurations

As an undisturbed state, we seek for one-dimensional steady-state solutions of Equations (2.1)–(2.6). The properties of magnetized IFs were presented by Redman et al. (1998). Here, we focus on finding the background configu-

²When the incident radiation is oblique to the front normal, the IF becomes overstable rather than unstable due to the phase differences between the front deformation and density perturbations (Vandervoort 1962; Williams 2002).

rations of IFs, the stability of which will be explored later. We also present approximate solutions of magnetized IFs for critical and weak D-type fronts.

We place an IF at $z = 0$, with $\hat{\mathbf{z}} = \hat{\mathbf{n}}$. Seen in the stationary IF frame, a cold neutral gas located at $z < 0$ is moving toward the positive- z direction, and becomes ionized and heated upon crossing the IF by absorbing UV photons. The ionized gas in the region at $z > 0$ flows away from the IF with speed and density different from those of the neutral gas. For simplicity, we assume that the initial magnetic fields are oriented along the x -direction such that $\mathbf{B} = B_x \hat{\mathbf{x}}$, parallel to the front. We further assume that the effect of $\mathbf{g} = g\hat{\mathbf{z}}$ is negligible in the initial configurations. Equations (2.1)–(2.6) are then combined to give

$$j_z \equiv \rho_1 v_{z1} = \rho_2 v_{z2} = m_H F_{\text{ph}}, \quad (2.7)$$

$$P_1 + \rho_1 v_{z1}^2 + \frac{B_{x1}^2}{8\pi} = P_2 + \rho_2 v_{z2}^2 + \frac{B_{x2}^2}{8\pi}, \quad (2.8)$$

$$B_{x1} v_{z1} = B_{x2} v_{z2}. \quad (2.9)$$

Here and hereafter, we use the subscripts “1” and “2” to indicate physical quantities evaluated at the neutral-gas region (at $z < 0$) and the ionized-gas region (at $z > 0$), respectively. In Equation (2.7), j_z denotes the (constant) mass flux across the IF.

We define the dimensionless expansion factor

$$\alpha \equiv \frac{v_{z2}}{v_{z1}} = \frac{\rho_1}{\rho_2} = \frac{B_{x1}}{B_{x2}}, \quad (2.10)$$

and the heating factor

$$\theta \equiv \frac{c_{s2}^2}{c_{s1}^2}. \quad (2.11)$$

The heating factor across the IF approximately equals $2T_2/T_1$, where T_1 and T_2 are the temperatures of the neutral and ionized gases, respectively. Since $T_1 = 10^2$ K and $T_2 = 10^4$ K typically, we in this work take a fiducial value of

$\theta = 200$. We define the plasma parameter as

$$\beta \equiv c_s^2/v_A^2, \quad (2.12)$$

with $v_A \equiv B_x/\sqrt{4\pi\rho}$ being the Alfvén speed. We also define the sonic Mach number, the Alfvénic Mach number, and the magnetosonic Mach number as

$$\mathcal{M}_S \equiv \frac{v_z}{c_s}, \quad \mathcal{M}_A \equiv \frac{v_z}{v_A}, \quad \mathcal{M}_M \equiv \frac{v_z}{(c_s^2 + v_A^2)^{1/2}}, \quad (2.13)$$

respectively. It then follows that $\mathcal{M}_M^2 = \mathcal{M}_S^2/(1 + \beta^{-1}) = \mathcal{M}_A^2/(1 + \beta)$.

Using Equations (2.10), (2.11), and (2.13), one can show that

$$\beta_2 = \alpha\theta\beta_1, \quad (2.14)$$

$$\mathcal{M}_{A2}^2/\mathcal{M}_{A1}^2 = \alpha^3, \quad (2.15)$$

and

$$\frac{\mathcal{M}_{M2}^2}{\mathcal{M}_{M1}^2} = \alpha^3 \frac{1 + \beta_1^{-1}}{\theta\alpha + \beta_1^{-1}}. \quad (2.16)$$

We combine Equations (2.7)–(2.9) to eliminate v_{z2} and B_{x2} in favor of ρ_2 and write the resulting equation in dimensionless form as

$$\mathcal{M}_{S1}^2\alpha^3 - \left(1 + \mathcal{M}_{S1}^2 + \frac{1}{2\beta_1}\right)\alpha^2 + \theta\alpha + \frac{1}{2\beta_1} = 0, \quad (2.17)$$

which is a cubic equation in α (Redman et al. 1998; see also Draine 2011a).

Unmagnetized IFs

For unmagnetized fronts ($\beta_1 \rightarrow \infty$), Equation (2.17) is reduced to the following quadratic equation:

$$\mathcal{M}_{S1}^2\alpha^2 - (\mathcal{M}_{S1}^2 + 1)\alpha + \theta = 0. \quad (2.18)$$

Equation (2.18) has real solutions only if $\mathcal{M}_{S1} \leq \mathcal{M}_D$ or $\mathcal{M}_{S1} \geq \mathcal{M}_R$, where

$$\begin{aligned}\mathcal{M}_D &= \sqrt{\theta} - \sqrt{\theta - 1} \approx 1/(2\sqrt{\theta}), \\ \mathcal{M}_R &= \sqrt{\theta} + \sqrt{\theta - 1} \approx 2\sqrt{\theta},\end{aligned}\tag{2.19}$$

denote the sonic Mach numbers of the D- and R-critical fronts, respectively (e.g., Kahn 1954; Spitzer 1978; Shu 1992). The corresponding expansion factors are

$$\begin{aligned}\alpha_D &= \theta + \sqrt{\theta^2 - \theta} \approx 2\theta, \\ \alpha_R &= \theta - \sqrt{\theta^2 - \theta} \approx 1/2,\end{aligned}\tag{2.20}$$

for the D- and R-critical fronts, respectively. Both D- and R-critical IFs satisfy

$$\mathcal{M}_{S2,D} = \mathcal{M}_{S2,R} = 1,\tag{2.21}$$

exactly in the downstream side.

Fronts with $\mathcal{M}_{S1} < \mathcal{M}_D$ and $\mathcal{M}_{S1} > \mathcal{M}_R$ are called D-type and R-type IFs, respectively. For these, Equation (2.18) has two real solutions for α . IFs with a smaller and larger density jump (i.e., smaller and larger $|\alpha - 1|$) are further termed “weak” and “strong” fronts, respectively. The fact that the inflow velocity \mathcal{M}_{S1} relative to an IF in a steady state cannot be arbitrary is because the temperature of the post-IF region is prespecified to θ greater than unity. In the limit of $\theta \rightarrow 1$, $\mathcal{M}_D = \mathcal{M}_R = 1$, and Equation (2.18) yields $\alpha = 1$ for a strong front and $\alpha = \mathcal{M}_{S1}^{-2}$ for a weak front, the second of which is simply the jump condition for an isothermal shock.

Magnetized IFs

The presence of magnetic fields certainly changes the critical Mach numbers as well as the expansion factors. Since the coefficients of the third- and zeroth-degree terms are real and positive, Equation (2.17) always has a negative real root. The other two roots should thus be real and positive for

physically meaningful fronts, which limits the ranges of \mathcal{M}_{S1} for magnetized IFs. Redman et al. (1998) showed that the critical Mach number $\mathcal{M}_{S1,crit}$ and β_1 are related to each other via α by

$$\mathcal{M}_{S1,crit}^2 = \frac{\theta(\alpha^2 + 1) - 2\alpha}{\alpha(\alpha - 1)^2(\alpha + 2)}, \quad (2.22)$$

and

$$\beta_1 = \frac{(\alpha - 1)^2(\alpha + 2)}{2\alpha(2\theta\alpha - \alpha^2 - \theta)}. \quad (2.23)$$

The smaller and larger values of $\mathcal{M}_{S1,crit}$ correspond to \mathcal{M}_D and \mathcal{M}_R , respectively, for magnetized fronts. Equations (2.22) and (2.23) are combined to give

$$\mathcal{M}_{S1,crit}^2 = \frac{\theta}{\alpha^2} \left[1 + \frac{1}{\alpha\theta\beta_1} \right], \quad (2.24)$$

which yields

$$\mathcal{M}_{M2,crit}^2 = \frac{\mathcal{M}_{S2,crit}^2}{1 + \beta_2^{-1}} = 1, \quad (2.25)$$

exactly. Therefore, weak D-type IFs always have $0 < \mathcal{M}_{M2} \leq 1$, while $\mathcal{M}_{M2} \geq 1$ for strong D-type IFs. Substituting Equation (2.24) into Equation (2.17), we have

$$\left(1 + \frac{1}{2\beta_1} \right) \alpha^3 - 2\theta\alpha^2 + \left(\theta - \frac{3}{2\beta_1} \right) \alpha + \frac{1}{\beta_1} = 0, \quad (2.26)$$

whose two positive roots correspond to the expansion factors for the magnetized D- and R-critical fronts. Note that Equation (2.26) reduces to Equation (2.20) for $\beta_1 \rightarrow \infty$.

Figure 2.1(a) plots the relationships between β_1 and $\mathcal{M}_{S1,crit}$ (black solid lines) and between β_1 and α_{crit} (black dashed lines) for $\theta = 200$. Clearly, \mathcal{M}_D and \mathcal{M}_R are close to the unmagnetized value given in Equation (2.19) for $\beta_1 \gtrsim 10$. They increase as β_1 decreases. For $\theta \gg 1$ and $\beta_1\theta \gg 1$, one can expand Equations (2.26) relative to the unmagnetized solutions to show that

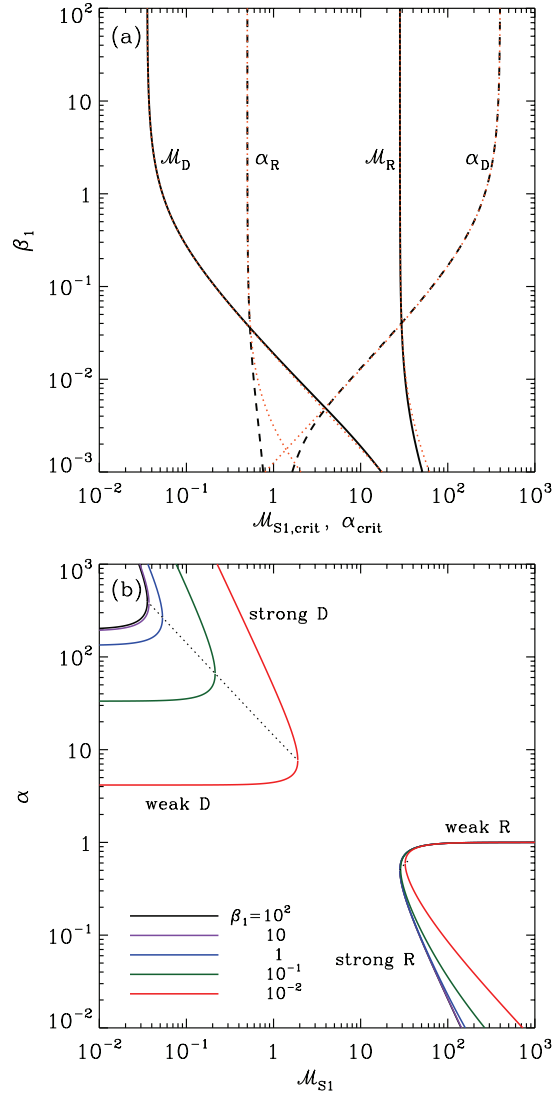


Figure 2.1 (a) Dependence on β_1 of the critical Mach numbers \mathcal{M}_D and \mathcal{M}_R (black solid lines) and the critical expansion factors α_D and α_R (black dashed lines) for $\theta = 200$. The red dotted lines give the analytic approximations (Equations (2.27) and (2.28)). (b) Expansion factors α of magnetic IFs with $\theta = 200$ for various β_1 . The dotted curves mark the loci of the critical fronts where strong and weak solutions merge.

the critical expansion factors are approximately

$$\begin{aligned}\alpha_{\text{D}} &\approx 2\theta \left(1 + \frac{1}{2\beta_1}\right)^{-1}, \\ \alpha_{\text{R}} &\approx \frac{1}{2} + \frac{5}{16\theta\beta_1}.\end{aligned}\tag{2.27}$$

The corresponding critical Mach numbers are

$$\begin{aligned}\mathcal{M}_{\text{D}}^2 &\approx \frac{1}{4\theta} \left(1 + \frac{1}{2\beta_1}\right)^2, \\ \mathcal{M}_{\text{R}}^2 &\approx 4\theta \left(1 + \frac{3}{4\beta_1\theta}\right).\end{aligned}\tag{2.28}$$

These are plotted as red dotted lines in Figure 2.1(a), in good agreement with the full solutions for $\beta_1 \gtrsim 10^{-2}$.³

Figure 2.1(b) plots the expansion factors of magnetized IFs for different values of β_1 as functions of $\mathcal{M}_{\text{S}1}$ for $\theta = 200$. The dotted lines draw the loci of the D- and R-critical IFs. Weak R-type IFs have $\alpha \approx 1$, and their physical conditions are almost unaffected by the presence of magnetic fields (Lasker 1966). For weak D-type IFs displayed in the lower parts of the left curves, however, magnetic fields lower the expansion factor considerably, especially for $\beta_1 \lesssim 1$.

Figure 2.2 plots $\mathcal{M}_{\text{M}1}$ and α as functions of $\mathcal{M}_{\text{M}2}$ for weak D-type IFs with $\theta = 200$. Magnetic fields clearly reduce α , while increasing $\mathcal{M}_{\text{M}1}$ for given $\mathcal{M}_{\text{M}2}$. Since $\mathcal{M}_{\text{S}1}^2 \ll 1$ and $\beta_2 \gg 1$ for weak D-type IFs, Equation (2.8) approximately gives

$$\alpha \approx \theta \frac{1 + \mathcal{M}_{\text{S}2}^2}{1 + 1/(2\beta_1)} \approx \theta \frac{1 + \mathcal{M}_{\text{M}2}^2}{1 + 1/(2\beta_1)},\tag{2.29}$$

³Draine (2011a) derived approximate expressions for the critical Mach numbers of magnetized IFs by taking $\alpha \gg 1$ and thus $B_{x1}/B_{x2} \gg 1$ in Equation (2.8). In the limit of $\theta \gg 1$ and $\beta_1\theta \gg 1$, his results are equal to ours only for \mathcal{M}_{D} . Since R-type IFs have $\alpha < 1$ and $B_{x1} < B_{x2}$, the approximation he made is not valid for \mathcal{M}_{R} .

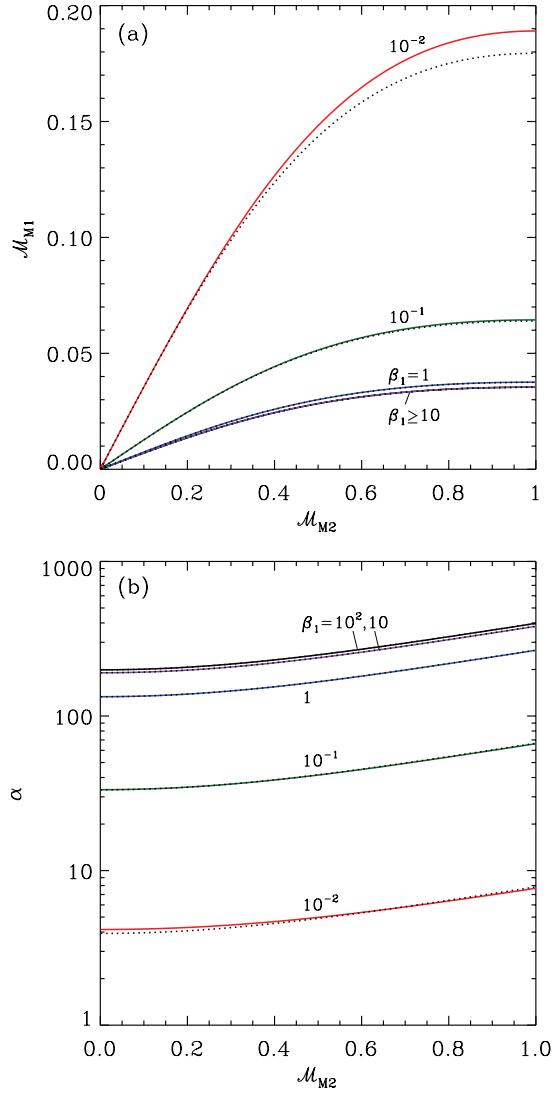


Figure 2.2 Dependence of (a) the upstream magnetosonic Mach number \mathcal{M}_{M1} and (b) the expansion factor α on the downstream magnetosonic Mach number \mathcal{M}_{M2} for weak D-type IFs with $\theta = 200$. The solid lines give the full numerical results, while the dotted lines draw the approximate solutions (Equations (2.29) and (2.30)).

which, combined with Equation (2.16), yields

$$\mathcal{M}_{M1} \approx \frac{1}{\theta^{1/2}} \frac{1 + 1/(2\beta_1)}{(1 + \beta_1^{-1})^{1/2}} \frac{\mathcal{M}_{M2}}{1 + \mathcal{M}_{M2}^2}, \quad (2.30)$$

These are plotted in Figure 2.2 as dotted lines, in good agreement with the full solutions (better than 6% for $\beta_1 \geq 10^{-2}$). Note that the second approximation in Equation (2.29) follows from the approximation $\beta_2 \gg 1$, which is usually the case unless $\beta_1\theta \lesssim 1$ (see Equation (2.14) and Figure 2.2). Equation (2.29) then indicates that the magnetic fields reduce the expansion factor α by a factor of $1 + 1/(2\beta_1)$ compared to the unmagnetized value.

2.3 Perturbation Equations

We now apply small-amplitude perturbations to a steady IF with $\mathbf{v}_A = v_A \hat{\mathbf{x}}$ found in the preceding section, and then explore their stability. Since the background flow is uniform except at $z = 0$, Equations (2.1)–(2.5) can be linearized on both sides of the front as

$$\left(\frac{\partial}{\partial t} + \mathbf{v} \cdot \nabla \right) \rho' = -\rho \nabla \cdot \mathbf{v}', \quad (2.31)$$

$$\left(\frac{\partial}{\partial t} + \mathbf{v} \cdot \nabla \right) \mathbf{v}' = -\frac{1}{\rho} \nabla \left(P' + \frac{\mathbf{B} \cdot \mathbf{B}'}{4\pi} \right) + \frac{1}{4\pi\rho} (\mathbf{B} \cdot \nabla) \mathbf{B}', \quad (2.32)$$

$$\left(\frac{\partial}{\partial t} + \mathbf{v} \cdot \nabla \right) \mathbf{B}' = (\mathbf{B} \cdot \nabla) \mathbf{v}' - \mathbf{B} (\nabla \cdot \mathbf{v}'), \quad (2.33)$$

$$\nabla \cdot \mathbf{B}' = 0, \quad (2.34)$$

$$P' = c_s^2 \rho', \quad (2.35)$$

where the primes denote the perturbed quantities. We assume that the perturbations vary in space and time as

$$\propto \exp(i\mathbf{k} \cdot \mathbf{x} + \Omega t), \quad (2.36)$$

where $\mathbf{k} = (k_x, k_y, k_z)$ and Ω are the wavenumber and the frequency of the perturbations, respectively. We take a convention that k_x and k_y are real, while Ω and k_z are complex.

Equations (2.31)–(2.35) are then reduced to

$$\Omega_D \rho' = -\rho(i\mathbf{k} \cdot \mathbf{v}'), \quad (2.37)$$

$$\Omega_D \mathbf{v}' = -i\mathbf{k} \left(\frac{c_s^2}{\rho} \rho' + v_A b'_x \right) + ik_x v_A \mathbf{b}', \quad (2.38)$$

$$\Omega_D \mathbf{b}' = ik_x v_A \mathbf{v}' - iv_A (\mathbf{k} \cdot \mathbf{v}') \hat{\mathbf{x}}, \quad (2.39)$$

$$\mathbf{k} \cdot \mathbf{b}' = 0, \quad (2.40)$$

where $\Omega_D \equiv \Omega + ik_z v_z$ is the Doppler-shifted frequency and $\mathbf{b}' \equiv \mathbf{B}' / \sqrt{4\pi\rho}$ has the units of velocity. Equations (2.37)–(2.40) are combined to yield

$$(\Omega_D^2 + k_x^2 v_A^2) \mathbf{v}' + [(c_s^2 + v_A^2)(\mathbf{k} \cdot \mathbf{v}') - k_x v_A^2 v'_x] \mathbf{k} - k_x v_A^2 (\mathbf{k} \cdot \mathbf{v}') \hat{\mathbf{x}} = 0, \quad (2.41)$$

(e.g., Lithwick & Goldreich 2001). This is a generic dispersion relation for waves in a uniform medium moving at a constant velocity.

2.3.1 Canonical Modes

As is well known, Equation (2.41) gives algebraic relations for three different kinds of propagating waves: Alfvén, fast, and slow waves (e.g., Shu 1992). In this subsection, we derive the dispersion relation of each mode and the corresponding eigenvector with arbitrary normalization, in a form suitable for our perturbation analysis.

Shear Alfvén modes

Shear Alfvén waves are transverse waves with $\mathbf{k} \cdot \mathbf{v}' = 0$, for which Equation (2.41) is reduced to

$$\Omega_D^2 + k_x^2 v_A^2 = 0. \quad (2.42)$$

It then follows from Equations (2.37)–(2.39) that $\mathbf{b}' = \pm \mathbf{v}'$, $(\mathbf{k} \cdot \mathbf{v}') = (\mathbf{k} \cdot \mathbf{b}') = 0$, and $v'_x = b'_x = 0$, indicating that Alfvén waves are incompressible and thus do not rely on thermal pressure. The eigenvector of shear Alfvén waves is thus

$$P' = 0, \quad (2.43)$$

$$\mathbf{v}' = (0, k_z, -k_y), \quad (2.44)$$

$$\mathbf{b}' = (0, \pm k_z, \mp k_y), \quad (2.45)$$

where the signs distinguish two oppositely propagating waves. As we will explain below, shear Alfvén waves with $k_z \neq 0$ are not excited by the distortions of an IF that we impose and thus out of consideration in our analysis.

Fast and Slow modes

When both the magnetic forces and the thermal pressure are important, we take the scalar product of Equation (2.41) with \mathbf{k} and \mathbf{v}_A . This results in two homogeneous linear equations for $(\mathbf{k} \cdot \mathbf{v}')$ and $(\mathbf{v}_A \cdot \mathbf{v}')$. The condition for the existence of non-trivial solutions yields

$$\Omega_D^4 + k^2(c_s^2 + v_A^2)\Omega_D^2 + k_x^2 k^2 c_s^2 v_A^2 = 0, \quad (2.46)$$

where $k = (k_x^2 + k_y^2 + k_z^2)^{1/2}$. This is a usual dispersion relation for fast and slow MHD waves, for which \mathbf{v}_A , \mathbf{v}' , and \mathbf{k} lie in the same plane. We use Equations (2.37)–(2.40) to write the perturbed quantities in terms of v'_z as

$$\frac{P'}{\rho} = -\frac{(\Omega_D^2 + k^2 v_A^2)}{ik_z \Omega_D} v'_z, \quad (2.47)$$

$$\mathbf{v}' = \left(\frac{k_x(\Omega_D^2 + k^2 v_A^2)}{k_z \Omega_D^2}, \frac{k_y}{k_z}, 1 \right) v'_z, \quad (2.48)$$

$$\mathbf{b}' = \left(\frac{-i(k_y^2 + k_z^2)v_A}{k_z \Omega_D}, \frac{ik_x k_y v_A}{k_z \Omega_D}, \frac{ik_x v_A}{\Omega_D} \right) v'_z, \quad (2.49)$$

for $\Omega_D \neq 0$ and $k_z \neq 0$. Note that the eigenvectors of fast and slow modes with $\Omega_D \neq 0$ can be completely specified by assigning one variable (e.g., v'_z).

Equation (2.46) has a special slow mode with $\Omega_D = 0$, occurring when $k_x v_A = 0$ (for $k \neq 0$). Equations (2.37)–(2.40) then give

$$k_y v'_y + k_z v'_z = 0, \quad (2.50)$$

and

$$\frac{P'}{\rho} + v_A b'_x = 0. \quad (2.51)$$

This corresponds to *vortex* modes⁴, requiring no perturbation in the total pressure. These modes are generated at a curved IF and then simply advected downstream from the front. Although Equation (2.51) is a general expression for the perturbed pressure of the vortex modes, the perturbations we consider in the present work require that $P' = b'_x = 0$ (see Section 2.5.1).

For later purposes, we introduce the following dimensionless quantities:

$$\sigma \equiv \frac{\Omega}{v_{z1}(k_x^2 + k_y^2)^{1/2}}, \quad \nu \equiv \frac{ik_z}{(k_x^2 + k_y^2)^{1/2}}, \quad \cos \psi \equiv \frac{k_x}{(k_x^2 + k_y^2)^{1/2}}. \quad (2.52)$$

Equation (2.46) can then be expressed as

$$\mathcal{M}_M^2 \sigma_D^4 + \hat{\alpha}^2 (1 - \nu^2) \sigma_D^2 + \hat{\alpha}^4 (1 - \nu^2) \frac{\cos^2 \psi}{(1 + \beta^{-1}) \mathcal{M}_A^2} = 0, \quad (2.53)$$

where $\sigma_D = \sigma + \hat{\alpha} \nu$, and $\hat{\alpha} \equiv v_z / v_{z1} = 1$ in the upstream side and $\hat{\alpha} = \alpha$ in the downstream side.

2.3.2 Perturbed Jump Conditions

Perturbations given in Equation (2.36) result from sinusoidal distortions of an IF which would otherwise remain planar. Since the IF involves discontinuities of fluid quantities, there are certain conditions that the perturbation variables

⁴The vortex mode is a special case of more general entropy-vortex modes (e.g., Landau & Lifshitz 1959). In our formulation, the entropy perturbations are absent due to the choice of an isothermal equation of state.

should obey at the perturbed IF. Let the shape of a deformed IF be described by

$$\mathcal{F}(x, y, z, t) = z - \zeta e^{\Omega t + ik_x x + ik_y y} = 0, \quad (2.54)$$

where $\zeta (\ll k^{-1})$ denotes the amplitude of the IF distortion. Then, the unit vector normal to the perturbed front is given by $\hat{\mathbf{n}} = \nabla \mathcal{F} / |\nabla \mathcal{F}| = \hat{\mathbf{z}} - ik_x \zeta \hat{\mathbf{x}} - ik_y \zeta \hat{\mathbf{y}}$, while the two unit vectors tangential to the front can be chosen as $\hat{\mathbf{t}}_a = \hat{\mathbf{x}} + ik_x \zeta \hat{\mathbf{z}}$ and $\hat{\mathbf{t}}_b = \hat{\mathbf{y}} + ik_y \zeta \hat{\mathbf{z}}$, to the first order in $k\zeta$.

It is straightforward to show that in the frame comoving with the perturbed IF, the velocity components parallel to $\hat{\mathbf{n}}$, $\hat{\mathbf{t}}_a$, and $\hat{\mathbf{t}}_b$ are given by

$$v_n = v_z + v'_z - \zeta \Omega, \quad (2.55)$$

$$\mathbf{v}_t = (v'_x + ik_x \zeta v_z, v'_y + ik_y \zeta v_z), \quad (2.56)$$

respectively. Similar expressions for the magnetic fields read

$$B_n = B'_z - ik_x \zeta B_x, \quad (2.57)$$

$$\mathbf{B}_t = (B_x + B'_x, B'_y), \quad (2.58)$$

respectively.

Equations (2.1)–(2.3) can be recast into flux-conservative form and integrated over the small volume located on the front. By applying the divergence theorem, we obtain the following set of jump conditions

$$\Delta [\rho v_n] = 0, \quad (2.59)$$

$$\Delta \left[\rho v_n \mathbf{v}_t - \frac{B_n \mathbf{B}_t}{4\pi} \right] = 0, \quad (2.60)$$

$$\Delta \left[\rho v_n^2 + P + \frac{B_t^2}{8\pi} \right] = -\Delta [\rho] g \zeta, \quad (2.61)$$

$$\Delta [v_n \mathbf{B}_t - B_n \mathbf{v}_t] = 0, \quad (2.62)$$

and

$$\Delta [B_n] = 0, \quad (2.63)$$

(see, e.g., Shu 1992). Here, $\Delta[f] \equiv f(z = \zeta + 0) - f(z = \zeta - 0) = f_2 - f_1$ indicates the difference of a quantity f evaluated at immediately behind and ahead of the front.

Substituting Equations (2.55)–(2.58) in Equations (2.59)–(2.63), one can show that the zeroth-order terms lead to Equations (2.7)–(2.9). Taking the first-order terms, one obtains

$$\Delta [\rho' v_z + \rho(v'_z - \Omega\zeta)] = 0, \quad (2.64)$$

$$\Delta [\rho v_z(v'_x + ik_x\zeta v_z) - \rho v_A(b'_z - ik_x\zeta v_A)] = 0, \quad (2.65)$$

$$\Delta [\rho v_z(v'_y + ik_y\zeta v_z)] = 0, \quad (2.66)$$

$$\Delta [\rho' v_z^2 + 2\rho v_z(v'_z - \Omega\zeta) + \rho v_z p' + \rho v_A b'_x] = -\Delta [\rho] g\zeta, \quad (2.67)$$

$$\Delta [\rho^{1/2}(b'_x v_z + v_A(v'_z - \Omega\zeta))] = 0, \quad (2.68)$$

$$\Delta [\rho^{1/2} b'_y v_z] = 0, \quad (2.69)$$

$$\Delta [\rho^{1/2}(b'_z - ik_x\zeta v_A)] = 0, \quad (2.70)$$

where $p' = P' / (\rho v_z)$. Note that only two among Equations (2.68)–(2.70) are independent since the induction equation automatically satisfies the divergence-free condition for magnetic fields.⁵ Therefore, the perturbed jump conditions at the front provide six constraints for the perturbation variables.

An additional constraint can be obtained by linearizing Equation (2.6) as

$$\rho'_1 v_{z1} + \rho_1(v'_{z1} - \Omega\zeta) = m_H F'_{\text{ph}}, \quad (2.71)$$

where F'_{ph} is the perturbed photon flux at the distorted IF. For simplicity,

⁵With help of the vertical component of Equation (2.39) and Equation (2.40), one can derive Equation (2.70) directly from a linear combinations of Equations (2.68) and (2.69).

we set $F'_{\text{ph}} = 0$ in the present work, implying that the mass flux per unit area through the IF is unchanged in the perturbed state. We note that F'_{ph} can be non-vanishing when the effect of finite probability for photon absorption in the ionized region is considered, suppressing the instability at scales larger than the recombination length scale (see Axford 1964; Williams 2002).

Defining $Z \equiv \zeta(k_x^2 + k_y^2)^{1/2}v_{z1}$ and $G \equiv g/((k_x^2 + k_y^2)^{1/2}v_{z1}^2)$, Equations (2.64)–(2.69) and (2.71) can be simplified as

$$\mathcal{M}_{S1}^2 p'_1 + v'_{z1} - \sigma Z = 0, \quad (2.72)$$

$$\mathcal{M}_{S2}^2 p'_2 + v'_{z2} - \sigma Z = 0, \quad (2.73)$$

$$v'_{x1} - \mathcal{M}_{A1}^{-1} b'_{z1} - v'_{x2} + \mathcal{M}_{A2}^{-1} b'_{z2} + i(1 + \mathcal{M}_{A1}^{-2} - \alpha(1 + \mathcal{M}_{A2}^{-2})) \cos \psi Z = 0, \quad (2.74)$$

$$v'_{y1} - v'_{y2} + i(1 - \alpha) \sin \psi Z = 0, \quad (2.75)$$

$$\left((1 + \beta_1^{-1})(1 - \mathcal{M}_{M1}^2) + \cos^2 \psi \frac{\mathcal{M}_{A1}^{-2}(1 - \alpha^{-2})}{(\sigma + \nu)^2} \right) p'_1 - (1 + \beta_2^{-1})(1 - \mathcal{M}_{M2}^2) p'_2 + (1 - \alpha^{-1}) G Z = 0, \quad (2.76)$$

$$b'_{x1} - \mathcal{M}_{A1}^{-1} \mathcal{M}_{S1}^2 p'_1 - \alpha^{1/2} (b'_{x2} - \mathcal{M}_{A2}^{-1} \mathcal{M}_{S2}^2 p'_2) = 0, \quad (2.77)$$

$$b'_{y1} - \alpha^{1/2} b'_{y2} = 0. \quad (2.78)$$

Of the equations above, the derivation of Equation (2.76) is not trivial, requiring to utilize Equations (2.46)–(2.49): we present the necessary steps for it in Appendix 2.A.

2.4 Instability of Unmagnetized IFs

We now want to explore the instability of an isolated, weak D-type IF. Here, the term “isolated” implies that disturbances are generated only at the front and decay at a large distance from the front. Of the MHD waves described above, therefore, we consider only waves that are evanescent away from the front, i.e., $\text{Im}(k_z) < 0$ in the upstream side ($z < 0$) and $\text{Im}(k_z) > 0$ in the

downstream side ($z > 0$), which is imposed by the regularity condition at infinity. In our method, finding the growth rate as well as the eigenstate of unstable modes takes two steps: (1) we express the perturbation variables as a linear superposition of the canonical waves at each side of the perturbed IF; (2) we then require the perturbation variables to fulfill the jump conditions at the perturbed IF.

Vandervoort (1962) was the first who studied the instability of unmagnetized IFs. In this section, we revisit the problem to exemplify our technique in the most simplest case, and to elucidate the physical nature of the instability in analogy to the DLI. The case of magnetized IFs will be presented in Section 2.5.

In the absence of magnetic fields, the background flows possess rotational symmetry with respect to the z -axis, so that we may take $k_y = 0$ (hence $\cos \psi = 1$) and $v'_y = 0$ without any loss of generality. The solutions of Equation (2.53) in the limit of $\mathcal{M}_A, \beta \rightarrow \infty$ are

$$\nu_a = \frac{1}{1 - \mathcal{M}_S^2} \left[\mathcal{M}_S^2 \frac{\sigma}{\hat{\alpha}} \pm \sqrt{\mathcal{M}_S^2 \left(\frac{\sigma^2}{\hat{\alpha}^2} - 1 \right) + 1} \right], \quad (2.79)$$

$$\nu_v = -\sigma/\hat{\alpha}, \quad (2.80)$$

where the subscripts “a” and “v” stand for acoustic and vortex modes, respectively, which are only modes that constitute the perturbations at each side of the IF. Since the vortex mode is produced by the front deformation and then passively advected by the background flows, it exists only in the downstream side.

Let $\mathbf{S} = (p', v'_x, v'_z)$ describe the eigenvectors of the canonical waves such that

$$\mathbf{S}_a = (-1 - \sigma/(\hat{\alpha}\nu_a), i/\nu_a, 1), \quad (2.81)$$

and

$$\mathbf{S}_v = (0, -i\sigma/\alpha, 1) . \quad (2.82)$$

The boundary conditions for isolated IFs require that $\text{Re}(\nu_a) > 0$ in the upstream neutral region, while $\text{Re}(\nu_a) < 0$ in the downstream ionized region, as mentioned above. For unstable modes with $\text{Re}(\sigma) > 0$ and $\mathcal{M}_S^2 < 1$, one can write the total perturbations as a linear combination of the canonical modes as

$$\mathbf{S}_1 = C_{a1}\mathbf{S}_{a1} , \quad (2.83)$$

in the upstream side, and

$$\mathbf{S}_2 = C_{a2}\mathbf{S}_{a2} + C_{v2}\mathbf{S}_{v2} , \quad (2.84)$$

in the downstream side. Here, C_{a1} , C_{a2} , and C_{v2} are the coefficients to be determined, and ν_a in Equation (2.79) should be calculated with the positive and negative signs for \mathbf{S}_{a1} and \mathbf{S}_{a2} , respectively.

Plugging Equations (2.83) and (2.84) into Equations (2.72)–(2.74) and (2.76) for $v_A = 0$, we are left with a set of linear equations for four variables ($C_{a1}, C_{a2}, C_{v2}, Z$). These can be cast into a matrix form as

$$\begin{pmatrix} 1 - \mathcal{M}_{S1}^2(1 + \sigma/\nu_{a1}) & 0 & 0 & -\sigma \\ 0 & 1 - \mathcal{M}_{S2}^2(1 + \sigma/(\alpha\nu_{a2})) & 1 & -\sigma \\ \nu_{a1}^{-1} & -\nu_{a2}^{-1} & \sigma/\alpha & 1 - \alpha \\ -(1 - \mathcal{M}_{S1}^2)(1 + \sigma/\nu_{a1}) & (1 - \mathcal{M}_{S2}^2)(1 + \sigma/(\alpha\nu_{a2})) & 0 & (1 - \alpha^{-1})G \end{pmatrix} \begin{pmatrix} C_{a1} \\ C_{a2} \\ C_{v2} \\ Z \end{pmatrix} = 0 . \quad (2.85)$$

In order to have a nontrivial solution, the 4×4 matrix in Equation (2.85) must have a vanishing determinant. This yields

$$(\sigma - \Gamma_2\alpha) \left[1 + \Gamma_1 \left(\frac{\sigma}{\alpha} - \frac{\alpha - 1}{\sigma} \right) \right] = (\alpha - \Gamma_2\sigma) \left[\sigma + \Gamma_1 \left(1 + \frac{1 - \alpha G}{\alpha \sigma} \right) \right] , \quad (2.86)$$

where

$$\Gamma_1 = [1 + \mathcal{M}_{S1}^2(\sigma^2 - 1)]^{1/2} , \quad (2.87)$$

$$\Gamma_2 = [1 + \mathcal{M}_{S2}^2(\sigma^2/\alpha^2 - 1)]^{1/2}, \quad (2.88)$$

which is our desired dispersion relation for instability of unmagnetized IFs. Note that Equation (2.86) is the same as Equation (79) of Vandervoort (1962, see also Bychkov et al. 2008) when the direction of radiation is normal to the front.⁶

In the incompressible limit of $\mathcal{M}_S \rightarrow 0$, Equation (2.86) reduces to

$$\sigma = \frac{\alpha}{\alpha + 1} \left(\sqrt{1 + \alpha - \frac{1}{\alpha} + \frac{\alpha^2 - 1}{\alpha^2} G} - 1 \right). \quad (2.89)$$

In more general, compressible cases, however, Equation (2.86) does not provide a closed-form expression for σ . Although it can be converted to a polynomial by repeated squaring (e.g., Sysoev 1997), the resulting 16-th order polynomial in σ is not so illuminating that we present only the numerical results here. Figure 2.3(a) plots as solid lines the dimensionless growth rate σ as a function of \mathcal{M}_{S2} for $\theta = 100, 200$, and 300 , when $G = 0$. For fixed θ , σ increases slightly with increasing $\mathcal{M}_{S2} \lesssim 0.7$ due to the increase in α (see Figure 2.2(b) and Equation (2.89)). As \mathcal{M}_{S2} increases further, σ starts to decrease and tends to zero at $\mathcal{M}_{S2} = 1$ corresponding to the D-critical front. Figure 2.3(a) also plots as dashed line σ for $\alpha = 100, 200$, and 300 , showing that σ monotonically decreases with increasing \mathcal{M}_{S2} for fixed α . This suggests that the stabilization of the IF instability is caused by gas compressibility, as we will explain below.

Note that the incompressible dispersion of Equation (2.89) with $G = 0$ is identical to the dispersion relation of the DLI of an evaporation front in an incompressible fluid (e.g., Zeldovich et al. 1985; Inoue et al. 2006; Kim & Kim 2013). Furthermore, Equation (2.86) is equal to the full dispersion relation of the DLI when the effect of compressibility is included (Bychkov et al. 2008).

⁶The conversion of symbols used in Vandervoort (1962) to those in the present chapter is $n \rightarrow \mathcal{M}_{S1}\sigma$, $y_1 \rightarrow \Gamma_1$, and $y_2 \rightarrow \theta^{1/2}\Gamma_2$.

This suggests that the physical nature of the instability of an IF is the same as that of the DLI. When an IF is disturbed, the gas expansion across the front makes the pressure drop (rise) on the part of the distorted IF convex (concave) toward the ionizing source. The changes in the pressure induce gas motions such that more (less) neutral gas is directed toward to the convex (concave) parts. Since the ionizing photon flux at the IF is assumed to be fixed, this makes the convex (concave) parts advance further toward (recede away from) the ionizing source in a runaway fashion, indicative of instability.

When gas compressibility is considered, the pressure drop (rise) is partly translated into the drop (rise) in the perturbed density via $\rho'/\rho \sim \mathcal{M}_S^{-2} P'/P$. This causes less changes in the perturbed velocities compared to the incompressible limit. Consequently, the amount of the perturbed mass flux at the distorted IF is reduced, making the instability grow at a slower rate. For the D-critical IF with $\mathcal{M}_{S2} = 1$, the perturbations in the downstream side are unable to propagate into the upstream side since the ionized gas is advected at the sound speed. Accordingly, the neutral gas does not respond to the deformation of the IF and remains unperturbed. This can be seen more quantitatively from Equation (2.76) which gives $p'_1 = 0$ when $G = 0$, which in turn gives $C_{a1} = 0$ in Equation (2.83) hence $\sigma = 0$ from Equation (2.72).

Figure 2.3(b) plots σ for $\theta = 200$ and differing G , showing the positive G corresponding to an accelerating front make the front more unstable. When the term involving G dominates, Equation (2.89) recovers the growth rate of the RTI. When $G > 0$, therefore, the DLI and RTI cooperate constructively. For decelerating IFs with $G < 0$, on the other hand, large scale modes with $kv_{z1}^2/|g| < \alpha$ are suppressed by buoyancy. The instability is completely quenched by buoyancy, provided

$$G < -\alpha(1 - \mathcal{M}_{S2}^2)^{1/2}, \quad (2.90)$$

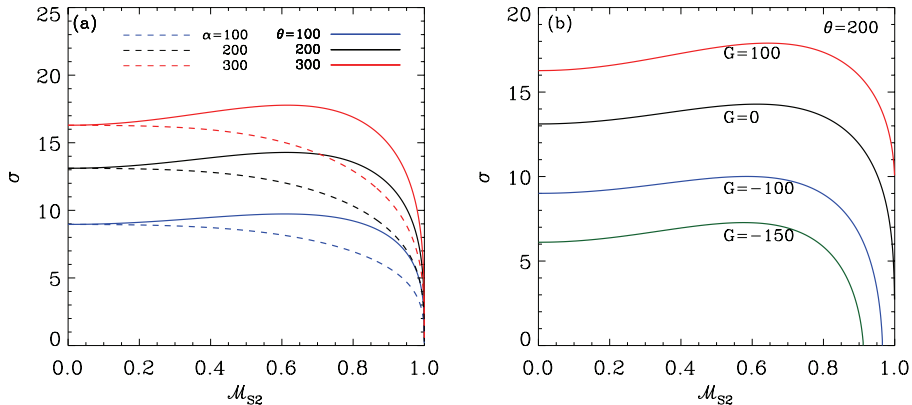


Figure 2.3 (a) Dimensionless growth rate σ of the instability of unmagnetized IFs as a function of the downstream sonic Mach number \mathcal{M}_{S2} for fixed heating factor θ (solid lines) and for fixed expansion factor α (dashed lines) with $G = 0$. (b) Dependence of σ on G for $\theta = 200$. Accelerating fronts with larger G are more unstable.

which can be obtained by imposing $\sigma \rightarrow 0$ in Equation (2.86).⁷

2.5 Instability of Magnetized IFs

For the stability of magnetized IFs, we consider only two types of perturbations: (1) perturbations with $k_x = 0$ and $k_y \neq 0$ (i.e., $\cos \psi = 0$) and (2) perturbations with $k_x \neq 0$ and $k_y = 0$ (i.e., $\cos \psi = 1$). While these perturbations are not most general, they can nevertheless capture the essential physics of magnetic fields in the IF instability.

⁷It has been known that an accelerating ablation front is stabilized by thermal conduction (e.g., Bychkov et al. 1994). The relevant dispersion relation is given by the Takabe formula, $\Omega = a\sqrt{k\bar{g}} - bkv_1$, where k is the perturbation wavenumber, v_1 is the velocity of the ablation front, and $a \sim 0.9$ and $b \sim 3-4$ are dimensionless constants (Takabe et al. 1985). The corresponding stability criterion written in our notation reads $G = g/(kv_1^2) < b^2/a^2 \sim 10$.

2.5.1 Cases with $k_x = 0$ and $k_y \neq 0$

Perturbations with $k_x = 0$ and $k_y \neq 0$ do not bend the field lines. Since the front deformation does not involve the x -direction, we only need to consider motions in the y - z plane (i.e., $v'_x = 0$). Equation (2.39) then gives $b'_y = b'_z = 0$, implying that the perturbed magnetic fields exert magnetic pressure only in the propagation direction of the disturbances and that shear Alfvén waves are not excited.

For $\cos \psi = 0$, Equation (2.53) has two solutions

$$\nu_f = \frac{1}{1 - \mathcal{M}_M^2} \left[\mathcal{M}_M^2 \frac{\sigma}{\hat{\alpha}} \pm \sqrt{\mathcal{M}_M^2 \left(\frac{\sigma^2}{\hat{\alpha}^2} - 1 \right) + 1} \right], \quad (2.91)$$

$$\nu_s = -\sigma/\hat{\alpha}, \quad (2.92)$$

where the subscripts “f” and “s” stand for fast and slow modes, respectively. Note that Equation (2.91) is identical to Equation (2.79) provided \mathcal{M}_S is changed to \mathcal{M}_M . Note also that Equation (2.92) is a dispersion relation for the magnetized vortex modes with $\Omega_D = 0$, which exist only in the downstream side from the IF, as explained in Section 2.3.1.

Now, let $\mathbf{S} = (p', v'_y, v'_z, b'_x)$ describe the eigenvectors of the basis modes. Then, Equations (2.47)–(2.49) give

$$\mathbf{S}_f = \left[-\frac{1}{1 + \beta^{-1}} \left(1 + \frac{\sigma}{\hat{\alpha}\nu_f} \right), \frac{i}{\nu_f}, 1, -\frac{\mathcal{M}_M^2}{\mathcal{M}_A} \left(1 + \frac{\sigma}{\hat{\alpha}\nu_f} \right) \right], \quad (2.93)$$

for the fast modes. On the other hand, the eigenvectors of the slow modes in the downstream side are given by

$$\mathbf{S}_{s2} = (0, -i\sigma/\alpha, 1, 0), \quad (2.94)$$

from Equation (2.50). Note that here we take $P' = b'_x = 0$ from Equation (2.51) since P' and b'_x arising from the front distortions should have the same sign when $k_x = 0$. Using the condition that the waves should decay far away

from the IF, one can then write the state vectors as

$$\mathbf{S}_1 = C_{f1}\mathbf{S}_{f1}, \quad (2.95)$$

$$\mathbf{S}_2 = C_{f2}\mathbf{S}_{f2} + C_{s2}\mathbf{S}_{s2}, \quad (2.96)$$

where C_{f1} , C_{f2} , C_{s2} are coefficients to be determined.

Following the same steps as in the case of unmagnetized IFs, we apply the jump conditions (Equations (2.72), (2.73), (2.75), and (2.76)) to obtain a linear system of four equations in four unknowns (C_{f1} , C_{f2} , C_{s2} , Z).⁸ From the condition for non-trivial solutions, we derive the dispersion relation for the instability of the magnetized IFs with $k_x = 0$ and $k_y \neq 0$, which is identical to Equation (2.86), provided \mathcal{M}_S is replaced by \mathcal{M}_M .

Figure 2.4 plots as solid lines the dimensionless growth rate σ for various β_1 when $\theta = 200$ and $G = 0$, as a function of \mathcal{M}_{M2} . While the overall shape of the dispersion relations is unchanged compared to the hydrodynamics cases, magnetic fields certainly reduce σ . The dotted lines plot the unmagnetized dispersion relation, Equation (2.86), with α replaced by $\alpha/(1+1/(2\beta_1))$ which is the reduced expansion factor due to magnetic fields (e.g., Equation (2.29)). The good agreement between the solid and dotted lines suggests that the reduced growth rate in the magnetized case results simply from a decreased α in the background state. When $k_x = 0$, magnetic fields remain straight and magnetized flows in the linear regime behave similarly to unmagnetized flows, with fast magnetosonic waves playing the exactly same role as acoustic waves.

2.5.2 Cases with $k_x \neq 0$ and $k_y = 0$

We examine the stability of magnetized IFs with respect to perturbations lying in the x - z plane, i.e., $k_x \neq 0$, $k_y = 0$, and $v'_y = b'_y = 0$, for which

⁸Equation (2.77) is automatically satisfied by our choice of the state vectors.

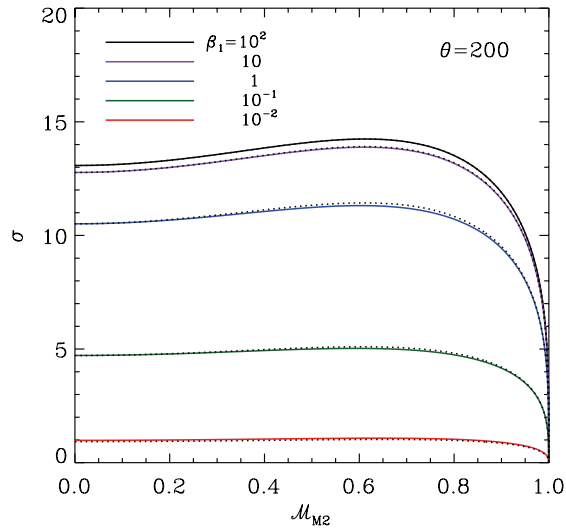


Figure 2.4 Growth rate of the instability of magnetized IFs with $\theta = 200$ and differing β_1 as a function of \mathcal{M}_{M2} , when the perturbations propagate perpendicular to the initial magnetic fields ($k_x = 0$). The solid lines plot the full numerical results of the magnetized cases, while the dotted lines draw the hydrodynamic counterparts (Equation (2.86)) with α reduced by a factor of $1 + 1/(2\beta_1)$.

not only magnetic pressure but also magnetic tension affect the stability. Note that these requirements preclude the presence of shear Alfvén waves in the perturbations (e.g., Equations (2.44) and (2.45)). We first consider the incompressible limit and then generalize the results to compressible cases.

Incompressible Limit

For simplicity let us take the limit $c_s \rightarrow \infty$ ($\rho' = 0$), while the Alfvén speed remains finite, so that $\beta \rightarrow \infty$ and $\mathcal{M}_M \rightarrow 0$. Equation (2.53) with $\cos \psi = 1$ then yields

$$\nu_{p\pm} = \pm 1, \quad (2.97)$$

and

$$\nu_{s\pm} = -\sigma/\hat{\alpha} \pm i\mathcal{M}_A^{-1}, \quad (2.98)$$

where the subscripts “p” and “s” refer to the potential modes and slow (or pseudo-Alfvén) modes, respectively. The potential modes are a special case of the acoustic mode (or fast mode). For unstable modes with $\text{Re}(\sigma) > 0$, it is apparent that the wave motions in the upstream side can be specified by the potential mode with $\nu_{p+} = 1$, while the other potential mode with $\nu_{p-} = -1$ and two slow modes with $\nu_{s\pm}$ (propagating in the opposite directions along the background magnetic fields) coexist in the downstream side.

Defining $\mathbf{S} = (p', v'_x, v'_z, b'_x, b'_z)$, one can use Equations (2.37)–(2.40) to construct the eigenvector of each mode as

1. Upstream potential mode:

$$\mathbf{S}_{p1} = \left(-(\sigma + 1), i, 1, -\frac{\mathcal{M}_{A1}^{-1}}{\sigma + 1}, \frac{i\mathcal{M}_{A1}^{-1}}{\sigma + 1} \right), \quad (2.99)$$

2. Downstream potential mode:

$$\mathbf{S}_{p2} = \left(\frac{\sigma - \alpha}{\alpha}, -i, 1, -\frac{\alpha\mathcal{M}_{A2}^{-1}}{\sigma - \alpha}, \frac{i\alpha\mathcal{M}_{A2}^{-1}}{\sigma - \alpha} \right), \quad (2.100)$$

3. Downstream slow modes:

$$\mathbf{S}_{s2\pm} = (\mp i\mathcal{M}_{A2}\nu_{s2\pm}, i\nu_{s2\pm}, 1, \pm i\nu_{s2\pm}, \pm 1), \quad (2.101)$$

where $\nu_{s2\pm}$ is the value of $\nu_{s\pm}$ in Equation (2.98) evaluated at the downstream side. The total perturbations are then given by

$$\mathbf{S}_1 = C_{p1}\mathbf{S}_{p1}, \quad (2.102)$$

and

$$\mathbf{S}_2 = C_{p2}\mathbf{S}_{p2} + C_{s2+}\mathbf{S}_{s2+} + C_{s2-}\mathbf{S}_{s2-}, \quad (2.103)$$

in the upstream and downstream sides, respectively.

Plugging these expressions into the perturbed jump conditions (Equations (2.72)–(2.74), (2.76), and (2.77)), one obtains a linear system of five equations in five unknowns ($C_{p1}, C_{p2}, C_{s2+}, C_{s2-}, Z$), which is given in a matrix form by

$$\begin{pmatrix} 1 & 0 & 0 & 0 & -\sigma \\ 0 & 1 & 1 & 1 & -\sigma \\ 1 - \frac{\mathcal{M}_{A1}^{-2}}{\sigma + 1} & 1 + \frac{\mathcal{M}_{A2}^{-2}\alpha}{\sigma - \alpha} & -\nu_{s2+} - i\mathcal{M}_{A2}^{-1} & -\nu_{s2-} + i\mathcal{M}_{A2}^{-1} & 1 + \mathcal{M}_{A1}^{-2} - \alpha(1 + \mathcal{M}_{A2}^{-2}) \\ \mathcal{A} & -\frac{\sigma - \alpha}{\sigma - \alpha} & i\mathcal{M}_{A2}^{-1}\nu_{s2+} & -i\mathcal{M}_{A2}^{-1}\nu_{s2-} & (1 - \alpha^{-1})G \\ -\frac{\mathcal{M}_{A1}^{-1}}{\sigma + 1} & -\frac{\alpha^{3/2}\mathcal{M}_{A2}^{-1}}{\sigma - \alpha} & -i\alpha^{1/2}\nu_{s2+} & i\alpha^{1/2}\nu_{s2-} & 0 \end{pmatrix} \begin{pmatrix} C_{p1} \\ C_{p2} \\ C_{s2+} \\ C_{s2-} \\ Z \end{pmatrix} = 0, \quad (2.104)$$

where $\mathcal{A} \equiv -(\sigma + 1) [1 + (1 - \alpha^{-2})\mathcal{M}_{A1}^{-2}/(\sigma + 1)^2]$.

We set the determinant of the matrix to zero to obtain the dispersion relation

$$\begin{aligned} \sigma^3 + \frac{3\alpha + 1}{\alpha + 1}\sigma^2 - \frac{1}{\alpha(\alpha + 1)} \left[\alpha^3 - \left(3 + \frac{1}{\mathcal{M}_{A1}^2} - G \right) \alpha^2 - G\alpha - \frac{1}{\mathcal{M}_{A1}^2} \right] \sigma \\ - \frac{\alpha - 1}{\alpha(\alpha + 1)} \left[\alpha^2 + \left(G - \frac{1}{\mathcal{M}_{A1}^2} \right) \alpha + \mathcal{M}_{A1}^{-2} \right] = 0. \end{aligned} \quad (2.105)$$

Note that Equation (2.105) is identical to Equation (112) of Dursi (2004), which is the dispersion relation for the incompressible DLI in a magnetized

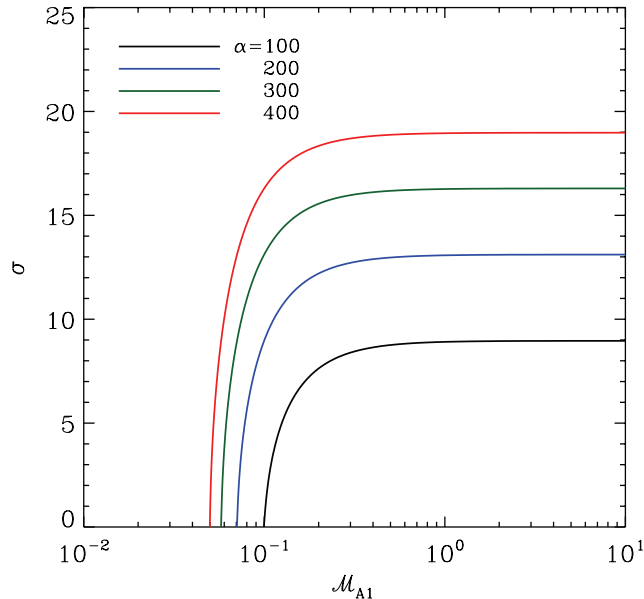


Figure 2.5 Incompressible growth rate σ of the instability of magnetized IFs as a function of the upstream Alfvénic Mach number \mathcal{M}_{A1} , for in-plane perturbations with $k_y = 0$. For given α , σ becomes smaller as the field strength increases (or \mathcal{M}_{A1} decreases). The instability is completely suppressed at sufficiently small \mathcal{M}_{A1} (see Equation (2.107)).

gas. This again demonstrates that the IF instability and the DLI share the common physical origin. In the limit of $\mathcal{M}_{A1} \rightarrow \infty$, Equation (2.105) recovers Equation (2.89) in the unmagnetized case. On the other hand, we write Equation (2.105) in dimensional form and collect lowest-order terms in v_{z1} to obtain

$$\Omega^2 = gk_x \frac{\alpha - 1}{\alpha + 1} - k_x^2 v_{A1}^2 \frac{1 + \alpha^2}{\alpha(\alpha + 1)}, \quad (2.106)$$

which is the usual dispersion relation for the RTI of a magnetized contact discontinuity, for which magnetic fields play a stabilizing role (e.g., Chandrasekhar 1961).

For given α and \mathcal{M}_{A1} , Equation (2.105) has only one, if any, purely-

growing solution with $\text{Re}(\sigma) > 0$ and $\text{Im}(\sigma) = 0$, while the other two correspond to decaying solutions. Figure 2.5 plots the growth rate of the unstable mode for various α as a function of \mathcal{M}_{A1} , showing that σ decreases as the field strength increases. It is a simple matter to show that the instability becomes completely suppressed, provided

$$\mathcal{M}_{A1} < \sqrt{\frac{\alpha - 1}{\alpha(\alpha + G)}}, \quad \text{for stability.} \quad (2.107)$$

The stabilization is due to magnetic tension forces that resist gas motions across the field lines. This can be seen more quantitatively as follows. The dimensionless growth rate with $v_A = G = 0$ in the incompressible limit is proportional to the fractional increase in the mass flux, i.e., $j'_z/j_z = v'_{z1}/v_{z1} = \sigma k_x \zeta \approx \sqrt{\alpha} k_x \zeta$ for $\alpha \gg 1$. The incoming velocity change v'_{z1} is due solely to the potential mode, which we denote by $v'_{z,p}$. On the other hand, the distorted front deforms the magnetic fields by an amount $B'_z/B_x \sim k_x v'_z/\Omega = k_x \zeta$ from Equations (2.39) and (2.71). The associated velocity change induced by magnetic tension is $|v'_{z,B}| = |B'_z|/\sqrt{4\pi\rho} \sim v_A k_x \zeta$, which tends to reduce $v'_{z,p}$ and hence j'_z . Note that $|v'_{z,p}| \sim |v'_{z,B}|$ when $\mathcal{M}_{A1} \sim \alpha^{-1/2}$, entirely consistent with Equation (2.107) for large α .

Compressible Cases

We now consider more general compressible perturbations that are still limited to the plane defined by the flow direction and magnetic fields in the initial configuration. Although Equation (2.53), a quartic equation in ν , has algebraic solutions, they are too complicated for practical uses, so that we calculate the four solutions numerically for given σ , $\hat{\alpha}$, \mathcal{M}_M , and \mathcal{M}_A . From Equations (2.47)–(2.49), the corresponding eigenvector $\mathbf{S} = (p', v'_x, v'_z, b'_x, b'_z)$ can

be written as

$$\mathbf{S} = \left(\frac{-\chi}{\hat{\alpha}\nu\sigma_D}, \frac{i\chi}{\nu\sigma_D^2}, 1, \frac{-\hat{\alpha}\nu\mathcal{M}_A^{-1}}{\sigma_D}, \frac{i\hat{\alpha}\mathcal{M}_A^{-1}}{\sigma_D} \right), \quad (2.108)$$

where $\chi \equiv \sigma_D^2 + \hat{\alpha}^2\mathcal{M}_A^{-2}(1 - \nu^2)$.

Similarly to the incompressible case, two of the solutions represent fast modes, while the remaining two are slow modes. For unstable modes with $\text{Re}(\sigma) > 0$, there is only one root with $\text{Re}(\nu) > 0$ in the upstream side, which is a fast mode denoted by ν_{f1} . On the other hand, the downstream side has three roots with $\text{Re}(\nu) < 0$: one pure real solution is a fast mode (ν_{f2}) and two complex roots are slow modes ($\nu_{s2\pm}$). Upon finding ν_{f1} , ν_{f2} , and $\nu_{s2\pm}$, we calculate the corresponding eigenvectors \mathbf{S}_{f1} , \mathbf{S}_{f2} , and $\mathbf{S}_{s2\pm}$ from Equation (2.108). We then construct the perturbations as

$$\mathbf{S}_1 = C_{f1}\mathbf{S}_{f1}, \quad (2.109)$$

and

$$\mathbf{S}_2 = C_{f2}\mathbf{S}_{f2} + C_{s2+}\mathbf{S}_{s2+} + C_{s2-}\mathbf{S}_{s2-}, \quad (2.110)$$

in the upstream and downstream sides, respectively, with the unknown coefficients C_{f1} , C_{f2} , and $C_{s2\pm}$.

Substituting Equations (2.109) and (2.110) in Equations (2.72)–(2.74) and (2.76)–(2.77), we obtain a set of five linear equations in five unknowns (C_{f1} , C_{f2} , C_{s2+} , C_{s2-} , Z). The resulting equation in a matrix form is displayed in Appendix 2.B. To obtain non-trivial solutions, we set the determinant of the matrix \mathbf{A} in Equation (2.118) equal to zero. To calculate σ numerically, we first take trial values for the real and imaginary parts of σ and calculate four ν 's, ensuring that the perturbed flow decays away from the front. We then check if the determinant vanishes or not. If the determinant is not sufficiently small, we return to the first step and change σ . We repeat the iterations until the converged solutions are obtained within tolerance of 10^{-6} . We have

confirmed that our numerical method gives the same dispersion relations as Equations (2.86) for unmagnetized cases and (2.105) for $c_s^2 \gg v_z^2, v_A^2$.

We find that σ of the unstable modes is pure real, as in the incompressible case, and goes to zero for the D-critical IF regardless of β_1 . Figure 2.6(a) plots the resulting growth rates as a function of \mathcal{M}_{M2} for $\theta = 200$ and $G = 0$ but differing β_1 , while Figure 2.6(b) plots contours of σ in the β_1 - \mathcal{M}_{M2} plane. For $\beta_1 \gg 1$, the growth rates are not much different from the unmagnetized counterparts, except for $\mathcal{M}_{M2} \ll 1$. As the magnetic field strength increases, however, not only do the growth rates decrease but also the unstable range of \mathcal{M}_{M2} shrinks. For small \mathcal{M}_{M2} , the magnetic tension forces stabilize the instability, as in the incompressible limit. For $\alpha \gg 1$ and $G = 0$, Equation (2.107) with the help of Equations (2.29) and (2.30) can be written as

$$\mathcal{M}_{M2} < \left(\frac{2}{2\beta_1 - 1} \right)^{1/2}, \quad \text{for stability,} \quad (2.111)$$

indicating that the instability of magnetized IFs is completely suppressed by magnetic tension when $\beta_1 \leq 3/2$. The dashed line in Figure 2.6(b) draws Equation (2.111), in excellent agreement with the stability criterion found numerically for the whole range of \mathcal{M}_{M2} .

2.6 Summary and Discussion

2.6.1 Summary

We have performed a linear stability analysis of magnetized, weak D-type IFs around H II regions. This work extends Vandervoort (1962) who analyzed the stability of IFs in the absence of magnetic fields. To simplify the situation, we consider an IF in plane-parallel geometry, perpendicular to the incident direction of ionizing photons, and ignore the effects of recombination in the ionized gas in the present work. We further assume that magnetic fields are parallel to the front and that the gas remains isothermal with different

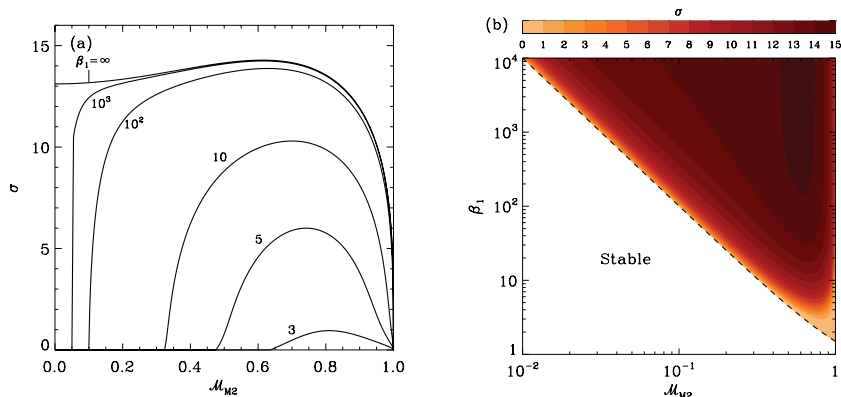


Figure 2.6 (a) Compressible growth rate σ of the instability of magnetized IFs as a function of \mathcal{M}_{M2} and (b) the contour of σ in the β_1 - \mathcal{M}_{M2} plane. The perturbations are limited to $k_y = 0$, and $\theta = 200$ and $G = 0$ are chosen. The instability is suppressed by magnetic tension at low \mathcal{M}_{M2} and by compressibility at $\mathcal{M}_{M2} \rightarrow 1$. The black dashed line in (b) draws the stability criteria (Equation (2.111)) in the limit $\theta \gg 1$, in good agreement with the full numerical results.

temperatures in the neutral and ionized sides of the front. We first solve for equilibrium configurations of steady IFs across which total mass, momentum, and magnetic fluxes are conserved. We find that for weak D-type IFs, magnetic fields tend to increase the maximum propagation speed of the IFs, while reducing the expansion factor α by a factor of $1 + 1/(2\beta_1)$ compared to the unmagnetized case (see Equations (2.29) and (2.30)). In the stationary IF frame, the magnetosonic Mach number of the ionized gas downstream from the IF always satisfies $\mathcal{M}_{M2}^2 \leq 1$ for weak D-type fronts, with the equality corresponding to the D-critical fronts. We provide the approximate expressions (Equations (2.27) and (2.28)) for the expansion factors and sonic Mach numbers when the fronts are either D- or R-critical.

We impose small-amplitude perturbations on a steady-state IF in isolation, and seek for unstable modes that grow exponentially in time. The perturbations are constructed as a superposition of MHD waves that are

evanescent far away from the IF; only the fast (or acoustic) mode propagates in the upstream side, while both fast and slow (or vortex) modes exist in the downstream side for an isolated magnetized (or unmagnetized) front. For the two-dimensional perturbations we impose, shear Alfvén waves are not excited. We require that the perturbation variables satisfy the perturbed jump conditions (Equations (2.72)–(2.78)) at the IF to derive the dispersion relations of the instability.

We first apply our technique to unmagnetized IFs. The resulting dispersion relation (Equation (2.86)) recovers the result of Vandervoort (1962). When the external gravity is ignored (i.e., $G = 0$), it is also identical to the dispersion relation of the DLI seen in laser ablation fronts in inertial confinement fusion (e.g., Bychkov et al. 2008; Modestov et al. 2009). This suggests that the physical mechanism behind the IF instability is the same as that of the DLI. The DLI is generic for any interfacial layer through which a cold dense gas absorbs heat and expands to turn to a warm rarefied gas. The DLI is multi-dimensional, requiring wavy deformation of the interface in the direction normal to the incident ionizing radiation. In the case of IFs, the front deformation grows due to mismatches between the perturbed mass flux and the ionization rate of the cold gas at the IF. This is in contrast to the claim of Vandervoort (1962) that the IF instability is due to the rocket effect (Kahn 1954; Oort & Spitzer 1955) which, unlike the DLI, does not require wavy deformation of the IF, and relies on high-speed evaporating gas from a dense cloud to exert thrust on it.

The unstable mode of the IF instability grows without oscillation, indicative of pure instability. The growth rate scales linearly with the wavenumber as well as the background fluid velocity relative to the front. The dimensionless growth rate increases with $\alpha^{1/2}$ for $\alpha \gg 1$ (Equation (2.89)). As \mathcal{M}_{S2} increases, the instability is stabilized by gas compressibility which tends to reduce the change in mass flux at the IF, becoming completely quenched

when the front is D-critical ($\mathcal{M}_{S2} = 1$). The IF instability cooperates with the RTI for IFs accelerating away from an ionizing source ($G > 0$), while it is suppressed by buoyancy for decelerating IFs at large scales (Equation (2.90)).

For magnetized fronts, we consider two cases of two-dimensional perturbations: (1) perturbations with $k_x = 0$ are in the plane perpendicular to the magnetic fields and (2) perturbations with $k_y = 0$ are confined to the plane defined by the magnetic fields and the background flows. For the $k_x = 0$ perturbations, the perturbed fields exert only magnetic pressure forces and the resulting dispersion relation is identical to the hydrodynamic case, provided the sound speed is replaced by the speed of magnetosonic waves. For the $k_y = 0$ perturbations, on the other hand, magnetic tension from the bent field lines stabilizes the instability. In the incompressible limit, the dispersion relation (Equation (2.105)) of the IF instability is again the same as that of the DLI studied by Dursi (2004). The IF instability is completely suppressed if the Alfvénic Mach number is sufficiently small (Equation (2.111)), suggesting that no instability is expected if the plasma parameter β_1 is less than $3/2$ in the upstream neutral region.

2.6.2 Discussion

Observations indicate that IFs are usually magnetized. Using the Zeeman effects of H I and OH lines, for instance, Brogan et al. (1999) and Brogan & Troland (2001) reported that the strength of line-of-sight magnetic fields toward the interface of H II region/molecular cloud complex in M17 is on average $\sim 200\text{--}500\ \mu\text{G}$ and reaches a value as high as $\sim 750\ \mu\text{G}$. Taking $B_1 \sim 300\ \mu\text{G}$, corresponding to the magnetic pressure support of $2.6 \times 10^7 k_B \text{ cm}^{-3} \text{ K}$, and assuming $T_1 = 100 \text{ K}$, β_1 is less than 1.5 unless $n_1 \gtrsim 8 \times 10^5 \text{ cm}^{-3}$. This large background density is highly unlikely since the equilibrium model of Pellegrini et al. (2007) favors n_1 of order of $\sim 10^4 \text{ cm}^{-3}$.

This suggests that the IF instability is readily stabilized by magnetic tension in the direction parallel to the fields. However, the IFs in M17 can still be unstable to perturbations (with $k_x = 0$ and $k_y \neq 0$) propagating in the direction perpendicular to the fields. The growth rate $\Omega = k_y v_{z1} \sigma$ in dimensional units can be written as

$$\Omega \approx 6.4 \times 10^{-5} \frac{\mathcal{M}_{M1} \sigma}{(1 + \beta_1^{-1})^{1/2}} \left(\frac{\lambda}{0.1 \text{ pc}} \right) \left(\frac{c_{s1}}{1 \text{ km s}^{-1}} \right) \text{ yr}^{-1}, \quad (2.112)$$

where λ is the perturbation wavelength. For $G = 0$ and $\theta = 200$, the maximum value of $\mathcal{M}_{M1} \sigma$ is (0.19, 0.3, 0.40) for $\beta_1 = (0.01, 0.1, 1)$, which occurs at $\mathcal{M}_{M2} = 0.75$ (see Figures 2.2(a) and 2.4). The corresponding e -folding growth time of the instability is (2.8, 1.5, 0.8) $\times 10^4$ yr for $\beta_1 = (0.01, 0.1, 1)$, respectively, which is an order of magnitude shorter than the typical expansion time scale of H II regions (typically 10^5 – 10^6 yr; see below). This indicates that the IF instability with $k_y \neq 0$ can grow significantly, but by keeping the magnetic field lines straight.

The relative importance of the front acceleration/deceleration to the the gas kinetic energy is measured by the dimensionless parameter $G = g/(k v_{z1}^2)$. Recently, Ricotti (2014) investigated the stabilizing effect of recombination on the RTI of accelerating IFs assuming that gas is incompressible. Due to the incompressibility assumption, however, his results (Equations (40) and (41) of (Ricotti 2014)) in the absence of recombination recovers the dispersion relation only for the RTI, but is unable to capture the IF instability of Vandervoort (1962). A simple comparison between the growth rates of the IF instability ($\sim \sqrt{\alpha} v_{z1} k_x$) and the RTI ($\sim \sqrt{g k_x}$) suggests that the perturbed flows are strongly affected by buoyancy for $|G| \gtrsim \alpha$. In a uniform medium without magnetic fields, Spitzer (1978) showed that a D-type IF expands as $r_{\text{IF}} \approx r_s (1 + 7t/4t_s)^{4/7}$, where $r_s = 3.2 \text{ pc} (Q/10^{49} \text{ s}^{-1}) (\rho_2/(100 m_{\text{H}} \text{ cm}^{-3}))^{-2/3}$ is the initial Strömngren radius, Q is the ionizing photon luminosity of a central

star, and $t_s = r_s/c_{s2} = 0.24 \text{ Myr}$ for $c_{s2} = 13 \text{ km s}^{-1}$. The effective gravity is then $g = -3c_{s2}/(4t_s)(1 + 4t/7t_s)^{-10/7}$. Taking $\theta = 200$, $g = -3c_{s2}/4t_s$, and $\mathcal{M}_{M2} = 0.5$, the IF instability is stabilized by buoyancy for perturbations with wavelength $\lambda/r_s > 8\pi\mathcal{M}_{S2}^2/(3\alpha) \sim 10^{-2}$ even for purely hydrodynamic IFs. On the other hand, for IFs accelerating outward in a stratified medium with density decreasing more steeply than $r^{-3/2}$ (e.g., Franco et al. 1990; Whalen & Norman 2008), the RTI would work together with the IF instability to make the fronts more unstable.

We have not considered thermal conduction in our analysis since its effect on the IF instability is thought to be insignificant. This can be seen quantitatively as follows. Let us take typical values for the mean photoionization cross section $\sigma_{\text{ph}} = 3 \times 10^{-18} \text{ cm}^2$, the mean kinetic energy of a photo-ejected electron $\langle E_{\text{ph}} \rangle = 2.4 \text{ eV}$ (e.g., Whalen et al. 2004), and the incident ionizing photon flux $F_{\text{ph}} = \rho_2 v_{z2}/m_{\text{H}}$. Then, the volumetric heating rate by photoionization amounts to

$$\begin{aligned} \mathcal{H} &= \frac{\rho_2}{m_{\text{H}}} \sigma_{\text{ph}} F_{\text{ph}} \langle E_{\text{ph}} \rangle \\ &= 1.5 \times 10^{-19} \left(\frac{\rho_2}{100 m_{\text{H}} \text{ cm}^{-3}} \right) \left(\frac{c_{s2}}{13 \text{ km s}^{-1}} \right) \mathcal{M}_{S2} \text{ erg cm}^{-3} \text{ s}^{-1} \quad (2.113) \end{aligned}$$

For the Spitzer conductivity of $\kappa_{\text{Sp}} \sim 10^4 \text{ erg cm}^{-1} \text{ s}^{-1} \text{ K}^{-1}$ in the ionized gas with $T_2 = 10^4 \text{ K}$ (McKee & Cowie 1977), the Field length is calculated to be $L_{\text{F2}} = \sqrt{\kappa_{\text{Sp}} T_2 / \mathcal{H}} = 8.4 \times 10^{-6} \text{ pc}$, while the thermal diffusion length is $L_{\text{D2}} = \kappa_2 / (j_z c_P) = 2 \times 10^{-5} \text{ pc}$, where c_P is the specific heat at constant pressure (e.g., Kim & Kim 2013). Note that the photon mean-free path $L_{\text{mfp2}} = 1/(n_2 \sigma_{\text{ph}}) = 10^{-3} \text{ pc}$ is much larger than the conduction length scales. Therefore, thermal diffusion is unlikely to be important in determining the structures of IFs as well as the IF instability (see also Spitzer 1978). This is in contrast to the case of evaporation fronts between cold and warm gases studied by Kim & Kim (2013), where thermal conduction not only

affects the front thickness but also stabilizes the DLI at small scales.

Can the IF instability manifest in numerical simulations of expanding H II regions? In Eulerian simulations, it is unavoidable to have spurious numerical viscosity, caused by a finite difference scheme, that dampens perturbations at small scale. Kim et al. (2008) found that the numerical diffusivity can be written as $\eta = A_d v_{\text{ad}} \Delta x (\Delta x / \lambda)^n$, where A_d is a dimensionless constant, λ is the characteristic length scale of perturbations, Δx is the grid spacing, v_{ad} is the advection velocity through a numerical grid, and n is the order of the spatial reconstruction in the numerical scheme. Since the corresponding damping time over the scale of λ is $\tau_\eta \sim \lambda^2 / \eta$, the numerical diffusion would prohibit the growth of the IF instability if $\tau_\eta \Omega \lesssim 1$ or if $\lambda / \Delta x \lesssim (A_d \alpha v_{\text{ad}} / 2\pi v_{z2} \sigma)^{1/(n+1)}$. Taking $A_d = 8.1 \times 10^4$ and $n = 2$ from Kim & Stone (2012) for the *Athena* code with piecewise-linear reconstruction scheme, for example, and taking $\alpha / \sigma \sim 10$ and $v_{\text{ad}} / v_{z2} = 1$, one can see that perturbations with $\lambda / \Delta x \gtrsim 50$ would be stabilized by numerical effects. Considering the typical resolution of $\Delta x \sim 10^{-2} - 10^{-1}$ pc in simulations of a single H II region (e.g., Krumholz et al. 2007b; Mackey & Lim 2011; Arthur et al. 2011), the DLI mode below $\sim 0.1 - 1$ pc would be suppressed by numerical diffusion. Modes with wavelength longer than these may still grow, but too slowly to be readily evident in numerical simulations. Therefore, very high-resolution simulations are desirable to resolve the IF instability at small scales.

Finally, we remark a few caveats made by our simplified model of an IF. First, the approximation of stationary IFs in plane-parallel geometry ignores the curvature effect as well as temporal changes in the background state, while IFs in reality have non-vanishing curvature, especially in the case of ablated globules. As an IF propagates, its curvature and the Mach number of the inflowing neutral gas would vary. For an expanding H II region, the perturbation wavelength increases in proportion to the size of the H II

region, resulting in a power-law growth rather than an exponential growth (Zeldovich et al. 1985). Second, IFs associated with blister-type H II regions and cometary globules (e.g., Kahn 1969; Bertoldi 1989; Bertoldi & McKee 1990) are strong D-type (or D-critical) and the ionized gas accelerates away from such IFs to achieve a supersonic speed. With spatially-varying density and velocity fields in the background state, instability of strong D-type IFs cannot be explored by our current technique that assumes uniform backgrounds in the upstream and downstream sides. Third, a D-type IF is usually preceded by a shock front, indicating that some waves launched by the IF would undergo reflection at the shock front, which is likely to alter the modal behavior of the perturbations in the upstream side. It is well known that after a shock breakout, the shocked layer is subject to a thin-shell instability due to the force imbalance between thermal and ram pressures at the boundaries (Giuliani 1979; Vishniac 1983; Garcia-Segura & Franco 1996). Right after the shock breakout (i.e., when the fronts are near D-critical), the gas ahead of the IF is subject to significant non-steady cooling and heating, so that the isothermal approximation in the neutral gas may not be applicable (Henney et al. 2009). In this case, a proper account of radiative cooling/heating is necessary to assess the impact of nonlinear development of the IF instability (Whalen & Norman 2008).

Appendix

2.A Derivation of Equation (2.76)

Here we present steps to derive Equation (2.76). Using Equations (2.72) and (2.73), Equation (2.67) is reduced to

$$(1 - \mathcal{M}_{S1}^2)p'_1 + \mathcal{M}_{A1}^{-1}b'_{x1} - \mathcal{M}_{A2}^{-1}b'_{x2} + (1 - \alpha^{-1})GZ = (1 - \mathcal{M}_{S1}^2)p'_2. \quad (2.114)$$

Combining Equations (2.77) and (2.114), one may write

$$(1 + \beta_1^{-1} - \mathcal{M}_{S1}^2)p'_1 + (1 - \alpha^{-2})(\mathcal{M}_{A1}^{-1}b'_{x1} - \beta_1^{-1}p'_1) + (1 - \alpha^{-1})GZ = (1 + \beta_2^{-1} - \mathcal{M}_{S2}^2)p'_2. \quad (2.115)$$

As we shall show in Sections 2.4 and 2.5, the perturbations in the upstream side (region 1) are described only by fast modes that obey Equations (2.47)–(2.49). Hence, one can write for fast modes

$$\mathcal{M}_{A1}^{-1}b'_{x1} - \beta_1^{-1}p'_1 = \left(\frac{\mathcal{M}_{A1}^{-2}(\nu^2 - \sin^2 \psi)}{\chi} - \frac{1}{\beta_1} \right) p'_1, \quad (2.116)$$

$$= \cos^2 \psi \frac{\mathcal{M}_{A1}^{-2}}{(\sigma + \nu)^2} p'_1, \quad (2.117)$$

where $\chi = \sigma_D^2 + \hat{\alpha}^2 \mathcal{M}_A^{-2}(1 - \nu^2)$ and we have used Equation (2.53) in the last equality. Combining Equations (2.115) and (2.117) gives Equation (2.76).

2.B Perturbation Equations for $k_x \neq 0$ and $k_y = 0$

We plug Equations (2.109) and (2.110) into Equations (2.72)–(2.74) and (2.76)–(2.77), and arrange terms to obtain

$$\mathbf{A} \cdot (C_{\text{fl}}, C_{\text{f2}}, C_{\text{s2+}}, C_{\text{s2-}}, Z)^T = 0, \quad (2.118)$$

where \mathbf{A} is a 5×5 matrix whose components are given by

$$\begin{aligned} A_{11} &= 1 - \mathcal{M}_{\text{S1}}^2 \chi_{\text{fl}} / (\nu_{\text{fl}} \sigma_{D,\text{fl}}), \\ A_{1j} &= 0, \end{aligned} \quad (2.119)$$

$$A_{15} = -\sigma,$$

$$A_{21} = 0,$$

$$A_{2j} = 1 - \mathcal{M}_{\text{S2}}^2 \chi_j / (\alpha \nu_j \sigma_{D,j}), \quad (2.120)$$

$$A_{25} = -\sigma,$$

$$A_{31} = \chi_{\text{fl}} / (\nu_{\text{fl}} \sigma_{D,\text{fl}}^2) - \mathcal{M}_{\text{A1}}^{-2} / \sigma_{D,\text{fl}},$$

$$A_{3j} = \chi_j / (\nu_j \sigma_{D,j}^2) - \alpha \mathcal{M}_{\text{A2}}^{-2} / \sigma_{D,j}, \quad (2.121)$$

$$A_{35} = 1 + \mathcal{M}_{\text{A1}}^{-2} - \alpha(1 + \mathcal{M}_{\text{A2}}^{-2}),$$

$$A_{41} = -\mathcal{B} \chi_{\text{fl}} / (\nu_{\text{fl}} \sigma_{D,\text{fl}}),$$

$$A_{4j} = (1 + \beta_2^{-1})(1 - \mathcal{M}_{\text{M2}}^2) \chi_j / (\alpha \nu_j \sigma_{D,j}), \quad (2.122)$$

$$A_{45} = (1 - \alpha^{-1})G,$$

$$A_{51} = -\nu_{\text{fl}} \mathcal{M}_{\text{A1}}^{-1} / \sigma_{D,\text{fl}} + \mathcal{M}_{\text{A1}}^{-1} \mathcal{M}_{\text{S1}}^2 \chi_{\text{fl}} / (\nu_{\text{fl}} \sigma_{D,\text{fl}}),$$

$$A_{5j} = \alpha^{3/2} \mathcal{M}_{\text{A2}}^{-1} \nu_j / \sigma_{D,j} - \mathcal{M}_{\text{A2}}^{-1} \mathcal{M}_{\text{S2}}^2 \chi_j / (\alpha^{1/2} \nu_j \sigma_{D,j}), \quad (2.123)$$

$$A_{55} = 0.$$

Here,

$$\mathcal{B} = (1 + \beta_1^{-1})(1 - \mathcal{M}_{\text{M1}}^2) + \frac{\mathcal{M}_{\text{A1}}^{-2}(1 - \alpha^{-2})}{(\sigma + \nu_{\text{fl}})^2}, \quad (2.124)$$

and the index j in Equations (2.120)–(2.123) runs from 2 to 4, with $j = 2, 3,$ and 4 corresponding to the downstream fast (f2), forward-propagating slow (s2+), and backward-propagating slow (s2–) modes, respectively.

Chapter 3

Disruption of Molecular Clouds by Expansion of Dusty H II Regions¹

Abstract

Dynamical expansion of H II regions around star clusters plays a key role in dispersing the surrounding dense gas and therefore in limiting the efficiency of star formation in molecular clouds. We use a semi-analytic method and numerical simulations to explore expansion of spherical dusty H II regions and surrounding neutral shells and the resulting cloud disruption. Our model for shell expansion adopts the static solutions of Draine (2011b) for dusty H II regions and considers the contact outward forces on the shell due to radiation and thermal pressures as well as the inward gravity from the central star and the shell itself. We show that the internal structure we adopt and the shell evolution from the semi-analytic approach are in good agreement with the results of numerical simulations. Strong radiation pressure in the

¹A version of this chapter has been published as “Disruption of Molecular Clouds by Expansion of Dusty H II Regions,” Kim, J.-G., Kim, W.-T., & Ostriker, E. C. 2016, *The Astrophysical Journal*, 819, 137.

interior controls the shell expansion indirectly by enhancing the density and pressure at the ionization front. We calculate the minimum star formation efficiency ε_{\min} required for cloud disruption as a function of the cloud’s total mass and mean surface density. Within the adopted spherical geometry, we find that typical giant molecular clouds in normal disk galaxies have $\varepsilon_{\min} \lesssim 10\%$, with comparable gas and radiation pressure effects on shell expansion. Massive cluster-forming clumps require a significantly higher efficiency of $\varepsilon_{\min} \gtrsim 50\%$ for disruption, produced mainly by radiation-driven expansion. The disruption time is typically of the order of a free-fall timescale, suggesting that the cloud disruption occurs rapidly once a sufficiently luminous H II region is formed. We also discuss limitations of the spherical idealization.

3.1 Introduction

Giant molecular clouds (GMCs) are the sites of star formation in galaxies. They are highly structured, consisting of hierarchy of clumps, filaments, and sheets resulting from shock interactions in supersonic turbulence (Elmegreen & Scalo 2004; André et al. 2014). Stars predominantly form in groups (later becoming OB associations or clusters) within dense, gravitationally-bound clumps inside GMCs (Lada & Lada 2003). Newborn star clusters have a profound influence on the surrounding interstellar medium (ISM) via proto-stellar outflows, stellar winds, ionizing radiation, and supernova explosions, which are collectively referred to as stellar feedback. The question of how each feedback process affects formation, evolution, and dispersal of their natal clouds is an active and contentious area of research (see Dobbs et al. 2014 and Krumholz et al. 2014 for recent reviews).

An important unsolved problem in star formation theory is what determines net star formation efficiency ε_* of a cloud, defined as the fraction of the cloud’s mass that is turned into stars over its lifetime. GMCs are known

to be inefficient in converting gas into stars. Over their lifetime, individual GMCs in the Milky Way appear to turn only a few to several percent of their mass into stars (Myers et al. 1986; Williams & McKee 1997; Carpenter 2000; Evans et al. 2009; Kennicutt & Evans 2012; García et al. 2014). Furthermore, observations of Galactic infrared dark clouds, nearby galaxies, and high-redshift star-forming galaxies all point to a conclusion that the depletion time of molecular gas is more than an order of magnitude longer than the internal dynamical timescale (e.g., Krumholz & Tan 2007; Genzel et al. 2010; Krumholz et al. 2012; Leroy et al. 2013).

Observations and theoretical arguments indicate that star formation efficiency tends to be higher within high-density environments (Elmegreen & Efremov 1997; McKee & Ostriker 2007). For example, the estimated star formation efficiencies of cluster-forming clumps for low-mass clusters in the solar neighborhood is ~ 0.1 – 0.3 , higher than the few percent efficiency of entire GMCs (Lada & Lada 2003). The Orion Nebula Cluster, which has been forming stars for several dynamical times (Tan et al. 2006), appears to have stellar fraction $\sim 50\%$ (Da Rio et al. 2014). Observations of massive, dense clouds in dwarf starburst galaxies containing nascent super star clusters indicate efficiencies $> 50\%$ (Meier et al. 2002; Turner et al. 2015). Gas expulsion from protoclusters is also important in the context of disruption or survival of a stellar cluster (e.g., Hills 1980; Elmegreen 1983; Goodwin 1997; Lada & Lada 2003; Banerjee & Kroupa 2015). If star formation efficiency is sufficiently high, a star cluster may remain gravitationally bound and thus become long-lived. If star formation efficiency varies with the mass of protocluster, it is likely to leave an imprint on the shape of the cluster mass function distinct from the cloud mass function (e.g., Ashman & Zepf 2001; Kroupa & Boily 2002; Fall et al. 2010).

A number of theoretical studies have proposed that H II regions may be the primary means of controlling the star formation efficiency within a clus-

ter’s birth cloud (e.g., Whitworth 1979; Williams & McKee 1997; Matzner 2002; Krumholz et al. 2006; Goldbaum et al. 2011; Dale et al. 2012, 2013a). A newborn cluster of stars embedded in a cloud emits abundant ultraviolet (UV) photons, creating an ionization front that separates the fully ionized gas close to the cluster from surrounding neutral gas. Thermal balance between heating by photoionization and cooling by line emission keeps the temperature of the ionized gas roughly at $\sim 10^4$ K (e.g., Osterbrock 1989; Draine 2011b). In the absence of radiation pressure (see below) and considering confined rather than blister-type H II regions, the density of ionized gas is relatively uniform. Expansion of the ionized gas due to its high thermal pressure (initially $\sim 10^3$ times ambient levels) drives a shock wave ahead of the ionization front. An expanding shell of dense gas between the ionization and shock fronts is created, incorporating the ambient neutral gas as the shock sweeps outward. Cloud disruption by shell expansion and/or associated photoevaporation create hostile conditions for further star formation. Whitworth (1979) and Franco et al. (1994) found that photoevaporation by massive stars born near the cloud boundary can limit ε_* to $\sim 5\%$ in a typical molecular cloud. Williams & McKee (1997) and Matzner (2002) found that clouds convert on average $\sim 10\%$ of their mass into stars before destruction by photoevaporation. Using the time-dependent virial theorem, Krumholz et al. (2006) found that both mass ejection by photoevaporation and momentum injection by expanding H II regions limit the net star formation efficiency of GMCs to $\sim 5\text{--}10\%$ before disruption.

The classical picture of an embedded H II region described above does not account for the effects of radiation pressure on dust grains, which are efficient at absorbing UV photons. If dust is tightly coupled to gas through mutual collisions, radiation forces exerted on the former are readily transmitted to the latter. Not only does dust reduce the size of the ionized zone (Petrosian et al. 1972), but it can also produce a central “hole” near the cluster by the

action of radiation pressure (Mathews 1967; Arthur et al. 2004). Recently, Draine (2011b, hereafter Dr11) obtained families of similarity solutions for the internal structure of dusty H II regions in static force balance. He found that radiation pressure is important for dense and luminous H II regions, forming a central cavity surrounded by an over-dense ionized shell just inside the ionization front. Krumholz & Matzner (2009, hereafter KM09) showed that while expansion of H II regions excited by a small number of massive stars is well described by the gas-pressure driven classical model (Spitzer 1978), the dynamics of H II regions around massive star clusters is dominated by radiation pressure. They presented an analytic formula for the shell evolution driven by the combination of gas and radiation pressures, finding that radiation pressure is more important during the early phase of the expansion, while the late stage is governed by a gas pressure force that increases with the shell radius.

Since gas expulsion by thermally driven expanding H II regions does not occur efficiently for clouds with high escape velocities ($\gtrsim 10 \text{ km s}^{-1}$) (e.g., Matzner 2002; Krumholz et al. 2006; Dale et al. 2012, 2013a), radiation pressure has been considered the most promising mechanism for disruption of massive clouds (e.g., Scoville et al. 2001; KM09; Fall et al. 2010; Murray et al. 2010). In particular, Fall et al. (2010) considered the potential for disruption of molecular clouds by various feedback mechanisms including protostellar outflows, photoionization, and supernova explosions, and concluded that radiation pressure may dominate momentum injection in dense and massive protoclusters. Utilizing the analytic solutions of KM09 for shell expansion, they argued that the minimum star formation efficiency, ε_{min} , required for cloud disruption primarily depends on the mean cloud surface density. With ε_{min} independent of the mass, this would explain the observed similarity between shapes of mass functions of molecular clouds and young star clusters. Murray et al. (2010, hereafter MQT10) analytically examined disruption of

massive GMCs for sample systems representative of various galactic environments, estimating effects of stellar feedback from protostellar jets, shocked stellar winds, thermal pressure of photoionized gas, radiation pressure, and the total gravity from stars and shell. They found that star formation efficiency for massive GMCs in the Milky Way is only a few percent, while clouds in starburst galaxies and star-forming giant clumps in high-redshift galaxies require $\sim 20\text{--}40\%$ of efficiency for disruption. In the part of parameter space they explored, direct and/or dust-reprocessed radiation pressure dominates ionized-gas pressure in driving shell expansion.

While the previous analytic works mentioned above are informative in understanding the effects of radiation pressure on the shell expansion and related cloud disruption, they are not without limitations. The minimum star formation efficiency derived by Fall et al. (2010) does not allow for the effect of gas pressure and inward gravity that may be important in the late stage of the shell expansion. MQT10 applied their expansion model to only a few representative cases, so that the general dependence of ϵ_* on the cloud mass and surface density has yet to be explored. In addition, KM09 and MQT10 set the radiation force on the shell equal to L/c , where L and c refer to the luminosity of the central source and the speed of light, respectively, assuming that all dust inside the H II region is pushed out to the shell. They also assumed the thermal pressure acting at the inner edge of the shell is equal to the mean thermal pressure in the ionized region. Since the static solutions of Dr11 indicate the ionized gas inside a dusty H II region is strongly stratified (at high luminosity) and absorbs radiation from the central source, the assumption of the unattenuated radiation up to the shell should be checked. All of the above also adopt the assumption of spherical symmetry and a source luminosity that is constant in time.

The numerical work of Dale et al. (2012, 2013a) is not limited by symmetry idealizations, allowing for fully turbulent gas dynamics and self-consistent

collapse to create sources of ionizing radiation. However, these works do not include effects of radiation pressure, and consider only a limited parameter space. Very recently, Raskutti et al. (2016) have conducted a set of numerical radiation hydrodynamic (RHD) simulations focusing exclusively on the effects of (non-ionizing) UV in turbulent clouds with surface densities in the range $10\text{--}300 M_{\odot} \text{pc}^{-2}$. The Raskutti et al. simulations showed that turbulent compressions of gas can raise the value of ε_* by a factor of ~ 5 for typical Milky Way GMC parameters, because strong radiation forces are required for dispersal of dense, shock-compressed filamentary structures. Skinner & Ostriker (2015) used numerical RHD simulations to consider the complementary regime of extremely high surface density clouds, evaluating the ability of radiation forces from dust-reprocessed infrared (IR) to disrupt clouds. This work showed that IR is effective only if $\kappa_{\text{IR}} > 15 \text{ cm}^2 \text{ g}^{-1}$, with κ_{IR} being the gas opacity to dust-reprocessed IR radiation, and even in this case the predicted efficiency is $\sim 50\%$, which may explain observations of nascent super star clusters (Turner et al. 2015).

In this chapter, we use a simple semi-analytic model as well as numerical simulations to investigate expansion of dusty H II regions and its effect on disruption of star-forming clouds across a variety of length and mass scales. This work improves upon previous analytic works in several ways. First, shells in our model expand due to both radiation and thermal pressures explicitly, extending Fall et al. (2010), which considered solely radiation pressure. We also include the inward force due to gravity of the stars and shell, which extends the non-gravitating models of KM09. Second, we adopt the static solutions of Dr11 for non-uniform internal structure of H II regions. This allows us not only to accurately evaluate the contact forces on the shell arising from thermal and radiation pressures, but also to compare them with the effective forces adopted in the previous studies (e.g., KM09; MQT10). Third, we have also run direct numerical simulation to check the validity of the

solutions of Dr11 for representing the interior structure in an expanding H II region and also to confirm our semi-analytic shell expansion solutions. Fourth, we conduct a systematic parameter survey in the full space of cloud mass and surface density, evaluating at each $(M_{\text{cl}}, \Sigma_{\text{cl}})$ the minimum efficiency ε_{min} required for disruption, the relative importance of radiation and ionized-gas pressures, and the timescale of cloud disruption. We also consider the effects of the mass-dependent light-to-mass ratio, the density distribution of the background medium, and the dust-reprocessed radiation. Our model does not allow for potentially important effects of stellar winds, which we briefly discuss in Section 3.5.2. The chief idealization of our study is the adoption of spherical symmetry. While real clouds are not symmetric, our results provide a guide and baseline for future work that will relax this restriction.

The rest of this chapter is organized as follows. In Section 3.2, we briefly summarize the solutions of Dr11 for dusty H II regions in static equilibrium. In Section 3.3, we describe our semi-analytic model for shell expansion, and evaluate the contact forces on the shell in comparison with the effective forces adopted by other authors. We also run numerical simulations for expanding H II regions, and compare the results with those of the semi-analytic model. In Section 3.4, we calculate the minimum efficiency of star formation required for cloud disruption. We also present analytic expressions for ε_{min} in the radiation or gas pressure driven limits. Finally, we summarize our results and discuss their astrophysical implications in Section 3.5.

3.2 Internal Structure of Dusty H II Regions

Dr11 studied the effect of radiation pressure on the internal structure of static, dusty H II regions, finding that radiation pressure acting on gas and dust gives rise to a non-uniform density profile with density (and gas pressure) increasing outward. In this section, we revisit Dr11 to obtain the parametric

dependence of various H II region properties on the strength of ionizing radiation. This information will be used for our dynamical models in Section 3.3.

Let us consider a central point source with luminosity $L = L_i + L_n$ embedded in a cloud, where L_i and L_n refer to the luminosities of hydrogen ionizing and non-ionizing photons, respectively. The number of ionizing photons per unit time emitted from the source is $Q_i = L_i/h\nu_i$, where $h\nu_i$ is the mean photon energy above the Lyman limit. For simplicity, we ignore the effect of He and assume that the ionized gas has a constant temperature $T_{\text{ion}} = 10^4$ K under photoionization equilibrium. Dust grains absorb both ionizing and non-ionizing radiation, with a constant absorption cross-section per hydrogen nucleus of $\sigma_d = 10^{-21} \text{ cm}^2 \text{ H}^{-1}$ (Dr11). The outward photon momentum absorbed by the dust is transferred to the gas via thermal and Coulomb collisions, resulting in a non-uniform gas density profile $n(r)$. Let f_{ion} denote the fraction of photons absorbed by the gas. Assuming ‘‘Case B’’ recombination, the radius of the Strömgen sphere centered at the source is then given by

$$r_{\text{IF}} \equiv \left(\frac{3f_{\text{ion}}Q_i}{4\pi\alpha_B n_{\text{rms}}^2} \right)^{1/3}, \quad (3.1)$$

where $\alpha_B = 2.59 \times 10^{-13} (T/10^4 \text{ K})^{-0.7} \text{ cm}^3 \text{ s}^{-1}$ is the effective recombination coefficient (Osterbrock 1989) and

$$n_{\text{rms}} \equiv \left(\frac{3}{r_{\text{IF}}^3} \int_0^{r_{\text{IF}}} n^2(r)r^2 dr \right)^{1/2} \quad (3.2)$$

is the root-mean-square number density within the ionized region.

The luminosity $L(r)$ at radius r inside the Strömgen sphere is given by $L(r) = L_i\phi(r) + L_n e^{-\tau_d}$, where $\phi(r)$ is the dimensionless quantity that describes attenuation of ionizing photons and $\tau_d = \int_0^r n\sigma_d dr$ is the dust optical depth of non-ionizing photons. The functions $\phi(r)$ and $\tau_d(r)$ ought to

satisfy

$$\frac{d\phi}{dr} = -n\sigma_d\phi - 4\pi\alpha_B n^2 r^2 / Q_i, \quad (3.3)$$

$$\frac{d\tau_d}{dr} = n\sigma_d. \quad (3.4)$$

The gas/dust mixture (assumed to be collisionally coupled) in the H II region is subject to both thermal pressure $P_{\text{thm}}(r) = 2n(r)k_B T_{\text{ion}}$ and radiation pressure $P_{\text{rad}}(r) = L(r)/(4\pi r^2 c)$. The condition of static force balance can thus be written as

$$\frac{1}{4\pi r^2 c} \frac{d}{dr} (L_i \phi + L_n e^{-\tau_d}) + 2k_B T_{\text{ion}} \frac{dn}{dr} = 0. \quad (3.5)$$

Equations (3.3)–(3.5) can be solved simultaneously for $n(r)$, $\phi(r)$, and $\tau_d(r)$ subject to the boundary conditions $\tau_d(0) = 0$, $\phi(0) = 1$, and $\phi(r_{\text{IF}}) = 0$. Dr11 showed that there exists a family of similarity solutions that are completely specified by three parameters: $\beta \equiv L_n/L_i$, $\gamma \equiv 2ck_B T_{\text{ion}}\sigma_d/(\alpha_B h\nu_i)$, and $Q_i n_{\text{rms}}$, characterizing the (inverse of) importance of ionizing photons, the dust content, and the radiation pressure, respectively. Throughout this chapter, we take $\beta = 1.5$, $h\nu_i = 18\text{ eV}$, and $\gamma = 11.1$ as standard values, appropriate for H II regions formed around massive star clusters (see Appendix 3.A).

Figure 3.1 plots the radial profiles of the normalized gas density and radiation pressure in the upper panel, and the radiation force per unit volume $f_{\text{rad}} = -r^{-2}d(r^2 P_{\text{rad}})/dr$ in the lower panel, for $Q_{i,49} n_{\text{rms}} = 1, 10^2, 10^4, 10^6\text{ cm}^{-3}$, where $Q_{i,49} \equiv Q_i/(10^{49}\text{ s}^{-1})$. For $Q_{i,49} n_{\text{rms}} \lesssim 10^4\text{ cm}^{-3}$, the internal structure is dominated by gas pressure, except in the very central regions where $P_{\text{rad}} > P_{\text{thm}}$, resulting in an almost flat density distribution with $n \approx n_{\text{rms}}$. In this case, the dust optical depth up to $r = r_{\text{IF}}$ is less than unity, indicating that a large fraction of non-ionizing radiation survives absorption by dust. For $Q_{i,49} n_{\text{rms}} \gtrsim 10^4\text{ cm}^{-3}$, on the other hand, radiation pressure is crucial in controlling the density structure. Gas close to the center is pushed out to

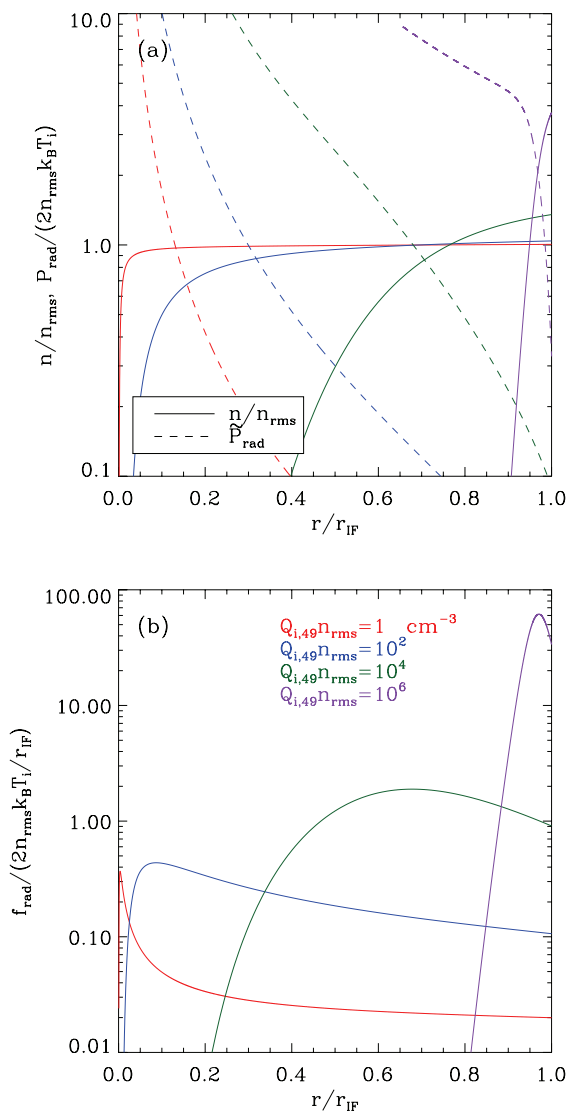


Figure 3.1 Radial distributions of (a) the normalized density n/n_{rms} (proportional to gas pressure, solid lines) and the normalized radiation pressure $\tilde{P}_{\text{rad}} = P_{\text{rad}} / (2n_{\text{rms}} k_B T_{\text{ion}})$ (dashed lines), and (b) the normalized radiation force per unit volume $\tilde{f}_{\text{rad}} = f_{\text{rad}} / (2n_{\text{rms}} k_B T_{\text{ion}} / r_{\text{IF}})$ (equal to gas pressure force per unit volume in magnitude and opposite in direction) for $Q_{i,49} n_{\text{rms}} = 1, 10^2, 10^4, 10^6 \text{ cm}^{-3}$.

large radii, forming a central cavity and an outer ionized shell, making the density at the ionization front $n_{\text{edge}} \equiv n(r_{\text{IF}})$ larger than n_{rms} .² Note that although $P_{\text{rad}} \gg P_{\text{thm}}$ in the cavity, the gas density there is too small to attenuate radiation significantly. Consequently, the radiation force exerted on the gas is almost negligible in the central cavity and rises only in the outer parts of the H II region, as Figure 3.1(b) illustrates. In fact, Equation (3.5) shows that f_{rad} achieves its maximum at the position of the steepest density gradient (see also Lopez et al. 2011, 2014). Thus, radiation strongly modifies the interior of the H II regions such that both gas and radiation forces are applied primarily in the outer portion.

Figure 3.2 plots the dependence on $Q_{i,49}n_{\text{rms}}$ of $\tau_{\text{d,IF}} \equiv \tau_{\text{d}}(r_{\text{IF}})$, f_{ion} , $n_{\text{edge}}/n_{\text{rms}}$, and $n_{\text{rms}}/n_{\text{mean}}$, where $n_{\text{mean}} = 3 \int_0^{r_{\text{IF}}} n(r)r^2 dr / r_{\text{IF}}^3$ is the mean density. Note that $\tau_{\text{d,IF}}$ and f_{ion} saturate to finite values ($\tau_{\text{d,IF}} = 1.97$ and $f_{\text{ion}} = 0.26$) as $Q_{i,49}n_{\text{rms}}$ increases. This is consistent with the results of Yeh & Matzner (2012) who showed that Equations (3.3)–(3.5) yield

$$\gamma(\beta + 1)e^{-\frac{\gamma-1}{\gamma}\tau_{\text{d,IF}}} = \beta(\gamma - 1)e^{-\tau_{\text{d,IF}}} + \beta + 1, \quad (3.6)$$

$$f_{\text{ion}} = \frac{\beta + 1}{\gamma - 1} \left[\tau_{\text{d,IF}} - \frac{\gamma}{\gamma - 1} \left(1 - e^{-\frac{\gamma-1}{\gamma}\tau_{\text{d,IF}}} \right) \right], \quad (3.7)$$

$$\frac{n_{\text{edge}}}{n_{\text{rms}}} = \frac{1 + \beta(1 - e^{-\tau_{\text{d,IF}}})}{3f_{\text{ion}}\gamma} n_{\text{rms}} r_{\text{IF}} \sigma_{\text{d}} \propto (n_{\text{rms}} Q_{\text{i}})^{1/3}, \quad (3.8)$$

in the limit of $Q_{\text{i}}n_{\text{rms}} \rightarrow \infty$. The saturation of $\tau_{\text{d,IF}}$ and f_{ion} occurs because the radiation-induced ionized shell near $r = r_{\text{IF}}$ has such large density that neutral hydrogen produced by recombinations can compete with dust in absorbing ionizing photons. This is in contrast to the classical case of uniform-density H II regions without radiation pressure, for which $\tau_{\text{d,IF}} \rightarrow \infty$, $f_{\text{ion}} \rightarrow 0$ as $Q_{\text{i}}n_{\text{rms}} \rightarrow \infty$ (Petrosian et al. 1972). Since the ionized shell has a saturated column $\int_0^{r_{\text{IF}}} n dr = \tau_{\text{d,IF}}/\sigma_{\text{d}}$, the gas mass M_{ion} within a dusty H II region in

²Dust-deficient H II regions with $\gamma < 1$ do not possess a cavity (Dr11, Yeh & Matzner 2012).

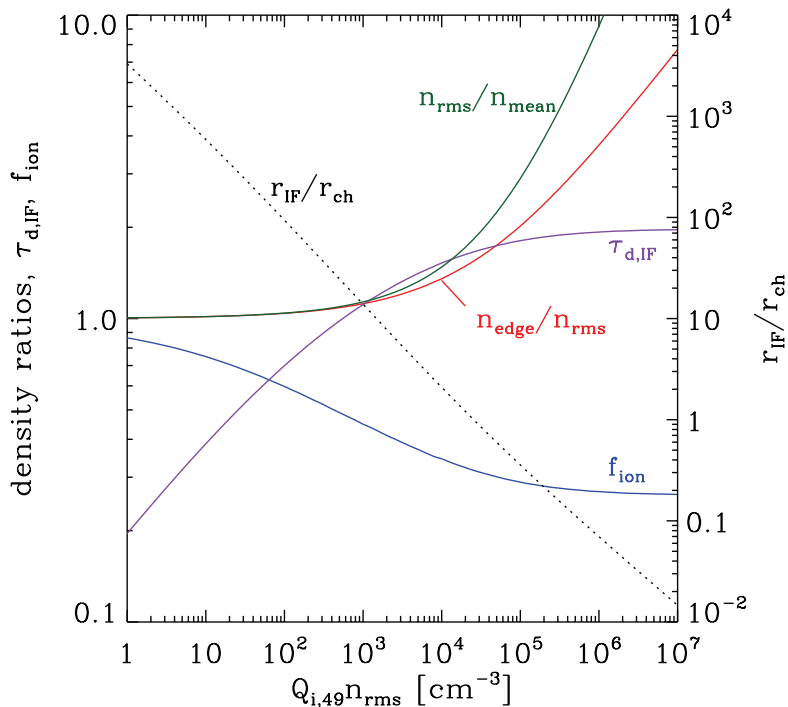


Figure 3.2 Dependence on $Q_{i,49}n_{\text{rms}}$ of the ratios of the edge-to-rms densities $n_{\text{edge}}/n_{\text{rms}}$ (red), the rms-to-mean densities $n_{\text{rms}}/n_{\text{mean}}$ (green), the dust optical depth to the ionization front $\tau_{\text{d,IF}}$ (purple), and the fraction f_{ion} (blue) of ionizing photons attenuated by photoionization prior to reaching the shell. The black dotted line shows the relationship between $Q_{i,49}n_{\text{rms}}$ and the ratio $r_{\text{IF}}/r_{\text{ch}}$ of the ionization front radius to the characteristic radius (see Equations (3.16) and (3.17)).

this limit depends on r_{IF} as $M_{\text{ion}} \propto r_{\text{IF}}^2$, as opposed to classical H II regions for which $n_{\text{mean}} \approx n_{\text{rms}}$ and $M_{\text{ion}} \propto n_{\text{mean}} r_{\text{IF}}^3 \propto r_{\text{IF}}^{3/2}$ for given Q_{i} .

3.3 Expansion of Dusty H II Regions

The high pressure in the interior of an H II region compared to the ambient levels leads to radial expansion. Spitzer (1978) provides approximate solutions for this expansion in the case where just gas pressure is included, under the assumption that ambient gas is swept up into a thin shell surrounding the ionized interior (see also Franco et al. 1990; Shu 1992). In this section, we explore expansion of spherically-symmetric, dusty H II regions driven by both thermal and radiation pressures, making a thin-shell approximation. Here we ignore pressure resulting from diffuse recombination radiation, which is negligible in comparison to gas pressure (e.g., Henney & Arthur 1998; KM09; Dr11). We also assume that the shell is optically thin to IR photons emitted by dust grains, the effect of which will be examined in Section 3.4.3. Expansion models by KM09 and MQT10 adopted the assumption that all of the radiation is absorbed only by the shell, while ionizing radiation produces a uniform pressure, uniform density interior. Here, we relax these assumptions and calculate the direct outward forces based on the Dr11 solutions.

3.3.1 Model

We consider a spherical neutral cloud with density distribution

$$n(r) = \begin{cases} n_c, & \text{for } r/r_c < 1, \\ n_c(r/r_c)^{-k_\rho}, & \text{for } r/r_c \geq 1, \end{cases} \quad (3.9)$$

where n_c and r_c are the density and radius of a flat core, respectively, and k_ρ is an index of a surrounding power-law envelope.³ A star cluster with total mass

³While GMCs do not appear to possess density stratification on a global scale (McKee & Ostriker 2007), the density distribution of clumps within them is well described by a power-

M_* , total luminosity L , and total ionizing power Q_i is born instantly at the cloud center. Copious energetic photons emitted by the cluster begin to ionize the surrounding medium, causing the ionization front to advance to the initial Strömgen radius, $r_{\text{IF},0}$, within a few recombination timescales ($\sim 10^3$ yr for $n \sim 10^2 \text{ cm}^{-3}$). The overpressured, ionized gas creates a shock front that moves radially outward, sweeping up the ambient neutral medium into a dense shell. We assume that the H II region remains in internal quasi-static equilibrium throughout its dynamical expansion, which is reasonable since the sound-crossing time over the ionized region is sufficiently small compared to the expansion timescale. We further assume that all of the swept-up gas resides in a thin shell of mass M_{sh} located at r_{sh} . Since we are interested in the evolution of the shell well after the formation phase, we may take $r_c \ll r_{\text{IF},0}$ in describing shell expansion in a power-law envelope.

The momentum equation for the shell is

$$\frac{d(M_{\text{sh}}v_{\text{sh}})}{dt} = F_{\text{tot}} = F_{\text{out}} - F_{\text{in}}, \quad (3.10)$$

where $v_{\text{sh}} = dr_{\text{sh}}/dt$ is the expansion velocity of the shell, and F_{out} and F_{in} denote the outward and inward forces acting on the shell, respectively. The inward force is due to the cluster gravity and shell self-gravity, given by

$$F_{\text{in}} = \frac{GM_{\text{sh}}(M_* + M_{\text{sh}}/2)}{r_{\text{sh}}^2}, \quad (3.11)$$

so that the cluster gravity and gaseous self-gravity depend on r_{sh} as $r_{\text{sh}}^{1-k_\rho}$ and $r_{\text{sh}}^{4-2k_\rho}$, respectively. The radiation and thermal pressures give rise to the total outward force

$$F_{\text{out}} = \frac{L_{\text{n}}}{c} e^{-\tau_{\text{d,IF}}} + 8\pi k_{\text{B}} T_{\text{ion}} n_{\text{edge}} r_{\text{sh}}^2. \quad (3.12)$$

law profile including a central core (see e.g., Franco et al. 1990; Hillenbrand & Hartmann 1998).

Note that F_{out} is the *contact* force acting on the surface immediately outside the ionization front. Only non-ionizing photons reach the neutral shell and exert the outward force, if the shell is optically thick to them.⁴

In Equation (3.10), we neglect the reaction force on the shell exerted by evaporation flows away from the ionization front because it is not significant for embedded H II regions. The thrust term would be important in driving expansion of classical, blister-type H II regions for which ionization fronts are kept D-critical (Matzner 2002; Krumholz et al. 2006; KM09). We also ignore the slowdown of the shell caused by turbulent ram pressure of the external, neutral medium (e.g., Tremblin et al. 2014; Geen et al. 2015a), which is difficult to model within our spherically-symmetric, one-dimensional model.

Figure 3.3 plots F_{out} as well as the respective contributions of radiative and thermal pressures against the shell radius r_{sh} , taken to equal r_{IF} , as the black, blue, and red solid lines, respectively, utilizing the Dr11 solutions with $\beta = 1.5$ and $\gamma = 11.1$. Apparently, the thermal term dominates the radiative term by non-ionizing photons over the whole range shown in Figure 3.3. This should *not* be interpreted as an indication that radiation is unimportant for the shell expansion. Rather, the effect of the radiation force is indirectly communicated to the shell by increasing the ionized gas density n_{edge} above n_{rms} , with the limiting ratio $n_{\text{edge}}/n_{\text{rms}}$ given by the factor in Equation (3.8) when $Q_i n_{\text{rms}} \rightarrow \infty$.

The behavior of the outward forces for varying r_{IF} can be readily understood in comparison with the usual approximation adopted by previous authors (e.g., Harper-Clark & Murray 2009; KM09; MQT10). Assuming that all the photons from the source are absorbed by the shell, that the H II region has uniform interior density n_{rms} , and that infrared photons re-radiated by

⁴The condition that the dusty shell should be opaque to UV photons can be expressed as $r_{\text{sh}} \lesssim (\kappa_{\text{UV}} M_{\text{sh}} / 4\pi)^{1/2} = 8.4 \text{ pc} (M_{\text{sh}} / 10^4 M_{\odot})^{1/2}$, where $\kappa_{\text{UV}} = \sigma_{\text{d}} / \mu_{\text{H}} = 4.3 \times 10^2 \text{ cm}^2 \text{ g}^{-1}$ (Thompson et al. 2015).

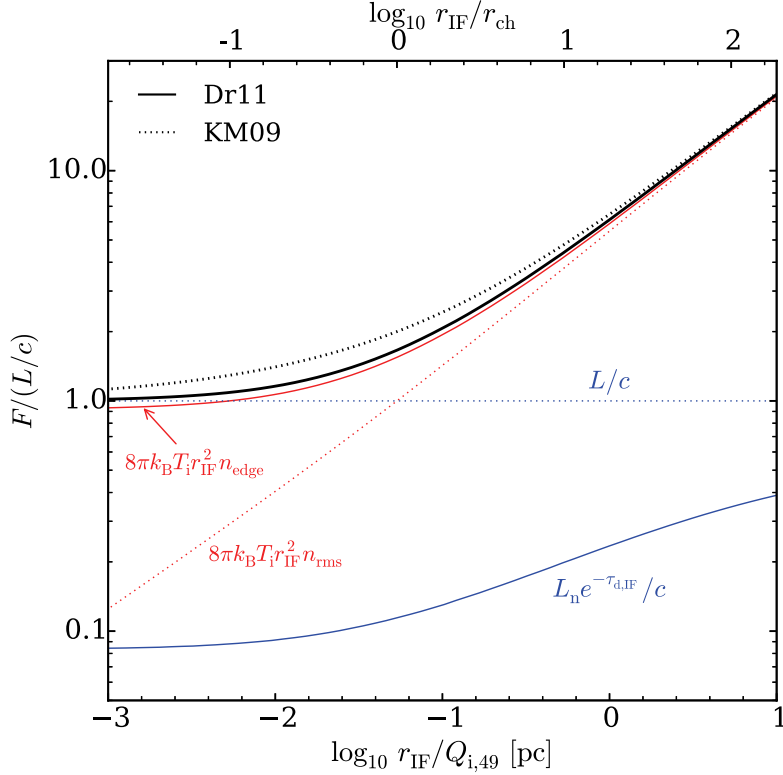


Figure 3.3 Outward forces on the shell surrounding the H II region, shown as a function of the shell radius $r_{\text{sh}} = r_{\text{IF}}$, scaled as $r_{\text{IF}}/Q_{i,49}$ (lower x -axis) or $r_{\text{IF}}/r_{\text{ch}}$ (upper x -axis). The solid lines denote the forces based on the quasi-static equilibrium model of Dr11, while the dotted lines are the effective forces assuming no attenuation of radiation inside the shell (e.g., KM09). The total forces and the radiative and thermal contributions are drawn as black, blue, and red curves, respectively. An H II region with given Q_i evolves from left to right. When $r_{\text{IF}} \ll r_{\text{ch}}$, the radiation force pushes the gas within the H II region outward, effectively communicating most of the radiation force L/c to the surrounding shell through a dense, ionized shell ($n_{\text{edge}}/n_{\text{rms}} \gg 1$). As the H II region expands to $r_{\text{sh}} > r_{\text{ch}}$, direct radiation forces become unimportant and $n_{\text{edge}} \approx n_{\text{rms}}$.

dust freely escape the system, the effective outward forces on the shell from direct radiation and gas pressure are taken as

$$F_{\text{rad,eff}} = L/c, \quad (3.13)$$

and

$$F_{\text{thm,eff}} = 8\pi k_{\text{B}} T_{\text{ion}} n_{\text{rms}} r_{\text{sh}}^2, \quad (3.14)$$

respectively, where n_{rms} is given in terms of Q_{i} , f_{ion} , and $r_{\text{sh}} = r_{\text{IF}}$ using Equation (3.1). These together with the total effective force $F_{\text{out,eff}} = F_{\text{rad,eff}} + F_{\text{thm,eff}}$ are plotted as dotted lines in Figure 3.3. Evidently, $F_{\text{out,eff}}$ agrees well (within 20%) with F_{out} from Equation (3.12). Comparison of the thermal term in Equation (3.12) with Equation (3.14) shows that the enhanced thermal force for small radius is due to increased $n_{\text{edge}}/n_{\text{rms}}$, which is caused by radiation pressure in the Dr11 solutions. At sufficiently small radius, the total outward force is in fact equal to $F_{\text{rad,eff}}$.⁵

Since $F_{\text{thm,eff}} \propto n_{\text{rms}} r_{\text{sh}}^2 \propto f_{\text{ion}}^{1/2} r_{\text{sh}}^{1/2}$, while $F_{\text{rad,eff}}$ remains constant, one can write

$$F_{\text{out,eff}} = \frac{L}{c} \left[1 + \left(\frac{f_{\text{ion}}}{f_{\text{ion,ch}}} \frac{r_{\text{sh}}}{r_{\text{ch}}} \right)^{1/2} \right], \quad (3.15)$$

with the characteristic radius r_{ch} at which $F_{\text{rad,eff}} = F_{\text{thm,eff}}$ defined by (KM09)

$$\begin{aligned} r_{\text{ch}} &\equiv \left(\frac{(1 + \beta)\sigma_{\text{d}}}{\gamma} \right)^2 \frac{Q_{\text{i}}}{12\pi\alpha_{\text{B}}f_{\text{ion,ch}}} \\ &\rightarrow 5.3 \times 10^{-2} \text{ pc } Q_{\text{i},49}, \end{aligned} \quad (3.16)$$

where $f_{\text{ion,ch}} \equiv f_{\text{ion}}(r_{\text{ch}})$ is 0.32 for our fiducial parameters $\beta = 1.5$ and $\gamma = 11.1$.⁶ Expansion is driven predominantly by radiation in the regime

⁵Combining Equations (3.1), (3.8), and (3.12), one can show that $F_{\text{out}} \rightarrow L/c$ in the limit of $Q_{\text{i},49} n_{\text{rms}} \rightarrow \infty$.

⁶KM09 adopted a constant value of 0.73 for both f_{ion} and $f_{\text{ion,ch}}$ for their approximate treatment.

with $r_{\text{sh}}/r_{\text{ch}} < 1$, while ionized-gas pressure is more important for $r_{\text{sh}}/r_{\text{ch}} > 1$. Thus, the relative importance of radiation pressure within an H II region can be assessed by the ratio

$$\begin{aligned} \frac{r_{\text{IF}}}{r_{\text{ch}}} &= f_{\text{ion,ch}} \left[\frac{\gamma(36\pi\alpha_{\text{B}})^{1/3}}{(1+\beta)\sigma_{\text{d}}} \right]^2 \left(\frac{f_{\text{ion}}}{Q_{\text{i}}^2 n_{\text{rms}}^2} \right)^{1/3} \\ &\rightarrow \left(\frac{f_{\text{ion}}}{0.32} \right)^{1/3} \left(\frac{Q_{\text{i},49} n_{\text{rms}}}{2.55 \times 10^4 \text{ cm}^{-3}} \right)^{-2/3}, \end{aligned} \quad (3.17)$$

shown as a black dotted line in Figure 3.2 as a function of $Q_{\text{i},49} n_{\text{rms}}$. Thus, shell expansion is dominated by radiation pressure when $Q_{\text{i},49} n_{\text{rms}} \gtrsim 10^4 \text{ cm}^{-3}$.

3.3.2 Non-gravitating Similarity solutions

In the absence of the inward gravitational forces ($F_{\text{in}} = 0$) and in the limit of negligible core radius, it is straightforward to show that Equations (3.10) and (3.15) yield the similarity solutions

$$n_{\text{mean}} r_{\text{sh}}^4 = \frac{4 - k_{\rho}}{2} \frac{L}{c} \frac{3}{4\pi\mu_{\text{H}}} t^2, \quad (3.18)$$

in the limit of $r_{\text{sh}}/r_{\text{ch}} \ll 1$, and

$$n_{\text{mean}} r_{\text{sh}}^{7/2} = \frac{3}{2} \frac{k_{\text{B}} T_{\text{ion}}}{\mu_{\text{H}}} \left(\frac{3f_{\text{ion}} Q_{\text{i}}}{4\pi\alpha_{\text{B}}} \right)^{1/2} \frac{(7 - 2k_{\rho})^2}{9 - 2k_{\rho}} t^2, \quad (3.19)$$

in the limit of $r_{\text{sh}}/r_{\text{ch}} \gg 1$, where f_{ion} is regarded as a constant and $\mu_{\text{H}} = 2.34 \times 10^{-24} \text{ g}$ is the mean atomic mass per hydrogen and $n_{\text{mean}} = 3n_{\text{c}}(r_{\text{sh}}/r_{\text{c}})^{-k_{\rho}}/(3 - k_{\rho})$ is the mean number density interior to r_{sh} (e.g., Krumholz et al. 2006; KM09). Therefore, the shell radius and velocity vary with time as $r_{\text{sh}} \propto t^{2/(4-k_{\rho})}$ and $v_{\text{sh}} \propto t^{(k_{\rho}-2)/(4-k_{\rho})}$ in the radiation-pressure driven limit, and $r_{\text{sh}} \propto t^{4/(7-2k_{\rho})}$ and $v_{\text{sh}} \propto t^{(2k_{\rho}-3)/(7-2k_{\rho})}$ in the gas-pressure driven limit. KM09 presented an analytic approximation valid in both limits by combining Equations (3.18) and (3.19). Note that for $k_{\rho} = 3/2$, the velocity approaches a constant at sufficiently late time.

3.3.3 Valid Range of k_ρ

When a cloud has too steep a density gradient, the shell mass becomes smaller than the ionized gas mass within the ionization front. In this case, the thin shell approximation we adopt would no longer be valid. For instance, Franco et al. (1990) found that for a thermally-driven H II region formed in a cloud with $k_\rho = 3/2$, the shock front moves twice as fast as than the ionized sound speed, without significant mass accumulation in the shocked shell. For $3/2 < k_\rho < 3$, an H II region becomes “density bounded” and develops “champagne” flows rather than forming a shell (see also self-similar solutions by Shu et al. 2002). To be consistent with our thin-shell approximation, therefore, we consider clouds only with $k_\rho < 1.5$ in the following analysis for shell expansion.

3.3.4 Shell Expansion

When stellar gravity is included, we can relate M_* to Q_i through $M_* = Q_i/\Xi$, where Ξ is the conversion factor representing the ionizing photon output per unit stellar mass. The corresponding light-to-mass ratio is $\Psi = L/M_* = (1 + \beta)h\nu_i\Xi$. Obviously, these quantities depend on M_* and vary from cluster to cluster, especially for low-mass ones due to stochastic fluctuations in the stellar population. In Appendix 3.A, we perform Monte-Carlo simulations for the spectra of coeval populations using the SLUG code (Krumholz et al. 2015) to find spectral properties as functions of M_* . Equations (3.33) and (3.34) provide the fits to the resulting median values of Ψ and Ξ . While Ψ and Ξ saturate to constant values for $M_* \gtrsim 10^4 M_\odot$, they decrease sharply as M_* decreases below $\sim 10^3 M_\odot$, due to a rapid decrease in the number of O-type stars in the realizations of low-mass clusters. In this work, we use Equation (3.33) for conversion between M_* and Q_i , while fixing to $\beta = 1.5$ and $h\nu_i = 18 \text{ eV}$: we have checked that varying β and $h\nu_i$ does not affect our

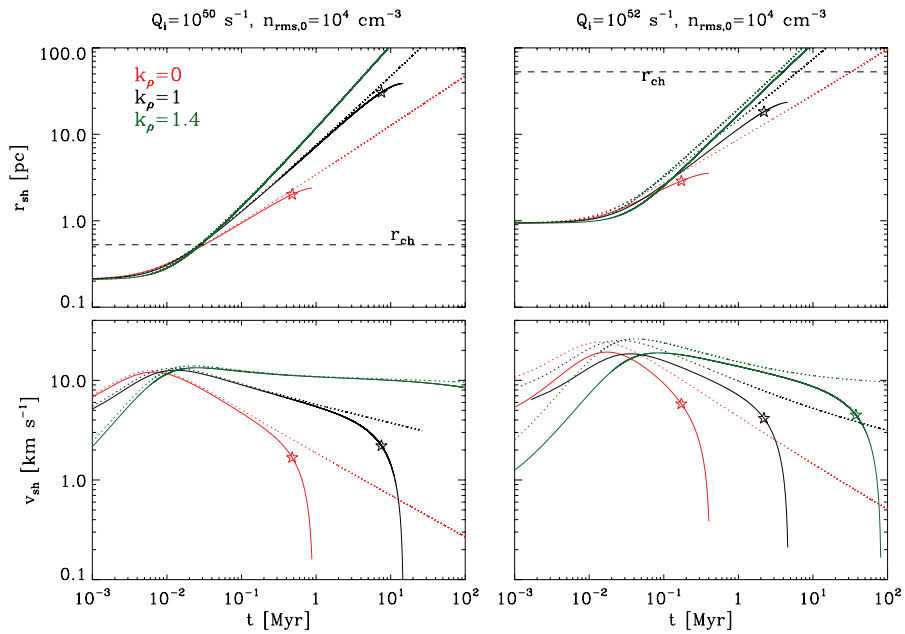


Figure 3.4 Temporal evolution of the shell radius (upper) and the shell velocity (lower) for $Q_i = 10^{50} \text{ s}^{-1}$ (left) and $Q_i = 10^{52} \text{ s}^{-1}$ (right). The initial rms density in the ionized region is fixed to $n_{\text{rms},0} = 10^4 \text{ cm}^{-3}$. The cases with $k_\rho = 0, 1,$ and 1.4 are plotted in red, black, and green. The solid and dotted lines correspond to the models with and without gravity, respectively. The thin horizontal lines in the upper panels mark the characteristic radius r_{ch} (Equation (3.16)), at which the dominant driving force switches from radiation to ionized-gas pressure. The star symbols indicate the radii where $F_{\text{tot}} = 0$.

results much.

To integrate Equation (3.10), we first choose a set of values for β , γ , Q_i , $n_{\text{rms},0}$, and k_ρ . We then specify f_{ion} from the Dr11 solutions and $r_{\text{IF},0}$ from Equation (3.1). At $t = 0$, a shell with a zero velocity is located at $r_{\text{sh}}(0) = r_{\text{IF},0}$. The outside density profile is taken as $n(r) = n_{\text{rms},0}(r/r_{\text{IF},0})^{-k_\rho}$ for $r \geq r_{\text{sh}}$ and the shell mass at any radius is given by $M_{\text{sh}} = 4\pi\mu_{\text{H}}n_{\text{rms},0}r_{\text{sh}}^{3-k_\rho}r_{\text{IF},0}^{k_\rho}/(3-k_\rho)$.

As illustrative examples, we fix $\beta = 1.5$, $\gamma = 11.1$, and $n_{\text{rms},0} = 10^4 \text{ cm}^{-3}$, and vary k_ρ and Q_i . Figure 3.4 plots as solid lines the temporal behavior of the shell radius (upper panels) and velocity (lower panels) for $Q_{i,49} = 10$ (left) and $Q_{i,49} = 10^3$ (right). The solutions without gravity are compared as dotted lines. The cases with $k_\rho = 0, 1$, and 1.4 , plotted in red, black, and green, respectively, show that the shell expansion is faster in an environment with a steeper density profile, because the shell mass increases more slowly for larger k_ρ . The horizontal dashed lines mark the characteristic radii, $r_{\text{ch}} = 0.53$ and 53 pc for $Q_{i,49} = 10$ and 10^3 , respectively, inside (outside) of which shell expansion is driven primarily by radiation (gas) pressure. The star symbols mark the radius where $F_{\text{tot}} = 0$, beyond which expansion is slowed down by the shell self-gravity significantly.

The solutions converge to the asymptotic power-law solutions discussed in Section 3.3.2 (Equations (3.18) and (3.19)), although strong stellar gravity in the case with $Q_{i,49} = 10^3$ makes the shell expansion deviate from the non-gravitating solutions early time. Self-gravity of the swept-up shell becomes important in the late stage, eventually halting the expansion. The maximum shell velocity is only mildly supersonic with respect to the ionized gas owing to the rapid increase in the shell mass. Note that when $Q_{i,49} = 10$, the driving force changes from radiation to gas pressure at small r_{sh} , while shell expansion is always dominated by radiation pressure when $Q_{i,49} = 10^3$.

3.3.5 Comparison with Numerical Simulations

So far we have used a very simple model to study dynamical expansion of a spherical shell surrounding an H II region. In order to check how reliable our results are, we run direct numerical simulations using the *Athena* code in spherical geometry (Stone et al. 2008), as described in Appendix 3.B. As an initial state, we consider a source of radiation at the center of a radially stratified cloud with $k_\rho = 1$. To handle the transfer of radiation from the source, we adopt a ray-tracing technique explained in Mellema et al. (2006b) and Krumholz et al. (2007a). While gas inside the H II region is evolved self-consistently, we ensure that the outer envelope unaffected by radiation maintains its initial hydrostatic equilibrium.

Figure 3.5 plots as solid lines the radial density distributions at a few epochs for Model A (with $Q_{i,49} = 1$ and $n(r_0) = 10^3 \text{ cm}^{-3}$; top), Model B (with $Q_{i,49} = 10^2$ and $n(r_0) = 10^4 \text{ cm}^{-3}$; middle), and Model C (with $Q_{i,49} = 10^3$ and $n(r_0) = 10^4 \text{ cm}^{-3}$; bottom), all with $k_\rho = 1$ and $r_0 = 1 \text{ pc}$. In Model A, the effect of radiation on shell expansion is almost negligible since $Q_{i,49}n_{\text{rms}} < 10^4 \text{ cm}^{-3}$. Its overall expansion is in good agreement with the classical picture of thermally driven expansion (e.g., Spitzer 1978). As soon as the ionization front reaches the initial Strömgen radius ($\sim 0.3 \text{ pc}$), an isothermal shock wave forms and propagates outward. At the same time, rarefaction waves excited at the ionization front propagate radially inward (e.g., Arthur et al. 2011), gradually turning into acoustic disturbances that travel back and forth between the ionization front and the center. In this model, the density profile in the ionized region is nearly flat.

On the other hand, Model C is dominated by radiation. Gas at small r is pushed out supersonically to create a central cavity together with an ionized shell within $t \sim 10^3 \text{ yr}$.⁷ After the shell formation, the gas in the ionized

⁷Assuming that the dust absorption dominates over the photoionization, the acceleration on dusty gas at r is given by $L(r)\sigma_d/(4\pi r^2 c\mu_H)$. Then, the timescale for a gas parcel to

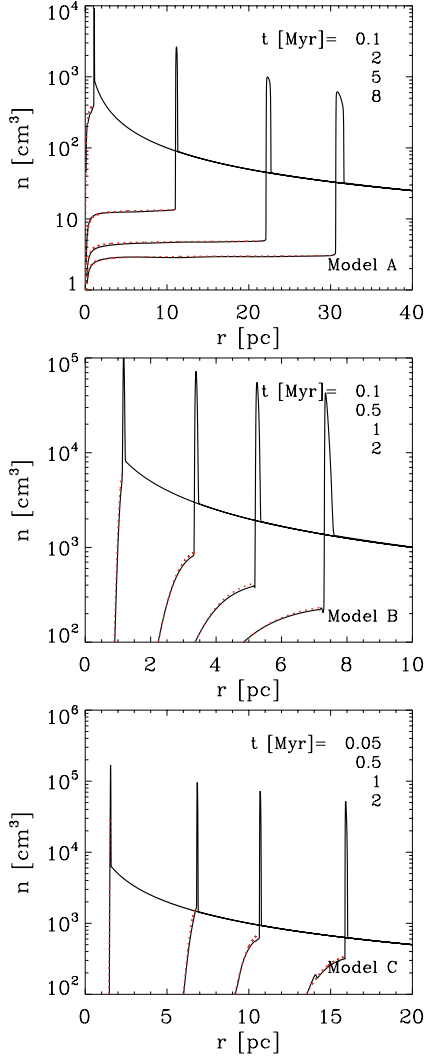


Figure 3.5 Evolution of the radial density distributions in numerical simulations of expanding H II regions in a power-law density background with $k_\rho = 1$ and $r_0 = 1$ pc for (a) Model A with $Q_i = 10^{49} \text{ s}^{-1}$ and $n(r_0) = 10^3 \text{ cm}^{-3}$, (b) Model B with $Q_i = 10^{51} \text{ s}^{-1}$ and $n(r_0) = 10^4 \text{ cm}^{-3}$, and (c) Model C with $Q_i = 10^{52} \text{ s}^{-1}$ and $n(r_0) = 10^4 \text{ cm}^{-3}$. The red dotted lines plot the corresponding static equilibrium solutions of Dr11, describing the interior of the H II region.

region relaxes into a quasi-static equilibrium state within a sound crossing time across the H II region. In Model B, the shell expands mostly due to radiation pressure until it reaches $r_{\text{sh}} = 6.3 \text{ pc}$ at $t = 0.82 \text{ Myr}$, after which the driving force switches to ionized-gas pressure.

Figure 3.5 also plots as red dashed lines the corresponding Dr11 quasi-static solutions inside the ionization front, which are in good agreement with the results of the time-dependent simulations. This not only confirms that the static solutions of Dr11 are applicable even for expanding H II regions, but also validates our ray-tracing treatment of radiation in the numerical simulations.

Figure 3.6 plots the temporal changes (solid lines) of the shell radius from the simulations in comparison with the solutions (dashed lines) of Equation (3.10). The cases with and without gravity are plotted in blue and red, respectively. Small differences at early time between the results from the different approaches are caused mainly by the assumption of a vanishing shell velocity at $t = 0$ in solving Equation (3.10), while the shell in simulations has a non-zero velocity when it first forms. Nevertheless, semi-analytic and numerical solution agree with each other within $\sim 5\%$ after 0.05 Myr , suggesting that our semi-analytic model of shell expansion is quite reliable. Although the inclusion of gravity does not make significant changes in the internal structure of the ionized region, it is self-gravity that makes the swept-up shell decelerate and eventually stall at $r_{\text{sh}} = 51 \text{ pc}$ when $t = 23 \text{ Myr}$ in Model A. Gravity becomes more significant for larger $Q_i n_{\text{rms}}$, stopping the shell expansion at $t \approx 3\text{--}4 \text{ Myr}$ in Models B and C, despite correspondingly stronger outward forces.

travel over a distance d in the ionized region is roughly $t \sim 10^3 (r^2 d / r_{\text{IF},0}^3)^{1/2} t_{\text{rec}}$, where $t_{\text{rec}} = (\alpha_B n)^{-1}$ is the recombination timescale (Arthur et al. 2004).

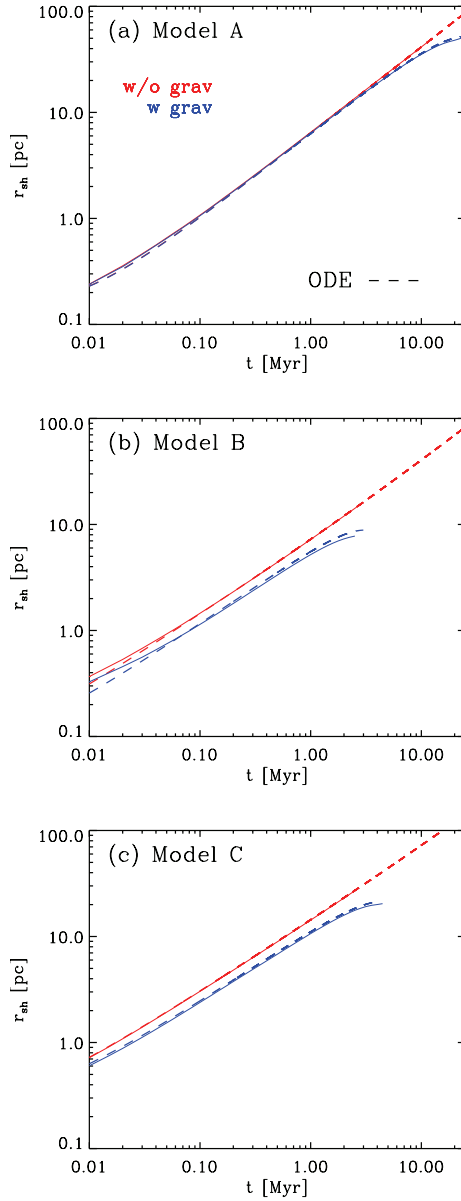


Figure 3.6 Temporal evolution of the shell radius in the simulations (solid lines) compared to the solutions of Equation (3.10) (dashed lines). The cases with and without gravity are plotted in blue and red, respectively. Other than small differences at early time, the semi-analytic results are overall in good agreement with those of the simulations.

3.4 Minimum Efficiency of Star Formation for Cloud Disruption

Consider a star cluster comprising a mass fraction ε_* of its birth cloud, and located at the cloud center. The H II region produced by the luminous cluster launches an expanding shell that sweeps up the bulk of the gas in the cloud as it grows. (see also, e.g., Harper-Clark 2011; MQT10). If it is luminous enough, the cluster is able to disrupt the entire parent cloud. For a low-mass cluster, on the other hand, only a small volume near the center is affected by the shell expansion, with the major portion of the cloud remaining intact. Therefore, there exists a minimum star formation efficiency ε_{\min} such that a cloud with $\varepsilon_* < \varepsilon_{\min}$ is not disrupted and will undergo further star formation, while a cloud with $\varepsilon_* > \varepsilon_{\min}$ will be disrupted completely, with no further star formation. In real turbulent clouds, both star formation and gas mass loss occur continuously (e.g., Dale et al. 2012, Skinner & Ostriker 2015, Raskutti et al. 2016), and one can expect ε_* increases with time until $\varepsilon_* \approx \varepsilon_{\min}$ at which point feedback is able to destroy or evacuate all the remaining gas (see Section 3.5.2 for more discussion).

In this section, we use the simple model of shell expansion described in Section 3.3 to evaluate ε_{\min} . Fall et al. (2010) studied how gas removal due to various feedback processes regulates the efficiency of star formation, and estimated ε_{\min} for massive, compact protoclusters by considering only the radiation pressure. Our model extends their work by including both ionized gas pressure and gravity. MQT10 integrated equations for shell expansion due to radiation pressure, gas pressure, stellar winds, and protostellar outflows, etc., as applied to several specific cases of massive GMCs. Our aim here is to find the systematic dependence of ε_{\min} on cloud parameters such as mass, surface density, and density profile, etc., which will be useful to assess the effectiveness of H II region feedback in a wider range of physical conditions.

3.4.1 Fiducial Case

Let us consider an isolated spherical cloud with mass M_{cl} , radius R_{cl} , and mean surface density $\Sigma_{\text{cl}} \equiv M_{\text{cl}}/(\pi R_{\text{cl}}^2)$. We assume the cloud is gravitationally bound with the one-dimensional turbulent velocity dispersion $\sigma = (\alpha_{\text{vir}}GM_{\text{cl}}/5R_{\text{cl}})^{1/2}$, where α_{vir} is the usual virial parameter of order unity (e.g., Bertoldi & McKee 1992). At $t = 0$, the cloud forms a star cluster with mass $M_* = \varepsilon_*M_{\text{cl}}$ instantaneously at its center. The remaining gas mass $(1 - \varepsilon_*)M_{\text{cl}}$ is distributed according to Equation (3.9) with $r_c = 0.1R_{\text{cl}}$ within the cloud radius R_{cl} ; we have checked that the choice of the core radius has little influence on the resulting ε_{min} as long as it is sufficiently small. The cluster emits ionizing photons at a rate $Q_i = \Xi M_*$, producing a shell at $r_{\text{sh}} = r_{\text{IF},0}$, which we determine by substituting $n_{\text{rms}}(< r_{\text{IF},0})$ for n_{rms} in Equation (3.1).

To determine ε_{min} , we first take a trial value of $0 < \varepsilon_* < 1$ and integrate Equation (3.10) over time until the shell reaches the cloud boundary. At $r_{\text{sh}} = R_{\text{cl}}$, we check if the shell meets one of the following four disruption criteria: (1) $v_{\text{sh}}(R_{\text{cl}}) = v_{\text{bind}} \equiv [(1 + \varepsilon_*)GM_{\text{cl}}/R_{\text{cl}}]^{1/2}$, corresponding to a vanishing total (kinetic plus gravitational) energy of the shell (cf. Matzner 2002; Krumholz et al. 2006)⁸; (2) $v_{\text{sh}}(R_{\text{cl}}) = \sigma$, corresponding to a stalling of the shell expansion by turbulent pressure inside the cloud (e.g., Matzner 2002; KM09; Fall et al. 2010); (3) $v_{\text{sh}}(R_{\text{cl}})$ equal to a large-scale turbulent ISM velocity dispersion, $v_{\text{turb}} \sim 7 \text{ km s}^{-1}$ (Heiles & Troland 2003), corresponding to merging of the shell with the diffuse ISM; and (4) $F_{\text{tot}}(R_{\text{cl}}) = 0$, corresponding to a balance between gravity and outward forces (e.g., Ostriker & Shetty 2011; MQT10). If none of these conditions are satisfied or if r_{sh} is unable to expand to R_{cl} , we return to the first step and repeat the calculations by

⁸As a disruption criterion, Matzner (2002) and Krumholz et al. (2006) took $v_{\text{sh}}(R_{\text{cl}}) = v_{\text{esc}} = \sqrt{2GM_{\text{cl}}/R_{\text{cl}}}$, which is the escape speed of an unbound test particle, rather than the minimum speed for unbinding a thin shell at $r = R_{\text{cl}}$.

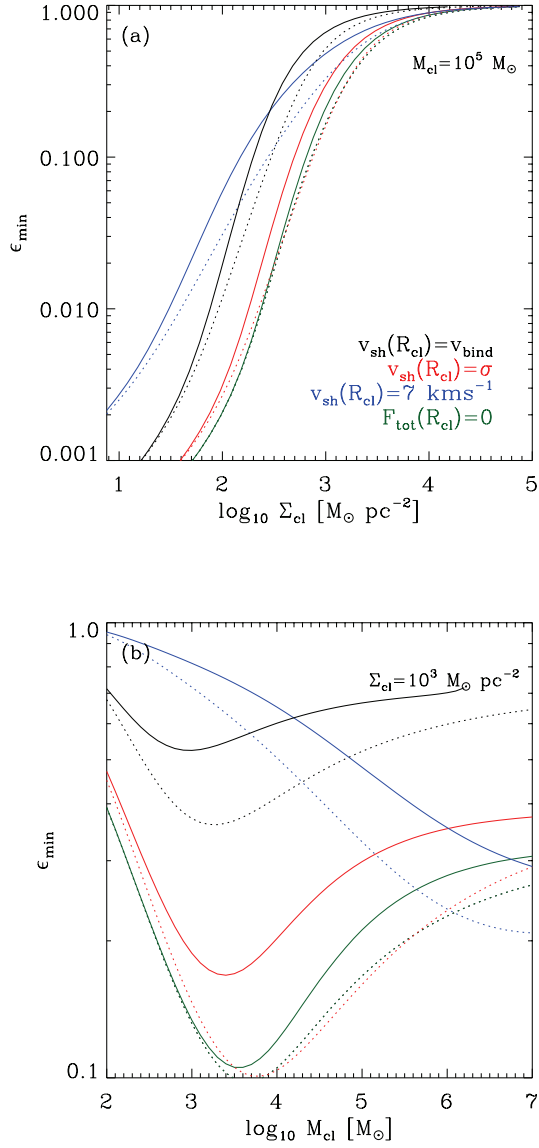


Figure 3.7 Minimum star formation efficiency ϵ_{\min} for cloud disruption by H II region expansion as a function of (a) the total mean surface density for fixed $M_{\text{cl}} = 10^5 M_{\odot}$, and (b) the total mass for fixed $\Sigma_{\text{cl}} = 10^3 M_{\odot} \text{ pc}^{-2}$, based on the four different criteria. Dotted lines show the analytic approximation using Equation (3.24).

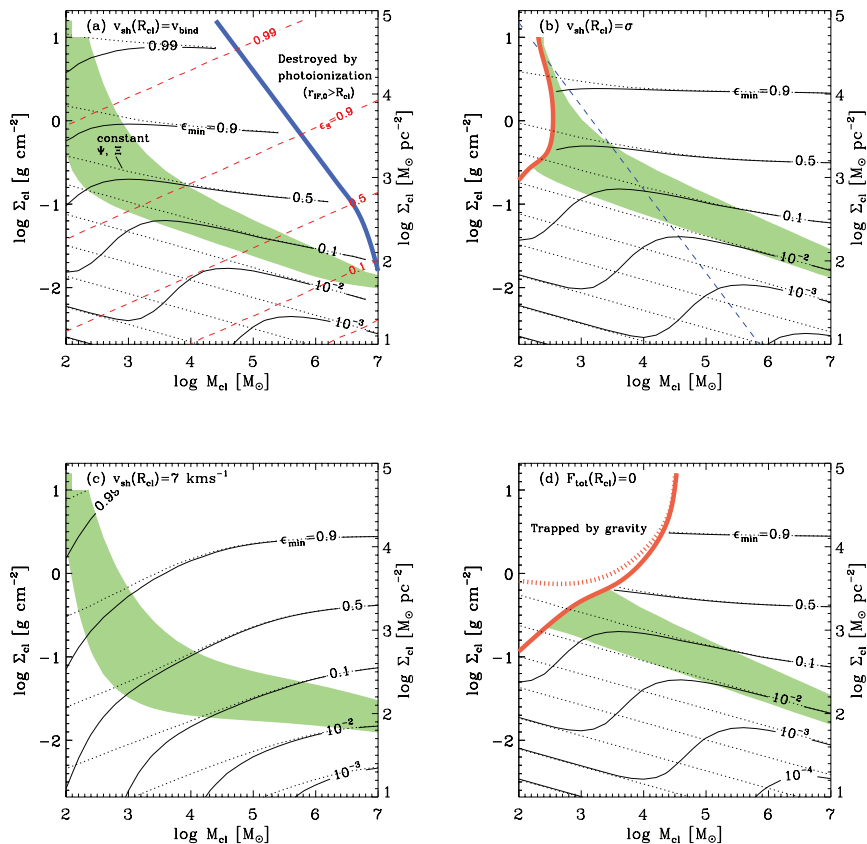


Figure 3.8 Contours of ϵ_{\min} for cloud disruption by H II region expansion, based on the criteria of (a) $v_{\text{sh}}(R_{\text{cl}}) = v_{\text{bind}} = [(1 + \epsilon_*)GM/R_{\text{cl}}]^{1/2}$, (b) $v_{\text{sh}}(R_{\text{cl}}) = \sigma = (GM/5R_{\text{cl}})^{1/2}$, (c) $v_{\text{sh}}(R_{\text{cl}}) = v_{\text{turb}} = 7 \text{ km s}^{-1}$, and (d) $F_{\text{tot}}(R_{\text{cl}}) = 0$. The solid and dotted contours correspond to variable and constant light-to-mass ratio, respectively. The red dashed contours in (a) plot the critical efficiency ϵ_S (Equation (3.21)) for $r_{\text{IF},0} = R_{\text{cl}}$, and the thick blue line draws the loci of $\epsilon_{\min} = \epsilon_S$, above which massive and compact clouds are subject to complete photodestruction. The upper left corner bounded by the thick red lines in (b) and (d) corresponds to “trapped” H II regions for which a shell experiences infall rather than expansion. The shaded area with $r_{\text{IF},0} < r_{\text{ch}} < R_{\text{cl}}$ indicates the part of parameter space for which an H II region undergoes a transition from radiation- to gas-pressure-driven expansion. Above the shaded region, $R_{\text{cl}} < r_{\text{ch}}$ so that the entire expansion is radiation-driven. Below the shaded region, $r_{\text{ch}} < r_{\text{IF},0}$ and the entire expansion is driven by gas pressure. Fall et al. (2010) proposed a demarcation between radiation- and gas-pressure-dominated cases assuming $\epsilon_* = 0.5$, shown as a blue dashed line in (b).

changing ε_* .

We take $\beta = 1.5$, $\gamma = 11.1$, $\alpha_{\text{vir}} = 1$, and $k_\rho = 1$ for our fiducial parameters. Figure 3.7 plots as solid lines ε_{min} (a) as a function of Σ_{cl} for clouds with $M_{\text{cl}} = 10^5 M_\odot$ and (b) as a function of M_{cl} for clouds with $\Sigma_{\text{cl}} = 10^3 M_\odot \text{pc}^{-2}$, for the four disruption criteria given above. As expected, clouds with smaller surface density are more easily destroyed by feedback, while more compact clouds need to have ε_{min} increasingly closer to unity for disruption. The minimum efficiency depends more sensitively on Σ_{cl} than M_{cl} . In the case of the condition $v_{\text{sh}}(R_{\text{cl}}) = v_{\text{bind}}$, for instance, ε_{min} rises rapidly from 0.02 to 0.66 as Σ_{cl} increases from 10^2 to $10^3 M_\odot \text{pc}^{-2}$ for fixed $M_{\text{cl}} = 10^5 M_\odot$, whereas it changes less than a factor of two over $10^2 M_\odot \leq M_{\text{cl}} \leq 10^6 M_\odot$ for fixed $\Sigma_{\text{cl}} = 10^3 M_\odot \text{pc}^{-2}$. Furthermore, a criterion based on a higher shell velocity at the cloud boundary results in higher ε_{min} .

Figure 3.8 plots the contours of ε_{min} on the $M_{\text{cl}}-\Sigma_{\text{cl}}$ plane for the various criteria. The solid curves draw the results for the variable light-to-mass ratio (see Equations (3.33) and (3.34)), while the case of constant $\Psi = 943 L_\odot M_\odot^{-1}$ and $\Xi = 5.05 \times 10^{46} \text{s}^{-1} M_\odot^{-1}$ are shown as dotted curves. The difference between the solid and dotted contours is caused by an incomplete sampling of the initial mass function (IMF) which lowers Ψ for low-mass clusters and thus yields higher ε_{min} for $M_* \lesssim 10^3 M_\odot$. For the criterion $v_{\text{sh}}(R_{\text{cl}}) = v_{\text{bind}}$, typical GMCs with $10^4 M_\odot \lesssim M_{\text{cl}} \lesssim 10^6 M_\odot$ and $\Sigma_{\text{cl}} \sim 10^2 M_\odot \text{pc}^{-2}$ in the Milky Way could be destroyed by a handful of O stars ($Q_{\text{i},49} \lesssim 10$) with efficiency of $\lesssim 10\%$. On the other hand, denser and more compact cluster-forming clouds or clumps with $\Sigma_{\text{cl}} \gtrsim 10^3 M_\odot \text{pc}^{-2}$ require the star formation efficiency larger than $\sim 50\%$ for disruption.

In our model, the gas density is proportional to $(1 - \varepsilon_*)$ and the ionizing rate Q_{i} is proportional to ε_* , so that the size of the H II region becomes increasingly larger for higher ε_* . It is thus possible to have $r_{\text{IF},0} \geq R_{\text{cl}}$, indicating that the whole cloud is completely photoionized from the beginning.

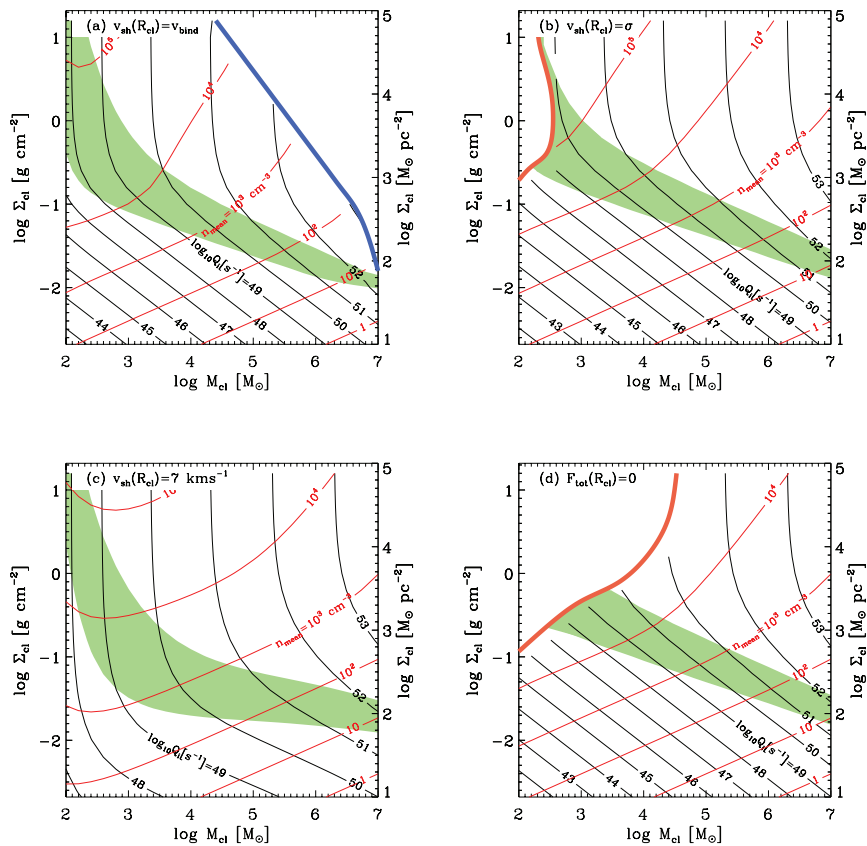


Figure 3.9 Contours of the rate of ionizing photons Q_i (black) and the mean gas density n_{mean} (red) for clouds with $\varepsilon_* = \varepsilon_{\text{min}}$.

The upper right part above the thick blue line in Figure 3.8(a) corresponds to these clouds destroyed by photoionization without involving shell expansion. This can be seen more quantitatively by considering the critical efficiency ε_{S} that makes the initial Strömgren radius equal to R_{cl} , for which Equation (3.1)

and

$$n_{\text{rms}}(< R_{\text{cl}}) \approx (1 - \varepsilon_*) \left(1 + \frac{k_\rho^2}{9 - 6k_\rho} \right)^{1/2} \frac{3\pi^{1/2} \Sigma_{\text{cl}}^{3/2}}{4\mu_{\text{H}} M_{\text{cl}}^{1/2}} \quad (3.20)$$

for $r_{\text{c}} \ll R_{\text{cl}}$

yield

$$\varepsilon_{\text{S}} = \mathcal{C} - \sqrt{\mathcal{C}^2 - 1}, \quad (3.21)$$

where

$$\mathcal{C} = 1 + \frac{f_{\text{ion}} \Xi \mu_{\text{H}}^2}{2\pi^{1/2} \alpha_{\text{B}}} M_{\text{cl}}^{1/2} \Sigma_{\text{cl}}^{-3/2}, \quad \text{for } k_\rho = 1. \quad (3.22)$$

The red dashed contours in Figure 3.8(a) plot ε_{S} , demonstrating that the photodestruction boundary corresponds to the loci of $\varepsilon_{\text{min}} = \varepsilon_{\text{S}}$. For the other criteria, $\varepsilon_{\text{min}} < \varepsilon_{\text{S}}$ for the ranges of M_{cl} and Σ_{cl} shown in Figure 3.8.

The region bounded by a thick red line (solid and dotted lines for varying and fixed Ψ and Ξ , respectively) in the upper left corner of Figure 3.8(b) and (d) corresponds to clouds with $F_{\text{tot}}(r_{\text{IF},0}) < 0$ from the beginning or $v_{\text{sh}} = 0$ somewhere before reaching the cloud boundary, indicating that a shell undergoes infall rather than expansion due to strong gravity. In order for the outward force to overcome gravity and drive expansion all the way to the cloud surface, clouds in these regions must have star formation efficiency higher than required by the respective criterion. To describe these “trapped” H II regions correctly, one needs to consider accretion flows as well as gas rotation in a flattened geometry, as in Keto (2002, 2003, 2007), which is beyond the scope of this thesis.

Once we calculate the minimum efficiency required for cloud disruption, we are positioned to derive various properties of H II regions and their host clouds. Figure 3.9 plots contours of Q_{i} (black) as well as the mean gas number density in the cloud (red) corresponding to ε_{min} for the various disruption criteria. Clearly, larger Q_{i} is necessary to destroy more massive and compact

clouds. The shaded regions shown in Figures 3.8 and 3.9 that run roughly diagonally from the upper left to lower right corners correspond to H II regions that make a transition from the radiation-dominated to thermally-dominated regime in the course of the expansion before disruption ($r_{\text{IF},0} < r_{\text{ch}} < R_{\text{cl}}$).⁹ For clouds with parameters above (below) the shaded area, radiation (thermal) pressure plays the dominant role throughout the expansion. As a demarcation line between thermal and radiation pressure dominated H II regions, Fall et al. (2010) suggested $\Sigma_{\text{cl}}/(1 \text{ g cm}^{-2}) = 0.15 \times [M_{\text{cl}}/(10^4 M_{\odot})]^{-1}$ by taking constant $\varepsilon_{\text{min}} = 0.5$. This is plotted as a blue dashed line in Figure 3.8(b). As will be shown below, the condition of $F_{\text{rad,eff}} = F_{\text{thm,eff}}$ at $R_{\text{cl}} = r_{\text{ch}}$ results in $\Sigma_{\text{cl}} \propto \varepsilon_{\text{min}}^{-2} M_{\text{cl}}^{-1}$ in our model. Therefore, since ε_{min} is a function of Σ_{cl} and M_{cl} instead of a fixed value as assumed by Fall et al. (2010), the shaded demarcation differs from their proposal.

We also calculate the time $t(R_{\text{cl}})$ for the shell to move from $r_{\text{sh}} = r_{\text{IF},0}$ to $r_{\text{sh}} = R_{\text{cl}}$, plotted in Figure 3.10 as red contours. Note that $t(R_{\text{cl}})$ is comparable to or smaller than the gas free-fall time $t_{\text{ff}} = (1 - \varepsilon_{\text{min}})^{-1/2} (3\pi^{1/2}/8G)^{1/2} M_{\text{cl}}^{1/4} \Sigma_{\text{cl}}^{-3/4}$ shown as gray contours. This is naturally expected for virialized clouds with $v_{\text{sh}}(R_{\text{cl}}) = \sigma$ or $v_{\text{sh}}(R_{\text{cl}}) = v_{\text{bind}}$ since the shell velocity approximately follows a power-law in time as $v_{\text{sh}}(r_{\text{sh}}) \approx v_{\text{sh}}(R_{\text{cl}})(t/t(R_{\text{cl}}))^{\alpha-1}$ before gravity takes over (see Figure 3.4), with an exponent $2/3 < \alpha < 4/5$ for $k_{\rho} = 1$, yielding $t(R_{\text{cl}}) = \alpha R_{\text{cl}}/v_{\text{sh}}(R_{\text{cl}}) \sim R_{\text{cl}}/\sigma$. This suggests that cloud disruption by an expanding H II region is rapid, occurring roughly over the free-fall timescale, provided the star formation efficiency is larger than the minimum value. For the condition of $v_{\text{sh}}(R_{\text{cl}}) = v_{\text{turb}}$, the slopes of the $t(R_{\text{cl}})$ -contours are different since $t(R_{\text{cl}}) \propto R_{\text{cl}}$. Nevertheless, the shell expansion takes less than the free-fall time, except for clouds with very large Σ_{cl} or very large M_{cl} .

⁹The upper and lower boundaries of the shaded regions correspond to clouds with $R_{\text{cl}} = r_{\text{ch}}$ and $r_{\text{IF},0} = r_{\text{ch}}$, respectively, for $\varepsilon_{\text{min}} = \varepsilon_{\text{min}}$.

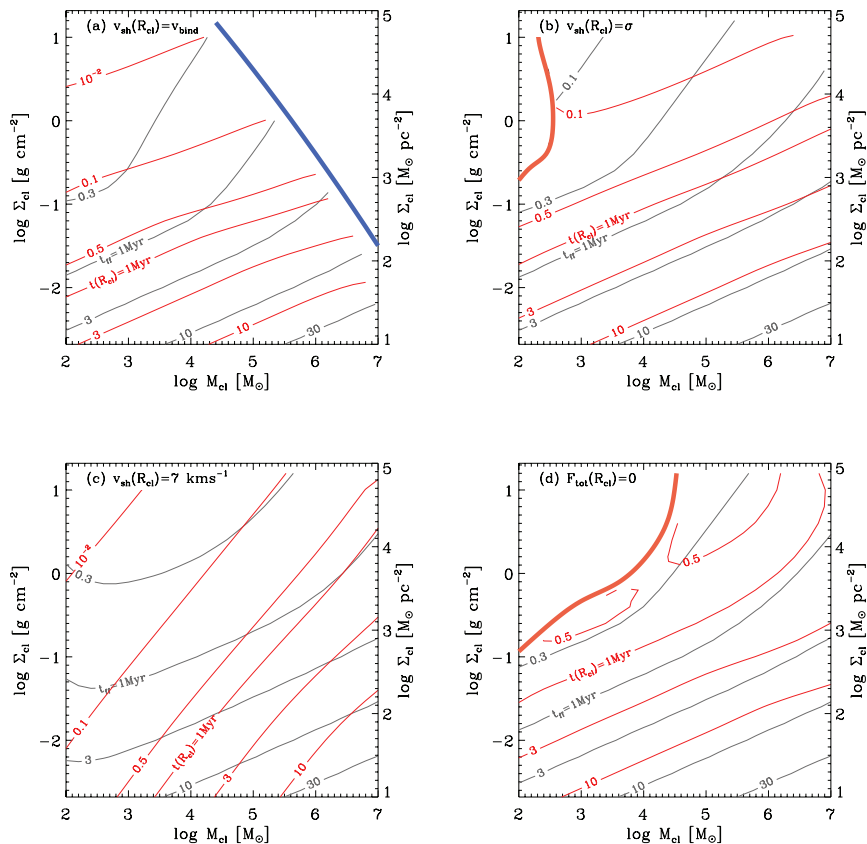


Figure 3.10 Contours of the expansion time $t(R_{\text{cl}})$ in red and the gas free-fall time t_{ff} in gray, for clouds with star formation efficiency $\varepsilon_* = \varepsilon_{\text{min}}$.

3.4.2 Analytic Estimates

One can deduce an approximate result for the minimum efficiency analytically by utilizing the effective outward force given in Equation (3.15). Multiplying both sides of Equation (3.10) by $M_{\text{sh}}v_{\text{sh}}$ and integrating the resulting equation over time, we obtain

$$\int dp_{\text{sh}}^2 = 2 \int M_{\text{sh}}(F_{\text{out,eff}} - F_{\text{in}})dr_{\text{sh}}, \quad (3.23)$$

where $p_{\text{sh}} = M_{\text{sh}}v_{\text{sh}}$ is the shell momentum. Assuming $r_c \ll R_{\text{cl}}$, $f_{\text{ion}} = 1$, and $p_{\text{sh}} \rightarrow 0$ as $r_{\text{sh}} \rightarrow 0$, Equation (3.23) yields an expression for the shell velocity at the cloud boundary as

$$v_{\text{sh}}^2(R_{\text{cl}}) = \eta_{\text{rad}} \frac{\Psi}{c} \frac{\varepsilon_*}{1 - \varepsilon_*} R_{\text{cl}} + \eta_{\text{thm}} \mathcal{T} \frac{\varepsilon_*^{1/2}}{1 - \varepsilon_*} \frac{R_{\text{cl}}^{3/2}}{M_{\text{cl}}^{1/2}} - [\eta_{\text{sh}}(1 - \varepsilon_*) + \eta_*\varepsilon_*] \frac{GM_{\text{cl}}}{R_{\text{cl}}}, \quad (3.24)$$

where $\eta_{\text{rad}} = 2/(4 - k_\rho)$, $\eta_{\text{thm}} = 4/(9 - 2k_\rho)$, $\eta_{\text{sh}} = 1/(8 - 3k_\rho)$, $\eta_* = 2/(5 - 2k_\rho)$, and $\mathcal{T} = 8\pi k_{\text{B}}T_{\text{ion}}[(3f_{\text{ion}}\Xi)/(4\pi\alpha_{\text{B}})]^{1/2}$. Note that the total force on the shell at $r_{\text{sh}} = R_{\text{cl}}$ is approximately given by

$$F_{\text{tot}} \approx \frac{\varepsilon_*\Psi M_{\text{cl}}}{c} + \frac{\mathcal{T}M_{\text{cl}}^{3/4}\varepsilon_*^{1/2}}{\pi^{1/4}\Sigma_{\text{cl}}^{1/4}} - \frac{\pi G\Sigma_{\text{cl}}M_{\text{cl}}}{2}(1 - \varepsilon_*^2). \quad (3.25)$$

The first and second terms in the right-hand-side of Equation (3.25) represent the radiative and thermal pressure forces, respectively, while the last term comes from the total gravity. The ratio of the first to second term is proportional to $\sim (\varepsilon_*^2\Sigma_{\text{cl}}M_{\text{cl}})^{1/4}$, suggesting that the relative role of radiation pressure to thermal pressure depends not only on the cloud mass and size but also on the star formation efficiency. The relation in Equation (3.24) may be combined with the disruption criterion $v_{\text{sh}}(R_{\text{cl}}) = v_{\text{bind}}$, $v_{\text{sh}}(R_{\text{cl}}) = \sigma$, and $v_{\text{sh}}(R_{\text{cl}}) = v_{\text{turb}}$ to obtain estimates for ε_* . Similarly, Equation (3.25) may be used with the disruption criterion $F_{\text{tot}}(R_{\text{cl}}) = 0$. The estimates for the minimum efficiencies are plotted as dotted lines in Figure 3.7. At high and low Σ_{cl} , the analytic estimates are very close to the solutions of the ODE (integrating Equation (3.10)), although they can depart by up to a factor of two between $\Sigma_{\text{cl}} = 10^2 - 10^3 M_\odot \text{pc}^{-2}$.

Radiation-pressure-driven Limit

When the expansion is dominated by radiation pressure, we can keep only the first term in the right-hand-side of Equation (3.24) to obtain

$$\frac{\varepsilon_{\min}}{1 - \varepsilon_{\min}^2} = \frac{\pi G c}{\eta_{\text{rad}} \Psi} \Sigma_{\text{cl}}, \quad \text{for } v_{\text{sh}}(R_{\text{cl}}) = v_{\text{bind}}, \quad (3.26)$$

and

$$\frac{\varepsilon_{\min}}{1 - \varepsilon_{\min}} = \frac{\pi \alpha_{\text{vir}} G c}{5 \eta_{\text{rad}} \Psi} \Sigma_{\text{cl}}, \quad \text{for } v_{\text{sh}}(R_{\text{cl}}) = \sigma. \quad (3.27)$$

These clearly show that the minimum efficiency increases with the mean surface density, independent of the mass. This is consistent with the results of Fall et al. (2010), although their effective outward force includes the trapping factor accounting for hot stellar winds and dust-reprocessed radiation. Similarly, a criterion based on radiation-gravity force balance at the cloud boundary in Equation (3.25) yields

$$\frac{\varepsilon_{\min}}{1 - \varepsilon_{\min}^2} = \frac{\Sigma_{\text{cl}}}{2\Psi/(\pi G c)}, \quad \text{for } F_{\text{tot}} = 0, \quad (3.28)$$

independent of M_{cl} again (see also MQT10 and Raskutti et al. 2016).

Gas-pressure-driven Limit

For expansions driven primarily by ionized-gas pressure, Equations (3.24) and (3.25) give

$$\frac{\varepsilon_{\min}}{(1 - \varepsilon_{\min}^2)^2} = \left(\frac{\pi^{5/4} G}{\eta_{\text{thm}} \mathcal{T}} \right)^2 M_{\text{cl}}^{1/2} \Sigma_{\text{cl}}^{5/2}, \quad \text{for } v_{\text{sh}}(R_{\text{cl}}) = v_{\text{bind}}, \quad (3.29)$$

$$\frac{\varepsilon_{\min}}{(1 - \varepsilon_{\min})^2} = \left(\frac{\pi^{5/4} \alpha_{\text{vir}} G}{5 \eta_{\text{thm}} \mathcal{T}} \right)^2 M_{\text{cl}}^{1/2} \Sigma_{\text{cl}}^{5/2}, \quad \text{for } v_{\text{sh}}(R_{\text{cl}}) = \sigma, \quad (3.30)$$

and

$$\frac{\varepsilon_{\min}}{(1 - \varepsilon_{\min}^2)^2} = \left(\frac{\pi^{5/4} G}{2 \mathcal{T}} \right)^2 M_{\text{cl}}^{1/2} \Sigma_{\text{cl}}^{5/2}, \quad \text{for } F_{\text{tot}} = 0. \quad (3.31)$$

Equations (3.29)–(3.31) imply $\varepsilon_{\min} \propto M_{\text{cl}}^{1/2} \Sigma_{\text{cl}}^{5/2}$ for $\varepsilon_{\min} \ll 1$.

3.4.3 Effects of k_ρ and Trapped Infrared Radiation

In Section 3.4.1, we considered a stratified cloud with $k_\rho = 1$ and assumed that infrared photons emitted by dust freely escape the cloud. Here we relax these two constraints to calculate ε_{\min} in more general situations.

First, we explore the cases with differing k_ρ . H II regions in clouds with a larger central density tend to be denser and smaller in size initially. As a result, the radiation pressure becomes more important in the initial expansion phase for larger k_ρ . Figure 3.11 plots ε_{\min} as a function of Σ_{cl} for $k_\rho = 0, 1$, and 1.4 in the case of the disruption criterion $v_{\text{sh}}(R_{\text{cl}}) = v_{\text{bind}}$. Three cloud masses $M_{\text{cl}} = 10^4, 10^5, 10^6 M_\odot$ are chosen. Although clouds with steeper density profile have smaller ε_{\min} and are thus more readily disrupted, ε_{\min} does not exhibit strong dependence on k_ρ . In fact, Equation (3.24) suggests that the shell momentum depends weakly on k_ρ only through the η coefficients.

Next, we examine the effect of dust reprocessed infrared radiation. In a high-column cloud optically thick to infrared radiation, dust-reprocessed radiation can be trapped within the cloud, providing significant boost to H II region expansion (e.g., KM09; MQT10; Hopkins et al. 2011; Ostriker & Shetty 2011; Skinner & Ostriker 2015). For the momentum injection rate by the trapped radiation, we adopt the usual simple prescription

$$F_{\text{rad,IR}} = \tau_{\text{IR}} \frac{L}{c}, \quad (3.32)$$

applicable to smooth and spherical clouds. Here, $\tau_{\text{IR}} = \kappa_{\text{IR}}(\Sigma_{\text{sh}} + \int_{r_{\text{sh}}}^{R_{\text{cl}}} \rho(r) dr)$ is the infrared optical depth through the cloud, with κ_{IR} being the Rosseland mean dust opacity (treated as a constant for simplicity).¹⁰ Note that we include the contribution to τ_{IR} from the portion of the cloud outside the shell

¹⁰The reader is referred to Skinner & Ostriker (2013) for a more rigorous treatment of spherical shell expansion driven by trapped radiation (without gravity).

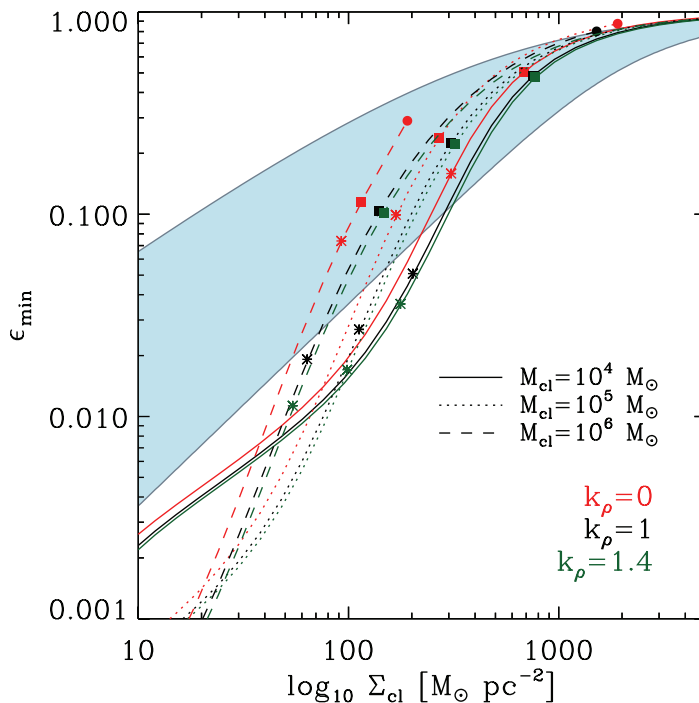


Figure 3.11 Effects of the power-law index k_ρ on ε_{\min} for the disruption criterion $v_{\text{sh}}(R_{\text{cl}}) = v_{\text{bind}}$. Three cloud masses $M_{\text{cl}} = 10^4, 10^5, 10^6 M_\odot$ are chosen. Solid circles mark the positions where $\varepsilon_{\min} = \varepsilon_{\text{S}}$, beyond which entire clouds are photoionized even before shell expansion. Asterisks and solid squares indicate the positions where $r_{\text{ch}} = r_{\text{IF},0}$ and $r_{\text{ch}} = R_{\text{cl}}$, respectively. Note that smaller k_ρ increases ε_{\min} but only slightly. The blue shaded area delineates the net star formation efficiency of turbulent clouds predicted by Raskutti et al. (2016), which includes radiation pressure but ignores gas pressure, for a range of variance $0 < \sigma_{\ln \Sigma} < 1$ of the lognormal surface density distribution (see Discussion in the text).

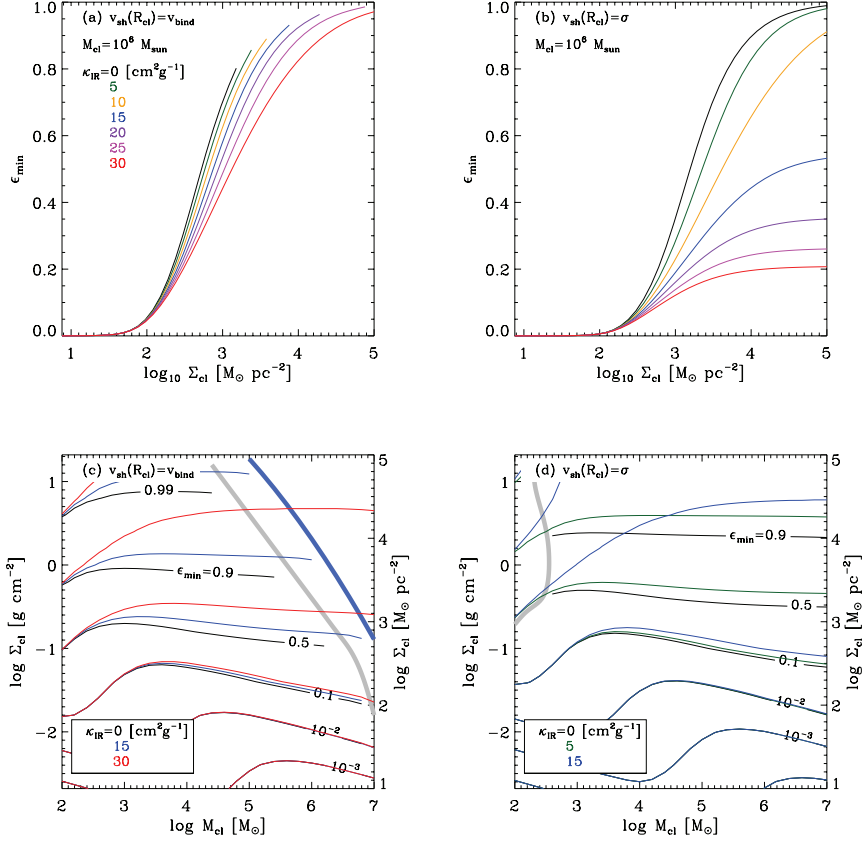


Figure 3.12 Effects of trapped infrared radiation on ϵ_{\min} for the disruption criteria $v_{\text{sh}}(R_{\text{cl}}) = v_{\text{bind}}$ (left) and $v_{\text{sh}}(R_{\text{cl}}) = \sigma$ (right). Upper panels: ϵ_{\min} as a function of Σ_{cl} for $\kappa_{\text{IR}} = 0, 5, \dots, 30 \text{ cm}^2 \text{ g}^{-1}$, when the cloud mass is $M_{\text{cl}} = 10^6 M_{\odot}$. Lower panels: Contours of ϵ_{\min} in the $M_{\text{cl}}-\Sigma_{\text{cl}}$ plane. The thick lines in panel (c) draw the photodestruction boundaries for $\kappa_{\text{IR}} = 0$ and $15 \text{ cm}^2 \text{ g}^{-1}$, on which $\epsilon_{\min} = \epsilon_{\text{S}}$. The upper left region in panel (d) bounded by the thick line experiences infall rather than expansion.

as well, corresponding to the maximum possible efficiency of feedback by the trapped radiation. As r_{sh} increases, τ_{IR} experiences a moderate decrease (by a factor of three from $r_{\text{sh}} = 0$ to $r_{\text{sh}} = R_{\text{cl}}$ for $k_{\rho} = 0$).

We integrate Equation (3.10) by adding $F_{\text{rad,IR}}$ to F_{out} . Figure 3.12 plots ε_{min} , determined from two disruption criteria, $v_{\text{sh}}(R_{\text{cl}}) = v_{\text{bind}}$ (left panels) and $v_{\text{sh}}(R_{\text{cl}}) = \sigma$ (right panels), for several different values of κ_{IR} , as functions of Σ_{cl} for $M_{\text{cl}} = 10^6 M_{\odot}$ (upper panels) and as contours in the $M_{\text{cl}}\text{-}\Sigma_{\text{cl}}$ plane (lower panels). The other parameters are the same as in the fiducial case. Clearly, κ_{IR} tends to reduce ε_{min} since clouds are more easily disrupted. But, its effect is significant only for sufficiently large κ_{IR} and/or sufficiently massive, high-column clouds so as to have $r_{\text{sh}} \lesssim r_{\text{ch}}$ and $\tau_{\text{IR}} \gtrsim 1$. When $\kappa_{\text{IR}} \approx 5 \text{ cm}^2 \text{ g}^{-1}$ appropriate for solar-metallicity gas (Semenov et al. 2003), ε_{min} is insensitive to $F_{\text{rad,IR}}$. For larger values of κ_{IR} , the minimum efficiency is reduced considerably and the photodestruction regime becomes less extended, as Figure 3.12(c) shows. For clouds with $\tau_{\text{IR}} \gg 1$, the trapped radiation dominates the direct radiation ($F_{\text{rad,IR}} > L/c$). In this case, ε_{min} computed from the criterion $v_{\text{sh}}(R_{\text{cl}}) = \sigma$ becomes close to $\varepsilon_{\text{min,IR}} = [\Psi \kappa_{\text{IR}} / (2\pi cG) - 1]^{-1}$, a prediction from the force balance between $F_{\text{rad,IR}}$ and gravity (Ostriker & Shetty 2011). The simulations of Skinner & Ostriker (2015) consider the evolution of turbulent clouds in the limit $\tau_{\text{IR}} > 1$ where reprocessed radiation dominates direct radiation.

3.5 Summary and Discussion

3.5.1 Summary

Young massive stars have dramatic effects on the surrounding ISM through ionizing radiation, winds, and supernova explosions. H II regions created by ionizing radiation from young star clusters embedded in molecular clouds are able to destroy their natal clouds under some circumstances, prevent-

ing further star formation in them. In this chapter we have used a simple semi-analytic model as well as hydrodynamic simulations to study dynamical expansion of a dusty H II region around a star cluster and its role in cloud disruption. Our expansion model is one-dimensional, assuming spherical symmetry, and treats the structure of the ionized region using the solution of Dr11. We assume that as the H II region expands, the swept-up shell formed at the interface between the ionized region and surrounding neutral gas remains very thin. We solve the shell's temporal evolution subject to outward contact forces arising from radiation and thermal pressures, and inward gravity from the cluster and the shell.

In our model, radiation pressure affects the shell expansion indirectly through the enhanced thermal pressure at the ionization front, a feature of the Dr11 solutions. The total outward contact force in our detailed model agrees within $\sim 20\%$ with the combination of the effective radiation force $F_{\text{rad,eff}} = L/c$ and the effective gas pressure force $F_{\text{thm,eff}} = 8\pi k_{\text{B}} T_{\text{ion}} r_{\text{sh}}^2 n_{\text{rms}}$ used in the simplified model KM09 (see Figure 3.3). Since $F_{\text{rad,eff}}$ is constant while $F_{\text{thm,eff}}$ depends on the shell radius r_{sh} as $F_{\text{thm,eff}} \propto r_{\text{sh}}^{1/2}$ (apart from the weak dependence on f_{ion}), expansion is driven primarily by radiation pressure when $r_{\text{sh}} < r_{\text{ch}}$ (or equivalently when $Q_{\text{i,49}} n_{\text{rms}} \gtrsim 10^4 \text{ cm}^{-3}$), and by thermal pressure when $r_{\text{sh}} > r_{\text{ch}}$. Here r_{ch} is the characteristic radius where $F_{\text{rad,eff}} = F_{\text{thm,eff}}$ (Equation (3.16)). We note that in practice, radiation forces are conveyed to the surrounding neutral shell indirectly, by compressing the ionized gas strongly to the outer portion of the H II region and increasing the density immediately interior to the shell. The cluster gravity is important in the early phase of shell expansion, especially in the radiation-driven limit, while shell self-gravity eventually halts expansion, after about the free-fall timescale of the whole cloud.

To validate the assumptions used in our expansion model, we also perform direct numerical simulations of expanding spherical H II regions for

sample cases. We find that despite the presence of small-amplitude acoustic disturbances, the radial density structure of the ionized region in our numerical simulations is overall in good agreement with the static equilibrium solutions of Dr11 throughout the shell expansion. This justifies the use of the Dr11 solutions even for expanding H II regions. The temporal changes in the shell position and velocity in our expansion model also agree with the results of the numerical simulations until gravity completely stops the expansion (Figures 3.5 and 3.6).

Using our expansion model, we explore requirements for cloud disruption by an expanding H II region around a star cluster in diverse star-forming environments, as characterized by the total cloud mass M_{cl} and the mean surface density Σ_{cl} . We also allow for power-law internal density profiles in the cloud. As criteria of cloud disruption, we consider the following four conditions: (1) the shell velocity at the cloud boundary R_{cl} is reduced to $v_{\text{sh}}(R_{\text{cl}}) = v_{\text{bind}} = [(1 + \varepsilon_*)GM_{\text{cl}}/R_{\text{cl}}]^{1/2}$, corresponding to a vanishing total energy; (2) $v_{\text{sh}}(R_{\text{cl}}) = \sigma$, the one-dimensional internal velocity dispersion of the cloud; (3) $v_{\text{sh}}(R_{\text{cl}}) = 7 \text{ km s}^{-1}$, the mean turbulent velocity dispersion of the diffuse ISM; and (4) the net force on the shell at the cloud boundary is zero. As a function of M_{cl} and Σ_{cl} , we calculate the minimum efficiency of star formation ε_{min} needed to satisfy each of the four conditions above (Figures 3.7 and 3.8). Using the effective outward forces, we also derive analytic expressions for ε_{min} in the radiation- and gas-pressure-driven limits (Section 3.4.2).

Based on the first criterion, $v_{\text{sh}}(R_{\text{cl}}) = v_{\text{bind}}$ (see Figure 3.8a), GMCs in normal disk galaxies (typically $10^4 M_{\odot} \lesssim M_{\text{cl}} \lesssim 10^6 M_{\odot}$ and $\Sigma_{\text{cl}} \sim 50\text{--}200 M_{\odot} \text{ pc}^{-2}$) can be destroyed with $\varepsilon_{\text{min}} \lesssim 10\%$. For $M_{\text{cl}} \leq 10^5 M_{\odot}$ and $\Sigma \leq 10^2 M_{\odot} \text{ pc}^{-2}$, expansion is primarily due to gas pressure, whereas both gas and radiation pressure are important at larger M_{cl} and Σ_{cl} . Disruption of cluster-forming clumps ($M_{\text{cl}} \gtrsim 10^3 M_{\odot}$ and $\Sigma_{\text{cl}} \gtrsim 10^3 M_{\odot} \text{ pc}^{-2}$, from Fig. 1 of

Tan et al. 2014) requires a significantly higher efficiency of $\varepsilon_{\min} \gtrsim 50\%$, and is mainly driven by radiation pressure. Massive clouds in starbursts ($M_{\text{cl}} \gtrsim 10^5 M_{\odot}$ and $\Sigma_{\text{cl}} \gtrsim 1 \text{ g cm}^{-2}$) would need to convert most of their gas into stars ($\varepsilon_{\min} \gtrsim 0.9$) for the H II region to achieve disruption by direct radiation forces. The minimum efficiency for the criterion $v_{\text{sh}}(R_{\text{cl}}) = \sigma$ is only slightly higher than that required from $F_{\text{tot}}(R_{\text{cl}}) = 0$, implying that the gravity is already taking over when the shell velocity drops to σ , naturally expected for a virialized cloud.

Star clusters with masses below $\sim 10^3 M_{\odot}$ are likely to have fewer OB stars and thus a smaller light-to-mass ratio than the predictions of a fully sampled IMF (see Appendix 3.A). The required ε_{\min} increases accordingly for these low-mass systems. Since the size of H II regions increases with increasing efficiency, there exists a critical efficiency ε_{S} (Equation (3.21)) at which the initial Strömngren radius is equal to the cloud size. Clouds with $\varepsilon_{\min} \geq \varepsilon_{\text{S}}$ are regarded as being disrupted by photoionization rather than shell expansion. Such clouds are located in the upper right corner in the $M_{\text{cl}}\text{-}\Sigma_{\text{cl}}$ plane in the case of the criterion $v_{\text{sh}}(R_{\text{cl}}) = v_{\text{bind}}$ (Figure 3.8(a)). Under the criterion $v_{\text{sh}}(R_{\text{cl}}) = \sigma$ or $F_{\text{tot}}(R_{\text{cl}}) = 0$, shells in the upper left corner are subject to gravitational infall rather than expansion. For clouds disrupted by shell expansion, the disruption time is typically comparable to or smaller than the gas free-fall time (Figure 3.10), implying that the disruption is rapid once an H II region is formed.

We also examine the effect of differing cloud density profiles by varying the power-law density index k_{ρ} . When all other quantities are held fixed, momentum deposition is only slightly larger for clouds with larger k_{ρ} (Figure 3.11). Therefore, disruption is quite insensitive to the degree of density concentration. Finally, we explore the effect of trapped IR radiation using a usual spherical symmetry prescription in which the associated radiation force is taken proportional to the IR optical depth through a whole cloud (see Fig-

ure 3.12). The minimum efficiency is lowered only slightly for a dust opacity of $\kappa_{\text{IR}} \approx 5 \text{ cm}^2 \text{ g}^{-1}$; a substantial reduction in ε_{min} requires $\kappa_{\text{IR}} \gtrsim 15 \text{ cm}^2 \text{ g}^{-1}$, appropriate for dust-enriched environments.

3.5.2 Discussion

In this chapter, we have calculated ε_{min} required for cloud disruption. Our results strongly suggest that GMCs are able to end their lives within a single internal crossing time after the formation of a large H II region with stellar mass $\varepsilon_{\text{min}} M_{\text{cl}}$. While this ε_{min} is a minimum, it would also be a reasonable estimate for the net star formation efficiency (at least in the idealized spherical case) for the following reasons. Consider a cloud with $\varepsilon_* < \varepsilon_{\text{min}}$. Since it cannot be destroyed by shell expansion, it will continue to form stars, and ε_* will increase. However, once ε_* reaches ε_{min} , if the disruption is rapid compared to the free-fall time, the efficiency would not increase much beyond this value.

Similarly to our study, MQT10 obtained $\varepsilon_{*,\text{GMC}}$ for five GMCs in various galactic environments. However, there are several notable differences between their and our expansion models. First, MQT10 made a distinction between the star formation efficiency of the GMC and that of cluster-forming gas at the center, the latter of which was fixed to 50%, assuming that a half of the “cluster gas” turns into stars and the other half goes into the initial shell mass. Second, the shell expansion in MQT10 begins at a radius (typically a few parsecs) that follows the observed mass-radius relations of star clusters, whereas our model starts from the initial Strömgren radius. Third, MQT10 included an additional inward force, of order $\sim GM_{\text{cl}}^2/R_{\text{cl}}^2$, due to turbulent pressure, which is not considered in our models. We omit this term as turbulent pressure is dominated by the largest scales, and is difficult to model; swept-up gas may add either inward or outward momentum to the shell. The expanding shells in MQT10 have a higher surface density and stronger inward

force initially than in our model, which is partly compensated by the outward forces they include to represent protostellar outflows and direct/dust-reprocessed radiation. Despite these differences, the conclusions of MQT10 that the $\varepsilon_{*,\text{GMC}}$ increases with surface density and that the disruption takes place in about a free-fall time of the cloud are all qualitatively consistent with our results.

Murray (2011) estimated star formation efficiency of Galactic star forming complexes by matching a WMAP sample of luminous free-free sources to host GMCs with typical mass $\sim 10^6 M_\odot$ and typical surface density $\sim 10^2 M_\odot \text{pc}^{-2}$, finding $\varepsilon_{\text{GMC}} = 0.08$ on average, for the luminosity limited samples (see his Figure 2). These observed star formation efficiencies are in the same range as our minimum efficiencies for the destruction criterion $v_{\text{sh}}(R_{\text{cl}}) = v_{\text{bind}}$ shown in Figure 3.8(a), suggesting that these clouds may be in the process of disruption by expanding H II regions. Indeed, most of these star forming complexes show evidence for expanding, bubble-like morphologies in infrared and radio recombination lines, in excess of turbulent motions (Rahman & Murray 2010; Lee et al. 2012). Murray (2011) also compared inward and outward forces to find $F_{\text{out}} > F_{\text{in}}$ and $F_{\text{rad,eff}} > F_{\text{therm,eff}}$, suggesting that expansion is driven by radiation in many of their samples. García et al. (2014) presented a catalog of GMCs in the inner southern Galaxy and estimated star formation efficiency of those associated with ultracompact H II regions. In their study, stellar mass was inferred from far-IR luminosity from IRAS point-like source catalog assuming that far-IR luminosity traces OB stellar population with an age of less than 100 Myr. They found the average star formation efficiency of 3%. While these observations are roughly consistent with our results, the data need to be interpreted with caution, because of selection bias (Murray 2011), neglect of extended emission (García et al. 2014), difficulty in identifying the boundary of a cloud that is being destroyed, and uncertainties involved in lifetime of stellar tracers. Also, it is

important to distinguish between net star formation efficiency ε_* and observational estimates of “current” star formation efficiency, the latter of which does not allow for the gas inflow/outflow experienced in the past as well as future star formation before cloud destruction (e.g., Matzner & McKee 2000; Feldmann & Gnedin 2011).

Whether dust-reprocessed radiation can be effective in dispersing star-forming clouds or not has been actively debated (e.g., KM09; MQT10, Skinner & Ostriker 2015). Because the mean free path of infrared photons can often be comparable to the system size, the non-local nature of radiation makes it difficult to obtain the solution of the radiative transfer equation. It is only in recent years that the usage of the simplified prescription for $F_{\text{rad,IR}}$ has been tested by numerical simulations. For example, Krumholz & Thompson (2012, 2013) used a flux limited diffusion scheme to investigate matter-radiation interaction in a radiation-supported dusty atmosphere. They found that the photon trapping efficiency can be greatly reduced by radiation-induced Rayleigh-Taylor instabilities that provide channels for photons to escape, resulting in an anti-correlation between matter and radiation. Using a more advanced (variable Eddington tensor) algorithm, Davis et al. (2014) revisited these calculations and found a reduced anti-correlation, corresponding to stronger matter-radiation coupling. More recently, Skinner & Ostriker (2015) adopted the M1 closure relation to run simulations of turbulent GMC disruption by reprocessed radiation feedback, self-consistently including self-gravitating collapse to produce sources of radiation. This work showed that the usual trapping factor based on the dust optical depth overestimates the radiation momentum deposition rate by a factor of ~ 4 – 5 , in part due to matter-radiation anticorrelation, and in part due to the cancellation of radiation forces where sources are distributed rather than centrally concentrated. Skinner & Ostriker (2015) also showed that reprocessed radiation is able to limit collapse only when the opacity is large, $\kappa_{\text{IR}} > 15 \text{ cm}^2 \text{ g}^{-1}$.

Here, we also find that reprocessing only significantly affects the minimum efficiency when κ_{IR} is large.

While in this thesis we exclusively focus on the effects of H II region expansion, diverse feedback mechanisms with different degrees of importance are believed to operate in star-forming environments (MQT10; Fall et al. 2010; Krumholz et al. 2014; Matzner & Jumper 2015). For example, outflows and jets from protostars feed turbulent motions within cluster-forming clumps, prevent global collapse, and reduce star formation efficiency therein (e.g., Matzner & McKee 2000; Matzner 2007; Wang et al. 2010). They are a dominant source of momentum injection before massive stars form, but are unlikely to be capable of destroying the intermediate-mass and massive clumps (e.g., Matzner 2002; Fall et al. 2010; Nakamura & Li 2014). Supernova explosions are regarded as the most powerful feedback mechanism for driving turbulence in the ISM (Joung & Mac Low 2006), providing vertical pressure support against gravity and regulating the star formation rates in galactic disks (e.g., Ostriker & Shetty 2011; Kim et al. 2013). Supernovae may also significantly impact or destroy molecular clouds if they are not dispersed by other feedback processes during the lifetime of massive cluster stars (e.g., Hennebelle & Iffrig 2014; Geen et al. 2015b; Walch & Naab 2015). Indeed, observations of mixed-morphology supernova remnants suggest that this is often the case (e.g., Rho & Petre 1998).

Traditionally, thermal pressure of hot gas created by shocked stellar winds is thought to dominate expansion of ionized bubbles (Castor et al. 1975; Weaver et al. 1977; Koo & McKee 1992). The pressure of hot gas trapped within the H II region would push the inner boundary of the H II region outward, indirectly doing mechanical work on the swept-up shell. A semi-analytic spherical model by Martínez-González et al. (2014) suggests that shocked wind pressure is more important than radiation pressure in driving H II region expansion. However, observed X -ray luminosity is lower than the

theoretical prediction of hot confined gas, casting doubt on the effectiveness of stellar winds in controlling the dynamics of gas around star clusters (Harper-Clark & Murray 2009; Yeh & Matzner 2012; Rosen et al. 2014). Estimates of wind energy lost via various mechanisms suggest that leakage of hot gas through holes in the shell and/or turbulent mixing at hot-cold interfaces can explain the observed low luminosity (Rosen et al. 2014). The approximate calculation by KM09 shows that a shocked wind brings only a modest increase in effective outward force on a porous shell, with a wind trapping factor of order unity. The star formation efficiencies we present here are the minimum for disruption solely by dynamical expansion of an H II region, but other feedback process could reduce ε_{\min} .

We now comment on caveats of the present study in various aspects. First, we have assumed that the ionizing luminosity remains constant during the shell expansion. For most clouds, this is acceptable as the expansion time $t(R_{\text{cl}})$ is shorter than 3.8 Myr, a typical main-sequence lifetime of ionizing stars (McKee & Williams 1997; Krumholz et al. 2006). For clouds located in the lower right corner in the $M_{\text{cl}}-\Sigma_{\text{cl}}$ plane (Figure 3.10), however, the ionizing output may experience a significant drop before cloud disruption. With a decrease in the outward force, the shell expansion would be slowed down and possibly fall back due to gravity, implying that higher ε_{\min} is required than in our models. Second, while we assume spherical symmetry, expanding shells may be subject to various non-radial instabilities such as ionization front instability (Vandervoort 1962; Kim & Kim 2014), Rayleigh-Taylor instability, and Vishniac instability (Garcia-Segura & Franco 1996; Whalen & Norman 2008) in the early phase, and gravitational instability assisted by external pressure in the late phase (Wünsch et al. 2010; Iwasaki et al. 2011b; Kim et al. 2012). At the nonlinear stage, the shell may break up into pieces and create holes through which photons and ionized gas can leak out, reducing feedback efficiency. Moreover, any shell that forms in an

inhomogeneous cloud would itself be inhomogeneous, such that acceleration would be nonuniform (see below).

Third, our model considers a situation where the shell expansion is driven solely by a single embedded H II region, as in Fall et al. (2010) and MQT10. In reality, however, star formation in a molecular cloud may be distributed spatially with a population of subclusters (McKee & Williams 1997). This results in expanding H II regions of various sizes interacting with each other. In early stage of expansion, the momentum injection by individual subclusters may not simply add up to the total due to cancelation; this effect is evident in the simulations of Skinner & Ostriker (2015). But once a main shell created by the most luminous H II region expands to a volume large compared to that of most ionizing sources (assuming some degree of subcluster concentration within the cloud), the effective radiation source is the same as for a single central cluster.

More importantly, we have ignored blister-type H II regions that can effectively vent ionized gas through low density regions. Since real turbulent clouds have a log-normal density distribution characterized by many clumps and holes, even an initially fully embedded H II region is likely to transform into blister-type. The analytic model of Matzner (2002) in which all H II regions are taken to be blister-type showed that photoevaporative mass loss from small subclusters (dominated by those around turnover in the cluster luminosity function (McKee & Williams 1997)) alone can limit star formation efficiency of galactic GMCs to below $\sim 10\%$, with the photodestruction time scale decreasing as a function of the cloud mass. When both mass loss mechanisms are considered, dynamical disruption by shell expansion is more frequent than photodestruction alone, but significant photoevaporative mass loss also occurs prior to disruption if clouds survive for several free-fall times (Krumholz et al. 2006). However, these analyses of photoevaporation did not allow for the reduced surface area that gas confined in dense filaments

presents to radiation, which tends to reduce photoevaporation. Indeed, Dale et al. (2012, 2013a) found that less than 10% of the gas is photoionized in their simulations. The reduced effective area of clumpy clouds also reduces radiation forces (Thompson & Krumholz 2016; Raskutti et al. 2016). The relative importance of the mass loss mechanisms in inhomogeneous clouds is difficult to assess and would require numerical simulations (but see Matzner & Jumper (2015)).

In inhomogeneous turbulent clouds, gas dispersal would take place in a gradual, rather than impulsive, fashion. Both analytic and numerical investigations of radiation-only feedback models show that broad distributions of surface density and/or radiation flux cause locally low-column, super-Eddington gas parcels to be ejected from the system early on, while higher surface density parcels are ejected only later, when the total luminosity of stars has increased. (e.g., Raskutti et al. 2016; Thompson & Krumholz 2016). For example, the blue shaded region in Figure 3.11 shows the range of net star formation efficiency of turbulent clouds with width of lognormal surface density distribution in the range $0 < \sigma_{\ln \Sigma} < 1$, predicted from the analytic model of Raskutti et al. (2016) (see their Equation (21)), which considers just radiation pressure on dust from non-ionizing radiation. Stellar mass grows until there is little gas above the critical surface density, making ε_* increase beyond what is expected from uniform case (lower bound). Note also that the inclusion of gas pressure in our model is responsible for the dramatic difference in efficiency for low Σ_{cl} clouds.

Because the current models consider only uniform spherical shells of gas rather than a broadened surface density probability distribution function, we underestimate the luminosity and hence ε_{min} required to eject the denser clumps in a cloud via direct radiation forces. However, the direct photoevaporation enabled by star formation close enough to the cloud periphery would also tend to lower ε_{min} . Additional star formation can also in principle be trig-

gered in shocked shells by the collect and collapse process (e.g., Elmegreen & Lada 1977; Hosokawa & Inutsuka 2006; Dale et al. 2007; Iwasaki et al. 2011b; Dale et al. 2013b). To address these complex issues, it is necessary to perform three-dimensional radiation hydrodynamic simulations of star cluster formation in a turbulent cloud with both ionizing and non-ionizing radiation.

Appendix

3.A Light-to-mass ratio of Star Clusters

The photon output produced per unit stellar mass can differ greatly from cluster to cluster at the low-mass end owing to stochastic fluctuations in the stellar populations (da Silva et al. 2012), and/or due to the correlation between cluster mass and the maximum stellar mass (Weidner & Kroupa 2006). To assess the likely magnitude of this effect, we use a new version of the SLUG code (Krumholz et al. 2015) to simulate spectral properties of star clusters as a function of mass. In its simplest setup, SLUG can simulate coeval stellar populations of finite mass and predict a full spectrum based on libraries of stellar evolutionary tracks and stellar atmosphere models. We use the IMF of Chabrier (2003), Starburst99 setting for spectral synthesis (which uses the stellar atmosphere model for OB stars by Pauldrach et al. (2001)), and the Geneva library for stellar evolutionary tracks.

We ran 1000 simulations for different cluster mass bins logarithmically spaced by 0.2 dex. Figure 3.13 shows probability distributions of the maximum stellar mass $m_{*,\max}$ in a cluster, the spectral parameter β , the ionizing photon rate per stellar mass Ξ , and the mean ionizing photon energy $h\nu_1$ at $t = 0.1$ Myr after birth. The cases with the total cluster mass of $M_* = 10^2$, 10^3 , and $10^4 M_\odot$ are shown as black, red, and blue histograms, respectively.

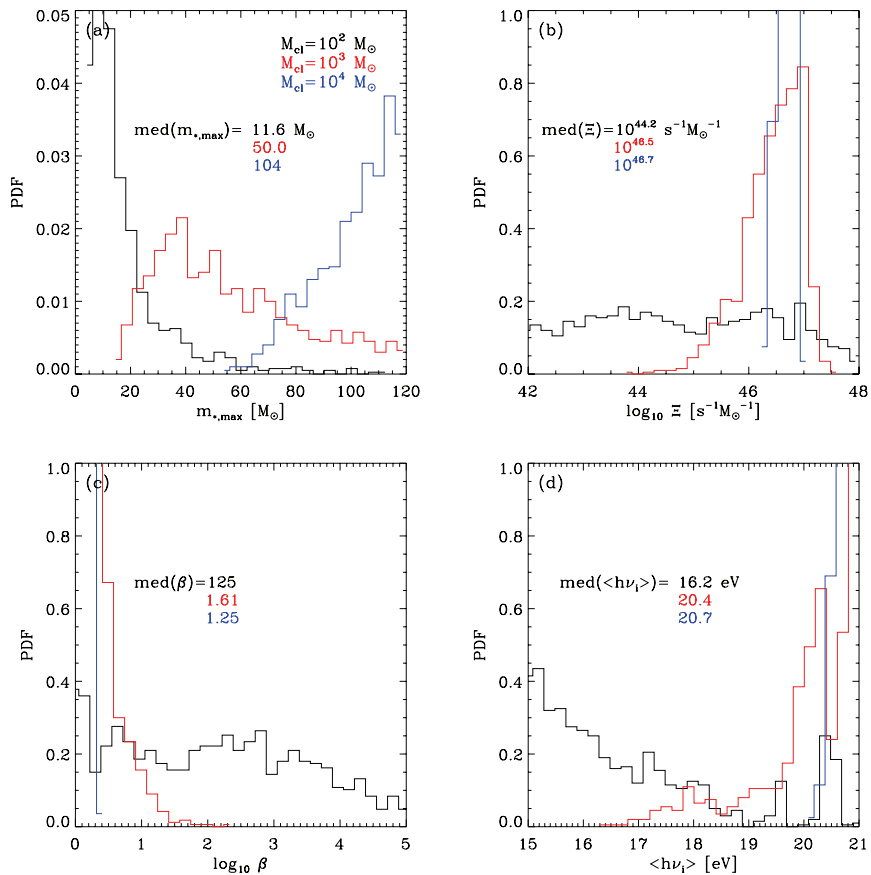


Figure 3.13 Probability distributions of (a) the maximum stellar mass $m_{*,\max}$, (b) the ionizing luminosity per stellar mass Ξ , (c) the spectral parameter β , and (d) the mean ionizing photon energy $h\nu_i$ from 10^3 realizations of a star cluster with mass $M_* = 10^2 M_\odot$ (black), $10^3 M_\odot$ (red), and $10^4 M_\odot$ (blue) using SLUG. The median values of the distributions are given in each panel.

The median values of $m_{*,\max}$, β , Ξ , and $h\nu_1$ are given in each panel. As expected, $m_{*,\max}$ of massive clusters with $M_* = 10^4 M_\odot$ is close to the theoretical maximum $120 M_\odot$, whereas low-mass clusters with $M_* = 10^2 M_\odot$ hardly contain O-type stars more massive than $\sim 20 M_\odot$. In the latter case, the distributions of β and Ξ span several orders of magnitude due to high stochasticity.

Figure 3.14 plots the median values (red solid lines with diamonds) and the 10–90th percentile range (green shade) of Ψ , Ξ , β , and $h\nu_1$ as functions of the cluster mass. We fit the median values to $\tilde{\Psi}$ and $\tilde{\Xi}$ using

$$\log_{10} \left(\frac{\tilde{\Psi}}{L_\odot / M_\odot} \right) = \frac{2.98 \mathcal{X}^6}{29.0 + \mathcal{X}^6}, \quad (3.33)$$

and

$$\log_{10} \left(\frac{\tilde{\Xi}}{1 \text{ s}^{-1} M_\odot^{-1}} \right) = \frac{46.7 \mathcal{X}^7}{7.28 + \mathcal{X}^7}, \quad (3.34)$$

where $\mathcal{X} = \log_{10} M_*/M_\odot$, which are drawn as dashed lines in Figure 3.14.

For $M_* \gtrsim 10^4 M_\odot$, $\tilde{\Psi} = 943 L_\odot M_\odot^{-1}$ and $\tilde{\Xi} = 5.05 \times 10^{46} \text{ s}^{-1} M_\odot^{-1}$, suitable for massive clusters that fully sample the IMF (see also Murray et al. 2010). But, both $\tilde{\Psi}$ and $\tilde{\Xi}$ decrease rapidly for clusters less massive than $10^3 M_\odot$. When $M_* = 10^2 M_\odot$, for example, $\tilde{\Xi}$ is smaller by more than two orders of magnitude compared to the fully sampled case. This is because a large number of samples with small M_* do not have (O-type) stars massive enough to emit ionizing photons.

3.B Method of Numerical Simulations

Here we describe the method of direct numerical simulations for the internal structure and expansion of an H II region. The equations of hydrodynamics we solve in spherical symmetry are

$$\frac{\partial \rho}{\partial t} + \frac{\partial}{\partial r}(\rho v) + \frac{2\rho v}{r} = 0, \quad (3.35a)$$

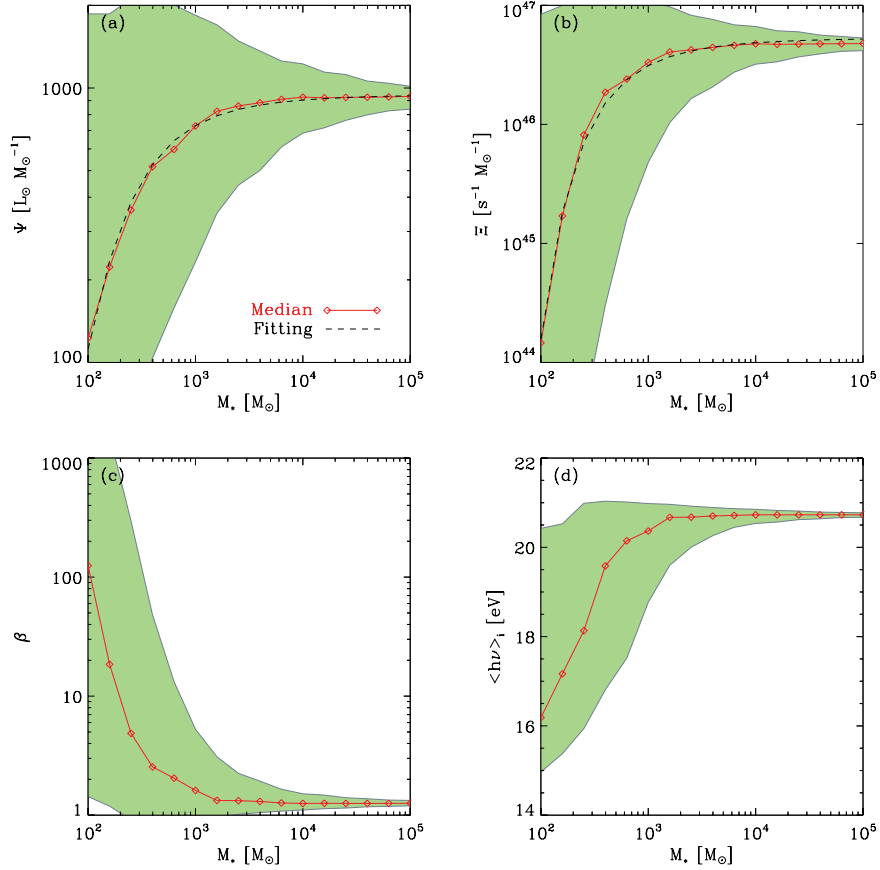


Figure 3.14 Dependence on the cluster mass of the median values of (a) the light-to-mass ratio Ψ , (b) the ionizing photon rate per unit mass Ξ , (c) the spectral parameter β , and (d) the mean ionizing photon energy $h\nu_1$. The solid lines with diamonds are the median values, while the shaded regions represent the 10-90th percentile range from the Monte Carlo simulations. The dashed lines in the upper panels are our fits (Equations (3.33) and (3.34)) to the median values of Ψ and Ξ .

$$\frac{\partial \rho v}{\partial t} + \frac{\partial}{\partial r}(P + \rho v^2) + \frac{2\rho v^2}{r} = f_{\text{grav}} + f_{\text{rad}}, \quad (3.35b)$$

$$\frac{\partial \rho_{\text{n}}}{\partial t} + \frac{\partial}{\partial r}(\rho_{\text{n}} v) + \frac{2\rho_{\text{n}} v}{r} = \mu_{\text{H}}(\mathcal{R} - \mathcal{I}), \quad (3.35c)$$

where ρ is the total gas density, ρ_{n} is the neutral gas density, v is the radial velocity, and $P = (1+x_e)n k_{\text{B}}T$ is the gas pressure with the ionization fraction $x_e = 1 - \rho_{\text{n}}/\rho$. The source terms in Equation (3.35b) include the gravitational acceleration ($f_{\text{grav}} = -GM(< r)\rho/r^2$) and radiative force (see Section 3.2). In Equation (3.35c), $\mathcal{R} = \alpha_{\text{B}}x_e^2 n^2$ and \mathcal{I} refer to the recombination rate and ionization rate, respectively. We evolve Equations (3.35a)–(3.35c) using a modified version of the *Athena* code in spherical coordinates (Stone et al. 2008). *Athena* is an Eulerian code for magnetohydrodynamics based on a directionally unsplit Godunov method. We use the van Leer algorithm for time integration, a piecewise linear method for spatial reconstruction, and the HLLC Riemann solver to compute the fluxes.

In order to handle radiation hydrodynamics coupled with non-equilibrium chemistry, we implement a simple radiative transfer algorithm based on the methods suggested by Mellema et al. (2006b) and Krumholz et al. (2007a). As in the Dr11 model, we regard the radiation as being dichromatic, consisting of ionizing and non-ionizing photons. Let $\phi_{j-1/2}$ ($\psi_{j-1/2}$) and $\phi_{j+1/2}$ ($\psi_{j+1/2}$) be the fractions of the ionizing (non-ionizing) photons per second arriving at the inner and outer boundaries of j -th cell, respectively. The photon consumption rate of ionizing radiation at the j -th shell is then computed as $\Gamma_j = Q_{\text{i}}(\phi_{j-1/2} - \phi_{j+1/2})/\Delta V_j = Q_{\text{i}}\phi_{j-1/2}(1 - e^{-\Delta\tau_j})/\Delta V_j$, where $\Delta V_j = (4\pi/3)[(r_j + \Delta r/2)^3 - (r_j - \Delta r/2)^3]$ is the shell volume and $\Delta\tau_j = (n_{\text{n},j}\langle\sigma_{\text{H}}\rangle + n_j\sigma_{\text{d}})\Delta r$ is the optical depth across the j -th cell. Here, $n_{\text{n},j}$ and n_j is the neutral and total density of the j -th cell, respectively, and $\langle\sigma_{\text{H}}\rangle = 6.3 \times 10^{-18} \text{ cm}^2$ is the mean photoionization cross-section. The volumetric photoionization rate of the j -th cell is then $\mathcal{I}_j = \Gamma_j \times (n_{\text{n},j}\langle\sigma_{\text{H}}\rangle\Delta r)/\Delta\tau_j$. The

calculation for non-ionizing radiation is carried out in a similar way, with dust being the lone source of opacity.

We set the gas temperature according to the ionization fraction as

$$T = T_{\text{ion}} - \left(\frac{1 - x_e}{1 + x_e} \right) (T_{\text{ion}} - T_n), \quad (3.36)$$

with $T_{\text{ion}} = 10^4$ K and $T_n = 10^2$ K (Henney et al. 2005). Clearly, $T = T_{\text{ion}}$ for $x_e = 1$ and $T = T_n$ for $x_e = 0$. The timestep for the radiation update is chosen by the requirement that the relative changes in T and x_e should be less than 10%. Since this timestep is usually much shorter than that for the hydrodynamic update, we subcycle the radiation update. The radiative force $f_{\text{rad},j} = [L_i(\phi_{j-1/2} - \phi_{j+1/2}) + L_n(\psi_{j-1/2} - \psi_{j+1/2})]/(c\Delta V_j)$ at the j -th cell is added to the momentum flux explicitly at the end of every subcycle. To ensure accuracy of hydrodynamics, we impose an additional constraint on the hydrodynamic timestep such that the temperature and ionization fraction should not change by more than a factor of 4 between the hydrodynamic updates.

In all models, we fix the spatial resolution to $\Delta r = 0.005$ pc and place the inner boundary at 0.1 pc. The location of the outer boundary is chosen large enough to cover the stalling radius of an expanding shell. We adopt the outflow boundary conditions at both inner and outer radial boundaries of the simulation domain. We have tested our implementation of the ionization chemistry against a standard problem for supersonic (R-type) propagation of an ionization front in a dustless, static medium (e.g., Test 1 in Iliev et al. 2006), confirming that our numerical results reproduce the analytic solutions within errors of 3%. We then apply the code to our main problem, namely, expansion of a dusty H II region in a stratified cloud with $k_\rho = 1$ and $T = T_n$. Without star formation and feedback, the cloud is supposed to be in force balance between gravity and turbulent pressure. Since our one-dimensional

models are unable to handle turbulence properly, we enforce the hydrostatic balance in the outer envelope unaffected by shell expansion. This is done effectively by turning off all body forces and taking $v = 0$ outside the shock front. Section 3.3.5 presents our numerical results for models with fixed $\beta = 1.5$ and $\gamma = 11.1$, and varying density and Q_i .

Chapter 4

Implementation of Adaptive Ray Tracing Method and Tests¹

Abstract

We present an implementation of an adaptive ray tracing (ART) module in the *Athena* hydrodynamics code that accurately and efficiently handles the radiative transfer involving multiple point sources on a three-dimensional Cartesian grid. We adopt a recently proposed parallel algorithm that uses non-blocking, asynchronous MPI communications to accelerate transport of rays across the computational domain. We validate our implementation through several standard test problems including the propagation of radiation in vacuum and the expansions of various types of H II regions. Additionally, scaling tests show that the cost of a full ray trace per source remains comparable to that of the hydrodynamics update on up to $\sim 10^3$ processors. To demonstrate application of our ART implementation, we perform a simulation of

¹A version of this chapter has been published as “Modeling UV Radiation from Massive Stars. I. Implementation of Adaptive Ray-tracing Method and Tests,” Kim, J.-G., Kim, W.-T., Ostriker, E. C., & Skinner, M. A. 2017, *The Astrophysical Journal*, 851, 93.

star cluster formation in a marginally bound, turbulent cloud, finding that its star formation efficiency is 12% when both radiation pressure forces and photoionization by UV radiation are treated. We directly compare the radiation forces computed from the ART scheme with that from the M_1 closure relation. Although the ART and M_1 schemes yield similar results on large scales, the latter is unable to resolve the radiation field accurately near individual point sources.

4.1 Introduction

Radiative feedback plays a vital role in regulating star formation on various scales (e.g., Krumholz et al. 2014). On small scales, radiation from (accreting) protostars raises the temperature of the surrounding gas, affecting the evolution of individual accretion disks and suppressing fragmentation of the dense cluster-forming gas into very low mass objects (e.g., Krumholz 2006; Whitehouse & Bate 2006; Offner et al. 2009). On intermediate scales, ultra-violet (UV) radiation emitted by massive stars not only reduces cold neutral gas available for star formation via photoionization and photodissociation (Whitworth 1979; Williams & McKee 1997; Matzner 2002; Krumholz 2006), but also produces thermal and radiation pressure that controls the dynamics of H II regions by inducing expansion (Krumholz & Matzner 2009; Murray et al. 2010; Lopez et al. 2011; Kim et al. 2016). Ionizing radiation that escapes from star-forming regions also produces diffuse ionized gas in the Milky Way and other galaxies (e.g., Haffner et al. 2009) and contributes to re-ionization of the intergalactic medium (IGM) in the Universe at high redshift (e.g., Barkana & Loeb 2001). On large scales in galaxies, far UV radiation from young OB associations is the dominant heating source of the diffuse neutral interstellar medium (ISM) via the photoelectric effect on small dust grains (e.g., Wolfire et al. 2003). This controls the thermal pressure that contributes

to supporting the vertical gravitational weight of the ISM in galactic disks, and thus represents an important feedback loop that self-regulates star formation (e.g., Ostriker et al. 2010; Kim et al. 2013). Therefore, it is essential to follow effects of radiative feedback to address questions such as star formation efficiencies and the mechanisms of cloud destruction for giant molecular clouds (GMCs), as well as a wide variety of other physical issues in the ISM and IGM.

Since star formation and feedback involve highly nonlinear processes, radiation hydrodynamic (RHD) simulations have become an indispensable tool in understanding the impact of radiation on star cluster formation occurring in turbulent clouds. For example, several recent studies relied on numerical simulations to investigate the effects of photoionization (Walch et al. 2012; Dale et al. 2012, 2013a; Howard et al. 2016; Gavagnin et al. 2017) and radiation pressure from dust-reprocessed infrared (Skinner & Ostriker 2015) or stellar UV (Raskutti et al. 2016) radiation on cloud dispersal. Dale et al. (2014) and Dale (2017) studied the combined effects of ionizing radiation with stellar winds. More recently, Geen et al. (2016), Grudić et al. (2018), and Shima et al. (2017) explored how the radiation feedback works together with supernova explosions to destroy parent molecular clouds.

To treat radiation feedback properly, it is important to solve radiative transfer (RT) equation accurately and efficiently. Despite increasing demand for RHD simulations, RT still remains numerically challenging for a number of reasons: high dimensionality, non-local and multiscale behavior of interactions between radiation and matter, and difficulty in choosing a suitable frame for evaluating radiation and fluid variables, to name a few (Mihalas 2001; Castor 2004). A common approach for the numerical solution of RT problems is to take the angular moments of the transfer equation and to adopt a closure relation to truncate the hierarchy of moments. As the time-dependent moment equations can be written as hyperbolic conservation laws,

high-order Godunov methods are often adopted to solve the time-dependent RT problem.

In astrophysics, the most widely-used moment method is the flux-limited diffusion approximation, in which the radiation flux is calculated by taking a local gradient of the radiation energy density (Levermore & Pomraning 1981; Krumholz et al. 2007a; González et al. 2015), applying a limiter if the gradient is very steep to prevent superluminal transport. RT solvers based on flux-limited diffusion are suitable for describing radiation fields in optically-thick fluids. However, they are of limited accuracy in treating an optically-thin medium with a complex source distribution as well as in casting shadows in the transition zones where the optical depth varies significantly (e.g., Hayes & Norman 2003; Davis et al. 2014).

Another approach for RT is to use the M_1 closure relation that assumes that the intensity is invariant under rotation about the direction of radiation flux (e.g., Levermore 1984; González et al. 2007; Skinner & Ostriker 2013; Rosdahl et al. 2013). For a single point source, the M_1 closure model can correctly describe the radiation field both in the optically thin and thick regimes (see Skinner & Ostriker 2013). When there are multiple sources distributed widely, however, M_1 can fail in the optically-thin regime. For example, when two beams going in different directions interact with each other, they unphysically merge rather than crossing (e.g., Frank et al. 2012), since the local flux is assumed to be unidirectional. For diffuse radiation in systems with both optically thin and thick regions, a more accurate closure relation can be obtained from the formal solution of the RT equation using the multidirectional method of short characteristics (Davis et al. 2012). For point-like sources that have strong angular variations in emissivity, however, artificial anisotropic structure can arise from inaccuracy in interpolating intensity over neighboring cells in the short characteristics method (Finlator et al. 2009).

For problems in which the total emission is dominated by a small number

of point sources (and in which the reprocessed diffuse radiation is negligible), one may directly integrate the RT equation by calculating the column density (or, equivalently, the optical depth) to every point in the simulation domain starting from the sources. A method utilizing short characteristics calculates the column densities from the sources by performing upwind interpolation over cells (Mellema et al. 2006b). Alternatively, the long-characteristics method computes the column densities to each zone by following rays emitted by all sources until they reach the domain boundary (Abel et al. 1999; Lim & Mellema 2003). This allows one to calculate the radiation field more accurately over the entire domain at the expense of excessively resolving the regions close to the sources when the number of ray directions is large.

To alleviate the inefficiency of the traditional long characteristics method, Abel & Wandelt (2002) developed a novel, adaptive ray tracing (ART) technique that has since been widely used to describe ionizing radiation originating from massive stars, in various astronomical contexts (e.g., Krumholz et al. 2007b; Bisbas et al. 2009; Wise & Abel 2011; Baczynski et al. 2015). In the ART method, rays are created at point sources and successively split as they are traced outward based on the Hierarchical Equal Area isoLatitude Pixelization (HEALPix) scheme (Górski et al. 2005). The salient feature of this method is that via ray splitting, the angular resolution of radiation adapts to the local hydrodynamical resolution, such that the number of rays from each point source intersecting each grid zone remains approximately constant. While this RT method is quite efficient in achieving an accurate solution for the radiation field, existing codes employing the ART method often suffer from poor parallel performance. This is due to excessive overhead for inter-processor communication as rays traverse the interfaces between subdomains (see Section 4.2.2), making some implementations of the ART method essentially inapplicable to large-scale simulations with multiple point sources.

Very recently, Rosen et al. (2017) developed a hybrid RHD module for

the *Orion* code by combining the ART method with the flux-limited diffusion method. It makes use of the former to describe direct radiation from point sources, while taking advantage of the latter to treat diffuse radiation arising from gas and dust. Their parallel algorithm for the ART uses completely non-blocking, asynchronous communication, which greatly improves the parallel scaling of ray tracing over previous implementations using a synchronous communication algorithm. The scaling tests in Rosen et al. (2017) showed that the cost of the ART module in *Orion* remains comparable to that of hydrodynamics up to $\sim 10^3$ processors.

In this work, we describe implementation of an ART module for multiple point sources in the grid-based magnetohydrodynamics (MHD) code *Athena* (Stone et al. 2008) and present test results. Our implementation closely follows the parallelization strategy proposed by Rosen et al. (2017) and includes a few new features that further improve parallel performance. To model hydrogen ionization and recombination processes, we adopt a simple and efficient explicit scheme based on an analytic approximation. We first measure the scalability of our implementation by performing weak and strong scaling tests. We then apply the code to the standard test problems, namely, the expansion of R-type and D-type ionization fronts as well as expansion of a dusty H II region driven by both thermal and radiation pressures. By comparing the numerical results with analytic or semi-analytic solutions, we demonstrate the accuracy of our ART implementation.

A key application for ART is to follow the detailed effects of radiation produced by OB stars on their natal GMCs. To this end, we have combined our ART module with other physics packages implemented in *Athena* and run numerical RHD simulations of star cluster formation in turbulent, self-gravitating, unmagnetized clouds; these models are similar to the RHD simulations of Skinner & Ostriker (2015); Raskutti et al. (2016), but include both ionizing and non-ionizing radiation computed using ART. In this chapter, we

demonstrate practical application of our ART module via an example simulation for a fiducial model. For comparison to the radiation field computed using the M_1 closure relation in the moment-based *Hyperion* code (Skinner & Ostriker 2013), we have also run an RT model with non-ionizing radiation only, using an identical set of sources and density distribution. We find that the large-scale radiation fields from the two RT methods are quite similar to each other, but there is non-negligible difference at small scale near the point sources, where resolution is inherently limited for pure moment methods like that in *Hyperion*.

The rest of this chapter is organized as follows. In Section 4.2, we present the basic equations that we solve and briefly review the algorithm of ART together with our parallelization strategy. We also describe the subcycling method to solve the equation for hydrogen ionization and recombination. Section 4.3 presents the results of the scaling tests as well as the tests of the expansion of H II regions. In Section 4.4, we describe the numerical setup for simulations of star cluster formation in turbulent molecular clouds and compare the radiation fields based on the ART method with those from the moment method with the M_1 closure relation. Finally, we summarize and discuss future applications of the code in Section 4.5.

4.2 Numerical Method

Stellar UV radiation can alter the chemical, thermal, and dynamical state of the ISM through various processes. In this chapter, we consider the two most basic processes: photoionization of hydrogen atoms and direct radiation pressure applied to the gas/dust mixture. The governing equations we adopt read:

$$\frac{\partial \rho}{\partial t} + \nabla \cdot (\rho \mathbf{v}) = 0, \quad (4.1)$$

$$\frac{\partial}{\partial t}(\rho \mathbf{v}) + \nabla \cdot (\rho \mathbf{v} \mathbf{v} + P \mathbf{I}) = -\rho \nabla \Phi + \mathbf{f}_{\text{rad}}, \quad (4.2)$$

$$\frac{\partial n_{\text{H}^0}}{\partial t} + \nabla \cdot (n_{\text{H}^0} \mathbf{v}) = \mathcal{R} - \mathcal{I}, \quad (4.3)$$

$$\nabla \Phi = 4\pi G \rho, \quad (4.4)$$

where $\rho = 1.4m_{\text{H}}n_{\text{H}}$ is the gas density with n_{H} representing the total hydrogen number density, \mathbf{v} is the velocity, P is the thermal pressure, Φ is the gravitational potential, and \mathbf{f}_{rad} is the force per unit volume due to absorption of stellar UV radiation. In Equation (4.3), n_{H^0} refers to the number density of neutral hydrogen, and \mathcal{I} and \mathcal{R} denote the volumetric ionization and recombination rates of hydrogen, respectively, whose functional forms are given in Section 4.2.3. Numerical solution of Equations (5.3) and (4.2) uses the methods described by Stone et al. (2008), with the radiation force source term updated using an operator splitting. The Poisson Equation (4.4) is solved using fast Fourier transforms (FFTs) with vacuum boundary conditions (Skinner & Ostriker 2015). At any location on the grid, the radiation flux and energy density are required to compute the source terms \mathbf{f}_{rad} and \mathcal{I} , respectively; these radiation terms are computed via our implementation of ART.

In what follows, we describe how the radiation fields are computed in the ART method in Section 4.2.1, while our method of parallelization is presented in Section 4.2.2. Our algorithms for updating radiation source terms and advancing Equation (4.3) are described in Section 4.2.3.

4.2.1 Adaptive Ray Tracing

Here we briefly review the RT problem for point sources in the framework of ART. We refer the reader to Wise & Abel (2011), Baczynski et al. (2015), and Rosen et al. (2017) for more detailed descriptions.

We consider only the direct radiation field from multiple point sources and ignore diffuse emission as well as scattered light. Under the assumption that the light crossing time is much shorter than both the sound crossing time

and the time scale for the change in opacity, streaming radiation reaches equilibrium with matter effectively instantaneously. The radiation intensity should, therefore, satisfy the time-independent transfer equation

$$\mathbf{n} \cdot \nabla I = -\chi I, \quad (4.5)$$

where I is the radiation intensity, $\chi = \rho\kappa$ is the (isotropic) extinction coefficient of matter per unit path length for κ the opacity, and \mathbf{n} is a unit vector parallel to the propagation direction of radiation. Both I and χ depend on the position \mathbf{x} , time t , and the frequency ν , which are suppressed for notational simplicity.

We solve Equation (4.5) along a set of rays that discretize the directions in solid angle with respect to individual radiation sources. For simplicity, we consider monochromatic radiation emergent from a single point source located at \mathbf{x}_{src} with luminosity L ; an extension to polychromatic radiation from multiple sources is straightforward by taking a summation over a discretized set of frequencies and over rays from different sources. We inject photon packets from \mathbf{x}_{src} and carry them radially outward along the direction of any given ray by calculating the absorption rates of the photon energy and momentum over the grid cells they pass through. The direction of propagation \mathbf{n}_{ray} is determined using the HEALPix scheme of Górski et al. (2005), which divides the unit sphere into $N_{\text{ray}}(\ell) = 12 \times 4^\ell$ equal-area pixels at the level $\ell \geq 0$. Denoting the initial level by ℓ_0 , each injected photon packet on a given ray carries luminosity $L_{\text{ray}}(r = 0) = L/N_{\text{ray}}(\ell_0)$, subtends a solid angle $\Omega_{\text{ray}}(\ell_0) = 4\pi/N_{\text{ray}}(\ell_0)$ from the source, and propagates along the ray $\mathbf{x} = \mathbf{x}_{\text{src}} + r\mathbf{n}_{\text{ray}}$, where $r = |\mathbf{x} - \mathbf{x}_{\text{src}}|$ measures the distance from the source.

Integrating Equation (4.5) over the whole solid angle gives the radiation energy equation

$$\nabla \cdot \mathbf{F} = -c\chi\mathcal{E}, \quad (4.6)$$

where c is the speed of light, \mathcal{E} is the radiation energy density, and \mathbf{F} is the radiation flux. With $\mathbf{F} = \hat{\mathbf{r}}Le^{-\tau(r,\mathbf{n})}/(4\pi r^2)$ and $\mathcal{E} = |\mathbf{F}|/c$ for streaming radiation, Equation (4.6) can be written as

$$\frac{\partial L_{\text{ray}}}{\partial r} = -\chi L_{\text{ray}}, \quad (4.7)$$

where $L_{\text{ray}}(r) = Le^{-\tau(r,\mathbf{n}_{\text{ray}})}/(4\pi)$ is the discretized luminosity at distance r in the region subtended by Ω_{ray} . We compute the length of a line segment Δr between the two consecutive cell interfaces intersected by a ray (see, e.g., Wise & Abel 2011; Baczynski et al. 2015). The corresponding cell optical depth is $\Delta\tau = \chi\Delta r$. The absorption rates of the radiation energy and momentum by the material along the path Δr in a given cell are then $\Delta L_{\text{ray}} = L_{\text{ray,in}}(1 - e^{-\Delta\tau})$ and $\mathbf{n}_{\text{ray}}\Delta L_{\text{ray}}/c$, respectively, where $L_{\text{ray,in}}$ is the luminosity of the ray entering the cell. The luminosity of a photon packet on a given ray is therefore reduced by ΔL_{ray} as it traverses the cell.

Utilizing the lab-frame equations of RHD (e.g., Mihalas 2001), these quantities are related to the volume-averaged radiation energy density and flux in a given cell as

$$\mathcal{E} = \frac{1}{\chi\Delta V} \sum_{\text{rays}} \frac{\Delta L_{\text{ray}}}{c}, \quad (4.8)$$

$$\mathbf{F} = \frac{1}{\chi\Delta V} \sum_{\text{rays}} \Delta L_{\text{ray}} \mathbf{n}_{\text{ray}}, \quad (4.9)$$

where ΔV is the cell volume and the summation is taken over all rays passing through the cell. Note that these expressions satisfy the flux-limiting condition $|\mathbf{F}| \leq c\mathcal{E}$ (Levermore 1984) and tend to the exact value in the limit of infinite angular resolution. In updating Equation (4.2) over time step Δt , an amount $\Delta t \mathbf{f}_{\text{rad}} = \Delta t \chi \mathbf{F}/c$ is added to the gas momentum in each cell using Equation (4.9) for \mathbf{F} (see Equation (4.22) below; in practice these operator-split increments to the gas momentum are applied after each radi-

ation subcycle). Since the photon momentum on a set of rays traversing a cell is reduced by $\sum_{\text{rays}} \Delta L_{\text{ray}} \mathbf{n}_{\text{ray}}/c$ per unit time, this update is manifestly conservative of momentum.

To ensure that each grid cell is sampled by at least m_{ray} rays, we split a parent ray into four child rays at one higher HEALPix level if the solid angle $(\Delta x)^2/r^2$ (corresponding to the maximum angle subtended by a given face of the current cell as seen from the source) is smaller than $m_{\text{ray}}\Omega_{\text{ray}}$. With a uniform grid spacing of Δx , this corresponds to the maximum distance $r_{\text{max}}(\ell) = [3/(\pi m_{\text{ray}})]^{1/2} 2^\ell \Delta x$ that rays can travel at level ℓ . The new child rays are cast at positions $\mathbf{x}_{\text{src}} + r_{\text{max}}(\ell) \mathbf{n}_{\text{ray}}$. We follow photon packets as they traverse rays, dividing them equally when a parent ray splits into children. A ray is terminated and its photon packet is destroyed either where a ray exits the computational domain or where the photon packet is completely absorbed. The latter occurs when the total optical depth $\tau(r, \mathbf{n}_{\text{ray}})$ from the source is larger than a specified value τ_{max} , which we set to 7 as a default value. In order to alleviate the geometrical artifacts arising from the use of the crossing length rather than the ray-cell volume intersection, we randomly rotate the injection directions of the rays at every time step (Krumholz et al. 2007b).

4.2.2 Parallelization

Although conceptually simple and easy to implement, the major drawback of the ART method so far has been its poor parallel performance. There are two chief impediments to achieving scalable performance on a distributed memory platform: load imbalance and communication overhead. First, the amount of work needed per processor for the ART is roughly proportional to the number of the ray-cell crossings. Since this depends not only on the spatial distribution of sources but also on the opacity of the material, processors most likely have unequal workload depending on the problem geometry.

This imposes an inherent limit to scalability of ART with static domain decomposition. One may alleviate this issue by dynamically adjusting the local domain sizes to evenly distribute the workload.

The second problem is more serious and common to long-characteristic methods implemented with domain decomposition, in which the data from different subdomains are local to individual processors. For rays traveling across multiple subdomains, processors need to share information such as the propagation directions of the rays, optical depth, etc., in order to integrate Equation (4.7) along the characteristics. Because a ray may be terminated by the $\tau > \tau_{\max}$ condition before traversing a subdomain that lies along the \mathbf{n}_{ray} direction, it cannot be determined in advance when, from where, or how many rays will enter a particular subdomain. The size and pattern of the data that need to be communicated among processors are therefore highly irregular. This poses a major challenge to the parallelization of the ART code. Indeed, the communication overhead has been the dominant performance bottleneck in the existing long-characteristic methods (e.g., Rijkhorst et al. 2006; Wise & Abel 2011).

Rosen et al. (2017) presented an efficient parallel algorithm for the ART module implemented in *Orion*, an adaptive mesh refinement (AMR) code. The key idea in their algorithm is to make use of the non-blocking message-passing operations (`MPI_Isend`, `MPI_Iprobe`, and `MPI_Test`) provided in the MPI-3 standard² for communication of ray information between processors. This allows processors to carry on their work (local transport of photon packets along rays) while communication is pending (see also Baczynski et al. 2015). Thus, the transport of rays within and between subdomains can be executed asynchronously, greatly reducing the idle time spent waiting for other processors to finish their work.

Another hallmark of the Rosen et al. (2017) algorithm is the use of a

²<http://mpi-forum.org/docs/mpi-3.1>

global “destroy” counter N_{dest} , which keeps track of how many rays have been terminated in the whole computational domain. Whenever a ray at the HEALPix level ℓ is terminated, we increment the local destroy counter by $N_{\text{dest,ray}} = 4^{\ell_{\text{max}} - \ell}$, where ℓ_{max} is the maximum level allowed. The global destroy counter is then a simple sum of the local destroy counters, and it stays synchronized across the processors by non-blocking communications. When all rays are terminated, we have $N_{\text{dest}} = N_{\text{dest,max}} = N_{\text{src}} \times 12 \times 4^{\ell_{\text{max}}}$, where N_{src} is the number of point sources in the entire domain. Updating the destroy counter as a global shared variable allows processors to determine when to exit the work-communication cycle without relying on synchronous, blocking communication.

We have implemented ART in *Athena* following the parallelization approach of Rosen et al. (2017), with some additional modifications to improve parallel performance. The schematic overview of the ray tracing algorithm is shown in Figure 4.1. Our ART algorithm runs the following steps:

Initialization: (Executed only once at the start of the simulation) Find neighbor grids³ that share faces, edges, or corners, and allocate memory for arrays `my_pp_list` and `exit_pp_list`, which will store local and outgoing ray (or photon packet) information, respectively. Each processor has one `my_pp_list` and n_{ngbr} `exit_pp_list`, where n_{ngbr} is the number of the neighbor grids.

Step 1: If any sources exist within my grid, create an initial set of directions \mathbf{n}_{ray} and corresponding L_{ray} values and store the photon packet information in `my_pp_list`. Compute $N_{\text{dest,max}}$ from N_{src} summed over all grids.

³In *Athena* without mesh refinement, the computational domain is divided into a set of rectangular “grids”, each of which is owned by a single processor. Thus, “grid” is equivalent to “subdomain” for *Athena*.

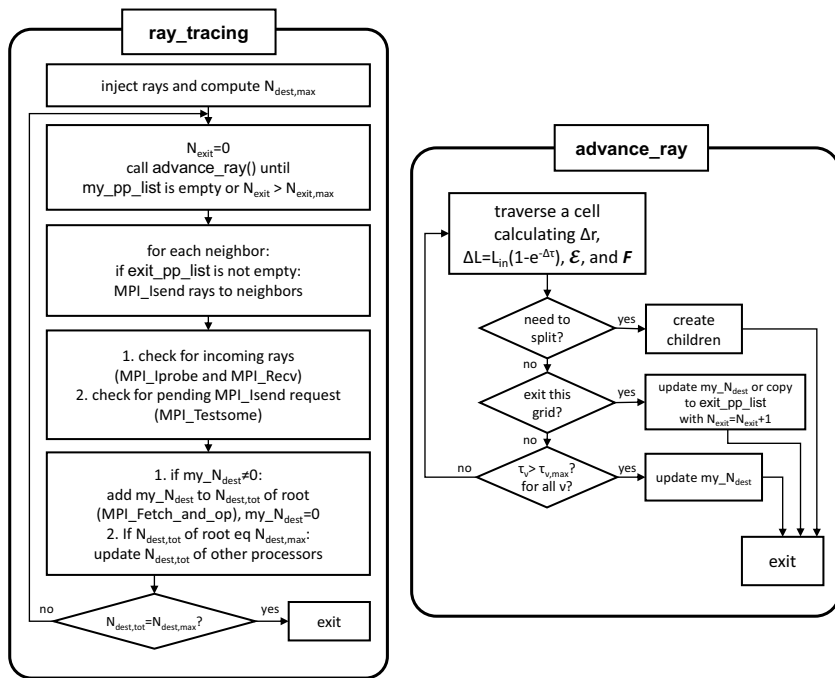


Figure 4.1 Flowchart of the ART algorithm: `ray_tracing` performs one ray tracing throughout the global computational domain while `advance_ray` traces one ray within a local subdomain (“grid” in *Athena*).

Step 2: Transport photon packets along their respective \mathbf{n}_{ray} directions within the local domain until either the total number of photon packets that need to be passed to neighbor grids exceeds $n_{\text{exit,max}}$ or no local ray is left in `my_pp_list`. Each ray is followed until it (1) needs to split, (2) reaches the grid boundaries, or (3) is terminated with $\tau \geq \tau_{\text{max}}$. Stack information on photon packets for rays leaving the local grid in the particular `exit_pp_list` for each neighbor. Calculate radiation energy density and flux for cells through which rays pass, as described in Section 4.2.1.

Step 3: Loop over the list of the neighbors and send photon packet information in `exit_pp_list` to the neighbor grids (`MPI_Isend`), checking if the previous operation has completed (`MPI_Testsome`).

Step 4: Check for incoming messages from neighbors (`MPI_Iprobe`). If there are any, execute a blocking receive for each of them (`MPI_Recv`) and copy the received data to `my_pp_list`.

Step 5: If `my_pp_list` is empty, add N_{dest} to the global destroy counter $N_{\text{dest,tot}}$ in the root processor (`MPI_Fetch_and_op`) and reset N_{dest} to 0.

Step 5-1: (Root processor only) If $N_{\text{dest,tot}} = N_{\text{dest,max}}$, update $N_{\text{dest,tot}}$ to $N_{\text{dest,max}}$ in the other processors (`MPI_Fetch_and_op`).

Step 6: Go back to Step 2 if $N_{\text{dest,tot}} \neq N_{\text{dest,max}}$. Exit the ray tracing when $N_{\text{dest,tot}} = N_{\text{dest,max}}$.

Our implementation of the ART method has two notable differences compared to that of Rosen et al. (2017). First, in Rosen et al. (2017), photon packets in a given grid are communicated to neighbors only after all rays have been traced to the grid boundaries. Therefore, processors without a

source have to wait, repeatedly checking for rays coming from neighbors, until the intervening grids toward the sources successively finish their work. In our implementation, instead of waiting until all local ray-tracing is complete, communications between neighbors are initiated as soon as the number of rays traced to the subdomain boundary exceeds a certain prescribed number $n_{\text{exit,max}}$, reducing the idle time spent by downstream processors (see also Baczynski et al. 2015). Although it is ideal to communicate a single photon packet right after the ray-tracing reaches the subdomain boundary to keep the downstream processors busy whenever possible, there is an optimal granularity, i.e., ratio of computation to communication, or an optimal value of $n_{\text{exit,max}}$ that gives the best performance due to the finite overhead required for function calls and synchronization. The choice of $n_{\text{exit,max}}$ certainly depends on the source distribution, the domain decomposition, and machine specifications. In the case of a single point source at the box center, we find $n_{\text{exit,max}} = 100$ gives the best performance, and we adopt this value for the rest of this chapter.

Second, unlike in Rosen et al. (2017), we perform atomic (that is, uninterruptible) memory updates⁴ of the destroy counter utilizing the `MPI_Fetch_and_op` function, which is one of the Remote-Memory-Access (RMA) operations in the MPI library. In the RMA operations, also called one-sided communications, processors are allowed to access a remote target memory without involving the explicit intervention of the remote processor. The RMA operations have comparatively low overheads since one processor specifies all communication parameters. We find that the use of the `MPI_Fetch_and_op` function helps to reduce substantially the overall cost of ray tracing when a large number of processors ($N_{\text{core}} \geq 256$) are used.

⁴Atomic operations are guaranteed to complete without interference from other operations, ensuring correct results even when multiple processors try to access $N_{\text{dest,tot}}$ simultaneously.

In addition to these differences, we find that the following implementation details can further improve parallel efficiency.

- We use arrays for storing a collection of local and outgoing/incoming rays, to enable copying data to/from the communication buffer in one chunk. We dynamically allocate memory for arrays, which doubles in size if the old array becomes full.
- As pointed out by Baczynski et al. (2015), we store only necessary information required for ray tracing, splitting, etc. in the ray data structure to minimize the amount of data transferred between processors. These include the HEALPix level ℓ , HEALPix pixel number, luminosity L_{ray} , source position \mathbf{x}_{src} , ray direction \mathbf{n}_{ray} , distance from the source, and the (integer) indices of the current cell in a grid.
- We treat `my_pp_list` as a stack and access its elements in a Last-In-First-Out manner. For example, if a parent ray splits, child rays are stacked immediately on top of one another or on a sibling of the parent. This implies that we recursively follow a ray and its child until the grid boundary is reached (see also Baczynski et al. 2015).
- In Step 1, photon packets are stacked in such a way that every 12 contiguous blocks of elements in `my_pp_list` have ray directions that belong to the distinct 12 pixels at the base HEALPix level. The pixel numbers (in the nested numbering scheme) are arranged in 12 hierarchical tree structures, corresponding to the 12 base-level pixels. With $\ell_0 = 4$, for example, the HEALPix numbers of injected rays can be ordered as $0, 4^4, 2 \times 4^4, \dots, 11 \times 4^4, 1, 1 + 4^4, 1 + 2 \times 4^4, \dots$.

All of the above help to distribute workload to downstream processors as fast as possible and at a similar rate in all directions.

4.2.3 Update of Radiation Source Terms

We make a number of simplifying assumptions in modeling the photochemistry of hydrogen and its thermodynamic state. First, we adopt the on-the-spot approximation in which every diffuse Lyman-continuum photon resulting from a recombination to the ground state is locally reabsorbed. We neglect the diffuse ionizing radiation that can be important in the evolution of radiatively-driven collapse and instabilities of ionization fronts (Haworth & Harries 2012). Second, we do not consider collisional ionizations, which are negligible compared to photoionizations in the temperature range of our interest ($T \lesssim 10^4$ K). Third, we do not solve an energy equation that accounts for radiative heating and cooling. Instead, we simply assign the gas temperature according to

$$T = T_{\text{ion}} - \left(\frac{x_{\text{n}}}{2 - x_{\text{n}}} \right) (T_{\text{ion}} - T_{\text{neu}}), \quad (4.10)$$

where $x_{\text{n}} \equiv n_{\text{H}^0}/n_{\text{H}}$ is the neutral gas fraction, and T_{ion} and T_{neu} are the prescribed temperatures of the fully ionized ($x_{\text{n}} = 0$) and purely neutral ($x_{\text{n}} = 1$) states, respectively (e.g., Henney et al. 2005; Kim et al. 2016).⁵ For our tests presented in this work, we adopt the constant temperatures $T_{\text{ion}} = 8000$ K and $T_{\text{neu}} = 20$ K, the latter of which falls within the temperature range inferred from the line ratios of low- J rotational transitions of CO molecules (e.g., Yoda et al. 2010). The gas thermal pressure is then set by $P = [1.1 + (1 - x_{\text{n}})]n_{\text{H}} k_{\text{B}}T$, accounting for a 10% of helium content. The two-temperature isothermal equation of state has been adopted by numerous numerical studies of H II regions and is valid as long as the time scale for approaching thermal equilibrium is short compared to the dynamical time scale (e.g., Lefloch & Lazareff 1994; Williams 2002; Gritschneider et al. 2009; Mackey et al. 2014;

⁵In reality, the gas temperature profile exhibits a peak immediate behind an ionization front due to spectral hardening. However, Lefloch & Lazareff (1994) found that the detailed functional form of $T(x_{\text{n}})$ does not significantly affect the dynamics of H II regions.

Steggles et al. 2017). Although idealized, Equation (4.10) is a simple and practical approach to following the pressure-driven dynamical expansion and internal structure of H II regions.

Equation (4.3) describes temporal changes of the neutral hydrogen fraction, with the recombination and ionization rates given by

$$\mathcal{R} = \alpha_B n_e n_{\text{H}^+}, \quad (4.11)$$

and

$$\mathcal{I} = n_{\text{H}^0} \int_{\nu_L}^{\infty} \frac{c\mathcal{E}_\nu}{h\nu} \sigma_{\text{H}}(\nu) d\nu, \quad (4.12)$$

respectively, where \mathcal{E}_ν is the radiation energy density per unit frequency, $\alpha_B = 3.03 \times 10^{-13} (T/8000 \text{ K})^{-0.7} \text{ cm}^3 \text{ s}^{-1}$ is the case B recombination coefficient (Osterbrock 1989; Krumholz et al. 2007b), $n_{\text{H}^+} = n_e = n_{\text{H}}(1 - x_{\text{n}})$ is the number density of protons and electrons, ν_L is the Lyman limit corresponding to $h\nu_L = 13.6 \text{ eV}$, and $\sigma_{\text{H}}(\nu)$ is the photoionization cross section. In practice, Equation (4.12) is evaluated as a discrete summation over a finite number of frequency bins. In this work, we use one frequency bin for ionizing radiation, denoted by the subscript “i”. Equation (4.12) then becomes

$$\mathcal{I} = n_{\text{H}^0} \frac{c\mathcal{E}_i}{h\nu_i} \langle \sigma_{\text{H}} \rangle \quad (4.13)$$

$$= \frac{1}{\Delta V} \frac{n_{\text{H}^0} \langle \sigma_{\text{H}} \rangle}{\chi_i} \sum_{\text{rays}} \frac{\Delta L_{\text{ray},i}}{h\nu_i}, \quad (4.14)$$

where $\mathcal{E}_i = \int_{\nu_L}^{\infty} \mathcal{E}_\nu d\nu$ is the energy density of ionizing radiation, as evaluated using Equation (4.8), $h\nu_i$ is the mean energy of the ionizing photons, and

$$\langle \sigma_{\text{H}} \rangle = \int_{\nu_L}^{\infty} \frac{\mathcal{E}_\nu/h\nu}{\mathcal{E}_i/h\nu_i} \sigma_{\text{H}}(\nu) d\nu, \quad (4.15)$$

is the frequency-averaged effective cross section. The actual value of $\langle \sigma_{\text{H}} \rangle$ depends on the spectral shape of the incident radiation \mathcal{E}_ν , which in turn depends both on the optical depth from the source and the spectral types of

ionizing stars. For simplicity, we take the constant values $h\nu_i = 18 \text{ eV}$ and $\langle\sigma_{\text{H}}\rangle = 6.3 \times 10^{-18} \text{ cm}^2$ in the present work.

We solve Equation (4.3) in two steps: hydrodynamic update and source update by treating \mathcal{R} and \mathcal{I} as source terms. The source update requires solving

$$\frac{dx_{\text{n}}}{dt} = \frac{\mathcal{R} - \mathcal{I}}{n_{\text{H}}} = \alpha_{\text{B}}n_{\text{e}}(1 - x_{\text{n}}) - x_{\text{n}}\Gamma, \quad (4.16)$$

where $\Gamma \equiv \mathcal{I}/n_{\text{H}}^0$. Since the time scale for changes of x_{n} is almost always smaller than the hydrodynamic time step, we update x_{n} explicitly using sub-cycling, as explained below.

Assuming that α_{B} and Γ are constant during a substep and using $n_{\text{e}} = n_{\text{H}}(1 - x_{\text{n}})$, the right-hand side of Equation (4.16) is quadratic in x_{n} . Altay & Theuns (2013) showed that this has an analytic solution⁶

$$x_{\text{n}}(t) = x_{\text{eq}} + \frac{(x_{+} - x_{\text{eq}})(x_0 - x_{\text{eq}})K}{(x_{+} - x_0) + (x_0 - x_{\text{eq}})K}, \quad (4.17)$$

where $x_0 = x_{\text{n}}(t_0)$, $K = \exp[-(x_{+} - x_{\text{eq}})(t - t_0)\alpha_{\text{B}}n_{\text{H}}]$, $x_{+} = x_{\text{eq}}^{-1}$, and

$$x_{\text{eq}} = \frac{2\alpha_{\text{B}}n_{\text{H}}}{\Gamma + 2\alpha_{\text{B}}n_{\text{H}} + \sqrt{\Gamma^2 + 4\alpha_{\text{B}}n_{\text{H}}\Gamma}} \quad (4.18)$$

is the equilibrium neutral fraction. When $\Gamma = 0$, Equation (4.16) has a solution

$$x_{\text{n}}(t) = \frac{x_0 + (1 - x_0)\alpha_{\text{B}}n_{\text{H}}t}{1 + (1 - x_0)\alpha_{\text{B}}n_{\text{H}}t}, \quad (4.19)$$

which should be applied to cells completely shielded from ionizing radiation. While Equation (4.17) is exact, it is not computationally robust when the denominator is close to zero, possibly resulting in inaccurate x_{n} due to amplified roundoff errors.

Alternatively, if we (incorrectly) treat n_{e} as being constant, Equation

⁶These expressions can be generalized to include the collisional ionizations as well as the contribution to n_{e} from heavy elements. See Appendix C3 in Altay & Theuns (2013).

(4.16) yields a solution

$$x_n(t) = x_{\text{eq},0} + (x_0 - x_{\text{eq},0})e^{-(t-t_0)/t_{\text{i-r}}}, \quad (4.20)$$

where $t_{\text{i-r}} = (\Gamma + \alpha_{\text{B}}n_e)^{-1}$ is the ionization-recombination time and $x_{\text{eq},0} = \alpha_{\text{B}}n_e/(\Gamma + \alpha_{\text{B}}n_e)$ is the equilibrium neutral fraction (e.g., Schmidt-Voigt & Koeppen 1987; Mellema et al. 2006b). Mellema et al. (2006b) adopted Equation (4.20) to implicitly update the time-averaged ionization fraction in their C²-ray method. In the Appendix, we present the test results of Equation (4.20) on the temporal changes of x_n in a single cell exposed to a fixed radiation field. It turns out that although Equation (4.20) is based on the incorrect assumption of constant n_e , in practice it gives almost identical results to those with Equation (4.16). In addition, Equation (4.20) is robust and guarantees that x_n always lies between x_0 and $x_{\text{eq},0}$. We also find (see Appendix) that it is more accurate than methods based on the backward-difference formula often used in the literature (e.g., Anninos et al. 1997). We thus use Equation (4.20) to calculate x_n in our implementation of the subcycle.

We determine the size of substeps as

$$\Delta t_{\text{ss}} = C \times \min\left(\frac{n_{\text{H}}}{|\mathcal{I} - \mathcal{R}|}\right), \quad (4.21)$$

with a constant coefficient C . Taking $C = 0.1$ restricts the change of x_n per substep to below 0.1 (see also Baczynski et al. 2015). The minimum value of Δt_{ss} is usually from the cells in transition layers where $0.1 \lesssim x_n \lesssim 1$ and $x_{\text{eq}} \approx 0$.

Our overall computation procedure is as follows. We first evolve the hyperbolic terms in Equations (5.3)–(4.3) for a full hydrodynamic time step Δt using the existing Godunov-type scheme in the *Athena* code. The total gas density n_{H} and the neutral gas density $n_{\text{H}0}$ are then available as inputs to the

ART module for radiation (and ionization/recombination) subcycles. Next, we perform the ART for each radiation subcycle to calculate \mathcal{E} and Γ and determine Δt_{ss} . We then update the neutral fraction by using Equation (4.20); given an updated x_{n} , the electron density is updated to $n_e = n_{\text{H}}(1 - x_{\text{n}})$. At each subcycle over Δt_{ss} , we explicitly calculate the radiation force

$$\mathbf{f}_{\text{rad}} = \frac{1}{c} \sum_{\nu_j} \chi_{\nu_j} \mathbf{F}_{\nu_j}, \quad (4.22)$$

using Equation (4.9) for each frequency bin and add $\mathbf{f}_{\text{rad}}\Delta t_{\text{ss}}$ to the gas momentum density if radiation pressure is switched on. The total opacity in the ionizing and non-ionizing bins is calculated as

$$\chi_{\text{i}} = n_{\text{H}^0} \langle \sigma_{\text{H}} \rangle + n_{\text{H}} \sigma_{\text{d}}, \quad (4.23)$$

and

$$\chi_{\text{n}} = n_{\text{H}} \sigma_{\text{d}}, \quad (4.24)$$

respectively, where we use the constant-attenuation cross section per hydrogen atom $\sigma_{\text{d}} = 1.17 \times 10^{-21} \text{ cm}^2 \text{ H}^{-1}$ (Draine 2011b).

4.3 Results of Code Tests

We now present the results of various tests intended to verify the performance and accuracy of our implementation of the ART, including its ability to simulate the dynamics of H II regions. Unless otherwise noted, we adopt $m_{\text{ray}} = 4$ and $\ell_0 = 4$ as fiducial values for the angular resolution and the initial HEALPix level, respectively (Baczynski et al. 2015; Rosen et al. 2017).

4.3.1 Scaling Tests

To measure the parallel performance of the ART and its cost relative to that of the hydrodynamic solver, we conduct weak and strong scaling tests similar to the ones presented in Rosen et al. (2017). The tests are run on 16-core

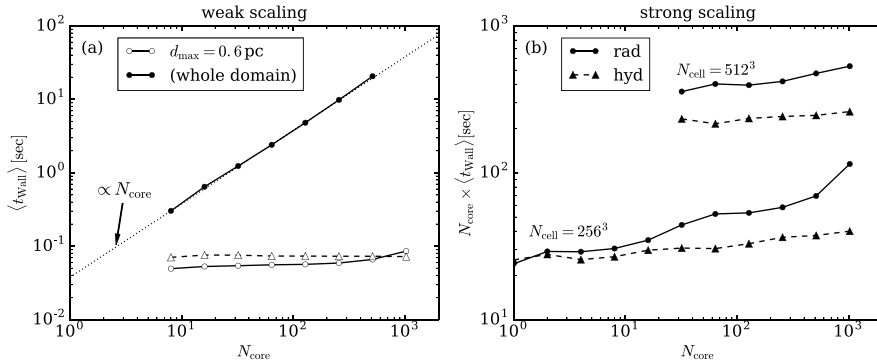


Figure 4.2 (a) Wall clock time *vs.* N_{core} in the weak scaling test for the ART (circles) and hydrodynamics solver (triangles) in which every 32^3 grid belonging to a given processor has a single point source at the center. The open circles correspond the case in which each ray is terminated 0.6 pc from its originating source, while filled circles denote the case in which all rays are extended until they hit the simulation domain boundary. (b) Wall clock time multiplied by N_{core} *vs.* N_{core} in the strong scaling test. A single point source is placed at the center of the box with 256 or 512 cells per side.

Intel Sandy Bridge nodes in the Tiger cluster at Princeton University.

In the weak scaling test, the whole computational domain is subdivided into N_{core} identical grids, each having 32^3 cells over a 1 pc^3 volume with a source at each grid center. Each grid is assigned to a processor, and we time the execution of the ART as well as the hydrodynamics solver, varying the number of processors N_{core} . Figure 4.2(a) shows the wall clock time $\langle t_{\text{Wall}} \rangle$, averaged over 10 cycles, taken for a single ART (circles) and hydrodynamics (triangles) update. We consider problem sizes between $N_{\text{core}} = 2^3$ and 2^{10} . The open circles correspond to the case in which rays are terminated at $d_{\text{max}} = 0.6 \text{ pc}$, such that communication is only with immediately adjacent neighbors. Overall, the wallclock time is nearly flat with varying N_{core} , indicating excellent parallel efficiency (a horizontal line would represent perfect weak scaling for this case). Quantitatively, the runtime to perform the ray tracing is 0.050 s when $N_{\text{core}} = 8$, slightly shorter than the hydrodynamics

update, and increases to 0.086 s when $N_{\text{core}} = 2^{10}$, with parallel efficiency of 58%. For the weak scaling test, we also consider the case where rays are followed until they exit the simulation domain, which is plotted as filled circles. This is in good agreement with the prediction of the perfect scaling for a processor workload that increases with the number of sources, and hence, rays per cell $\propto N_{\text{source}} \propto N_{\text{core}}$, with $\langle t_{\text{Wall}} \rangle \propto N_{\text{core}}$ shown as a dotted line, indicating that the processors are busy most of the time.

In the strong scaling test, the total problem size remains fixed, with the domain decomposed into varying number of grids. We consider a domain with 256^3 or 512^3 cells and add a single point source at the domain center. We do not restrict the distance that rays can travel from the source: rays extend to the domain boundaries. Figure 4.2(b) plots the wall clock time to complete one ray tracing (solid) and hydrodynamics update (dashed) multiplied by N_{core} . A horizontal line would represent perfect strong scaling for this case. For the domain with 256^3 cells, the run time increases by a factor of 4.74 as N_{core} varies from 1 to 1024, corresponding to a scaling efficiency of 21%. For the domain with 512^3 cells, we start from $N_{\text{core}} = 32$, since the problem becomes memory bound, and obtain a relative parallel efficiency of 67% on 1024 cores. It is remarkable that the cost of ray tracing in our implementation is comparable to that of hydrodynamic updates even though rays pass through multiple subdomains to reach the domain boundaries. This indicates that our communication approach is successfully distributing work throughout the domain, and in particular, that “downstream” processors do not suffer from being idle.

Compared to the strong scaling presented by Rosen et al. (2017) (their Figure 8), our result for the 256^3 box shows a performance improvement by a factor of more than 10. Differences in machine specifications and hierarchical grid structures may contribute to these differences in scaling results. For instance, the *Orion* AMR code used by Rosen et al. (2017) employs a patch-

based AMR method in which the domain is decomposed into a set of grids of uniform cell spacing, and multiple grids may be assigned to a single core. The same patch-based method is applied even without mesh refinement. Finding neighbors on the patch-based mesh is non-trivial and requires looping over local grids until the next grid is found. This is in contrast to the domain decomposition method adopted by *Athena*, in which a single core covers only a single grid. Therefore, the patch-based scheme requires the additional cost of finding neighbor grids when a ray needs to be passed between grids even when those grids reside on a single core. This most likely accounts for some of the differences in the scaling results. Further optimizations described in Section 4.2.2 may also contribute to the performance improvement.

4.3.2 Radiation in a Vacuum

We now assess the accuracy of our implementation of the ART method for recovering the inverse-square law of radiation energy density around a point source in vacuum. With a limited angular resolution, the ART method is unable to achieve perfect spherical symmetry under Cartesian geometry. We study the effects of the angular resolution parameter m_{ray} as well as the ray rotation on the accuracy of the calculated radiation energy density.

As a computational domain, we consider a cubic box with a side length of 2 pc and place a point source with luminosity $L = 1 L_{\odot}$ at the center. The box is discretized into 128^3 cells. Figure 4.3(a) shows the distributions of the volume-averaged radiation energy density \mathcal{E} for $(m_{\text{ray}}, \ell_0) = (4, 4)$ (blue), $(m_{\text{ray}}, \ell_0) = (10, 4)$ (red), and $(m_{\text{ray}}, \ell_0) = (10^3, 10)$ (yellow) against the normalized distance from the source. Each distribution is shifted by a constant factor along the ordinate for clear comparison. The deviations of \mathcal{E} relative to the cell-centered value $L/(4\pi r^2 c)$, plotted as the black dashed line, is mostly on the order of a few percent for $m_{\text{ray}} = 4$. We also run 10 different instances of the ray-trace with $m_{\text{ray}} = 4$, randomly varying the ray

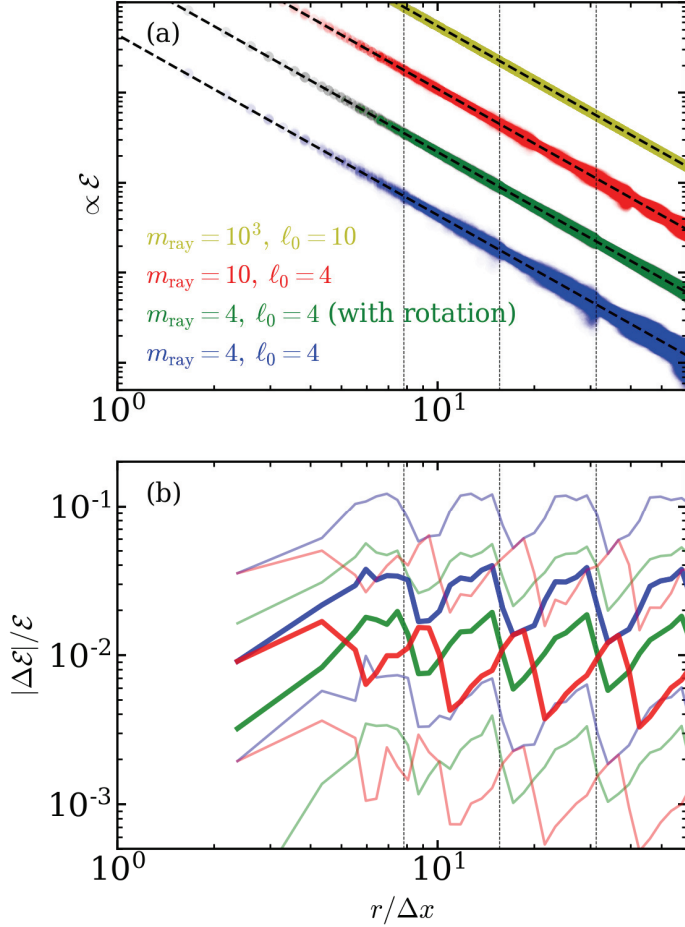


Figure 4.3 Test of the ART on the radiation field around a single point source in vacuum. (a) Radiation energy density *vs.* the distance from the source (normalized by the grid spacing Δx) with $(m_{\text{ray}}, \ell_0) = (4, 4)$ (blue and green), $(m_{\text{ray}}, \ell_0) = (10, 4)$ (red), and $(m_{\text{ray}}, \ell_0) = (10^3, 10)$ (yellow). The data for each case are shifted along the ordinate for clear comparison. The green dots show the averages of ten ARTs, each with different ray orientation. The black dashed lines denote the analytic solution $\mathcal{E} \propto r^{-2}$. (b) The 10th, 50th (median; heavy line), and 90th percentile values of the relative error in each radial bin. The vertical dashed lines indicate the distance at which rays split for $(m_{\text{ray}}, \ell_0) = (4, 4)$.

orientation. The mean values of the resulting \mathcal{E} are plotted as green symbols, demonstrating that the errors introduced by geometrical artifacts can be reduced by rotating the directions of ray injection (Krumholz et al. 2007b).

Figure 4.3(b) plots as solid lines the 10th, 50th (median), and 90th percentiles of the relative errors $|\Delta\mathcal{E}|/\mathcal{E}$ within spherical shells centered at the source, after taking the case with $(m_{\text{ray}}, \ell_0) = (10^3, 10)$ as the reference solution. The median value of the relative error is 1–4% for $(m_{\text{ray}}, \ell_0) = (4, 4)$. The case with ray rotation achieves a median accuracy similar to that with $m_{\text{ray}} = 10$. The sawtooth patterns in the relative errors reflect the radial variation of the angular resolution: the resolution becomes gradually worse with increasing r at a given HEALPix level and suddenly increases at the ray-splitting radii $r_{\text{max}}(\ell)$, plotted as the vertical dashed lines for $(m_{\text{ray}}, \ell_0) = (4, 4)$. Varying m_{ray} from 2 to 256, we find that the median value of the relative errors can be fitted as $2.0(m_{\text{ray}}/4)^{-1.32}\%$, which is steeper than $\propto m_{\text{ray}}^{-0.6}$ obtained by Wise & Abel (2011).

4.3.3 Expansion of H II Regions

Next we perform three tests of the expansion of an H II region embedded in a uniform medium. These are classical problems in astrophysics with well-known analytic solutions, and have thus been the standard tests for RHD codes incorporating the effects of ionization and recombination (e.g., Mellema et al. 2006b; Krumholz et al. 2007b; Wise & Abel 2011; Baczynski et al. 2015; Bisbas et al. 2015). In this section, we adopt $T_{\text{neu}} = 100$ K and $T_{\text{ion}} = 8000$ K.

R-type Ionization Front

We consider an R-type ionization front created by a central source in a uniform static medium with hydrogen number density n_{H} . At $t = 0$, the source starts to emit ionizing photons at a constant rate of Q_{i} . The expansion of the ionization front is very rapid at early time, without inducing significant

gas motions. If there is no dust extinction and the recombination coefficient is taken as constant, the ionization front expands as

$$r_{\text{IF}} = R_{\text{St},0}(1 - e^{-t/t_{\text{rec}}})^{1/3}, \quad (4.25)$$

where $t_{\text{rec}} = 1/(\alpha_{\text{B}}n_{\text{H}})$ is the recombination time and $R_{\text{St},0} = [3Q_{\text{i}}/(4\pi\alpha_{\text{B}}n_{\text{H}}^2)]^{1/3}$ is the dustless Strömngren radius (Spitzer 1978). For our test, we take $n_{\text{H}} = 10^2 \text{ cm}^{-3}$, $Q_{\text{i}} = 10^{49} \text{ s}^{-1}$, $\sigma_{\text{H}} = 6.3 \times 10^{-18} \text{ cm}^2$, and $\alpha_{\text{B}} = 3.02 \times 10^{-13} \text{ cm}^3 \text{ s}^{-1}$. The simulation domain is a cubic box with side of $2.4R_{\text{St},0} = 7.2 \text{ pc}$, which is resolved by a grid of $N_{\text{cell}} = 128^3$ cells. The optical depth over one neutral cell is $\Delta\tau = n_{\text{H}0}\sigma_{\text{H}}\Delta x = 109(128/N_{\text{cell}}^{1/3})(Q_{\text{i}}/10^{49} \text{ s}^{-1})^{1/3}(n_{\text{H}}/10^2 \text{ cm}^{-3})^{1/3}$, so that the background medium is highly optically thick initially. The test simulations are run until $t = 8t_{\text{rec}}$, with the hydrodynamic updates turned off.

We first examine the effect of differing time step in the subcycling. Figure 4.4 plots the temporal changes of r_{IF} , defined as the radius at which $x_{\text{n}} = 0.5$, and the relative errors compared to Equation (4.25). The results based on Equation (4.17) (Method A) with $C = 0.01, 0.1$, and 1 in Equation (4.21) are shown as squares. For $C = 0.1$, the simulation results agree with the analytic solution within $\lesssim 5\%$, similar to the results of Baczynski et al. (2015). The results using Equation (4.20) (Method B) with $C = 0.1$ and 1 are shown as circles, which are almost identical to those from Equation (4.17) with the same C . We also explore the effect of varying spatial resolution by taking the Method B with $C = 0.1$. Figure 4.5 plots the resulting r_{IF} for $N_{\text{cell}} = 64^3, 128^3$, and 256^3 , all of which agree within 2% . The relative errors are $\sim 4\text{--}5\%$ at early time and decrease to less than 1% at $t/t_{\text{rec}} = 8$.

The above results suggest that Method B with $C = 0.1$ reproduces the evolution of R-type ionization fronts quite well. They can be followed more accurately, albeit at a higher cost, if one restricts Δt_{ss} more strictly, for

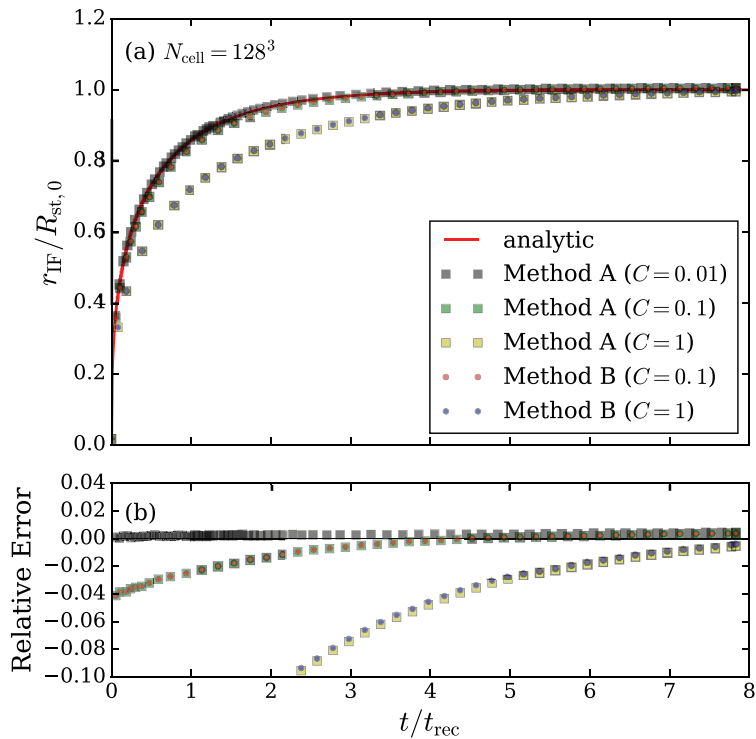


Figure 4.4 Test of the expansion of an R-type ionization front in a uniform medium. Method A (squares) and B (circles) refer to using Equations (4.17) and (4.20), respectively. (a) Ionization front radius *vs.* time with different time-stepping coefficient C in Equation (4.21). The analytic solution is shown as the red solid line. (b) Fractional errors relative to the analytic solution.

example, by limiting the relative changes in x_n to less than 10% per update (e.g., Krumholz et al. 2007b; Mackey 2012).

D-type Ionization Front

As an R-type ionization front approaches $R_{\text{St},0}$, its expansion speed falls below twice the sound speed c_{ion} in the ionized region. This develops an isothermal shock in front of the ionization front, which in turn undergoes a

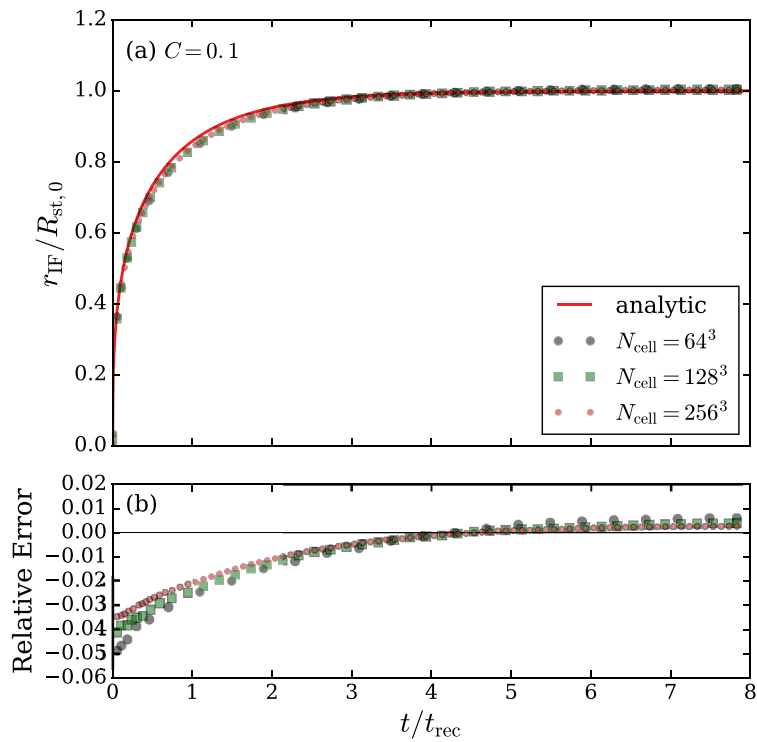


Figure 4.5 Test of the expansion of an R-type ionization front in a uniform medium. Same as Figure 4.4 using Method B with $C = 0.1$ but with a range of spatial resolution.

transition to a (weak) D-type front (Shu 1992). If the shell of the swept-up material between the ionization and shock fronts is geometrically thin, the radius of the shell r_{sh} ought to satisfy the following momentum equation

$$\frac{d}{dt} \left(M_{\text{sh}} \frac{dr_{\text{sh}}}{dt} \right) = 4\pi r_{\text{sh}}^2 c_{\text{ion}}^2 \rho_{\text{ion}}, \quad (4.26)$$

where $M_{\text{sh}} = (4\pi/3)\rho_0 r_{\text{sh}}^3$ is the shell mass for ρ_0 the density of the background medium, and $\rho_{\text{ion}} = \rho_0 (r_{\text{sh}}/R_{\text{St},0})^{-3/2}$ is the density in the ionized region (assuming instantaneous ionization equilibrium). Hosokawa & Inutsuka (2006) found that Equation (4.26) has a self-similar solution

$$r_{\text{sh}} = R_{\text{St},0} \left(1 + \frac{7}{2\sqrt{3}} \frac{c_{\text{ion}} t}{R_{\text{St},0}} \right)^{4/7}. \quad (4.27)$$

Spitzer (1978) also solved for a self-similar solution by employing the requirement of $\rho_0 (dr_{\text{sh}}/dt)^2 \approx c_{\text{ion}}^2 \rho_{\text{ion}}$ and derived a similar expression, with $2\sqrt{3}$ in the denominator of the coefficient in Equation (4.27) replaced by 4 (see also Bisbas et al. 2015).

For the test of D-type fronts, we set up a cubic domain with 128^3 cells whose side is $20R_{\text{St},0}$ long. The domain is filled with neutral gas with $T_{\text{neu}} = 100$ K, and a source placed at the center starts to emit Q_i ionizing photons per unit time from $t = 0$. Unlike in the R-type front tests, we turn on the hydrodynamics updates so that the gas responds self-consistently to the pressure of gas at T_{ion} produced by the ionizing radiation. The simulations are run up to $t = 10R_{\text{St},0}/c_{\text{ion}}$ using Method B with $C = 0.1$. At each time, we determine the shell radius r_{sh} as the position where the gas density is maximal. Figure 4.6 plots the resulting r_{sh} and the relative errors as functions of time for $(Q_i/\text{s}^{-1}, n_{\text{H}}/\text{cm}^{-3}) = (10^{49}, 10^2)$, $(10^{51}, 10^3)$, and $(10^{51}, 10^4)$. Shown also as black solid and dotted lines are the solutions of Hosokawa & Inutsuka (2006) and Spitzer (1978), respectively. Our results agree with the former better, with typical relative errors less than 3%, which is consistent with the

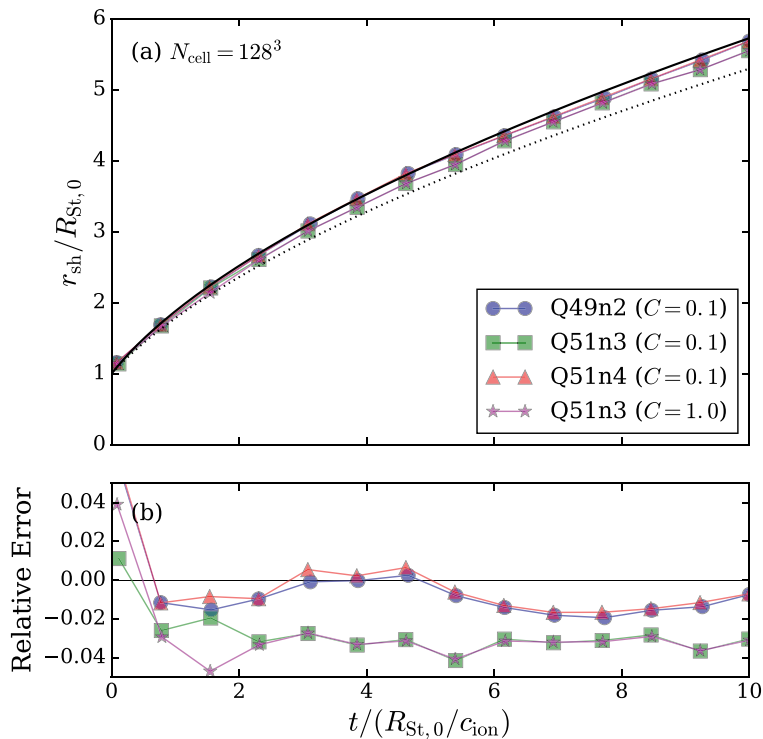


Figure 4.6 Test of the expansion of a D-type ionization front in a uniform medium. (a) Shell radius r_{sh} vs. time. The black solid and dotted lines represent the analytic solution of Hosokawa & Inutsuka (2006) and Spitzer (1978), respectively. (b) Errors relative to the analytic solution of Hosokawa & Inutsuka (2006).

results of Bisbas et al. (2015).⁷ Using a less stringent time step size with $C = 1.0$, the errors become slightly larger, but the computational cost of the radiation module is reduced by a factor of 2.5.

⁷We note that the benchmark tests in Bisbas et al. (2015) considered hydrogen-only gas and adopted $T_{\text{ion}} = 10^4$ K and $\alpha_{\text{B}} = 2.7 \times 10^{-13} \text{ cm}^3 \text{ s}^{-1}$, corresponding to a $\sim 30\%$ and $\sim 10\%$ difference in c_{ion} and α_{B} from ours, respectively. However, our result is unlikely to be affected by the specific choice of T_{ion} provided that $T_{\text{ion}} \gg T_{\text{neu}}$.

Dusty H II Region with Radiation Pressure

In the preceding tests, we have ignored the presence of dust grains and radiation pressure on them. They are efficient in absorbing (both ionizing and non-ionizing) UV photons and transfer momentum to the gas through collisional coupling. The momentum deposition from radiation pressure may dominate in driving the expansion of H II regions in dense, massive star-forming environments (Krumholz & Matzner 2009; Murray et al. 2010; Fall et al. 2010; Kim et al. 2016). Radiation pressure also causes a non-uniform density distribution inside an H II region in static equilibrium (Draine 2011b). Time-dependent, spherical models developed by Kim et al. (2016) confirmed that when $Q_i n_H$ is large, the expansion of dusty H II regions is dominated by radiation pressure, with internal structure non-uniform.

Let L_n denote the photon luminosity below energy $h\nu_L = 13.6\text{ eV}$ from a source, and τ_{edge} and ρ_{edge} be the dust optical depth and gas density at the edge of the ionized region, respectively. The equation of motion of the shell is then modified to

$$\frac{d}{dt} \left(M_{\text{sh}} \frac{dr_{\text{sh}}}{dt} \right) = \frac{L_n}{c} e^{-\tau_{\text{edge}}} + 4\pi r_{\text{sh}}^2 c_{\text{ion}}^2 \rho_{\text{edge}} \quad (4.28)$$

(Kim et al. 2016). Given τ_{edge} and ρ_{edge} as a function of r_{sh} from Draine (2011b), Equation (4.28) can readily be integrated to yield r_{sh} as a function of time, to which our test results are compared.

We consider an initially uniform medium with $n_H = 10^3\text{ cm}^{-3}$ and a central source with $Q_i = 10^{51}\text{ s}^{-1}$ and $L_n = 1.5Q_i h\nu_i$, where $h\nu_i = 18\text{ eV}$ is the mean energy of hydrogen ionizing photons. We take a constant dust absorption cross section $\sigma_d = 10^{-21}\text{ cm}^2\text{ H}^{-1}$ and ionized gas temperature $T_{\text{ion}} = 8000\text{ K}$, corresponding to the dust opacity parameter of $\gamma \equiv (2ck_B T_{\text{ion}} \sigma_d) / (\alpha_B h\nu_i) = 7.58$ (Eq. 7 of Draine 2011b)⁸. We take a compu-

⁸For the numerical value of γ , we took $\alpha_B \simeq 2.59 \times 10^{-13} (T/10^4\text{ K})^{-0.7}\text{ cm}^3\text{ s}^{-1}$

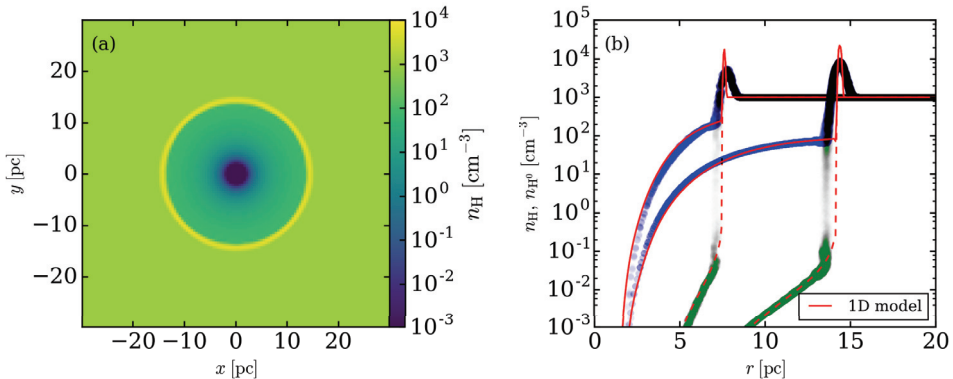


Figure 4.7 Test of the expansion of a dusty H II region with $Q_i = 10^{51} \text{ s}^{-1}$ and $n_{\text{H}} = 10^3 \text{ cm}^{-3}$. (a) Slice of n_{H} through the $z = 0$ plane at $t = 2.26 \text{ Myr}$. (b) Radial profiles of n_{H} (blue) and n_{H^0} (green) at $t = 0.67$ and $t = 2.26 \text{ Myr}$. The red lines represent the results of one-dimensional simulation in spherical coordinates.

tational domain with side $20R_{\text{St},0} = 60 \text{ pc}$, resolved by 128^3 cells. For comparison, we also run a one-dimensional simulation in spherical coordinates with the same set of the physical parameters, but resolving the radial domain $0.1 \text{ pc} < r < 30.1 \text{ pc}$ using 512 cells (see Kim et al. 2016 for details of simulation setup).

Figure 4.7 plots (a) the density distribution in the $z = 0$ plane at $t = 2.26 \text{ Myr}$ and (b) the radial profiles of n_{H} (blue) and n_{H^0} (green) at $t = 0.67$ and 2.26 Myr . The corresponding one-dimensional results are compared as the red lines. As expected, radiation pressure on dust creates a central cavity devoid of gas and dust, with the density decaying toward the center approximately as $n_{\text{H}} \propto \exp(-r_0/r)$, where $r_0 = \sigma_{\text{d}}(Q_i h\nu_i + L_{\text{n}})/(8\pi c k_{\text{B}} T_{\text{ion}})$ (Rodríguez-Ramírez et al. 2016). Although the shocked shell in the three-dimensional model has a larger thickness than the one-dimensional counterpart due to poor spatial resolution, the shell radius agrees quite well.

from Krumholz et al. (2007b), which is slightly different from $\alpha_{\text{B}} \simeq 2.56 \times 10^{-13} (T/10^4 \text{ K})^{-0.83} \text{ cm}^3 \text{ s}^{-1}$ adopted by Draine (2011b).

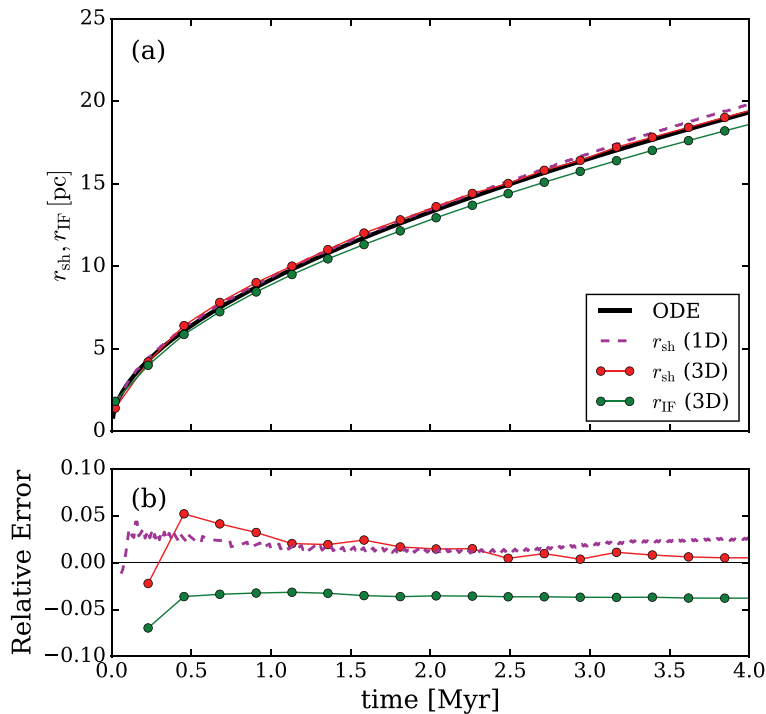


Figure 4.8 (a) Shell radius (red) and ionization front radius (green) *vs.* time for an expanding dusty H II region with $Q_i = 10^{51} \text{ s}^{-1}$ and $n_{\text{H}} = 10^3 \text{ cm}^{-3}$. The black solid line draws the solution of Equation (4.28), while the dashed line gives the shell radius obtained from the one-dimensional simulation. (b) Relative errors with respect to the solution of Equation (4.28).

Figure 4.8 compares $r_{\text{sh}}(t)$ in the simulations with that from the solution of Equation (4.28), again showing good agreement (within 5% for $t > 0.5 \text{ Myr}$) between the numerical and semi-analytic results. The difference between r_{IF} and r_{sh} in the three-dimensional model is primarily due to the limited spatial resolution; the true physical difference between r_{IF} and r_{sh} is smaller.

4.4 Application to Star Cluster Formation in Turbulent Clouds

So far our tests have been limited to idealized problems, in which the background is a uniform medium. By combining our implementation of ART with other physics modules already existing in the *Athena* code, we now demonstrate application of our ART module to an important practical astronomical problem, namely the formation of a star cluster in a molecular cloud. We follow the collapse of a turbulent, self-gravitating cloud and subsequent star formation until the associated UV radiation feedback from multiple sources halts further star formation and disperses the remaining gas. In this section, we first describe the numerical setup and report strong scaling for the fiducial model. We then compare the non-ionizing UV radiation field computed by the ART with that based on the M_1 closure scheme of Skinner & Ostriker (2013), as implemented for point sources in the single-scattering approximation.

4.4.1 Numerical Setup

We solve Equations (5.3)–(4.4) to study evolution of self-gravitating gas interacting with UV radiation from multiple point sources. We adopt *Athena*'s HLLC Riemann solver, the van Leer integrator (Stone & Gardiner 2009), piecewise-linear spatial reconstruction, and strict outflow boundary conditions.

We use the sink particle method of Gong & Ostriker (2013) to treat cluster formation and gas accretion processes. For this, we create a sink particle when a cell meets the following three conditions simultaneously: (1) its density exceeds the threshold corresponding to the Larson-Penston solution of an isothermal collapse; (2) it is a local minimum of the gravitational potential; and (3) it has a converging velocity field along all three principal axes. The mass accretion rate onto the sink particle is determined by the flux returned from the Riemann solver at the boundary faces of the 3^3 ghost cells surround-

ing the sink particle. The ghost cells in this sink particle control volume are reset after the hydrodynamics integration by extrapolation from the nearest active cells. To prevent spurious mass and momentum flows from the ghost cells to the active cells, we use the “diode”-like boundary condition.⁹ When two sink particles come close enough together to make their control volumes overlap, we simply merge them in such a way that conserves the total mass and momentum. We have also tested the sink particle method of Bleuler & Teyssier (2014) and found similar results.

The gravitational potential from gas and star particles are calculated using a FFT Poisson solver with open boundary conditions (Skinner & Ostriker 2015) after mapping star particles’ mass onto the mesh via the triangular-shaped-cloud scheme (Gong & Ostriker 2013). For the ART, we adopt $m_{\text{ray}} = 4$ and $C = 0.1$ in the subcycling and rotate ray orientation randomly every hydrodynamic cycle. Since the control volume encompassing a star particle is regarded as a ghost zone, we do not allow radiation to interact with the gas in the control volume.

Due to limited mass resolution, star particles in our simulation represent subclusters rather than individual stars. Star particles emit radiation in two frequency bins: hydrogen ionizing and non-ionizing photons with luminosity denoted by $L_i = Q_i h \nu_i$ and $L_n = L - L_i$, respectively. To assign the luminosity, we first calculate the total sink mass M_* in the whole domain at a given time. We then use the stellar population synthesis code SLUG based on the Chabrier initial mass function (Krumholz et al. 2015) to calculate the light-to-mass ratio $\Psi(M_*)$ and the ionizing photon rate per unit mass $\Xi(M_*)$ for a cluster with mass M_* at birth (Kim et al. 2016)¹⁰.

⁹This boundary condition is the same as the outflow boundary condition, except that the normal velocity component at the boundaries is set equal to zero if gas flows from the ghost to active cells.

¹⁰Equation (34) in Kim et al. (2016) for the conversion factor $\Xi(M_*)$ contains typographical errors. The correct equation should read $\Xi = 10^{46.7\mathcal{X}^7/(7.28+\mathcal{X}^7)} \text{s}^{-1} M_\odot^{-1}$, where $\mathcal{X} = \log_{10}(M_*/M_\odot)$.

Finally, a sink particle with mass m_* is assigned to emit $L = \Psi(M_*)m_*$ and $Q_i = \Xi(M_*)m_*$. Using these conversion factors, for example, a stellar cluster of mass $(10^2, 10^3, 10^4) M_\odot$ has the total bolometric luminosity and ionizing photon production rate $(1.1 \times 10^4, 7.3 \times 10^5, 8.9 \times 10^6) L_\odot$ and $(1.5 \times 10^{46}, 3.5 \times 10^{49}, 4.8 \times 10^{50}) \text{ s}^{-1}$, respectively. For simplicity, we do not allow for age variation of Ψ and Ξ and take constant values of $h\nu_i = 18 \text{ eV}$ for the mean energy of ionizing photons and $\sigma_{\text{H}} = 6.3 \times 10^{-18} \text{ cm}^2$ for the photoionization cross section.

Our problem initialization is largely similar to the approach of Skinner & Ostriker (2015) and Raskutti et al. (2016). We consider an isolated, uniform-density sphere of mass M_{cl} and radius R_{cl} placed at the center of the cubic box with side $L = 4R_{\text{cl}}$. The rest of the box is filled with a rarefied medium with density 10^3 times smaller than that of the cloud. The total gas mass inside the box is thus $1.014M_{\text{cl}}$. We impose a turbulent velocity field realized by a Gaussian random distribution with power spectrum $|\mathbf{v}^2| \propto k^{-4}$ over the wavenumber range $k \in [2, 64] \times 2\pi/L$ (Stone et al. 1998). The amplitude of the velocity field is adjusted such that the total kinetic energy E_{kin} is equal to the absolute value of the gravitational potential energy $E_{\text{G}} = -\frac{3}{5}GM_{\text{cl}}^2/R_{\text{cl}}$, making the initial cloud marginally gravitationally bound. The corresponding virial parameter is $\alpha_{\text{vir}} \equiv 2E_{\text{K}}/|E_{\text{G}}| = 2$ at $t = 0$. For the particular model presented here, we set $M_{\text{cl}} = 5 \times 10^4 M_\odot$ and radius $R_{\text{cl}} = 15 \text{ pc}$, and we resolve the simulation box using 256^3 cells. The initial cloud conditions are therefore the same as listed in Table 1 for the fiducial model of Raskutti et al. (2016), although here with $T_{\text{neu}} = 20 \text{ K}$, the sound speed in the neutral gas is $c_s = 0.27 \text{ km s}^{-1}$ and the opacity for non-ionizing radiation is $\kappa = 500 \text{ cm}^2 \text{ g}^{-1}$ (rather than $c_s = 0.2 \text{ km s}^{-1}$ and $\kappa = 1000 \text{ cm}^2 \text{ g}^{-1}$ in Raskutti et al. 2016), and also, here Ψ varies with total stellar mass rather than being set to a fixed value $\Psi = 2000 \text{ erg s}^{-1} \text{ g}^{-1}$.

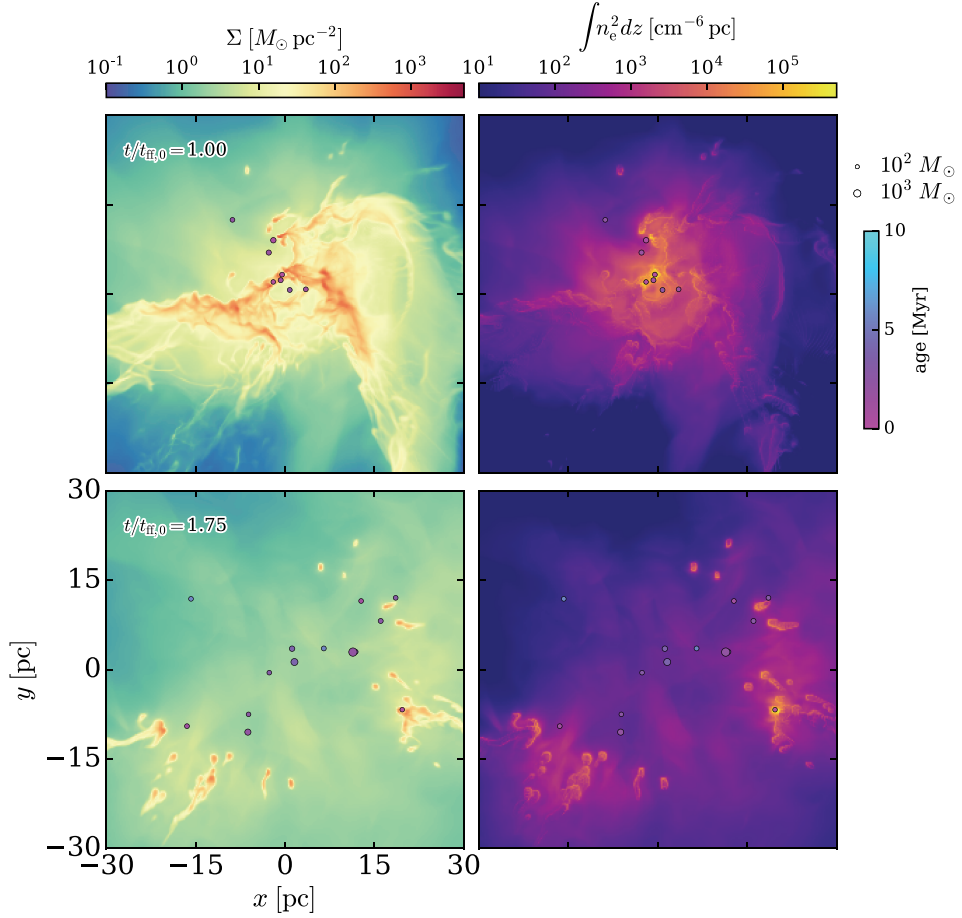


Figure 4.9 Snapshots of gas surface density (left) and emission measure of ionized gas (right) integrated along the z -axis at $t/t_{\text{ff},0} = 1.0$ (top) and 1.75 (bottom) for the model with $M_{\text{cl}} = 5 \times 10^4 M_{\odot}$ and $R_{\text{cl}} = 15$ pc. The circles mark the projected positions of star particles, with color and size representing their age and mass, respectively.

4.4.2 Overall Evolution & Scaling Test

The initial supersonic turbulence creates filamentary structure via shock compression. Subsequently, the filaments become gravitationally unstable and fragment into clumps that undergo runaway collapse to form stars. The first star particle is spawned at $t/t_{\text{ff},0} = 0.44$, where $t_{\text{ff},0} = 4.3$ Myr is the initial free-fall time of the cloud. Star formation continues until $\sim 1.7t_{\text{ff},0}$, creating a total of 24 sink particles. Figure 4.9 plots the snapshots of gas surface density (left) and emission measure of the ionized gas (right) on the x - y plane at $t/t_{\text{ff},0} = 1.0$ and 1.75, when 32% and 99% of the final stellar mass has assembled, respectively. The star particle positions are marked as circles with their size proportional to the mass. At $t/t_{\text{ff},0} = 2$, the net star formation efficiency is only 12%, with the most of the gas ($\gtrsim 70\%$) pushed out of the simulation box due to photoionization as well as radiation pressure. We defer to a forthcoming work a detailed presentation of simulation results on the star formation efficiency, cloud lifetime, the role of photoevaporation *vs.* radiation pressure in cloud disruption, etc., and their dependence on the cloud parameters.

We perform a strong scaling test for this realistic star-formation model, varying the number of cores from $N_{\text{core}} = 64$ to 1024. While the time for the hydrodynamic and self-gravity updates remains roughly constant throughout the simulation, the cost of the radiation update scales with the number of sources as well as the number of ART substeps taken per hydrodynamic update (typically ~ 10 – 20). Figure 4.10 plots the average zone-cycles per second (i.e., the total number of cells divided by the CPU time) for different physics modules during the time interval of $1.16 \leq t/t_{\text{ff},0} \leq 1.19$ when $\sim 97\%$ of the computational domain is filled with ionized gas and the number of point sources is 13. The zone-cycles per second for hydrodynamics and gravity are weakly-decreasing functions of N_{core} because of the increasing computation-

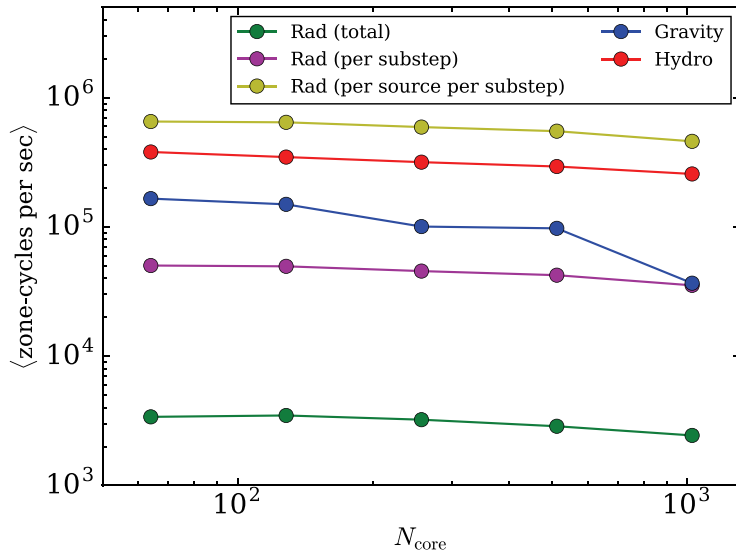


Figure 4.10 Strong scaling test of a star cluster simulation with $N_{\text{cell}} = 256^3$. The average zone-cycles per second during $1.16 \leq t/t_{\text{ff},0} \leq 1.19$ against the number of cores for different physics modules. During this time interval, there are 13 radiation sources and the typical number of substeps taken per hydrodynamic update is 14. The parallel efficiency of the radiation module from 64 to 1024 cores is 72%.

to-communication ratio. Although the radiation update is the most expensive part owing to multiple sources and subcycling, the cost of the ART normalized by the number of sources and the number of substeps remains roughly constant and is in fact cheaper than the hydrodynamics update. The relative parallel efficiency from 64 to 1024 processors is 72%, 22%, and 67% for the radiation, gravity, and hydrodynamic updates, respectively.¹¹

4.4.3 Comparison of Radiation Field Computed from M_1 -Closure and ART

Raskutti et al. (2016) performed RHD simulations of star formation in tur-

¹¹Inefficient scaling of the FFT gravity module for the largest N_{core} is likely caused by communication overhead associated with global transpose of data among processors.

bulent molecular clouds regulated by non-ionizing radiation pressure on dust alone. They used the *Hyperion* code (Skinner & Ostriker 2013) employing the M_1 -closure relation to evolve the two-moment RT equations. The *Hyperion* radiation solver uses explicit integration in time with a reduced speed of light, employing an HLL-type Riemann solver to compute radiation fluxes between cells, the piecewise linear spatial reconstruction, and the first-order backward Euler method for radiation energy and flux absorption source term updates. For their fiducial model with $M_{\text{cl}} = 5 \times 10^4 M_{\odot}$, $R_{\text{cl}} = 15 \text{ pc}$, and $\alpha_{\text{vir}} = 2.0$, Raskutti et al. (2016) obtained a final star formation efficiency of 42%, larger than the 12% found in our ART simulation that considers both ionizing and non-ionizing radiation, as described above.

To study whether the difference in the star formation efficiency owes to the effect of ionizing radiation and/or to the method of solving the RT equations, we have run an additional ART simulation with the same set of cloud parameters, but by turning off ionizing radiation. To match the parameters of Raskutti et al. (2016), for this comparison run we adopt a constant mass-to-light ratio $\Psi = 2000 \text{ erg s}^{-1} \text{ g}^{-1}$, dust absorption cross section $\sigma_{\text{d}} = 2.34 \text{ cm}^2 \text{ g}^{-1}$, and an isothermal equation of state with isothermal sound speed $c_{\text{s}} = 0.2 \text{ km s}^{-1}$. While overall evolution of this model is very similar to that of Raskutti et al. (2016), the resulting final star formation efficiency is $\varepsilon_{*} = 0.25$. This discrepancy in ε_{*} between the two results can be largely attributed to the difference in the radiation solvers.

Although the M_1 -closure scheme has been benchmarked for a variety of idealized test problems (e.g., González et al. 2007; Skinner & Ostriker 2013; Rosdahl et al. 2013; Rosdahl & Teyssier 2015), it is valuable to check how reliable its radiation field is compared to that based on the ART method for a problem with complex distributions of sources and matter. For this purpose, we take the data at two different epochs from the ART simulation with only non-ionizing radiation and use them as inputs to the *Hyperion* radiation

solver. With *Hyperion* we read in the gas density as well as the positions \mathbf{r}_* and masses m_* of all sink particles, and assign the source function j_* of a Gaussian form to each sink as

$$j_*(\mathbf{r}) = \frac{m_* \Psi}{(2\pi\sigma_*^2)^{3/2}} \exp\left(-\frac{|\mathbf{r} - \mathbf{r}_*|^2}{2\sigma_*^2}\right), \quad (4.29)$$

where the width is taken to be $\sigma_* = (2 \log 2)^{-1/2}$ pc: the corresponding full width at half maximum is 1 pc (Raskutti et al. 2016). We then perform radiation updates, while fixing hydrodynamic variables and the star particles. We integrate radiation variables over 10^3 yr, sufficiently long for the radiation field to reach a steady state.

To explore the differences between the two radiation solutions, we choose two epochs, $t_{10\%} = 0.7t_{\text{ff},0}$ and $t_{90\%} = 1.75t_{\text{ff},0}$, when 10% and 90% percent of the final stellar mass has assembled, respectively. The former corresponds to an early stage of cluster formation when 5 sink particles have been created, which are mostly embedded in dense nodes of filaments. At $t = t_{90\%}$, 39 sources are distributed more evenly around the center of the domain with half-mass radius 8.2 pc; radiation has cleared out most of the gas in the immediate surroundings. At the latter time, the system is globally super-Eddington, with the remaining gas actively expelled from the domain by the radiation force. The center of mass, \mathbf{r}_{CM} , of the sink particles is $(-1.9, 5.9, -5.6)$ pc and $(1.1, 0.3, 0.6)$ pc at $t_{10\%}$ and $t_{90\%}$, respectively.

Figure 4.11 shows the gas structure for the (a) $t_{10\%}$ and (b) $t_{90\%}$ epochs, in slices centered at the star particle located at $\mathbf{r}_{\text{sink}} = (-0.8, -0.4, -20.3)$ pc and the center of mass of the all star particles $\mathbf{r}_{\text{CM}} = (1.1, 0.3, 0.6)$ pc, respectively. The white circles mark the positions of star particles within 3 pc from the slice plane. The arrows indicate the directions of the radiation fluxes computed by the ART scheme (white) and M_1 scheme (red). At $t_{10\%}$, there are some discrepancies in the direction of the radiation fluxes. In the imme-

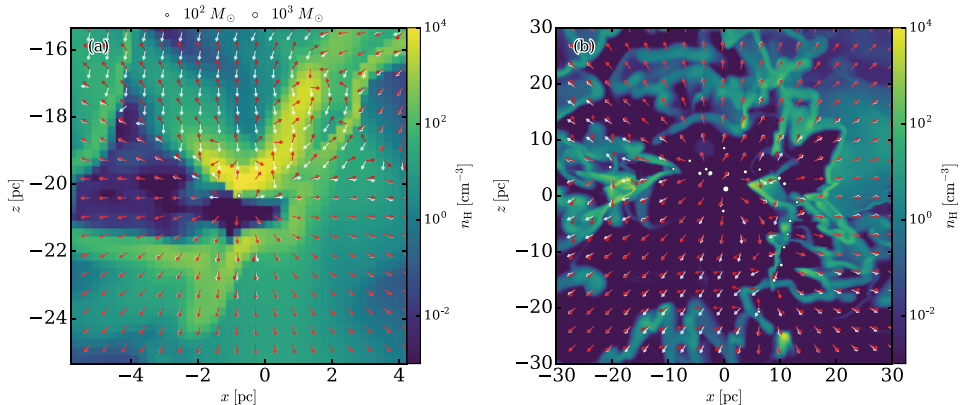


Figure 4.11 Snapshots of the control model with radiation pressure alone in the plane (a) with $y = -0.4$ pc at $t_{10\%} = 0.7t_{\text{ff},0}$ and (b) with $y = 0.3$ pc at $t_{90\%} = 1.75t_{\text{ff},0}$. All star particles lying within ± 3 pc of the slice plane are shown as white circles. The arrows in white and red represent the direction of the radiation flux \mathbf{F} calculated from the ART and M_1 method, respectively.

mediate vicinity of the star particle, the radiation fluxes computed by the ART scheme are directed radially outward from the sink particle, while those from the M_1 scheme have non-radial component. In the upper middle region, the radiation flux computed by the ART scheme is directed downward (resulting from a star particle at $z \sim -15$ pc outside the panel), while the M_1 radiation flux is directed upward. We note that this region is heavily shielded by an intervening dense clump located at $(x, y) \sim (-1, -20)$ pc and the radiation field is very weak compared to that in the immediate vicinity of the sink or in other regions at the same distance from the sink. Therefore, while the M_1 flux is inaccurate in this region, it is much smaller (typically by a factor of 10–30) than the mean value at similar distances. At $t_{90\%}$, the radiation fields from the two methods are in good overall agreement with each other, although the flux directions are somewhat different in the lower-middle region where the gas density is quite low and multiple beams going in different directions cross.

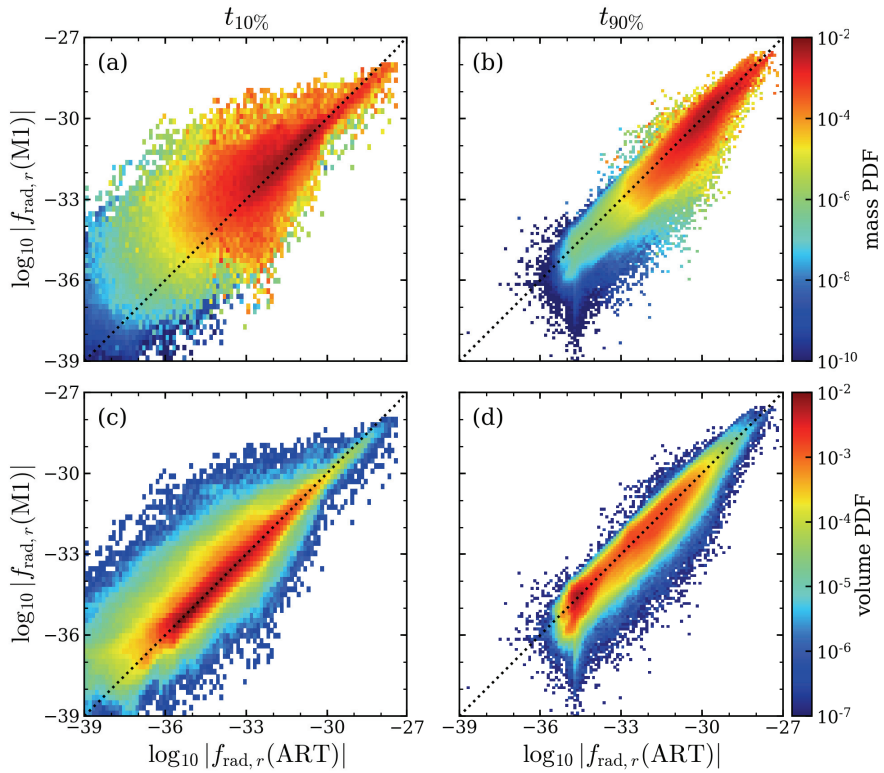


Figure 4.12 Comparison of radial component (relative to the CM) of the radiation force (in units of dyne cm^{-3}) computed by the ART and M_1 schemes at times $t_{10\%}$ (left) and $t_{90\%}$ (right). The upper and lower panels show mass- and volume-weighted probability density distributions, respectively. For comparison, the dashed lines show the relation that would be obtained if the radiation force were identical for the two methods.

One quantitative measure of the global dynamical impact of radiation fields is the radial component, $f_{\text{rad},r}$, of the radiation force (per unit volume) relative to \mathbf{r}_{CM} . At each point \mathbf{r} in the domain, this is given by

$$f_{\text{rad},r} = \frac{\chi \mathbf{F}}{c} \cdot \frac{\mathbf{r} - \mathbf{r}_0}{|\mathbf{r} - \mathbf{r}_0|}, \quad (4.30)$$

where $\mathbf{r}_0 = \mathbf{r}_{\text{CM}}$. Figure 4.12 compares the probability distribution functions (pdfs) of $|f_{\text{rad},r}|$ computed from ART and from the M_1 method at $t = t_{10\%}$ (left) and $t_{90\%}$ (right); pdfs are shown weighted by the cell mass (top) and volume (bottom). Overall, the M_1 method reproduces the ART radiation field reasonably well, with $|f_{\text{rad},r}(M_1)|/|f_{\text{rad},r}(\text{ART})| \approx 1.0$ at $t_{10\%}$ and 0.89 at $t_{90\%}$, when averaged over the entire range of $|f_{\text{rad},r}|$. At $t = t_{10\%}$ there is a significant scatter relative to the one-to-one relationship (dashed lines), which is likely to be caused by the inability of the M_1 scheme to describe the superposition of streaming radiation from multiple sources going in different directions. The scatter is small at $t = t_{90\%}$ because the radiation sources are more centrally concentrated relative to the gas.

A careful examination of Figure 4.12(a) shows that $|f_{\text{rad},r}(M_1)|/|f_{\text{rad},r}(\text{ART})| \approx 0.55$ for the largest values of $|f_{\text{rad},r}(\text{ART})| \gtrsim 10^{-29}$ dyne cm^{-3} at $t = t_{10\%}$. The corresponding physical locations are in immediate regions surrounding sink particles where both density and radiation flux are high. This discrepancy is suggestive of a possible reason why the total star formation efficiency in the the *Hyperion* simulation is larger: with a lower radiation force in the immediate vicinity of sink particles, accretion of material onto sinks may not be limited as strongly as it is in the ART simulation.

To investigate this issue in more detail, we examine the radial component of the radiation force centered on individual star particles. This is computed as in Equation (4.30), except now \mathbf{r}_0 is the location \mathbf{r}_{sink} of an individual star particle. For example, Figure 4.13(a) compares the angle-averaged radiation

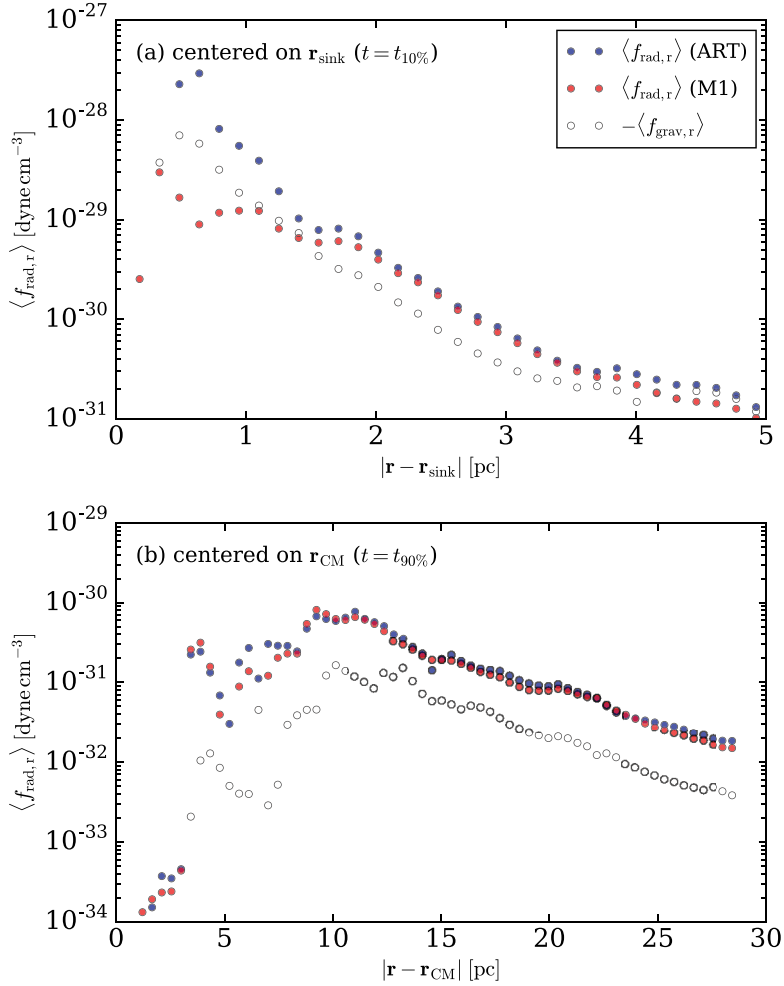


Figure 4.13 Angle-averaged radial radiation force computed by ART (blue) and M_1 (red) centered (a) at a sink particle at $t = t_{10\%}$, and (b) at the center of mass of all sinks at $t = t_{90\%}$. The absolute values of the angle-averaged gravitational forces are shown as open circles.

force $\langle f_{\text{rad},r} \rangle = \int f_{\text{rad},r} d\Omega / \int d\Omega$ relative to a sink particle located at $\mathbf{r}_{\text{sink}} = (-0.8, -0.4, -20.3)$ pc, isolated from other sink particles. Although the M_1 radiation force is in good agreement with the ART radiation force for $|\mathbf{r} - \mathbf{r}_{\text{sink}}| > 1.5$ pc, the former significantly underestimates the radiation force

within $\lesssim 1.5$ pc of the source. Since the source function in the M_1 -scheme (Equation [4.29]) is smoothed over the finite width of ~ 1 pc, it takes ~ 4 – 5 cells to build up the flux expected for a point source radiation. In contrast, the ART scheme with the adopted parameters has been proven successful in reproducing a point source radiation field with errors of only a few percent (see Section 4.3.2). Interestingly, the magnitude of the gravitational force (open circles) at $|\mathbf{r} - \mathbf{r}_{\text{sink}}| \lesssim 1$ pc is larger than the radiation force from the M_1 scheme, but smaller than that from the ART scheme. This suggests that the direct radiation pressure feedback in the former is less effective in halting accretion than in the latter. The difficulty in resolving flux $\propto r^{-2}$ near point sources in the M_1 scheme may explain the difference in the star formation efficiency between the two simulations.

Although the radiation fields from the two methods are quite different within a few zones of the point sources, they agree at both larger distances from individual sources and on global scales, particularly at late times. Figure 4.13(b) plots the angle-averaged radial force as computed with ART and with M_1 as functions of the distance from the center of mass of all sinks at $t = t_{90\%}$. Despite a complex source geometry, the results from the two methods agree very well. The fraction of radiation escaping the surface of a sphere of radius $r_{\text{max}} = 2R_{\text{cl}} - |\mathbf{r}_{\text{CM}}| = 29$ pc centered at \mathbf{r}_{CM} is equal at $f_{\text{esc}} = 0.63$ between the two methods.

We also calculate the normalized volume-integrated radial force

$$\mathcal{F}_{\text{out}} = \frac{4\pi c}{(1 - f_{\text{esc}})L_{*,\text{tot}}} \int_0^{r_{\text{max}}} \langle f_{\text{rad},r} \rangle r^2 dr, \quad (4.31)$$

which would be equal to unity had all sources with total luminosity $L_{*,\text{tot}}$ been located at \mathbf{r}_{CM} . For multiple sources distributed in space, \mathcal{F}_{out} is reduced due both to flux cancellation and to misalignment of the radiation force vectors from the radial direction toward \mathbf{r}_{CM} . The values of f_{esc} and \mathcal{F}_{out}

Table 4.1. Global properties of the radiation fields from the ART and M_1 schemes

f_* (%) (1)	$t/t_{\text{ff},0}$ (2)	$f_{\text{esc,ART}}$ (3)	$f_{\text{esc},M1}$ (4)	$\mathcal{F}_{\text{out,ART}}$ (5)	$\mathcal{F}_{\text{out},M1}$ (6)
10	0.7	0.29	0.28	0.079	0.073
50	1.0	0.29	0.30	0.20	0.15
90	1.75	0.63	0.63	0.64	0.59

Note. — Column (1) is the fraction of the total stellar mass formed. Column (2) is the time in units of the initial free-fall time. Columns (3) and (4) are the escape fraction of the photons through an enclosing sphere computed by the ART and M_1 methods, respectively. Columns (5) and (6) are the normalized, volume-integrated radial force from the ART and M_1 methods, respectively. The measurements of f_{esc} and \mathcal{F}_{out} are made for spheres with radii 22 pc, 25 pc, and 29 pc centered at \mathbf{r}_{CM} at $t_{10\%}$, $t_{50\%}$, and $t_{90\%}$, respectively.

from the ART and M_1 schemes are quite comparable to each other. Table 4.1 summarizes these global properties of the radiation fields for the two radiation solvers at $t = t_{10\%}$, $t_{50\%}$, and $t_{90\%}$.

4.5 Summary

Radiation feedback from young massive stars has profound influence on the evolution of their natal clouds and subsequent star formation. Stellar radiation that escapes from dense molecular clouds is also essential in controlling the thermal and ionization states of the diffuse ISM in galaxies and contributes to ionization of the IGM at even further distances. Because of the long-range, multiscale nature of the interactions between matter and radiation in three dimensions and of the highly inhomogeneous spatial structure of the gas and radiation source distribution, it is non-trivial to handle RT properly in hydrodynamic simulations. The ART algorithm developed by

Abel & Wandelt (2002) provides an accurate means of treating RT from point sources, which retains spatial resolution at moderate cost by splitting rays as the distance from a given source increases. Rosen et al. (2017) recently improved the parallel performance of the ART method by implementing completely non-blocking, asynchronous MPI communication.

In this chapter, we describe our implementation of ART in the Eulerian grid-based code *Athena* and present results of performance tests. We adopt the non-blocking, asynchronous parallelization algorithm suggested by Rosen et al. (2017) for exchanges of information along rays between processors. We further improve the parallel performance by (1) passing photon packets to neighbor processors whenever a certain number of local ray-traces have been completed and (2) making use of one-sided communications to update the “destroy count” of terminated rays. The radiation source terms, hydrogen photoionization, radiation pressure, etc. are all substepped (relative to the hydrodynamic timestep) and updated in an operator-split manner after each ART sweep, with the substepping time interval set by the ionization/recombination time via Equation (4.21). To update the hydrogen ionization state we use an approximate solution (Equation [4.20]) of the rate equation, which we find is more numerically robust and gives results that are essentially the same as the full analytic solution (Equation [4.17]).

We have verified the performance and accuracy of our implementation of the ART scheme on a wide variety of test problems. The results of weak and strong scaling tests (Figure 4.2) show that the cost of the ART (per source) remains comparable to that of the hydrodynamic update on up to 10^3 processors. The vacuum radiation test shows that if the number of rays passing through a cell is $m_{\text{ray}} = 4$, the median value of the errors in the calculated radiation energy density is only $\sim 1\text{--}4\%$, and the accuracy can be further improved by rotating the ray directions randomly (Krumholz et al. 2007b) at each step (Figure 4.3). Through standard test problems for the ex-

pansion of H II regions, we demonstrate that our radiation solver reproduces quite well the expected solutions of expanding R-type and D-type ionization fronts as well as the expansion of a dusty H II region with radiation pressure (Figures 4.4–4.8).

As a practical application demonstrating the use of our code, we conduct a simulation of star cluster formation in a turbulent, self-gravitating molecular cloud with $M_{\text{cl}} = 5 \times 10^4 M_{\odot}$, $R_{\text{cl}} = 15 \text{ pc}$, and initial virial parameter of $\alpha_{\text{vir}} = 2$. We find that the net star formation efficiency is $\varepsilon_{*} = 0.12$, with most of the gas expelled from the simulation box when both photoionization and radiation pressure from UV radiation are present. The strong scaling test for this problem (Figure 4.10) shows that the parallel efficiency of the ART module is as good as that of the hydrodynamics module. The total cost is however dominated by the radiation update, which involves multiple sources as well as subcycling.

We have also run an analogous model with radiation pressure alone (i.e., without photoionizing radiation), in order to directly compare with results obtained from the *Hyperion* code, which solves the two-moment radiation equations with an M_1 closure relation. Considering an identical radiation source and density distribution, the radiation field computed using the M_1 scheme agrees with that from ART on large scales, even for distributed sources. Since, however, point sources are smoothed over a finite volume in *Hyperion*, it is not able to reproduce the radiation field accurately near individual sources. As a consequence of the reduced radiation flux near point sources, radiation feedback is less able to limit accretion of nearby material, which likely accounts for the increased net star formation efficiency found with *Hyperion* ($\varepsilon_{*} = 0.42$) compared to that with our ART implementation ($\varepsilon_{*} = 0.25$). We conclude that one should be cautious when modeling point sources using the M_1 scheme if radiation feedback is important to limiting accretion; one approach might be to expand the control volume of each sink

particle such that the radiation flux is well resolved at its boundary.

The test results presented in this chapter confirm that our implementation of ART in the *Athena* code is accurate and efficient. In a subsequent work, we shall present results from application of the code to cluster formation and radiation feedback in turbulent molecular clouds. With an accurate and efficient method for treating the effects of radiation, we are able to survey a range of parameters, studying the dependence on the cloud mass and surface density of the star formation efficiency and cloud lifetime, as well as the relative roles of photoevaporation and radiation pressure in shaping and disrupting GMCs.

Appendix

4.A One-Cell Test of Photoionization Update

Here we present test results for the hydrogen photoionization update. We consider a single cell with width $\Delta x = 2 \text{ pc}$ initially filled with completely neutral hydrogen of density n_{H} . The cell is exposed to a fixed ionizing radiation field $Q_{\text{i}} = 10^{49} \text{ s}^{-1}$ from $t = 0$. The temporal evolution of the neutral hydrogen fraction in the cell is described by Equation (4.16), with the photoionization rate given as

$$\Gamma = \frac{1}{n_{\text{H}}x_{\text{n}}} \frac{Q_{\text{i}}}{(\Delta x)^3} (1 - e^{-n_{\text{H}}x_{\text{n}}\sigma_{\text{H}}\Delta x}) . \quad (4.32)$$

The cell has initial optical depth $\tau_0 = n_{\text{H}}\sigma_{\text{H}}\Delta x = 3880 \gg 1$, and initial ionization rate $\Gamma_0 = Q_{\text{i}}/(n_{\text{H}}\Delta x^3) = 1.7 \times 10^{-6} \text{ s}^{-1} \approx 14\alpha_{\text{B}}n_{\text{H}}$. The cell is expected to be ionized on the time scale Γ_0^{-1} , eventually settling into a balanced state with equilibrium neutral fraction of $x_{\text{eq}} \approx \alpha_{\text{B}}n_{\text{H}}/(\Gamma_0\tau_0) = 1.8 \times 10^{-5}$.

To evolve x_{n} according to Equation (4.16), we try three different schemes. First, we directly use the exact expression of Equation (4.17) with varying values of C in Equation (4.21), which we call Method A. The second method (Method B) uses Equation (4.20), again with varying C . We also use a semi-

implicit difference method (Method C) to discretize Equation (4.16) as

$$\frac{x_n^{n+1} - x_n^n}{\Delta t_{ss}} = \alpha_B n_H (1 - x_n^n)(1 - x_n^{n+1}) - x_n^{n+1} \Gamma, \quad (4.33)$$

which gives a recurrence relation

$$x_n^{n+1} = \frac{x_n^n + (1 - x_n^n)^2 \alpha_B n_H \Delta t_{ss}}{1 + \Gamma \Delta t_{ss}}, \quad (4.34)$$

where the superscripts “ n ” and “ $n + 1$ ” denote the values at $t = t_0$ and $t = t_0 + \Delta t_{ss}$, respectively.

Figure 4.14 plots the resulting temporal changes of x_n from the various methods with different C . The results of Methods A and B with $C = 0.001$, which are almost identical to each other, can be regarded as the true solution. The neutral fraction settles to an equilibrium value at $t\Gamma_0 \gtrsim 1$. The bottom panel plots the errors relative to the $C = 0.001$ results. It is remarkable that the difference between the results of Methods A and B is very small even for C as large as unity and that they are better than those from Method C. The error is largest when $x_n \sim 0.1$ – 0.2 , for which $|dx_n/dt|$ is quite large.

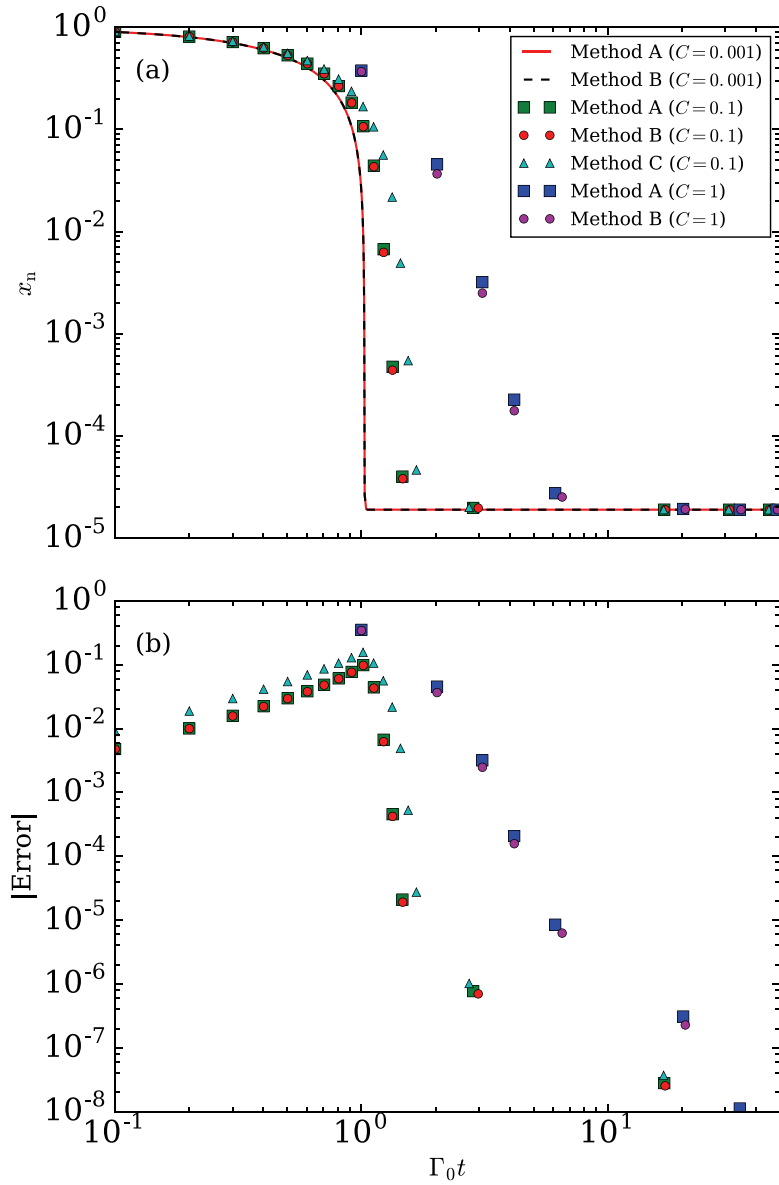


Figure 4.14 (a) Neutral fraction x_n vs. time obtained using the different update schemes for x_n with various C . Methods A and B use Equations (4.16) and (4.17), respectively, while Method C employs Equation (4.34). (b) Difference of x_n relative to the results with $C = 0.001$, shown as the red solid line in (a).

Chapter 5

Dispersal of Star-Forming Giant Molecular Clouds by Photoionization and Radiation Pressure¹

Abstract

UV radiation feedback from young massive stars plays a key role in the evolution of giant molecular clouds (GMCs) by photoevaporating and ejecting the surrounding gas. We conduct a suite of radiation hydrodynamic simulations of star cluster formation in marginally-bound, turbulent GMCs, focusing on the effects of photoionization and radiation pressure on regulating the net star formation efficiency (SFE) and cloud lifetime. We find that the net SFE depends primarily on the initial gas surface density, Σ_0 , such that the SFE increases from 4% to 51% as Σ_0 increases from $13 M_\odot \text{pc}^{-2}$ to $1300 M_\odot \text{pc}^{-2}$.

¹A version of this chapter has been published as “Modeling UV Radiation from Massive Stars. II. Dispersal of Star-Forming Giant Molecular Clouds by Photoionization and Radiation Pressure,” Kim, J.-G., Kim, W.-T., & Ostriker, E. C. 2018, *The Astrophysical Journal*, 859, 68.

Cloud destruction occurs within 2–10 Myr after the onset of radiation feedback, or within 0.6–4.1 freefall times (increasing with Σ_0). Photoevaporation dominates the mass loss in massive, low surface-density clouds, but because most photons are absorbed in an ionization-bounded Strömngren volume the photoevaporated gas fraction is proportional to the square root of the SFE. The measured momentum injection due to thermal and radiation pressure forces is proportional to $\Sigma_0^{-0.74}$, and the ejection of neutrals substantially contributes to the disruption of low-mass and/or high-surface density clouds. We present semi-analytic models for cloud dispersal mediated by photoevaporation and by dynamical mass ejection, and show that the predicted net SFE and mass loss efficiencies are consistent with the results of our numerical simulations.

5.1 Introduction

Ultraviolet (UV) radiation produced by newborn star clusters profoundly affects the evolution of giant molecular clouds (GMCs), where most star formation in the local Universe takes place. The UV photons dissociate and ionize cold molecular gas that could otherwise fuel further star formation (e.g., Whitworth 1979). Photoionization increases the thermal pressure within GMCs by three orders of magnitude, and expansion of high-pressure ionized bubbles (H II regions) can not only mechanically unbind the parent cloud but also induce turbulent motions in the surrounding interstellar medium (ISM) (Gritschneider et al. 2009; Walch et al. 2012; Medina et al. 2014). In addition to photoionization, UV photons exert radiation pressure on dust, which is collisionally coupled to the gas. This radiation pressure force alters the internal structure of H II regions surrounding newborn luminous clusters (Draine 2011b) and helps to expel the gas from GMCs. While the above processes help to quench star formation locally and globally, it has also been proposed

that UV radiation can stimulate star formation either in the “collect and collapse” scenario in which swept-up shells around H II regions grow in mass and gravitationally collapse (e.g., Elmegreen & Lada 1977; Whitworth et al. 1994; Hosokawa & Inutsuka 2006; Dale et al. 2007; Deharveng et al. 2010) or via “radiation-driven implosion” in which an ionization front drives converging shock waves toward the centers of pre-existing globules (e.g., Bertoldi 1989; Sugitani et al. 1989; Lefloch & Lazareff 1994; Bisbas et al. 2011). Still, although localized “triggering” may occur, existing simulations (see below) show that UV radiation feedback overall has a negative impact on star formation.

Compared to what would be expected from unimpeded freefall collapse, star formation in GMCs is empirically a rather slow and inefficient process (e.g. Zuckerman & Palmer 1974; Zuckerman & Evans 1974; Evans 1991). While the typical GMC freefall time is only of order $\sim 1\text{--}10$ Myr, the gas depletion timescale t_{dep} estimated from the ratio between gas mass and star formation rate is ~ 1 Gyr for molecular gas averaged over \sim kpc scales in normal disk galaxies (e.g., Bigiel et al. 2008; Leroy et al. 2013) and somewhat shorter in galactic centers and starburst environments (e.g., Daddi et al. 2010; Leroy et al. 2015; Pereira-Santaella et al. 2016) as well as individual molecular clouds (e.g., Kennicutt & Evans 2012; Vutisalchavakul et al. 2016). In Galactic star-forming clouds, the observed star formation efficiency (SFE)—defined as the ratio of stellar to gas mass— varies widely, ranging over $\sim 0.0001\text{--}0.3$, and is only a few percent on average (e.g., Myers et al. 1986; Mooney & Solomon 1988; Williams & McKee 1997; Carpenter 2000; Evans et al. 2009; Murray et al. 2010; García et al. 2014; Lee et al. 2016; Vutisalchavakul et al. 2016), while evidence is accumulating that clouds in extremely dense environments may have higher SFEs (e.g., Meier et al. 2002; Turner et al. 2015; Consiglio et al. 2016; Turner et al. 2017). Yet, it is still uncertain what physical processes are responsible for the diversities in observed

SFEs.

A related issue concerns the lifetime of clouds. For an idealized isolated cloud with steady star formation, the cloud lifetime t_{cl} would be related to the depletion timescale via $t_{\text{cl}} = \varepsilon_* t_{\text{dep}}$, where the net SFE, ε_* , is the fraction of the initial cloud mass that will *ever* become stars. No consensus exists over how long an individual molecular cloud survives as a coherent entity (Heyer & Dame 2015). On the one hand, it has been argued that the short age spreads ($\lesssim 5$ Myr) of stellar populations in nearby star-forming clouds supports the picture that star-forming clouds are dispersed rapidly—on the cloud’s dynamical timescale (e.g. Hartmann 2001; Hartmann et al. 2001, but see also Da Rio et al. 2014, who argue that cluster formation takes several local dynamical timescales). On the other hand, estimates based on the fraction of GMCs that are spatially coincident with H II regions and young star clusters in nearby galaxies favor lifetimes of a few tens of Myrs (Engargiola et al. 2003; Blitz et al. 2007; Kawamura et al. 2009; Miura et al. 2012; see also Murray 2011; Meidt et al. 2015; Lee et al. 2016). The cloud lifetime also has implications for the origin and maintenance of turbulence in GMCs. While supersonic turbulence appears to be pervasive in GMCs (Elmegreen & Scalo 2004), its energy begins to decay within one large-scale crossing time in the absence of driving (e.g., Mac Low et al. 1998; Stone et al. 1998). If GMCs are very long lived, turbulence must be driven continuously (but not excessively) by internal or external processes to support them against gravitational collapse without dispersal (Krumholz et al. 2006; Goldbaum et al. 2011), while this kind of finely calibrated turbulent driving is not needed if GMCs are dispersed rapidly (Elmegreen 2000; Ballesteros-Paredes 2006; Ballesteros-Paredes et al. 2011).

A number of theoretical studies have invoked the destructive role of UV radiation feedback to explain the observed SFEs and lifetimes of GMCs (see reviews by McKee & Ostriker 2007; Krumholz et al. 2014). Analytic models

based on idealized solutions for expanding blister-type H II regions found that the net SFE of $\epsilon_* \sim 5\text{--}15\%$ is sufficient to disperse typical GMCs in the Milky Way (mass $M \sim 10^5\text{--}10^6 M_\odot$ and surface density $\Sigma \sim 10^2 M_\odot \text{pc}^{-2}$) by photoevaporation and dynamical disruption in a few tens of Myr (Whitworth 1979; Williams & McKee 1997; Matzner 2002; Krumholz et al. 2006). Krumholz & Matzner (2009), Fall et al. (2010), and Murray et al. (2010) highlighted the importance of radiation pressure on dust grains in controlling the dynamics of H II regions in dense, massive star-forming environments. Kim et al. (2016) studied dynamical disruption of clouds by considering the expansion of a swept-up spherical shell surrounding a central H II region, and found that the minimum SFE required for cloud disruption increases primarily with the cloud’s surface density and that the disruption timescale is comparable to the freefall time. These models also suggest that radiation pressure is expected to be more important than ionized-gas pressure in massive and high surface density clouds (see also Krumholz & Matzner 2009; Fall et al. 2010). More recently, Rahner et al. (2017) developed a semi-analytic model for the dynamics of an expanding shell formed around a star cluster including the effects of radiation pressure, stellar winds, and supernovae (SNe) (but not including effects of ionized-gas pressure), and evaluated the minimum SFE as well as the relative importance of each feedback mechanism.

While analytic approaches offer valuable insights into the physical processes involved in cloud dispersal, they are limited to smooth and/or spherically symmetric density distributions. Real GMCs are turbulent and extremely inhomogeneous. As a consequence, shell expansion induced by H II regions from multiple subclusters is not spherically symmetric, and neither embedded nor blister H II regions present smooth interior surfaces to photoionizing radiation. To quantitatively follow the formation and evolution of multiple cluster-containing H II regions in highly turbulent, inhomogeneous clouds, and to quantitatively assess the consequences of the complex

interplay between gas and UV radiation, numerical radiation hydrodynamic (RHD) simulations are necessary (see recent reviews by Krumholz et al. 2014; Dale 2015).

Several numerical studies have investigated the effects of photoionization feedback on dynamical evolution of GMCs. For instance, Vázquez-Semadeni et al. (2010) and Colín et al. (2013) allowed for photoheating by ionizing radiation in the evolution of GMCs produced by colliding flows and showed that the feedback reduces SFEs significantly. Using smoothed particle hydrodynamics simulations, Dale et al. (2012, 2013a) performed RHD simulations of star cluster formation in turbulent GMCs over a 3 Myr timescale before the first supernova event occurs. Their parameter study showed that while photoionization can unbind a significant fraction of material in low-mass, diffuse clouds, it has a limited impact for clouds with escape velocities larger than the sound speed of ionized gas. Gavagnin et al. (2017) studied the early (2 Myr) dynamical evolution of a star cluster formed in a turbulent cloud with mass $2.5 \times 10^4 M_\odot$ and surface density $250 M_\odot \text{pc}^{-2}$ and found that photoionization can limit the net SFE to 20%. Geen et al. (2017) performed RHD simulations of magnetized, $10^4 M_\odot$ -mass clouds of varying size and found that the net SFE increases from 0.04 to 0.6 as the surface density increases from 14 to $1100 M_\odot \text{pc}^{-2}$.

Considering the effects of non-ionizing UV, Raskutti et al. (2016) conducted RHD simulations of cluster-forming turbulent clouds, focusing exclusively on the radiation pressure from singly-scattered, non-ionizing UV. They found that the resulting net SFE ($\epsilon_* \sim 0.1\text{--}0.6$ for $\Sigma \sim 10\text{--}300 M_\odot \text{pc}^{-2}$) in turbulent cloud simulations is much higher than that expected for the case of a uniform shell. This is because turbulent shock compression leads to a broad (log-normal) distribution of the gas surface density, which in turn increases the fraction of super-Eddington, high surface-density gas that is difficult to unbind and hence subject to star formation (see also Thompson & Krumholz

2016). Raskutti et al. (2016) concluded that feedback from radiation pressure alone is unable to explain the low SFEs of observed GMCs.

More recently, Howard et al. (2017) performed a series of RHD simulations to study the early phase ($\lesssim 5$ Myr) of GMC evolution, including both photoionization and radiation pressure. They considered a set of GMC models with the same mean density ($n_{\text{H}} \sim 150 \text{ cm}^{-3}$) but differing mass (10^4 – $10^6 M_{\odot}$), and found a modest degree of suppression in the SFE compared to the runs in which they turned off radiation feedback. In their models, the impact of radiative feedback varied without a clear trend with the cloud mass; only intermediate-mass clouds ($5 \times 10^4 M_{\odot}$ and $10^5 M_{\odot}$) were fully ionized and destroyed in 5 Myr.

While the above numerical studies have improved our understanding of the effects of UV radiation on GMC evolution and star formation regulation, several important issues still need to be addressed. First, although several studies have emphasized the importance of photoionization and radiation pressure for cloud dispersal, as yet there is no systematic accounting that quantifies to what extent each mechanism, alone and combined, is responsible for the net SFE and cloud disruption. Second, most of the previous simulations have only used approximate methods for treating the radiative transfer problem for multiple point sources. For example, Vázquez-Semadeni et al. (2010) incorporated photoionization feedback by depositing thermal energy to a gas cell where a stellar particle resides. Dale et al. (2012, 2013a) adopted the “Strömgen volume technique” to calculate the ionization state of gas, but did not consider the effects of radiation pressure on dust. Simulations by Raskutti et al. (2016, 2017), Gavagnin et al. (2017), and Geen et al. (2017) adopted two-moment methods to evolve the radiation energy and momentum on a grid with the M_1 -closure. Although the M_1 -closure is accurate for a spatially concentrated source distribution, it becomes less accurate when multiple point sources are widely distributed; this method also

has inherently limited resolution in the immediate vicinity of point sources (see Chapter 4 and Kim et al. (2017b)). Thus, a firm quantitative assessment of the importance of both photoionization and radiation pressure on cloud dispersal requires a more accurate solution of the radiative transfer equation than has previously been available.

In this work, we have carried out RHD simulations of star cluster formation in turbulent clouds employing the adaptive ray tracing method (Abel & Wandelt 2002), which enables us to accurately solve the radiative transfer problem for multiple point sources and both ionizing and non-ionizing radiation. In Chapter 4 we described our implementation and tests of adaptive ray tracing in the *Athena* magnetohydrodynamics code (Stone & Gardiner 2009), for which we adopted the novel parallelization algorithm proposed by Rosen et al. (2017) as well as several other improvements. The excellent parallel performance this has enabled for ray tracing allows us to run a large number of simulations, probing a range of cloud masses and sizes efficiently. In this chapter, our primary goals are (1) to quantify the dependence on the cloud properties of the net SFE, timescale for cloud disruption, mass of ionized outflows, and momentum transferred to gas outflows, and (2) to assess the relative importance of photoionization and radiation pressure in various environments. In addition, we develop analytic predictions for mass loss based on the physical scalings for photoevaporation and momentum injection, and we compare the predictions for the net SFE with the numerical results.

The organization of this chapter is as follows. Section 5.2 presents the numerical methods and cloud parameters that we adopt. Section 5.3 first describes the overall evolution of our fiducial model, and then explores the parameter dependence of various integrated physical quantities for different models. In Section 5.4, we present a detailed analysis of the mass loss caused by photoevaporation and momentum injection. In Section 5.5, we construct the semi-analytic models for the net SFE and mass loss efficiencies of GMCs

regulated by UV radiation feedback, and compare the model predictions with the numerical results. In Section 5.6, we summarize and discuss the astronomical implications of our results. In Appendix 5.A, we present the results of convergence study for the fiducial model. In Appendix 5.B, we compare our numerical results for SFE in radiation-pressure only models to analytic predictions.

5.2 Numerical Methods

For our numerical simulations, we use the Eulerian grid-based code *Athena* (Stone et al. 2008) equipped with additional physics modules for self-gravity, sink particles, and radiative transfer from point sources. In Chapter 4, we presented a detailed description of our implementation of the adaptive ray tracing algorithm for multiple point sources in *Athena*, including parallelization and the methods for solving photoionization and recombination. Chapter 4 also described the initial conditions and problem setup for our simulations of cluster-forming turbulent clouds. Below we briefly summarize the highlights of our numerical methods and describe the initial cloud parameters.

5.2.1 Radiation Hydrodynamics Scheme

For hydrodynamics, we employ *Athena*'s van Leer-type time integrator (Stone & Gardiner 2009), the HLLC Riemann solver, and a piecewise linear spatial reconstruction scheme. We use the fast Fourier transformation Poisson solver with open boundary conditions (Skinner & Ostriker 2015) to calculate the gravitational forces from gas and stars; the stellar contribution is handled with the particle-mesh method using the triangular-shaped-cloud interpolation scheme (Hockney & Eastwood 1981).

We apply the sink particle technique of Gong & Ostriker (2013) to model the formation and growth of star clusters. We create a star particle if a cell with density above the Larson-Penston threshold density ($\rho_{\text{crit}} \equiv 8.86c_{\text{s,neu}}^2/(\pi G\Delta x^2)$)

for the sound speed of neutral gas $c_{s,\text{neu}}$ and the grid spacing Δx) has a converging velocity field and corresponds to the local minimum of the gravitational potential. The accretion rates of mass and momentum onto each sink are computed from the flux through the surfaces of the 3^3 -cell control volume centered at the sink particle; this control volume acts like internal ghost zones within the simulation domain. The positions and velocities of sink particles are updated using a leapfrog integrator. We allow sink particles to merge if their control volumes overlap.

Due to limited resolution, the sink particles in our simulations represent subclusters rather than individual stars², and may not fully sample the initial mass function. Using the mass-dependent light-to-mass ratios from Kim et al. (2016), we determine the total UV luminosity of cluster particles for two frequency bins, L_i and L_n , representing Lyman continuum photons and far-UV photons, such as $L \equiv L_i + L_n = \Psi M_*$ and $Q_i \equiv L_i/(h\nu_i) = \Xi M_*$, where M_* is the total cluster mass, $\Psi = 10^{2.98\mathcal{X}^6/(29.0+\mathcal{X}^6)} L_\odot M_\odot^{-1}$, $\Xi = 10^{46.7\mathcal{X}^7/(7.28+\mathcal{X}^7)} \text{s}^{-1} M_\odot^{-1}$ with $\mathcal{X} = \log_{10}(M_*/M_\odot)$, and $h\nu_i = 18 \text{ eV}$ is the mean energy of ionizing photons. Note that $\Psi \simeq 943 L_\odot M_\odot^{-1}$ and $\Xi \simeq 5.05 \times 10^{46} \text{ s}^{-1} M_\odot^{-1}$ are almost constant for $M_* \gtrsim 10^3 M_\odot$, while varying steeply for $M_* < 10^3 M_\odot$ (see Figure 14 of Kim et al. 2016). The luminosity of individual cluster particles are assumed to be proportional to their mass. The use of mass-dependent conversion factors approximately captures the effect of undersampling at the massive end of the initial mass function when the total cluster mass is below $\sim 10^3 M_\odot$.

In this chapter, we do not consider evolution of the stellar light-to-mass ratio. The UV luminosity of a coeval stellar population that well samples the initial mass function remains approximately constant for the main sequence

²The typical mass of newly formed sink particles is $M_{\text{sink}} \sim 10\rho_{\text{crit}}\Delta x^3 \approx 240 M_\odot (R_0/20 \text{ pc})(N_x/256)^{-1}$, where ρ_{crit} is the threshold for sink particle creation, R_0 is the initial cloud radius, and N_x is the number of grid zones in the domain in one direction.

lifetime of the most massive star, implying that ionizing and non-ionizing luminosities would in practice decay rapidly after timescales of 3 Myr and 8 Myr, respectively (e.g., Parravano et al. 2003). Caveats related to our adoption of age-independent luminosity are discussed in Section 5.6.2.

The radiative transfer of ionizing and non-ionizing photons is handled by the adaptive ray tracing method (Abel & Wandelt 2002). For each radiating star particle, we generate $12 \times 4^4 = 3072$ initial rays and allow photon packets to propagate radially outward, computing the cell-ray intersection length and the corresponding optical depth on a cell-by-cell basis. The volume-averaged radiation energy and flux densities of a cell are computed from the sum of the contributions from all rays that pass through the cell (see Section 2.1 of Chapter 4). These averages are used to compute the radiation force from the combined non-ionizing and ionizing radiation fields, and the ionization rate of neutral gas. Because the fluid variables and gravity in the 3^3 cells surrounding each sink/source particle are unresolved, we do not allow photon packets to interact with the gas within these control volumes. The radiation field directions are angularly well resolved, and the rays contain all of the photon packets from each source, when they emerge from the control volume around each source particle. This eliminates the potential problem of momentum cancellation caused by volume-averaging in the cell containing a source, noted recently by Hopkins & Grudic (2018), without the need to introduce assumptions regarding the sub-cell distributions of gas density, gravity, or the radiation field within individual zones that contain sink/source particles.

The rays are discretized and split based on the HEALPix framework (Górski et al. 2005), ensuring that each grid cell is sampled by at least four rays per source. We rotate ray propagation directions randomly at every hydrodynamic time step to reduce the numerical errors due to angle discretizations (Krumholz et al. 2007b). For simplicity, we use constant photoionization

cross-section for neutral hydrogen atom $\sigma_{\text{H}^0} = 6.3 \times 10^{-18} \text{ cm}^{-2}$ (Krumholz et al. 2007b)³ and constant dust absorption (and pressure) cross-section per H nucleon $\sigma_{\text{d}} = 1.17 \times 10^{-21} \text{ cm}^{-2} \text{ H}^{-1}$ both for ionizing and non-ionizing radiation (e.g., Draine 2011b). We determine the degree of hydrogen ionization by solving the time-dependent rate equation for hydrogen photoionization and recombination (under the on-the-spot approximation). The ray-trace and ionization update are subcycled relative to the hydrodynamic update. The timestep size for each substep is determined to ensure that the maximum change in the neutral fraction $x_{\text{n}} = n_{\text{H}^0}/n_{\text{H}}$ is less than 0.1. The source term updates for the ionization fraction and radiative force are explicit and performed at every substep in an operator-split fashion. The gas temperature is set to vary according to x_{n} between $T_{\text{neu}} = 20 \text{ K}$ and $T_{\text{ion}} = 8000 \text{ K}$, the temperature of the fully neutral and ionized gas, respectively. The corresponding isothermal sound speeds are $c_{\text{s,neu}} = 0.26 \text{ km s}^{-1}$ and $c_{\text{s,ion}} = 10.0 \text{ km s}^{-1}$.

We note that determining gas temperature solely based on the neutral fraction, together with adoption of constant cross-sections for photoionization and dust absorption, will certainly simplify temperature distributions inside H II regions compared to what would be more complex in realistic environments. To properly model ionization and temperature structure, as well as small-scale dynamical instabilities of ionization fronts that may operate (e.g., Kim & Kim 2014), one has to accurately solve the energy equation after considering various cooling and heating processes as well as the frequency dependence of the cross-sections.

³Our adopted photoionization cross-section corresponds to the value at the Lyman edge. The frequency-averaged cross-section depends on the local radiation spectrum and is typically smaller by a factor of ~ 2 (e.g., Baczynski et al. 2015). Although the use of smaller σ_{H^0} can increase the neutral fraction of ionized gas inside the H II region, we have checked that it has little impact on the simulation outcome.

5.2.2 Initial and Boundary Conditions

Our initialization and boundary treatment are the same as in Skinner & Ostriker (2015) and Raskutti et al. (2016). The initial conditions for each model consist of an isolated, uniform-density sphere of neutral gas with mass M_0 and radius R_0 surrounded by a tenuous external medium situated in a cubic box with sides $L_{\text{box}} = 4R_0$.⁴ The cloud is initially supplied with turbulent energy with velocity power $|\delta\mathbf{v}_k|^2 \propto k^{-4}$ for $2 \leq kL_{\text{box}}/(2\pi) \leq 64$ and zero power otherwise. We adjust the amplitude of the velocity perturbations to make the cloud marginally bound gravitationally, with the initial virial parameter of $\alpha_{\text{vir},0} = 5\sigma_0^2 R_0 / (3GM_0) = 2$, where σ_0 denotes the initial (three-dimensional) velocity dispersion. There is no subsequent artificial turbulent driving. The standard resolution for the simulation domain is $N_{\text{cell}} = 256^3$ cells.

We apply diode-like outflow boundary conditions both at the boundaries of the simulation box and at the boundary faces of the control volume of each sink particle. The diode-like conditions allow mass and momentum to flow into ghost zones but not out from it. When sink particles accrete while moving across grid zones, we ensure that the total mass and momentum of gas and stars are conserved by taking into account differences in the mass and momentum of cells entering and leaving the control volume. Over the course of evolution, we separately monitor the mass outflow rates of neutral and ionized gas from the computational domain, as well as escape fractions of ionizing and non-ionizing photons.

5.2.3 Models

Our aim is to explore the effects of radiation feedback on cloud dispersal across a range of cloud masses and sizes, corresponding to GMCs observed in the Milky Way and nearby galaxies. These clouds are usually optically

⁴Including the tenuous external medium, the initial gas mass in our simulation domain is $1.015M_0$.

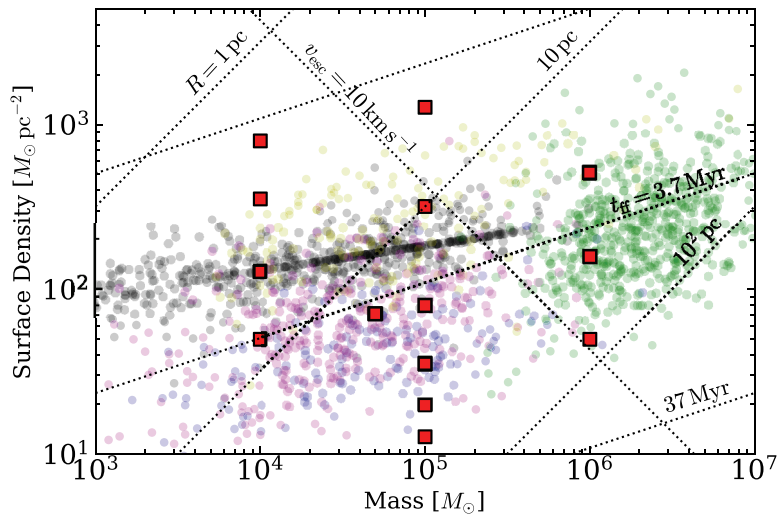


Figure 5.1 Locations of our model clouds (red squares) in the M - Σ plane. Other symbols denote the observed molecular clouds in the literature: ^{13}CO Galactic Ring Survey from Heyer et al. (2009) (blue) and Roman-Duval et al. (2010) (black), ^{12}CO survey of Galactic Center Oka et al. (2001) (yellow), ^{12}CO survey of Large Magellanic Clouds from Wong et al. (2011) (magenta), and ^{12}CO survey of M51 from Colombo et al. (2014) (green). Dotted lines draw the loci of constant radius, escape velocity, and freefall time.

Table 5.1. Model Cloud Parameters

Model (1)	M_0 (2)	R_0 (3)	Σ_0 (4)	$n_{\text{H},0}$ (5)	$t_{\text{ff},0}$ (6)	$v_{\text{esc},0}$ (7)
M1E5R50	1×10^5	50.0	12.7	5.5	18.5	4.1
M1E5R40	1×10^5	40.0	19.9	10.8	13.2	4.6
M1E5R30	1×10^5	30.0	35.4	25.5	8.6	5.4
M1E4R08	1×10^4	8.0	49.7	134.7	3.7	3.3
M1E6R80	1×10^6	80.0	49.7	13.5	11.8	10.4
M5E4R15	5×10^4	15.0	70.7	102.2	4.3	5.4
M1E5R20	1×10^5	20.0	79.6	86.2	4.7	6.6
M1E4R05	1×10^4	5.0	127.3	551.8	1.9	4.1
M1E6R45	1×10^6	45.0	157.2	75.7	5.0	13.8
M1E5R10	1×10^5	10.0	318.3	689.7	1.7	9.3
M1E4R03	1×10^4	3.0	353.7	2554.6	0.9	5.4
M1E6R25	1×10^6	25.0	509.3	441.4	2.1	18.6
M1E4R02	1×10^4	2.0	795.8	8621.6	0.5	6.6
M1E5R05	1×10^5	5.0	1273.2	5517.8	0.6	13.1

Note. — Parameters listed are for initial conditions of spherical clouds. Column 1: model name. Column 2: cloud mass (M_\odot). Column 3: cloud radius (pc). Column 4: gas surface density ($M_\odot \text{pc}^{-2}$). Column 5: number density of neutral gas (cm^{-3}). Column 6: freefall time (Myr). Column 7: escape velocity at the cloud surface (km s^{-1}). The fiducial model **M1E5R20** is shown in bold.

thick to UV radiation ($\Sigma \gtrsim \kappa_{\text{UV}}^{-1} \sim 10^1 M_\odot \text{pc}^{-2}$) but transparent to dust-reprocessed infrared radiation ($\Sigma \lesssim \kappa_{\text{IR}}^{-1} \sim 10^3 M_\odot \text{pc}^{-2}$). The momentum deposition by multiple scatterings of infrared photons may play an important role in the dynamics of extremely dense and massive clouds, such as the progenitors of super star clusters, in dust-rich environments (e.g., Skinner & Ostriker 2015; Tsang & Milosavljevic 2017).

We consider 14 clouds with M_0 in the range of $10^4 M_\odot$ to $10^6 M_\odot$ and R_0 from 2 pc to 80 pc: the resulting initial surface density $\Sigma_0 = M_0/(\pi R_0^2)$ is in the range from $12.7 M_\odot \text{pc}^{-2}$ to $1.27 \times 10^3 M_\odot \text{pc}^{-2}$. Figure 5.1 plots the locations (red squares) of our model clouds in the M - Σ domain, compared

to observed GMCs (circles) compiled from the literature (note that a range of different methods have been adopted in the literature to estimate observed cloud surface density and mass). Table 5.1 lists the initial physical parameters of our model clouds. Column 1 gives the name of each model. Columns 2–4 list M_0 , R_0 , and Σ_0 , respectively. Columns 5 and 6 give the number density of hydrogen atoms $n_{\text{H},0}$ and the freefall time $t_{\text{ff},0} = \sqrt{3\pi/(32G\rho_0)}$. Finally, Column 7 gives the escape velocity $v_{\text{esc},0} = \sqrt{2GM_0/R_0}$ at the cloud surface. The initial turbulent velocity dispersion in each cloud is $\sigma_0 = 0.77v_{\text{esc},0}$. We take model M1E5R20 with $M_0 = 10^5 M_\odot$, $R_0 = 20$ pc, and $t_{\text{ff},0} = 4.7$ Myr as our fiducial model, which is typical of Galactic GMCs and comparable in mass and size to the Orion A molecular cloud (e.g., Wilson et al. 2005).

In addition to the standard runs including both photoionization and radiation pressure (PH+RP), we run two control simulations for each cloud, in which either only photoionization (PH-only) or only radiation pressure (RP-only) is turned on. This enables us to isolate the effect of each feedback mechanism and thus to indirectly assess their relative importance in cloud dispersal. For the fiducial cloud, we additionally run low- and high-resolution models (M1E5R20_N128 and M1E5R20_N512) with $N_{\text{cell}} = 128^3$ and 512^3 as well as a no-feedback run (M1E5R20_nofb), in the last of which stellar feedback is turned off. In Appendix 5.A, we compare the results from the models with different resolution. Although star formation completes slightly later in simulations with higher resolution, the overall evolutionary behavior is qualitatively the same and key quantitative outcomes (such as the SFE) are quite close at different resolution, following a converging trend. All simulations are run over 4–7 freefall times, long enough for star formation to complete and for radiation feedback to evacuate the remaining gas from the simulation domain.

5.3 Simulation Results

We begin by presenting the overall temporal evolution of the fiducial model M1E5R20 in Section 5.3.1. Other models exhibit a similar evolutionary behavior, although there are significant changes in the net SFE, timescales for star formation and cloud dispersal, and velocity of outflowing gas. These will be presented in Section 5.3.2–5.3.4.

5.3.1 Overall Evolution: Fiducial Model

Similarly to the simulations of Raskutti et al. (2016), the early evolution of our fiducial model is governed by turbulence and self-gravity. The density structure becomes increasingly filamentary as a result of shock compression. The densest regions—which may be at junctions of filaments, or simply overdense clumps within filaments—undergo gravitational collapse, leading to the formation of sink particles. In the fiducial model the first collapse occurs at $t_{*,0}/t_{\text{ff},0} = 0.4$.

Due to star formation and the ensuing feedback, the gas in our simulations is ultimately channelled into three distinct states. One portion of the gas gravitationally collapses and is accumulated in sink particles as a total stellar mass $M_*(t)$. Strong ionizing radiation from newly-formed stars ionizes a portion of the initially-neutral gas, with the total mass of photoevaporated gas increasing in time as $M_{\text{ion}}(t)$. This includes the ionized gas currently in the simulation box and the cumulative ionized gas that has left the simulation domain. Over time, all of the neutral gas in the domain either collapses to make stars, is photoevaporated and ejected, or is ejected while still neutral. We denote the cumulative ejected mass of the neutral gas by $M_{\text{ej,neu}}(t)$.⁵ Of course, gas that is photoionized may recombine before it flows

⁵We regard the neutral gas as being ejected if it reaches the outer boundary of the simulation box, although one can use a more rigorous criterion by testing the gravitational boundedness of individual gas parcels (e.g., Dale et al. 2012).

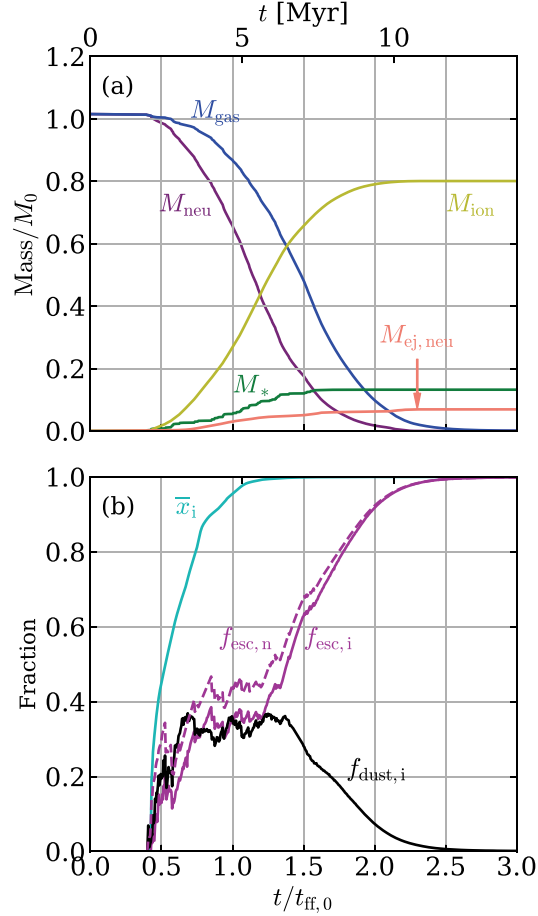


Figure 5.2 Evolutionary histories of the fiducial model with $M_0 = 10^5 M_\odot$ and $R_0 = 20$ pc. (a) The total gas mass M_{gas} in the simulation volume (blue), the neutral gas mass M_{neu} in the simulation volume (purple), the stellar mass M_* (green), the ejected neutral gas mass $M_{\text{ej,neu}}$ (salmon), and the mass of the photoevaporated gas M_{ion} (yellow). (b) The volume fraction of the ionized gas \bar{x}_i (cyan), the fraction of ionizing radiation absorbed by dust $f_{\text{dust,i}}$ (black), and the escape fractions of ionizing ($f_{\text{esc,i}}$; solid magenta) and non-ionizing ($f_{\text{esc,n}}$; dashed magenta) radiation are plotted as functions of time.

out of the box, but at the end of the simulation when no gas remains in the domain, $M_{\text{ion,final}} = M_{\text{ion}}(t_{\text{final}})$. The condition of mass conservation requires $M_0 = M_{*,\text{final}} + M_{\text{ion,final}} + M_{\text{ej,neu,final}}$ at the end of the run.

Figure 5.2(a) plots the temporal changes of the total gas mass M_{gas} in the simulation volume as well as M_* , M_{ion} , and $M_{\text{ej,neu}}$, all normalized by the initial cloud mass M_0 . Figure 5.2(b) plots the temporal evolution of the volume filling factor of the ionized gas $\bar{x}_i = \int (n_{\text{H}^+}/n_{\text{H}})dV / \int dV$, the escape fractions of ionizing ($f_{\text{esc,i}}$) and non-ionizing ($f_{\text{esc,n}}$) radiation, and the fraction of ionizing photons absorbed by dust ($f_{\text{dust,i}}$). These escape fractions and dust absorption fraction here are the instantaneous probabilities of escape or absorption from a single ray-trace at a given time.

Figure 5.3 plots selected snapshots of the fiducial model in the x - y plane. From top to bottom, the rows show column density of neutral gas projected along the z -axis, slices through the stellar center of mass of the neutral hydrogen number density n_{H^0} , electron number density n_{e} , ionizing radiation energy density \mathcal{E}_i , non-ionizing radiation energy density \mathcal{E}_n . The projected positions of star particles are marked by circles colored by their ages. In the top row, all star particles in the simulation volume are shown, while in the bottom four rows only those within $\Delta 5$ pc of the slice are shown. The selected times (columns from left to right) are $t/t_{\text{ff},0} = 0.57, 0.80, 1.07,$ and 1.40 when 10%, 25%, 50%, and 90% of the final stellar mass has been assembled, respectively: here and hereafter, these epochs will be referred to as $t_{*,10\%}$, $t_{*,25\%}$, $t_{*,50\%}$, and $t_{*,90\%}$, respectively. Figure 5.4 displays volume rendered images of the fiducial model at these epochs.

Because of the initial turbulence, the background medium is highly clumpy and filamentary. Young H II regions formed around star particles quickly break out of their dense natal clumps, and in the larger-scale turbulent cloud some lines of sight have quite low optical depth. As a result, a substantial fraction of both ionizing and non-ionizing photons escape from the simula-

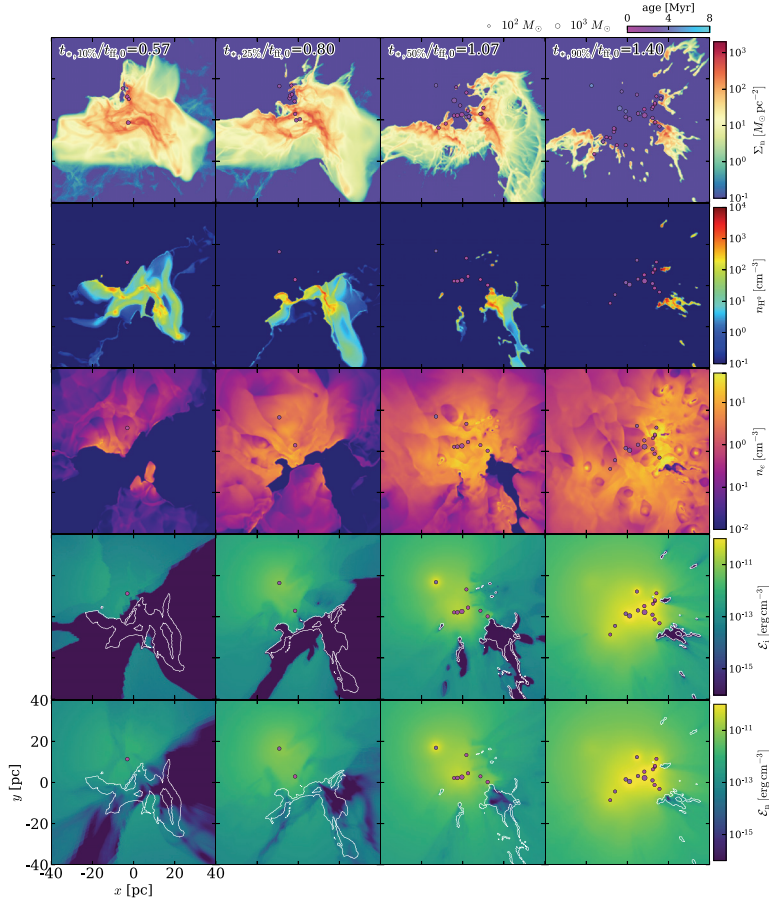


Figure 5.3 Snapshots of the fiducial model in the x - y plane. The columns show times $t/t_{\text{ff},0} = 0.58, 0.8, 1.07,$ and 1.40 , and when 10%, 25%, 50%, 90% of the final stellar mass has been assembled, respectively. From top to bottom: surface density of neutral gas (projected along the z -axis) Σ_n , slices (passing through the position of the stellar center of mass) of neutral hydrogen number density $n_{\text{H}0}$, electron number density n_e , energy density of ionizing radiation \mathcal{E}_i , energy density of non-ionizing radiation \mathcal{E}_n . The white contours in the bottom two rows show the number density of neutral gas at $n_{\text{H}0} = 10 \text{ cm}^{-3}$. Small circles in each frame mark the projected positions of the star particles that have formed, with their color and size corresponding to their age and mass, respectively. In the bottom four rows, only star particles whose distance from the slicing plane is less than 5 pc are shown.

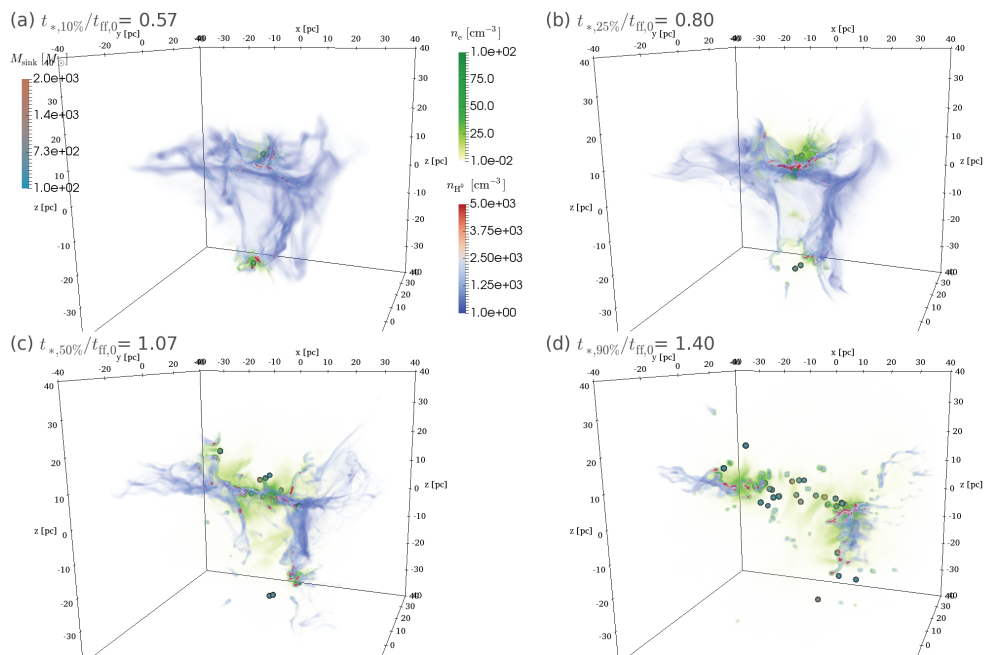


Figure 5.4 Volume rendering of the neutral hydrogen number density $n_{\text{H I}}$ (blue-white-red) and the electron number density n_e (green-yellow) of the fiducial model at (a) $t = t_{*,10\%}$, (b) $t_{*,25\%}$, (c) $t_{*,50\%}$, and (d) $t_{*,90\%}$. Sink particles representing stellar clusters are shown as spheres colored by mass M_{sink} .

tion box even at quite early stages of evolution. For example, at $t_{*,10\%}$ (only $0.17t_{\text{ff},0} = 0.8 \text{ Myr}$ after the first collapse), five star particles have been created and more than 50% of computational box is filled with ionized gas, although it accounts for only 3% of the total gas mass in the domain. By this time, 13% of the radiation has escaped from the domain overall (with an instantaneous escape probability of 16%). Even though the second quadrant in the x - y plane is rapidly ionized, at early times (persisting through $t_{*,25\%}$) there are still regions (see lower-left panels of Figure 5.3) that are fully neutral because they are shadowed by dense gas that absorbs all the ionizing photons on rays emerging from the central star-forming cluster.

At $t_{*,25\%}$, star formation is concentrated in the central 10 pc region. Multiple H II regions expand simultaneously and merge with each other, accompanying a rapid increase of M_{ion} by intense photoevaporation. Due to thermal pressure gradients, the ionized gas is pushed to the outer low-density regions, developing a roughly exponential radial density profile outside the central cavity. Ionized gas starts to escape from the box at mildly supersonic outflow velocities of $\sim 20 \text{ km s}^{-1}$. Simultaneously, the remaining neutral gas filaments are pushed away from the central collection of stars by a combination of radiation pressure forces and the rocket effect as gas photoevaporates from their surfaces (see top two rows of Figure 5.3). At later time, star formation occurs mainly in dense clumps within structures that have been pushed to the periphery of the combined H II region. We note that the expansion over time of the loci of star formation is not primarily due to shock-induced collapse as the H II region expands (collapse in filaments would have occurred anyway), but because dense gas is progressively evacuated from a larger and larger volume.

Figure 5.5 plots the maps of the emission measure (EM) $\int n_e^2 d\ell$ integrated along the z -direction of the fiducial model at $t_{*,10\%}$, $t_{*,25\%}$, $t_{*,50\%}$, and $t_{*,90\%}$. In the early phase of star formation, the EM map is dominated by bright,

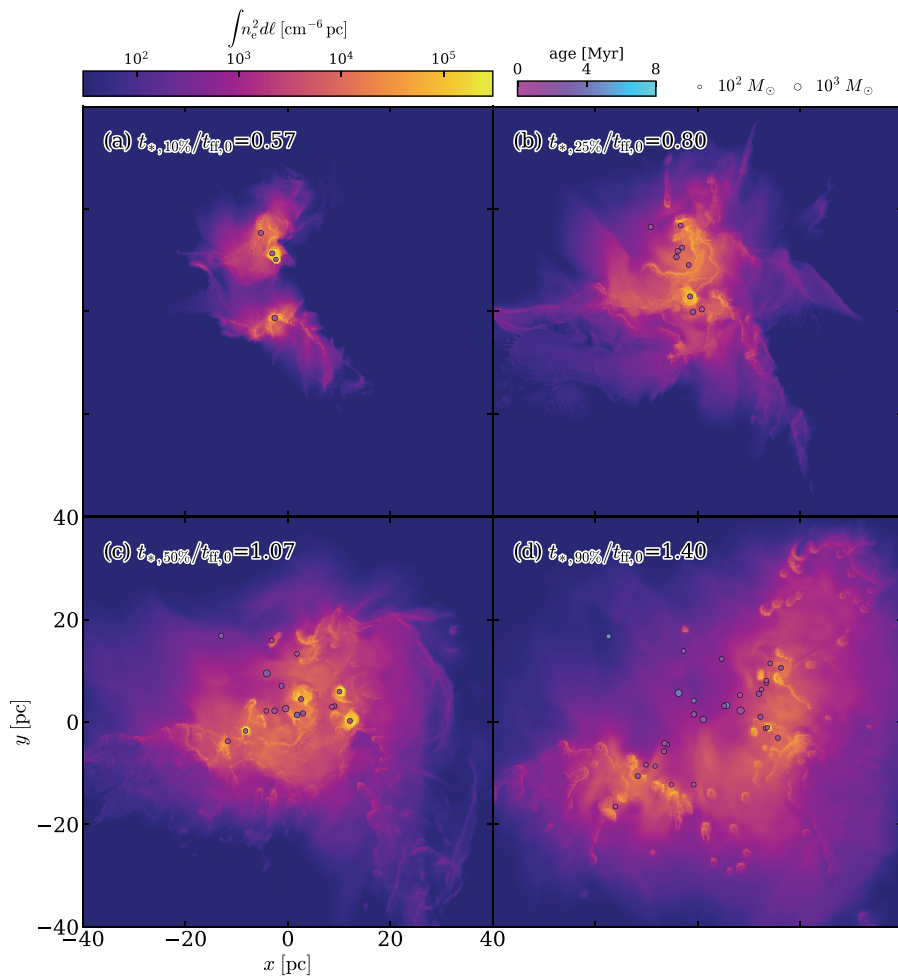


Figure 5.5 Snapshots projected on the x - y plane of the emission measure of the fiducial model at (a) $t = t_{*,10\%}$, (b) $t_{*,25\%}$, (c) $t_{*,50\%}$, and (d) $t_{*,90\%}$. Circles mark the projected positions of all the star particles that have formed, with their color and size corresponding to their age and mass, respectively.

compact H II regions around newly formed stars, while at later times it becomes rich in substructures resembling observed pillars and bright-rimmed globules (e.g., Koenig et al. 2012; Hartigan et al. 2015); these features are also apparent in the n_e slices of Figure 5.3. Similar structures have also been seen in previous numerical simulations of expanding H II regions in a turbulent medium (e.g., Mellema et al. 2006a; Gritschneider et al. 2009, 2010; Walch et al. 2012). The globules exhibit ionization-driven ablation flows and distinctive elongated tails pointing away from the ionizing sources. Anisotropic mass loss, preferentially from the sides of globules facing the star particles, exerts a recoil force on them; the globules rocket away from the stellar sources at a typical radial velocity of $v_{\text{ej,neu}} \sim 5 \text{ km s}^{-1}$.

By $t_{*,90\%}$, not only has the H II region engulfed the entire cloud, but the ionized region has expanded to twice the original cloud radius. Furthermore, the central 10 pc has mostly been cleared of dense gas. The escape fractions of ionizing and non-ionizing photons keep increasing with time as neutral gas surrounding ionizing sources is pushed away (see also, e.g., Rogers & Pittard 2013; Raskutti et al. 2017).

The cloud has been completely destroyed by $t/t_{\text{ff},0} \sim 2$, with the fraction of the remaining neutral gas $< 2\%$ of the initial cloud mass. The final star formation efficiency is $\varepsilon_* \equiv M_{*,\text{final}}/M_0 = 0.13$ in the fiducial model. Only 7% of the initial cloud mass is ejected in the neutral phase, while 81% is lost to photoevaporation. The remaining cluster of star particles is loosely bound gravitationally and dissolves rapidly; 30% of the final stellar mass leaves the computational domain from $t/t_{\text{ff},0} = 2.09$ to $t/t_{\text{ff},0} = 4$.

5.3.2 Star Formation and Mass Loss Efficiencies

In our simulations, the SFE of a cloud rises until the associated feedback photoevaporates and dynamically ejects the remaining gas, completely halting further star formation. We define the final net SFE as $\varepsilon_* \equiv M_{*,\text{final}}/M_0$. In

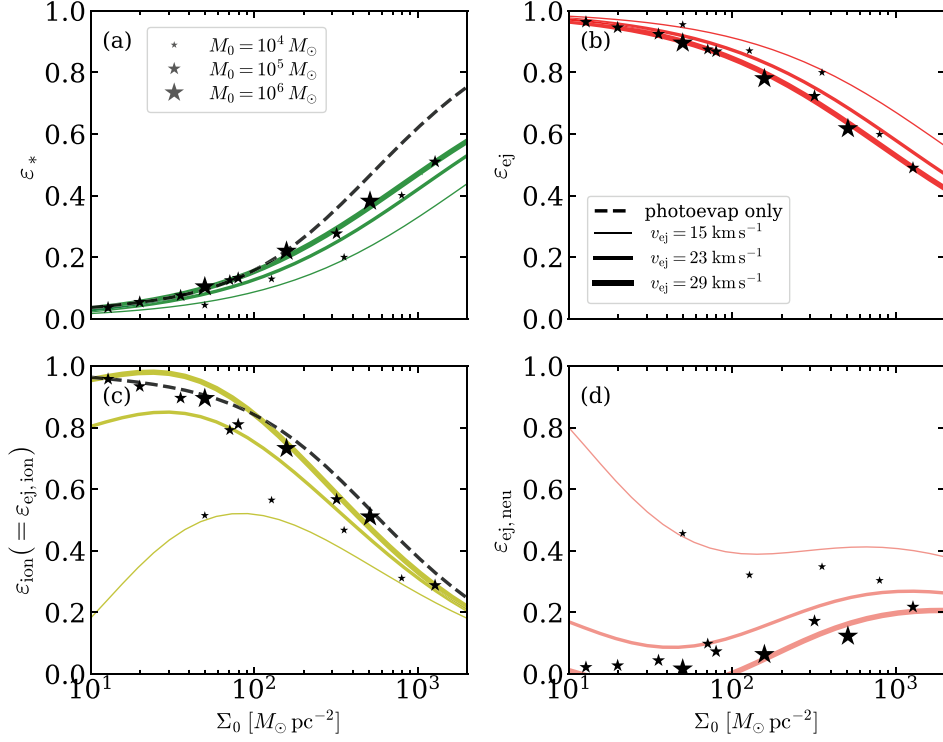


Figure 5.6 (a) Net star formation efficiency ε_* , (b) ejection efficiency ε_{ej} , (c) photoevaporation efficiency ε_{ion} , and (d) neutral ejection efficiency $\varepsilon_{ej,neu}$ for the PH+RP runs (star symbols) as functions of the initial gas surface density Σ_0 . The symbol size is proportional to the initial cloud mass M_0 (this notation will be kept throughout this chapter). Lines in each panel compare to our semi-analytic models for cloud disruption, as presented in Section 5.5: the dashed lines correspond to the prediction when photoevaporation dominates mass loss, while the solid lines are based on our numerical measurement of momentum injection applied to different cloud masses.

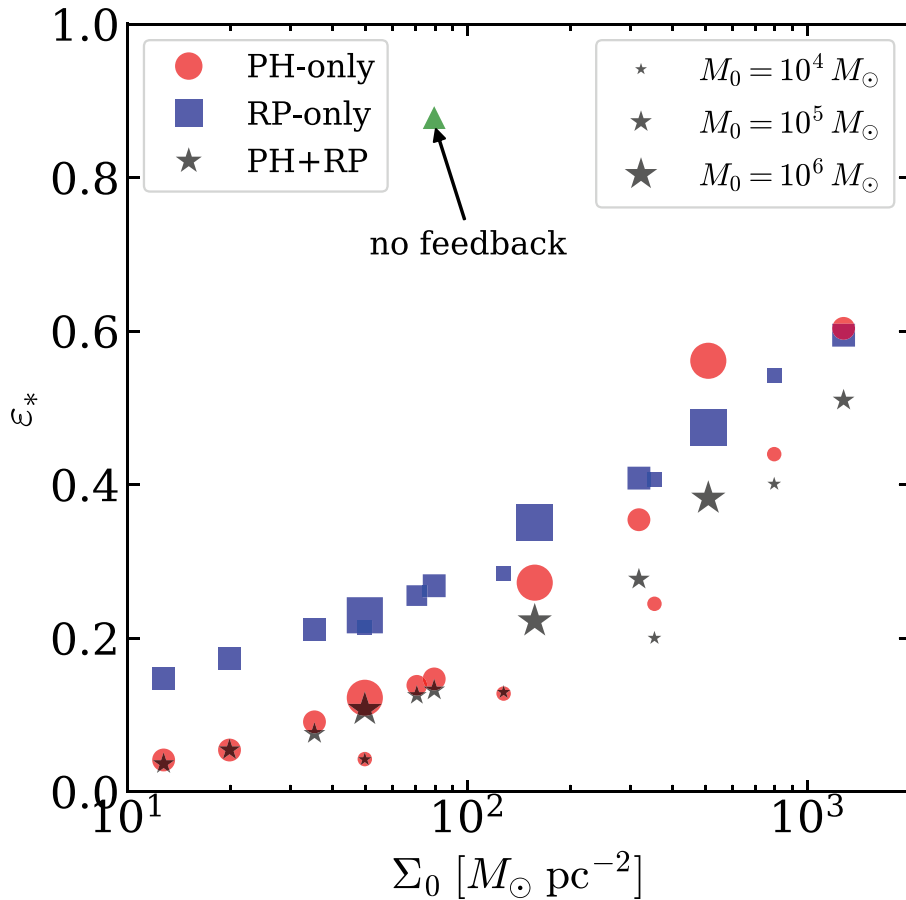


Figure 5.7 Net SFE ϵ_* as a function of initial surface density Σ_0 for the models with photoionization only (PH-only, red circles), models with radiation-pressure only (RP-only, blue squares), and models with both photoionization and radiation pressure included (PH+RP, black stars). Symbol sizes denote the initial cloud mass. The green triangle represents ϵ_* of the fiducial cloud with no feedback. For low surface density clouds, the net SFEs of PH-only runs are smaller than that of RP-only runs and are closer to that of PH+RP runs. This suggests that photoionization is more important than radiation pressure in cloud destruction. For dense and massive clouds (M1E5R05 and M1E6R25), radiation pressure has a greater impact on cloud destruction.

addition to the net SFE, we similarly define photoevaporation and ejection efficiencies as $\varepsilon_{\text{ion}} \equiv M_{\text{ion,final}}/M_0$ and $\varepsilon_{\text{ej}} \equiv M_{\text{ej,final}}/M_0$, respectively, the latter of which counts both neutral and ionized gases. Note that these quantities are related by mass conservation through $\varepsilon_{\text{ej}} = 1 - \varepsilon_* = \varepsilon_{\text{ion}} + \varepsilon_{\text{ej,neu}}$, where $\varepsilon_{\text{ej,neu}} \equiv M_{\text{ej,neu,final}}/M_0$ and $\varepsilon_{\text{ion}} = \varepsilon_{\text{ej,ion}}$ since no ionized gas is left inside the box at the end of the runs.

Figure 5.6 plots as star symbols (a) the net SFE ε_* , (b) the ejection efficiency ε_{ej} , (c) the photoevaporation efficiency ε_{ion} , and (d) the neutral ejection efficiency $\varepsilon_{\text{ej,neu}}$ for all of our PH+RP runs as functions of the initial surface density; ε_* , ε_{ion} , and $\varepsilon_{\text{ej,neu}}$ are also tabulated in Columns 2–4 of Table 5.2. The size of the symbols represents the initial cloud mass, a convention that will be adopted throughout this chapter. The net SFE depends weakly on M_0 but strongly on Σ_0 , increasing from 0.04 for M1E5R50 to 0.51 for M1E5R05. For clouds with low Σ_0 and intermediate-to-high M_0 (M5E4R15, M1E5R20, M1E5R30, M1E5R40, M1E5R50, M1E6R45, M1E6R80), photoevaporation is effective in destroying clouds: $\varepsilon_{\text{ion}} \gtrsim 0.7$ and the resulting SFE is $\varepsilon_* \lesssim 0.2$. By contrast, the low mass clouds with $M_0 = 10^4 M_\odot$ (M1E4R02, M1E4R03, M1E4R05, M1E4R08) and/or high surface density (M1E5R10, M1E5R05, M1E6R25) clouds have $\varepsilon_{\text{ej,neu}} \gtrsim 0.1$, implying that dynamical ejection of neutral gas is non-negligible for disruption and quenching of further star formation in these clouds.

The effect of radiation feedback on cloud disruption is limited in the highest- Σ_0 clouds such as M1E4R02, M1E5R05 and M1E6R25. These reach $\varepsilon_* \gtrsim 0.4$ before the remaining gas is dispersed. This is due to a deep gravitational potential well, which outflowing gas must overcome to escape from the system (e.g., Dale et al. 2012). These clouds also have a comparatively dense and thick layer of recombining gas and dust that absorbs most ionizing photons, resulting in relatively inefficient photoevaporative mass loss (see Section 5.4.1). Thus, radiation pressure plays a relatively more important role

for the highest surface density clouds.

One can assess the relative (negative) impact of photoionization and radiation pressure feedback on star formation by comparing the net SFEs of the PH-only or RP-only runs with those of PH+RH models. Figure 5.7 plots ε_* of PH-only (red circles), RP-only (blue squares), and PH+RP (dark stars) models as a function of Σ_0 . Overall, the increasing trend of ε_* with Σ_0 is similar for all models. For most of our models, the net SFE of the PH-only run is smaller than that of the RP-only counterpart and closer to that of the PH+RP run, indicating that photoionization feedback plays a more important role than radiation pressure in disrupting the parent clouds. The two exceptions are the massive, high-surface density clouds (M1E5R05 and M1E6R25), for which the net SFE of the RP-only run is smaller than that of the PH-only run.

The net SFEs of the RP-only runs lie approximately on a single sequence as a function of Σ_0 , regardless of M_0 , also in accordance with the recent theoretical predictions of the regulation of star formation by the radiation pressure feedback alone (Raskutti et al. 2016; Thompson & Krumholz 2016). We quantitatively show in Appendix 5.B that our RP-only results are indeed in good agreement with the analytic predictions. Our net SFE is slightly lower than those obtained in the numerical simulations of Raskutti et al. (2016), which employed a grid-based moment method for radiation. Chapter 4 showed that this method does not adequately resolve the radiation field near individual star particles (because radiation sources have finite size), leading to more gas accretion and thus a higher SFE.

Figure 5.7 also shows that model M1E5R20_nofb (green triangle) in the absence of feedback converts 87% of the gas into stars over the course of evolution. The reason that even this no-feedback run has a non-zero ejection efficiency of $\varepsilon_{ej} = 0.13$ is that initial turbulence makes a small fraction of the gas gravitationally unbound. Raskutti et al. (2016) found that the initial

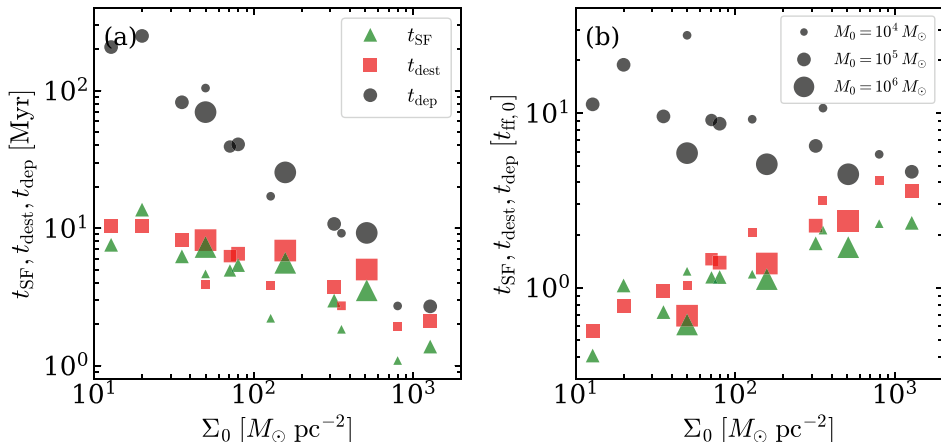


Figure 5.8 (a) Timescales for star formation $t_{\text{SF}} = t_{*,95\%} - t_{*,0}$ (triangles), cloud destruction $t_{\text{dest}} = t_{\text{neu},5\%} - t_{*,0}$ (squares), and effective gas depletion $t_{\text{dep}} = t_{\text{SF}}/\varepsilon_*$ (circles) for all PH+RP models as functions of the initial cloud surface density Σ_0 . (b) Same as (a) but with the timescales normalized by the initial freefall time $t_{\text{ff},0}$.

“turbulent outflow ejection” efficiency is $\varepsilon_{\text{ej,turb}} = 10\text{--}15\%$ for all models (see their Figure 17a). In principle, this can be used to derive an “adjusted” feedback-induced SFE of $\varepsilon_{*,\text{adj}} = \varepsilon_*/(1 - \varepsilon_{\text{ej,turb}})$.

Finally, we note that the feedback effects of photoionizing radiation and non-ionizing radiation on quenching star formation are not simply additive. If feedback effects were additive, the naive expectation would be $1/\varepsilon_{*,\text{PH+RP}} = 1/\varepsilon_{*,\text{PH}} + 1/\varepsilon_{*,\text{RP}}$. However, we find that the true value of $\varepsilon_{*,\text{PH+RP}}$ is 20–30% larger than this naive expectation.

5.3.3 Timescales for Star Formation and Cloud Destruction

The cloud lifetime is important to understanding the life cycle of GMCs within the context of other ISM phases, yet observational constraints on it remain quite uncertain (Heyer & Dame 2015). We use our simulations to directly measure the relevant timescales as follows. We define the star

Table 5.2. Simulation Results

Model (1)	ε_* (2)	ε_{ion} (3)	$\varepsilon_{\text{ej,neu}}$ (4)	$t_{*,0}$ (5)	t_{SF} (6)	t_{dest} (7)	t_{ion} (8)	$v_{\text{ej,neu}}$ (9)	$v_{\text{ej,ion}}$ (10)	$\langle f_{\text{ion}} \rangle$ (11)	$\langle q \rangle$ (12)
M1E5R50	0.04	0.95	0.02	0.52	0.41	0.56	0.60	8.3	24.4	0.19	61
M1E5R40	0.05	0.93	0.03	0.46	1.03	0.78	0.75	9.4	24.3	0.22	81
M1E5R30	0.08	0.89	0.04	0.44	0.72	0.95	0.98	7.8	23.9	0.24	116
M1E4R08	0.04	0.52	0.45	0.56	1.24	1.04	0.96	6.3	18.1	0.42	69
M1E6R80	0.10	0.89	0.02	0.33	0.62	0.69	0.74	10.7	26.3	0.37	320
M5E4R15	0.12	0.79	0.09	0.44	1.14	1.45	1.31	7.1	23.1	0.26	148
M1E5R20	0.13	0.81	0.07	0.40	1.15	1.39	1.32	7.9	24.1	0.26	203
M1E4R05	0.13	0.56	0.32	0.52	1.19	2.07	1.61	6.8	20.2	0.36	199
M1E6R45	0.22	0.73	0.06	0.27	1.12	1.37	1.44	13.2	28.6	0.37	753
M1E5R10	0.28	0.56	0.17	0.33	1.79	2.26	2.08	8.3	25.6	0.42	807
M1E4R03	0.20	0.47	0.34	0.44	2.13	3.16	2.48	6.0	20.9	0.36	402
M1E6R25	0.38	0.52	0.11	0.24	1.70	2.41	2.38	14.7	35.6	0.43	2032
M1E4R02	0.40	0.32	0.29	0.40	2.32	4.10	2.97	6.7	24.1	0.46	1630
M1E5R05	0.51	0.31	0.19	0.27	2.35	3.59	3.46	9.7	30.2	0.50	2950
M1E6R20_M128	0.15	0.79	0.07	0.42	0.92	1.13	1.26	8.7	23.3	0.25	261
M1E5R20_M512	0.12	0.82	0.07	0.38	1.35	1.53	1.39	7.6	24.2	0.26	188
M1E6R20_nofb	0.88	...	0.13	0.40	5.85	3.9

Note. — Column 1: model name. Column 2: net star formation efficiency. Column 3: photoevaporation efficiency. Column 4: neutral ejection efficiency. Column 5: time of first star formation (in units of $t_{\text{ff},0}$). Column 6: star formation duration $t_{\text{SF}} = t_{*,95\%} - t_{*,0}$ (units $t_{\text{ff},0}$). Column 7: timescale for cloud destruction $t_{\text{dest}} = t_{\text{neu},5\%} - t_{*,0}$ (units $t_{\text{ff},0}$). Column 8: timescale for photoevaporation (units $t_{\text{ff},0}$; Equation (5.12)). Column 9: time-averaged outflow velocity of the neutral gas (km s^{-1}). Column 10: time-averaged outflow velocity of the ionized gas (km s^{-1}). Column 11: time-averaged hydrogen absorption fraction (see Equation (5.8)). Column 12: time-averaged shielding factor. The fiducial model M1E5R20 is shown in bold.

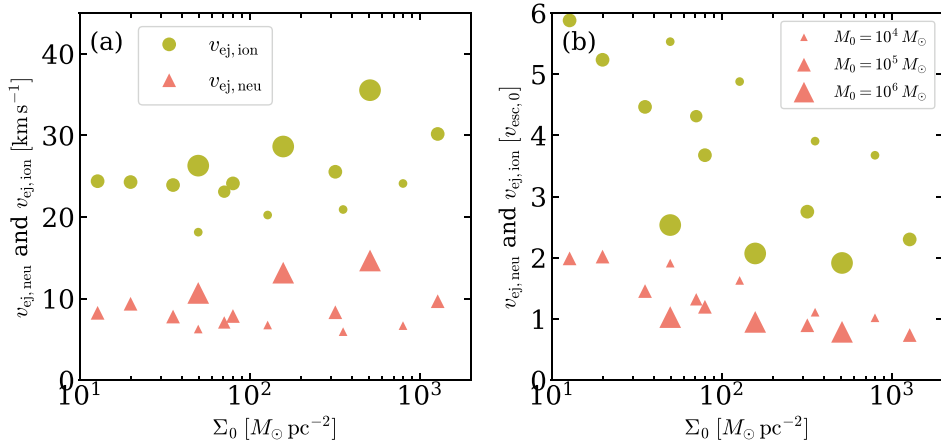


Figure 5.9 (a) Mean radial velocity of the outflowing neutral gas (triangles) and ionized gas (circles) for all PH+RP models as functions of the initial cloud surface density Σ_0 . (b) Same as (a) but normalized by the initial escape velocity $v_{\text{esc},0}$.

formation timescale in our models as the time taken to assemble 95% of the final stellar mass after the onset of radiation feedback, i.e., $t_{\text{SF}} \equiv t_{*,95\%} - t_{*,0}$. The approximate gas depletion timescale by star formation is then $t_{\text{dep}} = t_{\text{SF}}/\varepsilon_*$. We regard a cloud as being effectively destroyed at $t = t_{\text{neu},5\%}$ when only 5% of the initial cloud mass is left over as the neutral phase in the simulation box, with the other 95% transformed into stars, photoionized, or ejected. We define the destruction timescale as $t_{\text{dest}} = t_{\text{neu},5\%} - t_{*,0}$.⁶ In most cases, $t_{\text{dest}} > t_{\text{SF}}$,⁷ but generally the two timescales are very similar. Columns 5–7 of Table 5.2 list $t_{*,0}$, t_{SF} , and t_{dest} , respectively.

Figure 5.8 plots t_{SF} (triangles), t_{dest} (squares), and t_{dep} (circles) of our

⁶For the M1E4R08 model, we take t_{dest} as the time difference between $t_{\text{neu},5\%}$ and the time at which second sink particle formed, because the first star particle, with its small ionizing photon output rate $Q_i \sim 2.1 \times 10^{46} \text{ s}^{-1}$, has limited impact on the cloud evolution (see also Figure 5.10).

⁷In the M1E5R40 model, late-time star formation (roughly $\sim 10\%$ of the final stellar mass) occurs in a dense globule even after $t_{\text{neu},5\%}$.

PH+RP runs in units of Myr (left panel) and in units of the initial freefall time (right panel). In physical units, t_{SF} and t_{dest} increase from $\sim 1\text{--}3$ Myr in the densest clouds ($n_{\text{H},0} \gtrsim 500 \text{ cm}^{-3}$ and $\Sigma_0 \gtrsim 300 M_{\odot} \text{ pc}^{-2}$) to $\sim 8\text{--}14$ Myr in the lowest-density clouds ($n_{\text{H},0} \lesssim 10 \text{ cm}^{-3}$ and $\Sigma_0 \lesssim 20 M_{\odot} \text{ pc}^{-2}$). Relative to the freefall time, t_{SF} (t_{dest}) decreases from $\sim 2t_{\text{ff},0}$ ($\sim 4t_{\text{ff},0}$) in the dense clouds to $\sim 0.4t_{\text{ff},0}$ ($\sim 0.6t_{\text{ff},0}$) in the low-density clouds. Our result that $t_{\text{SF}} \lesssim 2t_{\text{ff},0}$ is consistent with the picture of rapid star formation envisaged by Elmegreen (2000). The depletion timescale decreases considerably with Σ_0 from 250 Myr for low- Σ_0 model (M1E5R40) to 2.7 Myr for high- Σ_0 models (M1E4R02 and M1E5R05).

5.3.4 Outflow Velocity

In the presence of ionizing radiation, the outflows in our simulations consist of both neutral and ionized gas, and it is interesting to measure the dependence of ejection velocities on cloud properties. We calculate the mass-weighted ejection velocities of neutral/ionized gas as

$$v_{\text{ej,neu/ion}} = \frac{p_{\text{ej,neu/ion,final}}}{M_{\text{ej,neu/ion,final}}}, \quad (5.1)$$

where

$$p_{\text{ej,neu/ion,final}} = \int dt \int_{\partial V} dA \rho_{\text{neu/ion}} (\mathbf{v} \cdot \hat{\mathbf{n}}) (\mathbf{v} \cdot \hat{\mathbf{r}}) \quad (5.2)$$

is the time-integrated total radial momentum of neutral/ionized outflowing gas with $\hat{\mathbf{r}}$ being the unit radial vector with respect to the stellar center of mass and $\hat{\mathbf{n}}$ being the unit vector normal to the surface area dA at the outer boundary of the box. These values are given in Columns 9 and 10 of Table 5.2.

Figure 5.9 plots $v_{\text{ej,neu}}$ (triangles) and $v_{\text{ej,ion}}$ (circles) in units of km s^{-1} (left panel) and in units of the initial escape velocity $v_{\text{esc},0}$ (right panel) for all the PH+RP runs. The outflow velocity of the ionized gas is $\sim 18\text{--}36 \text{ km s}^{-1}$ and larger than $v_{\text{esc},0}$ across the whole range of Σ_0 . In low-surface density

clouds, these supersonic outflows of the ionized gas are driven primarily by thermal pressure. Since ionized gas has low optical depth and hence high Edington ratios, its ejection in high-surface density clouds is further helped by radiation pressure, while strong gravity tends to reduce the outflow velocity.

The neutral gas is ejected at a typical velocity of $\sim 6\text{--}15\text{ km s}^{-1}$, about $\sim 2\text{--}4$ times smaller than the ejection velocity of the ionized gas. This is roughly consistent with the characteristic rocket velocity $\sim 5\text{--}10\text{ km s}^{-1}$ of cometary globules in a photoevaporation-dominated medium (e.g., Bertoldi & McKee 1990), although the outflow velocity is also affected by gravity as well as radiation pressure forces especially for high-surface density clouds. Note that $v_{\text{ej,neu}}/v_{\text{esc},0} \sim 0.7\text{--}2.0$ decreases slowly with increasing Σ_0 owing to gravity.

5.4 Mass Loss Processes

For all of our simulations, radiative stellar feedback leads to at least half of the original mass in the cloud being ejected. Thus, radiation from newly formed stars actively quenches future star formation. As Figure 5.6 shows, most of the ejected gas is in the ionized phase, especially for typical GMCs in normal disk galaxies with $\Sigma_0 \lesssim 10^2 M_\odot \text{ pc}^{-2}$ and $M_0 \gtrsim 10^5 M_\odot$. For high-density or low-mass clouds, ejection of the neutral phase is non-negligible, but $\varepsilon_{\text{ej,neu}}$ never exceeds $\varepsilon_{\text{ej,ion}}$. In this section, we first develop and calibrate a simple theoretical models of mass loss by photoevaporation. We then analyze the momentum injection in our models, including both ionized and neutral gas. These results for photoevaporation and momentum injection will be used in Section 5.5 to make predictions for the net SFEs and mass-loss efficiencies in comparison with our numerical results.

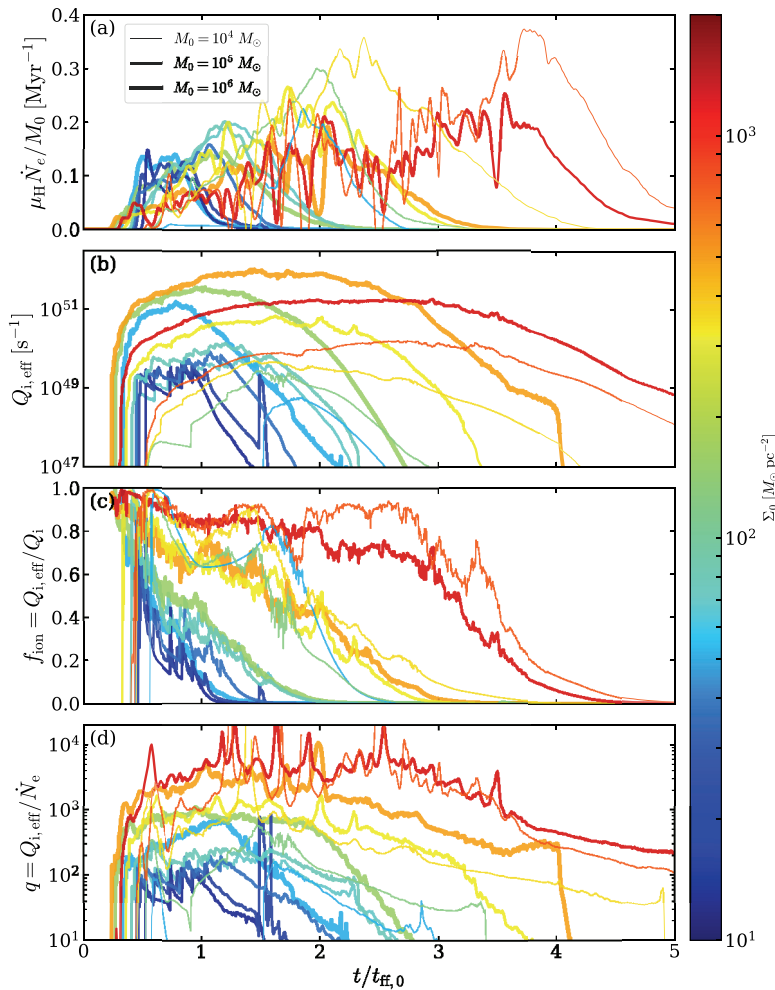


Figure 5.10 (a) Mass loss rate $\mu_{\text{H}}\dot{N}_{\text{e}}$ via photoevaporation normalized by the initial cloud mass M_0 , (b) total photoionization rate $Q_{\text{i,eff}}$, (c) fraction of ionizing photons absorbed by neutral hydrogen $f_{\text{ion}} = Q_{\text{i,eff}}/Q_{\text{i}}$, and (d) shielding factor $q = Q_{\text{i,eff}}/\dot{N}_{\text{e}}$ as functions of time. The line color and thickness respectively correspond to the surface density and mass of the initial cloud. The shielding factor is much larger than unity in all models, indicating that most ionizing photons are used in maintaining ionization equilibrium within the H II region rather than creating new ionized gas.

5.4.1 Mass Loss by Photoevaporation

We first consider the case in which star formation is quenched solely by photoevaporation. Ionizing photons emitted by star particles arrive at ionization fronts (IFs) after passing through an intervening volume in which the gas is nearly fully ionized, with a balance between ionization and recombination. Ionized gas created at IFs does not participate in star formation (provided it remains sufficiently exposed to radiation) and will be eventually pushed out of the cloud and simulation volume by thermal and radiation pressures. Here we use physical scaling arguments to estimate the net photoevaporation rate in a star-forming cloud.

Ionization Analysis

H II regions formed in our simulations are highly irregular in shape. The EM map is dominated by pillars, ridges, and cometary globules near the H II region peripheries, as Figure 5.5 illustrates. Each of these bright features marks the IF on the surface of an optically-thick, neutral gas structure that is facing the ionizing sources. These neutral structures are photoevaporated as the IF advances. Since the newly ionized gas can expand into the surroundings, the IFs are typically D-critical or of strong-D type, and the ionized gas streams off the IF at approximately the sound speed and forms an ionized boundary layer (e.g., Oort & Spitzer 1955; Kahn 1969; Elmergreen 1976; Bertoldi 1989). In addition to the bright IF regions, Figures 5.3-5.5 show that there is substantial diffuse ionized gas in the volume, filling the space between and beyond the filaments and clumps of neutral gas. Along some lines of sight from stellar sources, ionizing photons moving toward optically-thin regions produce a weak-R type IF that quickly propagates out of the simulation domain, such that in those directions the H II region is effectively density bounded. In other directions, lines of sight from ionizing sources propagate

through diffuse ionized gas until they end at an IF on the surface of dense neutral structure. As we will see below, almost all of the ionizations and recombinations in our simulations occur in the ionization-bounded Strömrgren volume (IBSV), and ionization and recombination are in global equilibrium.

The equation for net electron production integrated over the entire domain reads

$$\dot{N}_e = \int \mathcal{I} dV - \int \mathcal{R} dV, \quad (5.3)$$

where $\mathcal{I} = n_{\text{H}0}(c\mathcal{E}_i/h\nu_i)\sigma_{\text{H}0}$ is the photoionization rate per unit volume with c being the speed of light; $\mathcal{R} = \alpha_{\text{B}}n_en_{\text{H}+}$ is the recombination rate per unit volume, with $\alpha_{\text{B}} = 3.03 \times 10^{-13}(T/8000 \text{ K})^{-0.7} \text{ cm}^3 \text{ s}^{-1}$ being the case B recombination coefficient. The rate at which ionized gas is newly created within the domain (from ionizations exceeding recombinations) is $\dot{M}_{\text{ion}} = \mu_{\text{H}}\dot{N}_e$, where $\mu_{\text{H}} = 1.4m_{\text{H}}$ is the mean atomic mass per hydrogen. Part of this may go into an increase in the mass of ionized gas within the box, and part may go into escape of ionized gas from the domain: $\dot{M}_{\text{ion}} = \dot{M}_{\text{ion,box}} + \dot{M}_{\text{ion,ej}}$.

In our simulations, some fraction of the ionizing photons emitted by the stars are absorbed by neutral hydrogen, while others are absorbed by dust or escape from the simulation domain. Let $f_{\text{ion}} = 1 - f_{\text{esc,i}} - f_{\text{dust,i}}$ denote the fraction of ionizing photons absorbed by neutral hydrogen. Then, the total photoionization rate of neutral hydrogen inside the H II region can be written as

$$\int \mathcal{I} dV = f_{\text{ion}}Q_i \equiv Q_{\text{i,eff}}. \quad (5.4)$$

Newly-ionized gas is created at IFs, and we denote the total effective area of these IFs as A_i . Gas streams away from the IFs with typical number density n_i and characteristic velocity $c_i = (2.1 k_{\text{B}}T_{\text{ion}}/\mu_{\text{H}})^{1/2} = 10.0 \text{ km s}^{-1}$ (e.g., Bertoldi 1989). We thus write

$$\dot{N}_e \equiv c_i n_i A_i \quad (5.5)$$

for the rate of electron production at the IFs. Equation (5.5) may be thought of as defining the product $n_i A_i$ in terms of \dot{N}_e .

To reach the IFs, photons traverse a volume of nearly fully ionized gas that is undergoing recombination (which is approximately balanced by ionization; see below). If we define the effective path length through this ionized volume as H_i , we can write the total recombination rate as

$$\int \mathcal{R} dV \equiv \alpha_B n_i^2 A_i H_i. \quad (5.6)$$

With $n_i A_i$ defined via Equation (5.5), we can think of Equation (5.6) as defining the ratio A_i/H_i , which has units of length.

The volume of highly-ionized gas between the source and the IF acts as an insulator, absorbing photons that would otherwise reach the IF in order to balance recombination. We define the ratio of available ionizing photons to photons that actually reach the IF as a shielding factor:

$$q \equiv \frac{Q_{i,\text{eff}}}{\dot{N}_e} = 1 + \frac{\int \mathcal{R} dV}{\int \mathcal{I} dV - \int \mathcal{R} dV} = 1 + \frac{\alpha_B n_i H_i}{c_i}. \quad (5.7)$$

With this definition, $q = 1$ would imply all the ionizing photons are used to ionize neutrals at the IF, while $q \gg 1$ when most of the ionizing photons are shielded by the IBSV. The second term on the right-hand side of Equation (5.7), $\alpha_B n_i H_i / c_i$, represents the ratio of the characteristic flow timescale to the recombination timescale, or the number of recombinations occurring over the time it would take the flow to cross the IBSV.

Figure 5.10 plots the temporal histories of (a) the specific evaporation rate $\mu_H \dot{N}_e / M_0$, (b) the total photoionization rate $Q_{i,\text{eff}}$, (c) hydrogen absorption fraction of ionizing photons f_{ion} , and (d) the shielding factor q , for all of our PH+RP runs. Both the evaporation rate and photoionization rate reach peak values and then decline with time as the cloud is destroyed.

The hydrogen absorption fraction is largest in the early, embedded phase

of star formation and decreases with time as optical depth drops and most of the ionizing photons escape the computational box. Column (11) of Table 5.2 gives

$$\langle f_{\text{ion}} \rangle \equiv \frac{\int \dot{N}_e f_{\text{ion}} dt}{\int \dot{N}_e dt}, \quad (5.8)$$

where the angle brackets $\langle \rangle$ denote the \dot{N}_e -weighted temporal average over the whole simulation period after $t_{*,0}$ (when \dot{N}_e is nonzero). The value of $\langle f_{\text{ion}} \rangle$ ranges from 0.19 to 0.50. Overall, a larger fraction of ionizing radiation is absorbed by hydrogen in higher surface density clouds as H II regions undergo a relatively longer embedded phase.

Figure 5.10 shows that the shielding factor is much larger than unity for all models at all times. Column (12) of Table 5.2 gives \dot{N}_e -weighted time-averaged values $\langle q \rangle$, which ranges from 61 to 2950, increasing with mass and surface density. This is consistent with the expectation (cf. the right-hand side of Equation (5.7)) that a higher recombination rate in denser clouds, as well as longer path lengths in larger clouds, increases shielding and therefore reduces the efficiency of photoevaporation.

The fact that our clouds have $q \gg 1$ justifies the assumption of a global equilibrium between ionization and recombination

$$Q_{\text{i,eff}} = \int \mathcal{I} dV \approx \int \mathcal{R} dV = \alpha_{\text{B}} n_{\text{i}}^2 A_{\text{i}} H_{\text{i}}. \quad (5.9)$$

We solve this to obtain $n_{\text{i}} \approx [Q_{\text{i,eff}}/(\alpha_{\text{B}} A_{\text{i}} H_{\text{i}})]^{1/2}$, and from Equation (5.7) we obtain the shielding factor

$$q \approx \frac{\alpha_{\text{B}} n_{\text{i}} H_{\text{i}}}{c_{\text{i}}} \approx \frac{\alpha_{\text{B}}^{1/2}}{c_{\text{i}}} \left(\frac{Q_{\text{i,eff}} H_{\text{i}}}{A_{\text{i}}} \right)^{1/2}, \quad (5.10)$$

while Equation (5.5) yields an approximate expression for the evaporation rate:

$$\dot{N}_e \approx \frac{c_{\text{i}}}{\alpha_{\text{B}}^{1/2}} \left(\frac{Q_{\text{i,eff}} A_{\text{i}}}{H_{\text{i}}} \right)^{1/2}. \quad (5.11)$$

The timescale for the photoevaporative mass loss tends to be longer in high surface density clouds, similarly to t_{dest} and t_{SF} . Despite the fact that they have a relatively high hydrogen absorption fraction and a small escape fraction of ionizing photons, the mass loss is inefficient because of large q . In addition, the motions of sink particles and the associated neutral envelopes cause a sudden change in the optical depth of ionizing photons. As a result, the size and shape of the H II region and photoevaporation rate fluctuate with time until they completely exhaust accretion flows and break out to larger radii at late time (e.g., Peters et al. 2010; Dale et al. 2012).

We shall define the cloud photoevaporation timescale as

$$t_{\text{ion}} \equiv \frac{N_e}{\langle \dot{N}_e \rangle} = \frac{N_e^2}{\int \dot{N}_e^2 dt}, \quad (5.12)$$

where $N_e = \int \dot{N}_e dt$ is the integrated number of electrons. Column (8) of Table 5.2 lists the value of t_{ion} for all models. Our numerical simulations show that this timescale is typically comparable to the initial freefall timescale for the cloud, $t_{\text{ff},0}$.

Constraints from Simulations

Once $Q_{\text{i,eff}}$, A_{i} , and H_{i} are known, Equation (5.11) can be used to estimate the photoevaporation mass loss rate in star-forming clouds. It is natural to expect that the total area A_{i} of the ionization front scales with the surface area $4\pi R_0^2$ of the cloud, while the thickness H_{i} of the IBSV scales with the cloud radius R_0 . Our numerical results, based on measured $Q_{\text{i,eff}}$, \dot{N}_e , and $\int n_e^2 dV / \int n_e dV \rightarrow n_i$, show that time-averaged values of $A_{\text{i}}/(4\pi R_0^2) = \dot{N}_e/(4\pi n_i c_{\text{i}} R_0^2)$ and $H_{\text{i}}/R_0 \approx c_{\text{i}} Q_{\text{i,eff}}/(\alpha_{\text{B}} n_i \dot{N}_e R_0)$ are indeed of order unity. In detail, the time-averaged values of $A_{\text{i}}/(4\pi R_0^2)$ and H_{i}/R_0 are in the ranges 0.5–2.0 and 0.6–1.9, respectively. Motivated by Equation (5.11), together with the characteristic dynamical time of clouds, we

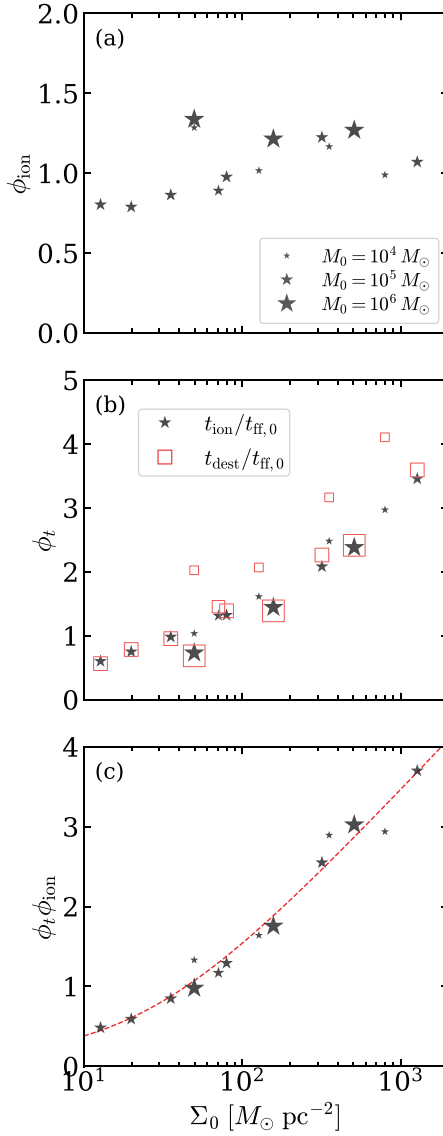


Figure 5.11 Dependence on Σ_0 of (a) the dimensionless ionization rate ϕ_{ion} , (b) the dimensionless photoevaporation timescale ϕ_t for clouds, and (c) the product $\phi_{\text{ion}}\phi_t$, displayed as star symbols for all PH+RP models. In (b), the cloud destruction timescale $t_{\text{dest}}/t_{\text{ff},0}$ is shown for comparison as open squares. The red dashed line in (c) is our fit to the numerical results (see Equation 5.16).

introduce the dimensionless evaporation rate ϕ_{ion} and evaporation timescale ϕ_t defined as

$$\phi_{\text{ion}} \equiv \langle \dot{N}_e \rangle \times \frac{\alpha_{\text{B}}^{1/2}}{c_i Q_{i,\text{max}}^{1/2} R_0^{1/2}}, \quad (5.13)$$

$$\phi_t \equiv \frac{t_{\text{ion}}}{t_{\text{ff},0}}, \quad (5.14)$$

where $Q_{i,\text{max}}$ is the maximum rate of the total ionizing photons over the lifetime of a star cluster (which is directly related to the SFE).

Figure 5.11 plots ϕ_{ion} and ϕ_t from our PH+RP models as star symbols. Note that $\phi_{\text{ion}} \sim 0.79\text{--}1.34$, roughly independent of the cloud mass and surface density. From the definition in Equation (5.13), an order-unity value of ϕ_{ion} implies a mass-loss rate from clouds in which the characteristic velocity is the ionized-gas sound speed, the characteristic spatial scale is the size of the cloud, and the characteristic density is consistent with ionization-recombination equilibrium; comparison to Equation (5.11) implies that $\langle (Q_{i,\text{eff}}/Q_{i,\text{max}})(A_i/H_i) \rangle^{1/2} / R_0^{1/2} \approx \phi_{\text{ion}} \sim 1$.

Figure 5.11 shows that ϕ_t ranges between 0.6 to 3.5 and increases with Σ_0 . A typical photoevaporation timescale is thus twice the freefall time in the cloud. Plotted as open squares is the normalized destruction timescale $t_{\text{dest}}/t_{\text{ff},0}$. This is very close to ϕ_t for low-density, massive clouds, suggesting that these clouds are destroyed primarily by photoevaporation. Low-mass and/or high-surface density clouds have a destruction timescale somewhat longer than the evaporation timescale, suggesting that cloud destruction involves ejection of neutrals (accelerated by a combination of rocket effect and radiation pressure) as well as ions.

The total number of electrons (and hence ions) created by photoevaporation over the lifetime of the cloud is $N_e = \int \dot{N}_e dt \equiv \langle \dot{N}_e \rangle t_{\text{ion}}$. The total mass

photoevaporated from the cloud can therefore be expressed as

$$M_{\text{ion}} = \mu_{\text{H}} N_e = \phi_t \phi_{\text{ion}} \frac{\mu_{\text{H}} c_i Q_{\text{i,max}}^{1/2} R_0^{1/2} t_{\text{ff},0}}{\alpha_{\text{B}}^{1/2}}. \quad (5.15)$$

Since the right-hand side is proportional to $M_{*,\text{final}}^{1/2}$, this shows that the fraction of mass photoevaporated over the cloud lifetime, M_{ion}/M_0 , scales as the square root (rather than linearly) of the star formation efficiency. We discuss this result further in Section 5.5.1. Figure 5.11(c) plots the product $\phi_t \phi_{\text{ion}}$ as a function of Σ_0 . We fit the numerical results as

$$\phi_t \phi_{\text{ion}} = c_1 + c_2 \log_{10}(S_0 + c_3), \quad (5.16)$$

where $c_1 = -2.89$, $c_2 = 2.11$, $c_3 = 25.3$, and $S_0 = \Sigma_0/(M_{\odot} \text{pc}^{-2})$, which is plotted as the red dashed line in Figure 5.11(c).

5.4.2 Momentum Injection

In our simulations, both neutral and ionized gas that does not collapse to make stars is eventually ejected, carrying both mass and momentum out of the cloud. In this section, we characterize the efficiency of the radial momentum injection by computing net momentum yields. We also separately assess the mean thermal and radiation pressure forces in the radial direction, where

$$\mathbf{f}_{\text{thm}} = -\nabla P, \quad \mathbf{f}_{\text{rad}} = \frac{n_{\text{H}^0} \sigma_{\text{H}^0}}{c} \mathbf{F}_{\text{i}} + \frac{n_{\text{H}} \sigma_{\text{d}}}{c} (\mathbf{F}_{\text{i}} + \mathbf{F}_{\text{n}}) \quad (5.17)$$

are the thermal and radiation pressure forces per unit volume, for \mathbf{F}_{i} and \mathbf{F}_{n} the ionizing and non-ionizing radiation fluxes, respectively.

Net Momentum Yield

When clouds are disrupted by feedback, the resulting outflow is roughly spherical, so it is useful to measure the total radial momentum of the ejected material induced by feedback. In Section 5.5, we shall use the momentum

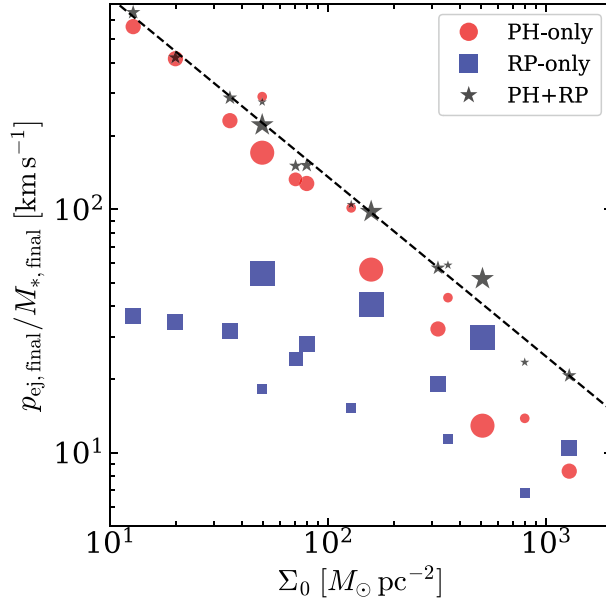


Figure 5.12 Total radial momentum yields $p_{\text{ej,final}}/M_{*,\text{final}}$ in the PH-only (circles), RP-only (squares), and PH+RP runs (stars), as a function of the cloud surface density Σ_0 . The dashed line shows the power-law best-fit to the numerical results of the PH+RP runs (Equation 5.18).

ejected per unit mass of stars formed, $p_*/m_* = p_{\text{ej,final}}/M_{*,\text{final}}$, which here we term the net “momentum yield.”

Figure 5.12 plots the p_*/m_* in the PH-only (circles), RP-only (squares), and PH+RP (stars) models as a function of Σ_0 .⁸ We measure this by integrating the radial component of the momentum flux over the outer boundary of the simulation and over all time, $\int dt \int_{\partial V} dA \rho \mathbf{v} \cdot \hat{\mathbf{n}} \mathbf{v} \cdot \hat{\mathbf{r}}$, where $\hat{\mathbf{n}}$ is the normal to area dA . The PH-only runs have momentum yields higher than the RP-only results except for models M1E5R05 and M1E6R25, and close to the PH+RP results. Similarly to Figure 5.7, this implies that thermal pressure in-

⁸A small fraction of the outflow momentum is associated with the initial radial component of the turbulent outflow. For the fiducial cloud with no radiation feedback, the final outflow momentum is 3% of that of the PH+RP run.

duced by photoionization controls the dynamics of H II regions in low surface density clouds, while radiation pressure is more important in dense, massive clouds. For the PH+RP and PH-only models, most of the outflow momentum is deposited in the ionized rather than neutral gas. We find that the total momentum yields in the PH+RP runs are well described by a power-law relationship

$$p_*/m_* = \frac{p_{\text{ej,final}}}{M_{*,\text{final}}} = 135 \text{ km s}^{-1} \left(\frac{\Sigma_0}{10^2 M_\odot \text{ pc}^{-2}} \right)^{-0.74}, \quad (5.18)$$

shown as the dashed line in Figure 5.12.

We note that by adopting a light-to-mass ratio that is time-independent, our numerical results are likely to overestimate the true feedback strength, especially for clouds with the destruction timescale longer than $t_{\text{SN}} = 3 \text{ Myr}$ or $t_{\text{UV}} = 8 \text{ Myr}$. Even with this overestimation, our results show that the momentum injection to the large-scale ISM from both ionizing and non-ionizing radiation feedback is substantially smaller than that from supernovae feedback, $p_*/m_* \sim 10^3 \text{ km s}^{-1}$ (e.g., Kim & Ostriker 2015; Kim et al. 2017a). Thus, while momentum injection from radiation feedback is quite important on the spatial scale of individual clouds and early life of clusters, it is subdominant in the large-scale ISM compared to other forms of massive-star momentum injection, and is therefore not expected to be important in regulating either large-scale ISM pressure and star formation rates (e.g. Ostriker & Shetty 2011; Kim et al. 2013) or galaxy formation (e.g. Naab & Ostriker 2017).

Efficiency of Radial Momentum Injection

Dynamical expansion of a spherical, embedded H II region in a uniform medium is well described by the thin-shell approximation. Force balance $\mathbf{f}_{\text{thm}} + \mathbf{f}_{\text{rad}} = 0$ holds in the interior (Draine 2011b) and most of the swept-up gas is compressed into a thin shell that expands due to the contact forces

on it. The effective momentum injection rate from gas pressure and direct radiation pressure are $\rho_i c_1^2 A_i$ and L/c , respectively (Krumholz & Matzner 2009; Kim et al. 2016). The former expression multiplied by a factor two has also been applied for blister H II regions, assuming that in addition to thermal pressure the cloud back-reacts to photoevaporation from a D-critical IF with $\rho_i c_1^2 A_i = \dot{M}_{\text{ion}} c_1$ (e.g., Matzner 2002; Krumholz et al. 2006). In analytic solutions, the ionized-gas density ρ_i estimate assumes uniform density and ionization equilibrium. For either embedded or blister H II regions, this leads to an expression for momentum injection that is given by Equation (5.11) for \dot{N}_e multiplied by $\mu_{\text{H}c_1}$ times an order-unity factor. For an idealized, dust-free, spherical, embedded H II region, the theoretical point of comparison for the gas pressure force is $\mu_{\text{H}} c_1^2 (12\pi Q_i R_0 / \alpha_{\text{B}})^{1/2}$.

In reality, H II regions possess many holes and ionizing sources are widely distributed in space. The momentum injection is then expected to be less efficient than in the idealized spherical case for the following reasons. First, the non-spherical distribution of radiation sources leads to momentum injection cancellation. Second, for applying back-reaction forces, normal vectors to irregular-shaped cloud surfaces have non-radial components with respect to the cluster center. Third, radiation escapes through holes (see also Dale 2017; Raskutti et al. 2017). Nevertheless, the results in Section 5.4.1 show that the numerically-computed mass-loss rates from photoevaporation are similar to the predictions from dimensional-analysis scaling arguments, so we may analogously expect the radial momentum injection rate from thermal pressure to be comparable to $\dot{M}_{\text{ion}} c_1$. This will be lower than the idealized spherical momentum injection because dust absorption and escape of radiation reduce $Q_{i,\text{eff}}$ below Q_i . Similarly, the radiation pressure applied to the cloud would be reduced to $(1 - f_{\text{esc}})L/c$ by the escape of radiation, where $f_{\text{esc}} = (L_{i,\text{esc}} + L_{n,\text{esc}})/L$ is the overall escape fraction of UV radiation; the total radiation force may be further reduced by lack of spherical symmetry.

To determine the degree of reduction in the radial momentum injection, we calculate the time-averaged, normalized thermal pressure force

$$\phi_{\text{thm}} \equiv \frac{\int_{t_i}^{t_f} \int \mathbf{f}_{\text{thm}} \cdot \hat{\mathbf{r}} dV dt}{\int_{t_i}^{t_f} \mu_{\text{H}} c_i^2 (12\pi Q_i R_0 / \alpha_{\text{B}})^{1/2} dt}, \quad (5.19)$$

$$\phi'_{\text{thm}} \equiv \frac{\int_{t_i}^{t_f} \int \mathbf{f}_{\text{thm}} \cdot \hat{\mathbf{r}} dV dt}{\int_{t_i}^{t_f} \dot{M}_{\text{ion}} c_i dt} \quad (5.20)$$

and normalized radiation pressure force

$$\phi_{\text{rad}} \equiv \frac{\int_{t_i}^{t_f} \int \mathbf{f}_{\text{rad}} \cdot \hat{\mathbf{r}} dV dt}{\int_{t_i}^{t_f} L/c dt}, \quad (5.21)$$

$$\phi'_{\text{rad}} \equiv \frac{\int_{t_i}^{t_f} \int \mathbf{f}_{\text{rad}} \cdot \hat{\mathbf{r}} dV dt}{\int_{t_i}^{t_f} (1 - f_{\text{esc}}) L/c dt}, \quad (5.22)$$

where the range of time integration is taken as $(t_i, t_f) = (t_{*,0}, t_{\text{ej},95\%})$.⁹

In the above, we consider both the radial momentum injection from thermal pressure and radiation pressure relative to the maximum for a spherical shell, and relative to the actual material and radiation momentum available.

Figure 5.13 plots the normalized forces ϕ_{thm} (circles), ϕ'_{thm} (diamonds), ϕ_{rad} (squares), and ϕ'_{rad} (triangles) averaged over the time interval $(t_{*,0}, t_{\text{ej},95\%})$ as functions of Σ_0 . There is significant reduction in both the gas and radiation pressure forces compared to the prediction for the “spherical maximum”; the normalized gas pressure force ϕ_{thm} is in the range 0.10–0.19 with a mean value 0.13, roughly independent of Σ_0 ; ϕ_{rad} is as small as 0.06 for model M1E5R50 and increases to 0.27 for high surface-density clouds. The values of ϕ'_{thm} range from 0.67 to 1.26, suggesting that the time-averaged radial momentum injection from thermal pressure force is within $\sim 30\%$ of the naive estimate $\dot{M}_{\text{ion}} c_i$. The values of ϕ'_{rad} are slightly larger than ϕ_{rad} and in the

⁹The cumulative momentum injection efficiencies $\phi_{\text{thm}/\text{rad}}$ become smaller for larger t_f since most photons escape at late time. For example, $t_f = t_{*,0} + t_{\text{dest}}$ increases $\phi_{\text{thm}/\text{rad}}$ by $\sim 30\text{--}50\%$ compared to the case with $t_f = t_{\text{ej},95\%} (> t_{\text{dest}})$.

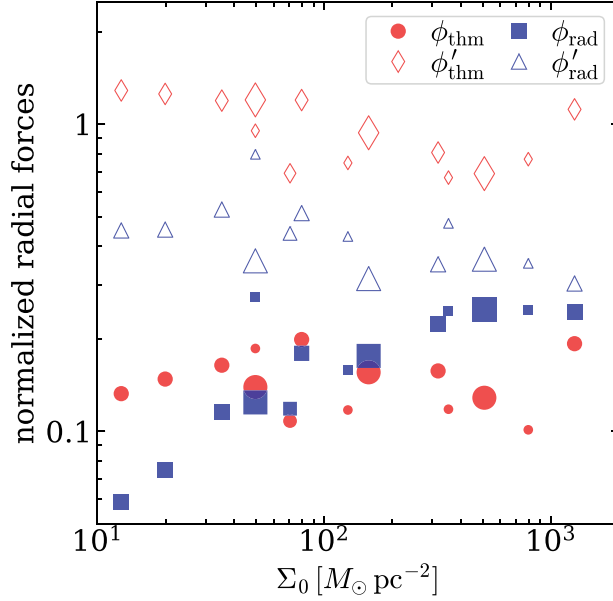


Figure 5.13 Average rates of the radial momentum injection due to gas pressure normalized by $\mu_{\text{H}}c_1^2(12\pi Q_i R_0/\alpha_{\text{B}})^{1/2}$ (circles) and by $\dot{M}_{\text{ion}}c_1$ (diamonds), due to radiation pressure normalized by L/c (squares) and $(1 - f_{\text{esc}})L/c$ (triangles) for all the PH+RP models (see Equations (5.19)–(5.22)).

range 0.3–0.5, indicating that the momentum injection by radiation pressure force is reduced by a factor of ~ 2 –3 by flux cancellation alone.¹⁰

Finally, we evaluate the relative importance of gas and radiation pressure forces in radial momentum injection for the PH+RP models. Figure 5.14 plots the total injected momentum from gas (circles) and radiation (squares) pressure forces per unit mass of stars formed:

$$\frac{p_{\text{ej,thm}}}{M_{*,\text{final}}} \equiv \frac{\iint \mathbf{f}_{\text{thm}} \cdot \hat{\mathbf{r}} dV dt}{M_{*,\text{final}}}, \quad (5.23)$$

¹⁰Relatively high values of ϕ_{rad} and ϕ'_{rad} for M1E4R08 model are likely caused by the fact that feedback is dominated by a single cluster particle that accounts for 75% of the final stellar mass.

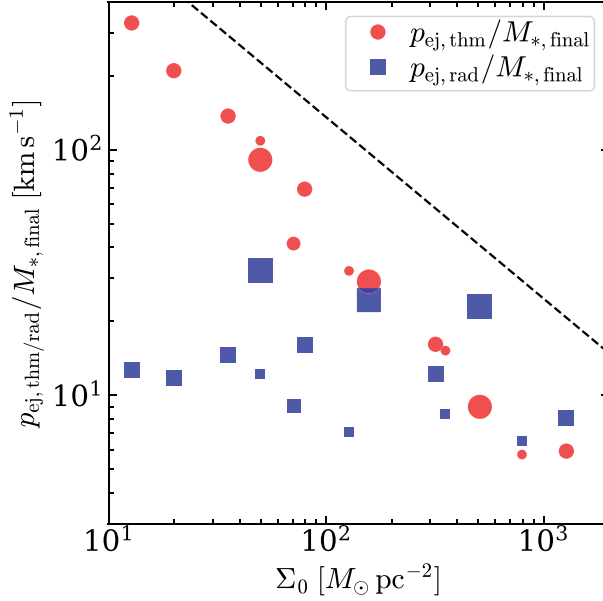


Figure 5.14 Injected radial momentum due to gas pressure (circles) and radiation pressure (squares) forces normalized by the final stellar mass $M_{*,\text{final}}$ for all the PH+RP models (see Equations (5.23) and (5.24)). The fit to the total momentum yield, Equation (5.18), is shown for comparison as a dashed line.

$$\frac{p_{\text{ej,rad}}}{M_{*,\text{final}}} \equiv \frac{\iint \mathbf{f}_{\text{rad}} \cdot \hat{\mathbf{r}} dV dt}{M_{*,\text{final}}}. \quad (5.24)$$

The results show trends similar to those exhibited by the total radial momentum yield in Figure 5.12 for models PH vs. RP; while the momentum injection due to gas pressure dominates in low surface density clouds, radiation pressure takes over for clouds with $\Sigma_0 \gtrsim 500 M_\odot \text{pc}^{-2}$. Our numerical results are consistent with the qualitative trend in the previous analytic models (Krumholz & Matzner 2009; Fall et al. 2010; Murray et al. 2010; Kim et al. 2016) in which radiation pressure becomes relatively more important compared to ionized-gas pressure for more massive, high surface density clouds.

Comparison of the dashed line (Equation (5.18)) and symbols in Fig-

ure 5.14 shows that the sum of injected momentum from gas and radiation pressure forces $p_{\text{ej,thm}} + p_{\text{ej,rad}}$ is not necessarily equal to the total momentum of outflowing gas $p_{\text{ej,final}}$. This difference arises because of the additional centrifugal and gravitational acceleration that contributes significantly to the latter.

5.5 Models for Cloud Dispersal and SFE

In this section, we use the photoevaporation rate and the momentum yield presented in the preceding section to develop semi-analytic models for cloud dispersal. We consider two models. First, we use the expected physical scaling relationship between photoevaporation and star formation efficiency (see Equation 5.15) to obtain a prediction for the SFE in the case that cloud destruction is mostly via ionization. In the second model, we use our numerical results for momentum injection per unit mass of stars formed to determine the SFE necessary to eject the remaining material (both ions and neutrals) from the cloud.

5.5.1 Destruction by Photoevaporation

We first consider a situation where the gas left over from star formation is all evaporated by photoionization. In this case, mass conservation requires

$$1 = \varepsilon_* + \varepsilon_{\text{ion}}, \quad (5.25)$$

where $\varepsilon_{\text{ion}} = M_{\text{ion}}/M_0 = \mu_{\text{H}}N_{\text{e}}/M_0$.

Using Equation (5.15), we express ε_{ion} as

$$\varepsilon_{\text{ion}} = \phi_t \phi_{\text{ion}} \left(\frac{\Sigma_{\text{ion}}}{\Sigma_0} \right) \varepsilon_*^{1/2}, \quad (5.26)$$

where

$$\Sigma_{\text{ion}} = \mu_{\text{H}\text{C}\text{i}} \left(\frac{\Xi}{8G\alpha_{\text{B}}} \right)^{1/2} \quad (5.27)$$

$$= 140 \left(\frac{\Xi}{5.05 \times 10^{46} \text{ s}^{-1} M_{\odot}^{-1}} \right)^{1/2} \left(\frac{T_{\text{ion}}}{8000 \text{ K}} \right)^{0.85} M_{\odot} \text{ pc}^{-2}, \quad (5.28)$$

with $\Xi = Q_{\text{i,max}}/M_{*,\text{final}}$ being the conversion factor between stellar mass and ionizing photon output. Since ϕ_{ion} is roughly constant in our numerical results, Equation (5.26) implies that the evaporation efficiency depends linearly on the duration (relative to t_{ff}) of photoevaporation, ϕ_t (Equation (5.14)), and the square root of the SFE, and inversely on the cloud surface density Σ_0 . The characteristic surface density Σ_{ion} can be regarded as a constant for most of the models since $M_{*,\text{final}} > 10^3 M_{\odot}$, while it varies sensitively with $M_{*,\text{final}}$ in models with $M_{*,\text{final}} < 10^3 M_{\odot}$, as described in Section 5.2.1. The dependence of ε_{ion} on $\varepsilon_*^{1/2}$ (rather than ε_*) is caused by shielding within the IBSV, which makes photoevaporation inefficient. Most photons are used up in offsetting recombination within the H II region, rather than in eroding neutral gas to create new ions at IFs.

We solve Equations (5.25) and (5.26) for ε_* to obtain

$$\varepsilon_* = \left(\frac{2\xi}{1 + \sqrt{1 + 4\xi^2}} \right)^2, \quad (5.29)$$

where $\xi \equiv \Sigma_0/(\phi_t\phi_{\text{ion}}\Sigma_{\text{ion}})$. In the limit $\xi \ll 1$, $\varepsilon_* \approx \xi^2 = [\Sigma_0/(\phi_t\phi_{\text{ion}}\Sigma_{\text{ion}})]^2$, while in the limit $\xi \gg 1$, $\varepsilon_* \approx 1 - 1/\xi = 1 - \phi_t\phi_{\text{ion}}\Sigma_{\text{ion}}/\Sigma_0$. The limiting behavior shows that photoevaporation becomes very efficient for destroying clouds when $\Sigma_0 \lesssim \Sigma_{\text{ion}}$.

Inserting the fit for $\phi_t\phi_{\text{ion}}$ of Equation (5.16) in Equation (5.29) allows us to calculate the net SFE as a function of Σ_0 . The resulting ε_* and ε_{ion} are compared to the numerical results as dashed lines in Figure 5.6(a) and (c). For low-surface density and massive clouds with $\varepsilon_{\text{ion}} \gtrsim 0.7$, the semi-analytic

ε_* agrees with the numerical results extremely well. The agreement is less good, however, for high-surface density ($\Sigma_0 \gtrsim 300 M_\odot \text{ pc}^{-2}$) or low-mass ($M_0 = 10^4 M_\odot$) clouds for which neutral gas ejection cannot be ignored; we address this next.

5.5.2 Destruction by Dynamical Mass Ejection

We consider the general case in which radiative feedback from star formation exerts combined thermal and radiation pressure forces on the surrounding gas. The gas is ejected from the cloud, quenching further star formation. In our simulations, the momentum ejected from the computational domain also includes a small contribution from the initial turbulence, which ejects a mass fraction $\varepsilon_{\text{ej,turb}} = M_{\text{ej,turb}}/M_0 \sim 0.1$ when the cloud is initially marginally bound.

Let v_{ej} denote the characteristic ejection velocity of the outgoing gas, and let p_*/m_* denote the momentum per stellar mass injected by feedback. The total momentum of the ejected gas can be written as

$$p_{\text{ej,tot}} = (1 - \varepsilon_*)M_0v_{\text{ej}} = (p_*/m_*)\varepsilon_*M_0 + \varepsilon_{\text{ej,turb}}M_0v_{\text{ej}}. \quad (5.30)$$

We divide the both sides of Equation (5.30) by M_0v_{ej} to obtain

$$\varepsilon_* = \frac{1 - \varepsilon_{\text{ej,turb}}}{1 + (p_*/m_*)/v_{\text{ej}}}. \quad (5.31)$$

From the results of model `M1E5R20_nofb` (see Table 5.2), we take $\varepsilon_{\text{ej,turb}} = 0.13$.¹¹ For v_{ej} , we take the mass-weighted outflow velocity $(\varepsilon_{\text{ej,neu}}v_{\text{ej,neu}} + \varepsilon_{\text{ej,ion}}v_{\text{ej,ion}})/\varepsilon_{\text{ej}}$, which is found to be roughly constant for fixed M_0 with mean values 15, 23, 29 km s^{-1} for $M_0 = 10^4, 10^5, 10^6 M_\odot$, respectively. Equation (5.31) gives ε_* as functions of M_0 and Σ_0 once p_*/m_* , v_{ej} and $\varepsilon_{\text{ej,turb}}$

¹¹Similar to our `M1E5R20_nofb` model, Raskutti et al. (2016) ran a suite of ‘no-feedback’ simulations and found that clouds with $\alpha_{\text{vir},0} = 2$ have roughly the same turbulence ejection efficiencies $0.10 < \varepsilon_{\text{ej,turb}} < 0.15$ regardless of M_0 and Σ_0 .

are specified. A fit to the momentum yield p_*/m_* from our numerical results as a function of Σ_0 is given in Equation (5.18). Altogether, Equation (5.31) then gives ε_* as a function of M_0 and Σ_0 . For $p_*/m_* \gg v_{\text{ej}}$ and $\varepsilon_{\text{ej,turb}} \ll 1$, the predicted scaling dependence is $\varepsilon_* \sim v_{\text{ej}}/(p_*/m_*) \propto v_{\text{ej}}\Sigma_0^{3/4}$.

Figure 5.6 overplots as solid lines the resulting (a) net SFE ε_* , (b) ejection efficiency $\varepsilon_{\text{ej}} = 1 - \varepsilon_*$, (c) photoevaporation efficiency ε_{ion} calculated from Equation (5.26), and (d) neutral ejection efficiency $\varepsilon_{\text{ej,neu}} = \varepsilon_{\text{ej}} - \varepsilon_{\text{ion}}$. The line thickness indicates the initial cloud mass. Overall, our semi-analytic model for the dynamical mass ejection reproduces the net SFE of the simulations fairly well, with the average difference of 0.03. The model also explains the increasing tendency of ε_* with increasing M_0 . This weak dependence of the semi-analytic ε_* on M_0 comes directly from v_{ej} , indicating that stronger feedback is required to unbind gas in a more massive cloud (e.g., Kim et al. 2016; Rahner et al. 2017). A drop in the photoevaporation efficiency with decreasing Σ_0 for $M_0 = 10^4 M_\odot$ and $\Sigma_0 \lesssim 10^2 M_\odot \text{pc}^{-2}$ is caused by the steep dependence of Ξ on $M_{*,\text{final}}$ below $10^3 M_\odot$, as mentioned above.

5.6 Summary and Discussion

In this work, we have used our new implementation of adaptive ray tracing in the *Athena* magnetohydrodynamics code to simulate star cluster formation and the effects of radiation feedback on turbulent GMCs. We consider a suite of clouds (initially marginally bound) with mass $M_0 = 10^4\text{--}10^6 M_\odot$ and radius $R_0 = 2\text{--}80 \text{pc}$; the corresponding range of the surface density is $\Sigma_0 \approx 13\text{--}1300 M_\odot \text{pc}^{-2}$. The primary goals of this chapter are to understand the role of (ionizing and non-ionizing) UV radiation feedback in controlling the net SFE and GMC lifetime and to assess the relative importance of photoionization and radiation pressure in various environments. We augment and compare our numerical results with semi-analytic models.

Our main findings are summarized as follows.

5.6.1 Summary

1. *Evolutionary stages*

All clouds in our simulations go through the following evolutionary stages (Figure 5.3), with some overlap and varying duration. (1) The initial turbulence creates filaments, and within these denser clumps condense. Some clumps undergo gravitational collapse and form star particles representing subclusters. (2) Individual H II regions form around each subcluster, growing towards directions of low optical depth until they merge and break out of the cloud. Simultaneously, both low- and high-density gas is accelerated away from the radiation sources due to thermal and radiation pressures. (3) At late stages of evolution the brightest EM features are small globules, pillars, and ridges marking individual IFs at the periphery of the H II region, quite similar to observed clouds (Figure 5.5). (4) At the end of the simulation, all of the gas has either collapsed into stars or been dispersed, flowing out of the computational domain.

2. *Timescales*

Cloud destruction takes $\sim 2\text{--}10$ Myr after the onset of massive star formation feedback (Figure 5.8(a)). In units of the freefall time, the destruction timescale is in the range $0.6 < t_{\text{dest}}/t_{\text{ff},0} < 4.1$ and systematically increases with Σ_0 (Figure 5.8(b)). The timescale for star formation is comparable to or somewhat smaller than the destruction timescale. The effective gas depletion timescale ranges from 250 Myr to 2.7 Myr, sharply decreasing with increasing Σ_0 .

3. *Star formation and mass loss efficiencies*

We examine the dependence on the cloud mass and surface density of the net SFE ε_* , photoevaporation efficiency ε_{ion} , and mass ejection efficiency ε_{ej} (Figure 5.6). The SFE ranges over $\varepsilon_* = 0.04\text{--}0.51$, increasing strongly with the initial surface density Σ_0 while increasing weakly with the initial cloud mass M_0 . Photoevaporation accounts for more than 70% of mass loss for clouds with $M_0 \gtrsim 10^5 M_\odot$ and $\Sigma_0 \lesssim 10^2 M_\odot \text{pc}^{-2}$. The ejection of neutral gas mass by thermal and radiation pressures also contributes in quenching further star formation in low-mass and high-surface density clouds. The comparison of the net SFE among the models in which we turn on and off photoionization and radiation pressure suggests that photoionization is of greater importance in destroying GMCs in normal disk galaxies, whereas radiation pressure is more effective in regulating star formation in dense, massive clouds (Figure 5.7; see also Figure 5.14). This controlled experiment also demonstrates that the combined effects of photoionization and radiation pressure do not work in a simply additive manner in suppressing star formation.

4. Photoevaporation

The photoevaporation rate \dot{N}_e (the number of free electrons produced per unit time) at IFs within the cloud is much smaller than the total number of ionizing photons absorbed by hydrogen per unit time $Q_{\text{i,eff}}$ throughout the cloud (Figure 5.10). Most of the ionizations instead offset recombinations in diffuse gas throughout the cloud. The time-averaged hydrogen absorption fraction $\langle f_{\text{ion}} \rangle = \langle Q_{\text{i,eff}}/Q_{\text{i}} \rangle$ ranges from 0.22 to 0.50, while the time-averaged shielding factor $\langle q \rangle = \langle Q_{\text{i,eff}}/\dot{N}_e \rangle$ ranges from 61 to 2950 (Table 5.2). Although dense, compact clouds tend to have a high hydrogen absorption fraction, they have a high shielding factor and hence inefficient photoevaporative mass loss. As-

suming that the area of the IFs and thickness of the shielding layer scale with the dimensions of the initial cloud, we derive and calibrate expressions for the photoevaporation rate (Equations (5.11), (5.13); Figure 5.11a).

5. *Outflow acceleration and properties*

We perform a detailed analysis of the momentum injection processes that are responsible for cloud disruption and mass loss. The total radial momentum yield (momentum per stellar mass formed) of outflowing gas ranges over $\sim 20\text{--}400 \text{ km s}^{-1}$ (Figure 5.12), scaling as $p_*/m_* \propto \Sigma_0^{-0.74}$ (Equation (5.18)). The time-averaged total radial gas pressure force is smaller than the dustless, spherical case by a factor of $\sim 5\text{--}10$ due to momentum cancellation and escape of radiation, but is within 30% of $\dot{M}_{\text{ion}}c_i$, where \dot{M}_{ion} and c_i refer to the mass evaporation rate and the sound speed of the ionized gas, respectively (Figure 5.13). This is consistent with expectations for both internal pressure forces within the ionized medium and the combined thermal pressure and recoil forces on neutral gas at IFs, both of which scale as $n_i c_i^2 A_i \sim \dot{M}_{\text{ion}} c_i$. Similarly, the time-averaged radial force from radiation pressure is much reduced below the naive spherical expectation to $\sim 0.08\text{--}0.27L/c$ because of flux cancellation and photon escape. Although the overall momentum injection by radiation feedback is less efficient in realistic turbulent clouds than suggested by analytic predictions based on spherical H II region expansion in smooth clouds (e.g. Krumholz & Matzner 2009; Murray et al. 2010; Fall et al. 2010; Kim et al. 2016), the ratio of radiation pressure forces to gas pressure forces increases for massive, high surface density clouds (Figure 5.14), consistent with expectations from these previous studies. The mean outflow velocity of ionized gas is mildly supersonic with $v_{\text{ej,ion}} \sim 18\text{--}36 \text{ km s}^{-1}$, while that of neutral

gas is $v_{\text{ej,neu}} \sim 6\text{--}15 \text{ km s}^{-1}$, at about 0.8–1.8 times the escape velocity of the initial cloud (Figure 5.9 and Table 5.2).

6. *Semi-analytic models*

Based on our analyses of mass loss processes, we develop simple semi-analytic models for the net SFE, ε_* , and photoevaporation efficiency, ε_{ion} , as limited by radiation feedback in cluster-forming clouds. The predicted ε_{ion} is proportional to $\varepsilon_*^{1/2} \Sigma_0^{-1}$ (Equation (5.26)), with an order-unity dimensionless coefficient $\phi_t \phi_{\text{ion}}$ that we calibrate from simulations (Equation (5.16), Figure 5.11). When photoevaporation is the primary agent of cloud destruction, the net SFE depends solely on the gas surface density (Equation (5.29)). The resulting predictions for ε_* and ε_{ion} agree well with the numerical results for massive ($\geq 10^5 M_\odot$) clouds (Figure 5.6(a) and (c)). In low-mass clouds ($10^4 M_\odot$), the back-reaction to ionized-gas pressure is effective at IFs, and these clouds lose 30 – 50% of their initial gas mass as neutrals. Allowing for both ionized and neutral gas in outflows and assuming that the ejection velocity is constant for fixed cloud mass, with total momentum injection calibrated from our simulations (Equation 5.18), the predicted net SFE (Equation (5.31)) has a weak dependence on the cloud mass, consistent with our numerical results (Figure 5.6).

5.6.2 Discussion

It is interesting to compare our results with those of previous theoretical studies on star-forming GMCs with UV radiation feedback. Our net SFE and relative role of photoionization to radiation pressure are in qualitative agreement with the predictions of Kim et al. (2016), which adopted the idealizations of instantaneous star formation and spherical shell expansion (see also Fall et al. 2010; Murray et al. 2010; Rahner et al. 2017). However, the

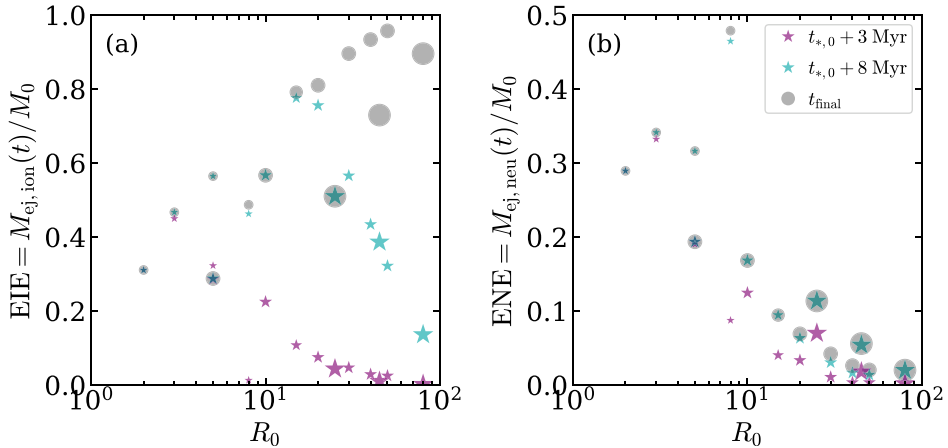


Figure 5.15 (a) Ejected ion efficiency (EIE) and (b) ejected neutral efficiency (ENE) at times $t_{*,0} + t_{\text{SN}}$ (magenta), $t_{*,0} + t_{\text{UV}}$ (cyan), and t_{final} (gray) as functions of the initial cloud radius R_0 .

minimum SFE required for cloud disruption by ionized-gas pressure found by Kim et al. (2016) ($\sim 0.002\text{--}0.1$ for $20 M_{\odot} \text{pc}^{-2} \leq \Sigma_0 \leq 10^2 M_{\odot} \text{pc}^{-2}$, see their Figure 11) is smaller than what we find here. Turbulence-induced structure can lead to higher SFE for several reasons. First, a fraction of the photons can easily escape through low-density channels, without either ionizing gas or being absorbed to impart momentum. Second, low-density but high pressure ionized gas can also vent through these channels, reducing the transfer of momentum from photoevaporated to neutral gas. Third, turbulence increases the mass-weighted mean density and therefore the recombination rate of ionized gas, so that a higher luminosity is required to photoevaporate gas.

In this chapter, we also find that radiation pressure becomes significant at $\Sigma_0 \sim 200\text{--}800 M_{\odot} \text{pc}^{-2}$, lower for higher-mass clouds. This transition value of surface density for low-mass clouds is somewhat higher than $\Sigma_0 \sim 100 M_{\odot} \text{pc}^{-2}$ in simple spherical models (e.g. Krumholz & Matzner 2009; Murray et al. 2010; Fall et al. 2010; Kim et al. 2016). These spherical

models predicted that the expansion of an H II region is dominated by radiation pressure force at least in the early phase of expansion (e.g., Krumholz & Matzner 2009; Kim et al. 2016). Even for the highest- Σ_0 models, however, we find that the volume-integrated radiation pressure force ($\int \mathbf{f}_{\text{rad}} \cdot \hat{\mathbf{r}} dV$) in the radial direction tends to be smaller than that of gas pressure force ($\int \mathbf{f}_{\text{thm}} \cdot \hat{\mathbf{r}} dV$) in the early phase of star formation, and that this tendency is reversed only at late time. This is due to the strong cancellation of radiation on a global scale, and should thus not be interpreted as evidence for radiation pressure being subdominant. Rather, radiation pressure plays a greater role in controlling the dynamics of sub H II regions surrounding individual sources.

The outflow momentum yield of $p_*/m_* \sim 20\text{--}400 \text{ km s}^{-1}$ by radiation feedback found from our simulations can be compared with those produced by other types of feedback. For example, the momentum yield of protostellar outflows is estimated as $\sim 40 \text{ km s}^{-1}$ (e.g., Matzner & McKee 2000), while recent numerical work on SNe-driven flows found a momentum yield of $\sim 1000\text{--}3000 \text{ km s}^{-1}$, weakly dependent on the background density and stellar clustering (e.g., Kim & Ostriker 2015; Kim et al. 2017a). These feedback mechanisms are expected to be important at different scales (e.g., Fall et al. 2010; Krumholz et al. 2014; Matzner & Jumper 2015). The momentum injection by protostellar outflows plays a key role in driving turbulence and regulating star formation in small-scale clumps before massive stars form (e.g., Nakamura & Li 2014), and SNe are capable of driving ISM turbulence to regulate galaxy-wide star formation and possibly winds from low-mass galaxies (e.g., Kim et al. 2017a). Momentum injection by UV radiation is important to controlling dynamics at intermediate, GMC scales.

In this chapter we have focused exclusively on the effects of radiation feedback, and as we neglect aging of stellar populations over the whole cloud lifetime, our mass-loss efficiencies place an upper limit to the actual damage

UV radiation can cause. To estimate lower limits to the destructive effects of radiation feedback, we can consider what UV feedback would be able to accomplish over two shorter intervals: $t_{\text{SN}} = 3 \text{ Myr}$, the minimum lifetime of most massive stars (i.e., the time when first supernova is expected to occur after the epoch of the first star formation); and $t_{\text{UV}} = 8 \text{ Myr}$, the time scale on which UV luminosity decays. Figure 5.15 shows the cumulative (a) ejected ion efficiency $\text{EIE} = M_{\text{ej,ion}}/M_0$ and (b) ejected neutral efficiency $\text{ENE} = M_{\text{ej,neu}}/M_0$ as functions of the initial cloud radius R_0 at $t_{*,0} + t_{\text{SN}}$ (magenta), $t_{*,0} + t_{\text{UV}}$ (cyan), and t_{final} (gray). In the case of compact, high-surface density clouds with short freefall times, the mass-loss efficiencies at $t_{*,0} + t_{\text{SN}}$ are close to the final values at t_{final} , suggesting that UV radiation is expected to clear out most of gas prior to the first supernova. For large, diffuse clouds with long freefall times, the mass ejection efficiencies at $t_{*,0} + t_{\text{SN}}$ and $t_{*,0} + t_{\text{UV}}$ are significantly smaller than the final values. For these diffuse clouds with long freefall timescales, a complete assessment of star formation efficiency and cloud destruction will have to include the effects of supernovae as well as radiation feedback. While some of the supernova energy escapes easily through low-density channels (e.g. Rogers & Pittard 2013; Walch & Naab 2015), and supernovae may undermine radiation feedback by compressing overdense structures, supernova feedback likely aids in destroying star-forming clouds overall (e.g. Geen et al. 2016). In principle, shocked stellar winds may also be important over the same period as radiation feedback is active, although recent studies have raised doubts about its effectiveness as this hot gas can easily leak through holes or mix with cool gas (Harper-Clark & Murray 2009; Rosen et al. 2014).

In this work, we have considered only unmagnetized, marginally bound clouds with $\alpha_{\text{vir},0} = 2$, while observed GMCs may have a range of virial values (e.g., Heyer et al. 2009; Roman-Duval et al. 2010; Miville-Deschênes et al. 2017). Preliminary simulations we have done reveal that the net SFE

decreases from 0.31 to 0.02 as $\alpha_{\text{vir},0}$ is varied from 0.5 to 5 for the fiducial mass and size. Clouds with large initial $\alpha_{\text{vir},0}$ tend to form stars less efficiently since turbulence unbinds a larger fraction of gas and reduces the gas mass in collapsing structures, as has been reported by recent simulations (e.g., Dale et al. 2013a; Bertram et al. 2015; Howard et al. 2016; Raskutti et al. 2016; Dale 2017). For clouds that are initially strongly-bound, an initial adjustment period leads to smaller cloud with order-unity α , in which the subsequent evolution is similar to clouds with $\alpha_{\text{vir},0} \sim 1$ (Raskutti et al. 2016). Magnetization is likely to increase the effectiveness of radiation feedback, as it reduces the density inhomogeneity that limits radiation pressure effects, and may also help to distribute energy into neutral gas (Gendelev & Krumholz 2012).

Finally, we comment on the resolution of our numerical models. Our standard choice of grid resolution ($N_{\text{cell}} = 256^3$) and domain size ($L_{\text{box}} = 4R_0$) is a compromise between computational time and accuracy, and this choice of moderate resolution enabled us to extensively explore parameter space. While the present simulations can capture the dynamics of cluster-forming gas and outflowing gas on cloud scales with reasonable accuracy, they do not properly resolve compressible flows in high-density regions where sink particles are created. Our models may overestimate star formation rates as all the gas that has been accreted onto sink particles is assumed to be converted to stars (cf. Howard et al. 2016, 2017), although a converging trend of ε_* with resolution (see Appendix 5.A) suggests that the final SFE may be primarily controlled by photoevaporation and injection of momentum in moderate density gas at large scales. Adaptive mesh refinement simulations can be used to address this and other resolution-related questions.

Appendix

5.A Resolution Study of the Fiducial Model

The high computational cost required for radiation transfer, especially for models involving numerous point sources, prevents us from running all our simulations at very high resolution. To study how our numerical results depend on the grid size, we run the fiducial model with $M_0 = 10^5 M_\odot$ and $R_0 = 20 \text{ pc}$ at three different spatial resolutions with $N_{\text{cell}} = 128^3$ (M1E5R20_N128), 256^3 (M1E5R20), and 512^3 (M1E5R20_N512). Here we compare the results of these models.

Figure 5.16 plots the temporal evolution of various volume- or surface-integrated quantities from M1E5R20_N128 (short dashed), M1E5R20 (solid), M1E5R20_N512 (long dashed). It is clear that all quantities exhibit qualitatively similar behavior with time, and the final values of key quantities such as stellar mass and photoevaporated gas mass listed in Table 5.2 are numerically quite close and follow a converging trend as the resolution increases. For example, the increment in the duration of star formation t_{SF} from the 128^3 to 256^3 runs is $\sim 25\%$, which is reduced to $\sim 17\%$ from the 256^3 to 512^3 runs. This resolution-dependent t_{SF} is due primarily to the fact that the minimum sink particle mass as well as the physical size of the control volume (or the effective area through which gas accretes) are proportional to Δx (or Δx^2),

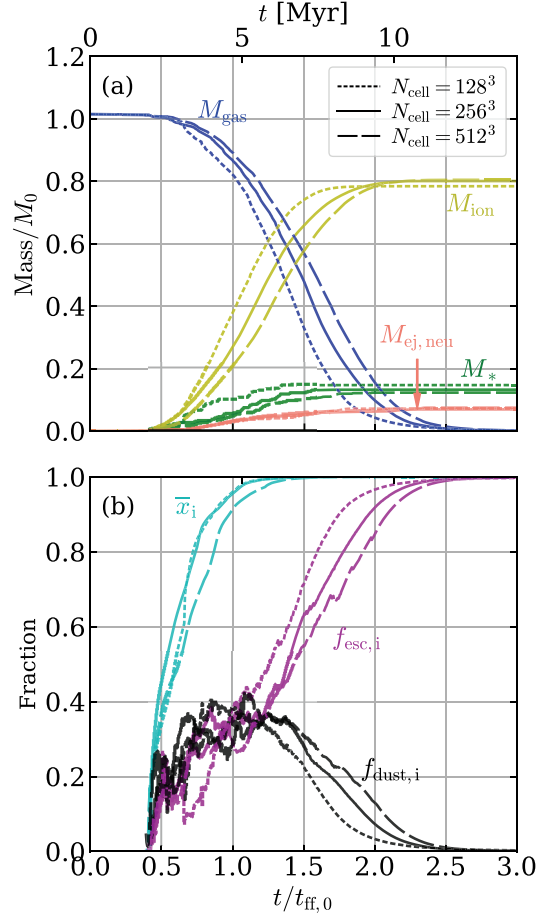


Figure 5.16 Evolutionary histories of key quantities for the fiducial cloud model ($M_0 = 10^5 M_\odot$ and $R_0 = 20$ pc) at varying resolution: $N_{\text{cell}} = 128^3$ (short dashed), 256^3 (solid), and 512^3 (long dashed). (a) The total gas mass M_{gas} in the simulation volume (blue), the stellar mass M_* (green), the ejected neutral gas mass $M_{\text{ej,neu}}$ (salmon), and the mass of the photoevaporated gas M_{ion} (yellow). (b) The volume fraction of the ionized gas \bar{x}_i (cyan), the fraction of ionizing radiation absorbed by dust $f_{\text{dust},i}$ (black), and the escape fractions of ionizing photons $f_{\text{esc},i}$ (magenta).

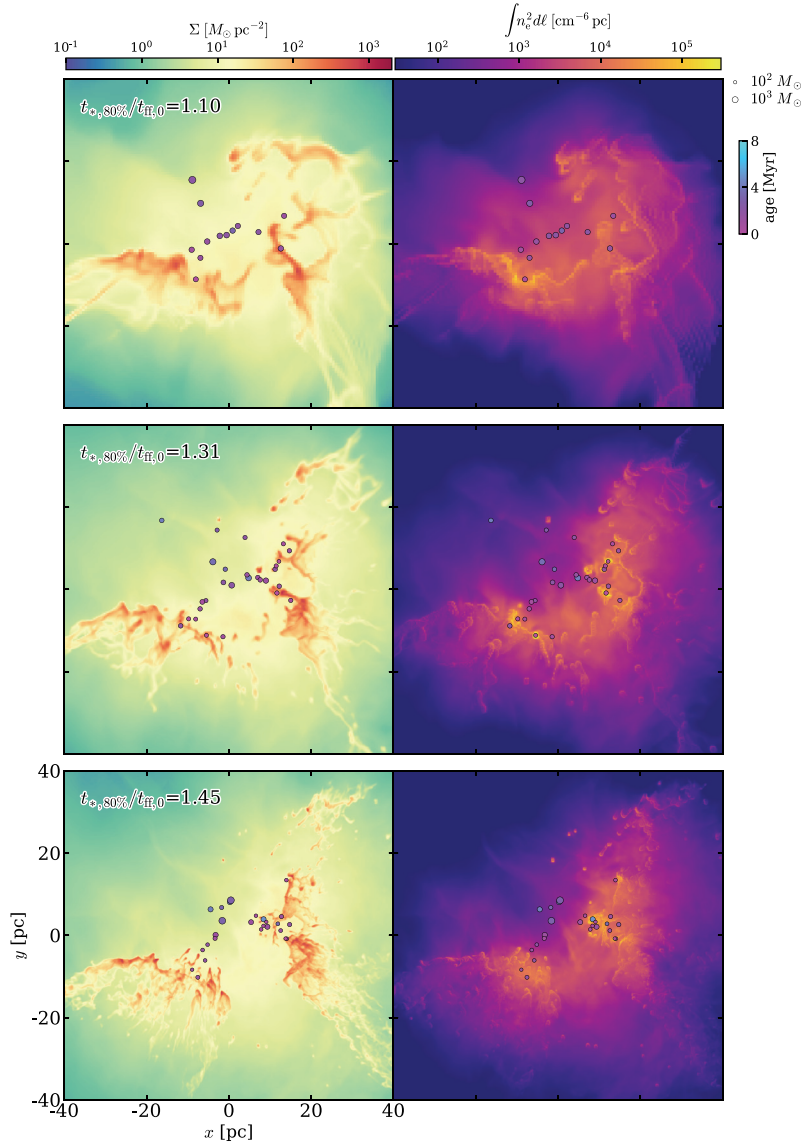


Figure 5.17 Snapshots of the gas surface density (left) and emission measure (right) in the fiducial model when 80% of the final stellar mass has been assembled. The top, middle, and bottom panels correspond respectively to the run with $N_{\text{cell}} = 128^3$ at $t/t_{\text{ff},0} = 1.10$, 256^3 at $t/t_{\text{ff},0} = 1.31$, and 512^3 at $t/t_{\text{ff},0} = 1.45$. The projected positions of star particles are shown as circles, with their color corresponding to age.

so that the stellar mass grows more rapidly and in a more discrete fashion at coarser spatial resolution. Despite this difference, the net SFE of 0.15, 0.13, and 0.12 for $N_{\text{cell}} = 128^3$, 256^3 , and 512^3 , respectively, is almost converged.

Figure 5.17 compares sample snapshots of the total (neutral + ionized) gas surface density and the emission measure projected along the z -axis when 80% of the final stellar mass has been formed (at $t/t_{\text{ff},0} = 1.10, 1.31, 1.45$ for $N_{\text{cell}} = 128^3$, 256^3 , and 512^3 , respectively). The higher-resolution model exhibits filaments, pillars, and bright-rimmed globules in greater detail, but the overall morphologies of gas and star particle distributions are very similar. Therefore, we conclude that the results based on $N_{\text{cell}} = 256^3$ presented in this chapter provide quantitatively reasonable estimates to the converged results.

5.B Net Star Formation Efficiency Regulated by Radiation-Pressure Feedback

Here we compare the net SFE from our RP-only simulations with the analytic predictions by Raskutti et al. (2016) and Thompson & Krumholz (2016). The key underlying assumptions of these models are that (1) the probability density function (PDF) of gas surface density follows a log-normal distribution, characteristic of supersonic isothermal turbulence and that (2) only the gas with surface density below the Eddington surface density is ejected. These analytic models predict a higher SFE for a turbulent cloud than for an equivalent uniform cloud (e.g., Fall et al. 2010; Kim et al. 2016) with the same mass and size because a greater luminosity is required to eject gas compressed to high surface density by turbulence.

Raskutti et al. (2016) argued that for a cloud with given log-normal variance in the surface density $\sigma_{\ln \Sigma^c}$, the luminosity would continue to rise until it reaches a level that maximizes the outflow efficiency. At this point, the final SFE would be bracketed between two levels, $\varepsilon_{*,\text{min}}$ and $\varepsilon_{*,\text{max}}$. At one

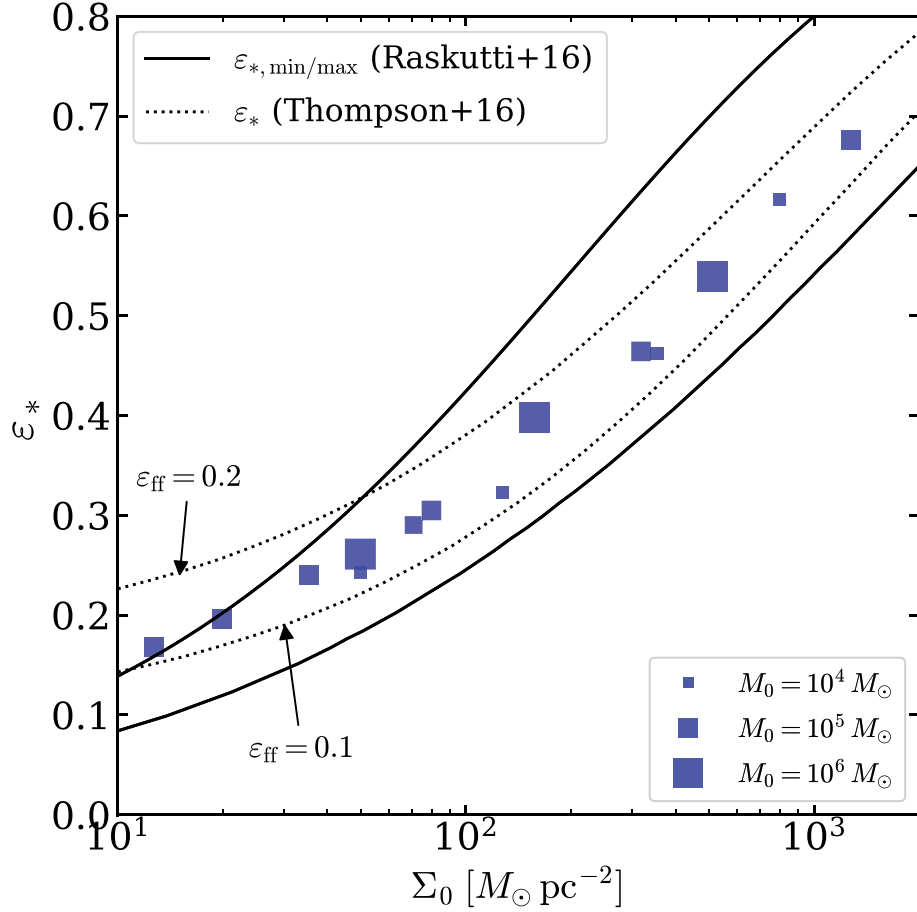


Figure 5.18 Comparison of the net SFE from the RP-only simulations (squares) with those from the theoretical predictions (lines). The solid lines show $\varepsilon_{*,\min}$ and $\varepsilon_{*,\max}$ based on the analytic model of Raskutti et al. (2016). The predictions of Thompson & Krumholz (2016) with $\varepsilon_{\text{ff}} = 0.1, 0.2$ are given as dotted lines. For both models we adopt $\sigma_{\ln \Sigma^c} = 1.4$ based on the typical variance in our simulations.

extreme, all the remaining gas can be ejected without forming stars, if the PDF adjusts itself rapidly to a successively lower peak as gas is expelled. At the opposite extreme, all of the remaining gas can turn into stars if it collapses before the PDF adjusts. Thompson & Krumholz (2016) considered a similar situation, but they allowed for a time-dependent star formation rate $\dot{M}_* = \varepsilon_{\text{ff}} M_{\text{gas}}(t)/t_{\text{ff}}$, where ε_{ff} is a free parameter. In both models, gas is assumed to be ejected rapidly.

In our simulations, the gas column density distribution remains broad over the entire evolution. The column density PDFs closely resemble log-normal functions with $\sigma_{\ln \Sigma^c} \sim 1.2\text{--}1.6$ that do not vary much over the star-forming period (from $t_{*,10\%}$ to $t_{*,90\%}$), roughly consistent with the results of Raskutti et al. (2016). The effective SFE per freefall time $\varepsilon_{\text{ff,eff}} = \varepsilon_* t_{\text{ff},0}/(t_{*,99\%} - t_{*,0})$ in each model turns out to vary in the range of 0.1–0.22 across our models. Both analytic models in principle allow for the cloud size to vary over time, although the numerical simulations of Raskutti et al. (2016) show that the effective radius in fact varies very little up until the cloud is rapidly dispersed. Here, to compare to the analytic models, we assume the cloud size is fixed at its initial radius ($x = 1$ in Raskutti et al. 2016 and $p = 0$ in Thompson & Krumholz 2016), and we take a fixed value $\sigma_{\ln \Sigma^c} = 1.4$.

Figure 5.18 compares the net SFE resulting from our RP-only runs (squares) with the theoretical predictions (various lines). For this purpose, we adjust the numerical results, i.e., $\varepsilon_{*,\text{adj}} = \varepsilon_*/(1 - \varepsilon_{\text{ej,turb}})$, to allow for initial turbulent outflow, similar to Raskutti et al. (2016). The numerical results lie between $\varepsilon_{*,\text{min}}$ and $\varepsilon_{*,\text{max}}$ (black solid lines) predicted by Raskutti et al. (2016). The net SFE is to some extent closer to $\varepsilon_{*,\text{min}}$ than $\varepsilon_{*,\text{max}}$, which is in contrast to the numerical results of Raskutti et al. (2016) (see their Figure 25). In Chapter 4, we previously showed that the net SFE obtained using the M_1 -closure as in Raskutti et al. (2016) is higher than that obtained from the adaptive ray tracing method, because in the former the source function

is smoothed out over a finite region and thus the radiation force in the immediate vicinity of star particles is lower than it should be, allowing additional accretion of nearby gas.

Figure 5.18 plots as a dotted lines the net SFE predicted by the Thompson & Krumholz formalism, adopting $\varepsilon_{\text{ff}} = 0.1$ and 0.2 to bracket our simulation results (note that they adopted a much lower value for their fiducial model). The prediction brackets the results of our simulations.

We conclude that the results of our RP-only simulations are overall in good agreement with the recent analytic models of Raskutti et al. (2016) and Thompson & Krumholz (2016) for the net SFE in turbulent star-forming clouds regulated by radiation pressure.

Chapter 6

Summary and Outlook

6.1 Summary

Most star formation in the local universe occurs in GMCs. Young massive stars strongly affect the evolution of their birth clouds and larger-scale galactic environment. In particular, intense UV photons emitted by massive stars excite H II regions, bubbles of photoionized hydrogen gas, around them and drive their expansion. The destructive effects of H II regions can regulate cloud-scale star formation and even destroy the parent molecular cloud. Therefore, to understand how galaxies build up their stellar mass and evolve through cosmic history, to understand the cycling of gas through different phases of the ISM, and to understand formation of star clusters and subsequent dynamical evolution, one must understand how individual star-forming molecular clouds form, evolve, and end their lives under the influence of UV radiation feedback.

In this thesis, we investigated the dynamics of H II regions formed around young massive stars and their impact on the evolution of GMCs. Our findings

can be summarized as follows:

1. *Instability of IFs*

We performed a linear stability analysis of magnetized, weak D-type IFs around H II regions. We imposed small-amplitude perturbations on a steady-state IF in isolation, and sought for unstable modes that grow exponentially in time. The growth rate of the IF instability scales linearly with the wavenumber as well as the background fluid velocity relative to the front. The physical mechanism behind the IF instability is the same as that of the Darrieus-Landau instability of deflagration fronts in terrestrial combustion and thermonuclear supernovae. Magnetic fields play a stabilizing role by reducing the density contrast across the IF and by exerting magnetic pressure and tension forces. The IF instability is completely suppressed if the Alfvénic Mach number is sufficiently small. The IF instability works together with the Rayleigh-Taylor instability for IFs accelerating away from an ionizing source.

2. *Cloud Disruption by Expansion of Dusty H II Regions*

We used a simple semi-analytic model as well as hydrodynamic simulations to study dynamical expansion of a dusty H II region around a star cluster and its role in cloud disruption. Our model for shell expansion considers the contact outward forces on the shell due to radiation and thermal pressures as well as the inward gravity from the central star and the shell itself. We showed that the internal structure we adopt and the shell evolution from the semi-analytic approach are in good agreement with the results of numerical simulations. Strong radiation pressure in the interior controls the shell expansion indirectly by enhancing the density and pressure at the ionization front. We calculated the minimum star formation efficiency ε_{\min} required for cloud disruption as a function of the cloud's total mass and mean surface density. Within

the adopted spherical geometry, we found that typical giant molecular clouds in normal disk galaxies have $\varepsilon_{\min} \lesssim 10\%$, with comparable gas and radiation pressure effects on shell expansion. Massive cluster-forming clumps require a significantly higher efficiency of $\varepsilon_{\min} \gtrsim 50\%$ for disruption, produced mainly by radiation-driven expansion. The disruption time is typically of the order of a free-fall timescale, suggesting that the cloud disruption occurs rapidly once a sufficiently luminous H II region is formed.

3. *Implementation of Adaptive Ray Tracing Method and Tests*

We presented an implementation of an adaptive ray tracing (ART) module in the *Athena* hydrodynamics code that accurately and efficiently handles the radiative transfer involving multiple point sources on a three-dimensional Cartesian grid. We adopted a recently proposed parallel algorithm that uses non-blocking, asynchronous MPI communications to accelerate transport of rays across the computational domain. We validated our implementation through several standard test problems including the propagation of radiation in vacuum and the expansions of various types of H II regions. Scaling tests showed that the cost of a full ray trace per source remains comparable to that of the hydrodynamics update on up to $\sim 10^3$ processors. To demonstrate application of our ART implementation, we performed a simulation of star cluster formation in a marginally bound, turbulent cloud, finding that its star formation efficiency is 12% when both radiation pressure forces and photoionization by UV radiation are treated. We directly compared the radiation forces computed from the ART scheme with that from the M_1 closure relation. Although the ART and M_1 schemes yield similar results on large scales, the latter is unable to resolve the radiation field accurately near individual point sources.

4. *Dispersal of Star-forming GMCs by Photoionization and Radiation Pressure*

We conducted a suite of radiation hydrodynamic simulations of star cluster formation in marginally-bound, turbulent GMCs, focusing on the effects of photoionization and radiation pressure on regulating the net star formation efficiency (SFE) and cloud lifetime. We found that the net SFE depends primarily on the initial gas surface density, Σ_0 , such that the SFE increases from 4% to 51% as Σ_0 increases from $13 M_\odot \text{pc}^{-2}$ to $1300 M_\odot \text{pc}^{-2}$. Cloud destruction occurs within 2–10 Myr after the onset of radiation feedback, or within 0.6–4.1 freefall times (increasing with Σ_0). Photoevaporation dominates the mass loss in massive, low surface-density clouds, but because most photons are absorbed in an ionization-bounded Strömngren volume the photoevaporated gas fraction is proportional to the square root of the SFE. The measured momentum injection due to thermal and radiation pressure forces is proportional to $\Sigma_0^{-0.74}$, and the ejection of neutrals substantially contributes to the disruption of low-mass and/or high-surface density clouds. We presented semi-analytic models for cloud dispersal mediated by photoevaporation and by dynamical mass ejection, and showed that the predicted net SFE and mass loss efficiencies are consistent with the results of our numerical simulations.

6.2 Outlook

While this thesis focused exclusively on the effects of UV radiation feedback, there are other important physical processes that have yet to be considered to gain a more comprehensive picture of the lifecycle of GMCs and star formation within them.

First, magnetic fields are believed to play an important role in star for-

mation by channeling gas flows and providing support against gravitational collapse (Crutcher 2012). A simulation study by Gendeleev & Krumholz (2012) showed that H II regions expanding into a smooth, magnetized cloud can supply a significant amount of magnetic energy to the cloud. However, only a few studies have investigated the dynamics of HII regions in a magnetized, turbulent medium, considering only photoionization (Arthur et al. 2011; Geen et al. 2017) or only radiation pressure (Raskutti 2016); it is not entirely clear how magnetized, cluster-forming clouds would evolve under the influence of both photoionization and radiation pressure.

Second, massive stars release a tremendous amount of energy and momentum into the surrounding interstellar medium (ISM) by means of *stellar winds* during their lifetime and SNe at the end of their lives. Historically, (confined) hot ($\gtrsim 10^6$ K) gas created by shock-heated stellar winds is thought to be the key agent driving expansion of H II regions (Weaver et al. 1977), but recent observational and theoretical studies have raised doubts on its effectiveness in disrupting inhomogeneous clouds because it can easily leak through holes or mix with cool gas (e.g., Rosen et al. 2014). Although an attempt has been made to assess the relative importance of radiation feedback and stellar winds in idealized geometry (Yeh & Matzner 2012), no simulations have investigated the coupling among photoionization, radiation pressure, and stellar winds in an inhomogeneous, turbulent medium.

SNe are considered to be the most powerful form of stellar feedback on galactic scales (e.g., Ostriker & Shetty 2011), but their impact on cloud evolution remains unclear. Since SNe begin to occur ~ 3 Myr after the formation of massive stars, dense and compact clouds are expected to end their lives by pre-SNe feedback (radiation and stellar winds) alone (Krumholz & Matzner 2009). In more diffuse and larger clouds, on the other hand, multiple SNe are expected to occur before complete destruction, as supported by observations of young supernova remnants interacting with GMCs (e.g., Chen et al. 2014).

A recent numerical study by Iffrig & Hennebelle (2015) found that the dynamical impact of SNe on an inhomogeneous cloud sensitively depends on the location of the event with respect to the cloud, but most simulations to date probed a limited range of parameter space and set the SN position rather arbitrarily without self-consistent model for star formation (e.g., Rogers & Pittard 2013; Geen et al. 2016).

As this thesis demonstrates, multiple feedback mechanisms do not operate in a simply additive manner and their relative importance is expected to vary across scales. Therefore, it is imperative for numerical models to advance into the next level of realism by including self-consistent treatment of star formation and all forms of massive star feedback (radiation, stellar winds, and SNe) in turbulent, magnetized GMCs. Taking a step-by-step approach, it will be interesting to first incorporate the effect of magnetic fields into the current numerical model. In the next step, the effects of stellar winds and SNe can be included, accounting for the time evolution of UV luminosity and mechanical luminosity (by stellar winds) from a population of stars. For this, we can employ a statistical method for assigning realistic stellar content to Lagrangian sink particles (Sormani et al. 2017). Performing a large suite of radiation magnetohydrodynamic simulations across a wide range of cloud parameters will enable us not only to assess how magnetic fields and various feedback mechanisms affect cloud evolution, but also to characterize structural properties of different phases of the ISM. Moreover, they will provide a more realistic estimate of the fraction of ionizing photons escaping from the cloud, which is the essential but poorly constrained parameter in understanding the physics of diffuse ionized gas (Haffner et al. 2009) and reionization of the Universe (Barkana & Loeb 2001).

Last but not least, it will be interesting to compare simulation results with real observations of star-forming GMCs. Recent observations that cross-correlate molecular gas mass with stellar mass show a wide scatter in the

distribution of SFE (e.g., Vutisalchavakul et al. 2016; Lee et al. 2016). Unfortunately, there are a number of factors that make reliable inference for SFE of individual clouds difficult; for example, real clouds are not isolated entities with well defined boundaries, they are at different evolutionary stages with ongoing star formation as well as mass loss, and most star formation indicators are strongly biased towards massive stars that are scarce in number and have short lifetimes. Our simulations can help alleviate the difficulties in interpreting observations of star-forming clouds. For comparison, we can produce maps of CO and dust emission from simulated clouds utilizing a chemistry solver (e.g., Gong et al. 2017) as well as publicly available radiative transfer code (e.g., Dullemond et al. 2012), and perform synthetic observations of them (e.g., Koepferl et al. 2017). This will allow us a detailed look at the relation between cloud properties and star formation at different evolutionary stages.

To summarize, future simulations will provide a more realistic picture of star cluster formation and cloud evolution, and synthetic observations will help bridge the gap between theory and observations. Ultimately, the resolution of the issues related to star formation and feedback on cloud scales will impact our view of the cycling of gas through different phases of the ISM, and provide valuable guidance for sub-resolution models of numerical galaxy formation.

Bibliography

- Abel, T., Norman, M. L., & Madau, P. 1999, *ApJ*, 523, 66
- Abel, T., & Wandelt, B. D. 2002, *MNRAS*, 330, L53
- Altay, G., & Theuns, T. 2013, *MNRAS*, 434, 748
- André, P., Di Francesco, J., Ward-Thompson, D., et al. 2014, *Protostars and Planets VI*, 27
- Anninos, P., Zhang, Y., Abel, T., & Norman, M. L. 1997, *NewA*, 2, 209
- Arthur, S. J., Henney, W. J., Mellema, G., de Colle, F., & Vázquez-Semadeni, E. 2011, *MNRAS*, 414, 1747
- Arthur, S. J., Kurtz, S. E., Franco, J., & Albarrán, M. Y. 2004, *ApJ*, 608, 282
- Ashman, K. M., & Zepf, S. E. 2001, *AJ*, 122, 1888
- Axford, W. I. 1961, *Philosophical Transactions of the Royal Society of London Series A*, 253, 301
- . 1964, *ApJ*, 140, 112
- Baczynski, C., Glover, S. C. O., & Klessen, R. S. 2015, *MNRAS*, 454, 380
- Ballesteros-Paredes, J. 2006, *MNRAS*, 372, 443
- Ballesteros-Paredes, J., & Hartmann, L. 2007, *RMxAA*, 43, 123
- Ballesteros-Paredes, J., Hartmann, L. W., Vázquez-Semadeni, E., Heitsch, F., & Zamora-Avilés, M. A. 2011, *MNRAS*, 411, 65
- Banerjee, S., & Kroupa, P. 2015, *ArXiv e-prints*, arXiv:1512.03074
- Barkana, R., & Loeb, A. 2001, *PhR*, 349, 125

- Bell, J. B., Day, M. S., Rendleman, C. A., Woosley, S. E., & Zingale, M. 2004, *ApJ*, 606, 1029
- Bertoldi, F. 1989, *ApJ*, 346, 735
- Bertoldi, F., & McKee, C. F. 1990, *ApJ*, 354, 529
- . 1992, *ApJ*, 395, 140
- Bertram, E., Glover, S. C. O., Clark, P. C., & Klessen, R. S. 2015, *MNRAS*, 451, 3679
- Bigiel, F., Leroy, A., Walter, F., et al. 2008, *AJ*, 136, 2846
- Bisbas, T. G., Wünsch, R., Whitworth, A. P., & Hubber, D. A. 2009, *A&A*, 497, 649
- Bisbas, T. G., Wünsch, R., Whitworth, A. P., Hubber, D. A., & Walch, S. 2011, *ApJ*, 736, 142
- Bisbas, T. G., Haworth, T. J., Williams, R. J. R., et al. 2015, *MNRAS*, 453, 1324
- Bleuler, A., & Teyssier, R. 2014, *MNRAS*, 445, 4015
- Blitz, L., Fukui, Y., Kawamura, A., et al. 2007, *Protostars and Planets V*, 81
- Bolatto, A. D., Wolfire, M., & Leroy, A. K. 2013, *ARA&A*, 51, 207
- Brogan, C. L., & Troland, T. H. 2001, *ApJ*, 560, 821
- Brogan, C. L., Troland, T. H., Abel, N. P., Goss, W. M., & Crutcher, R. M. 2005, in *Astronomical Society of the Pacific Conference Series*, Vol. 343, *Astronomical Polarimetry: Current Status and Future Directions*, ed. A. Adamson, C. Aspin, C. Davis, & T. Fujiyoshi, 183
- Brogan, C. L., Troland, T. H., Roberts, D. A., & Crutcher, R. M. 1999, *ApJ*, 515, 304
- Bromm, V., & Yoshida, N. 2011, *ARA&A*, 49, 373
- Burkhart, B., Stalpes, K., & Collins, D. C. 2017, *ApJL*, 834, L1
- Bychkov, V., Modestov, M., & Marklund, M. 2008, *Physics of Plasmas*, 15, 032702
- Bychkov, V. V., Golberg, S. M., & Liberman, M. A. 1994, *Physics of Plasmas*, 1, 2976
- Carpenter, J. M. 2000, *AJ*, 120, 3139
- Carruthers, G. R. 1970, *ApJL*, 161, L81
- Castor, J., McCray, R., & Weaver, R. 1975, *ApJL*, 200, L107

- Castor, J. I. 2004, *Radiation Hydrodynamics*, 368
- Chabrier, G. 2003, *PASP*, 115, 763
- Chandrasekhar, S. 1961, *Hydrodynamic and hydromagnetic stability*
- Chen, Y., Jiang, B., Zhou, P., et al. 2014, in *IAU Symposium, Vol. 296, Supernova Environmental Impacts*, ed. A. Ray & R. A. McCray, 170–177
- Cho, W., & Kim, J. 2011, *MNRAS*, 410, L8
- Churchwell, E., Povich, M. S., Allen, D., et al. 2006, *ApJ*, 649, 759
- Colín, P., Vázquez-Semadeni, E., & Gómez, G. C. 2013, *MNRAS*, 435, 1701
- Colombo, D., Hughes, A., Schinnerer, E., et al. 2014, *ApJ*, 784, 3
- Consiglio, S. M., Turner, J. L., Beck, S., & Meier, D. S. 2016, *ApJL*, 833, L6
- Crutcher, R. M. 1999, *ApJ*, 520, 706
- . 2012, *ARA&A*, 50, 29
- Da Rio, N., Tan, J. C., & Jaehnig, K. 2014, *ApJ*, 795, 55
- da Silva, R. L., Fumagalli, M., & Krumholz, M. 2012, *ApJ*, 745, 145
- Daddi, E., Elbaz, D., Walter, F., et al. 2010, *ApJL*, 714, L118
- Dale, J. E. 2015, *NewAR*, 68, 1
- . 2017, *MNRAS*, 467, 1067
- Dale, J. E., Bonnell, I. A., & Whitworth, A. P. 2007, *MNRAS*, 375, 1291
- Dale, J. E., Ercolano, B., & Bonnell, I. A. 2012, *MNRAS*, 424, 377
- . 2013a, *MNRAS*, 430, 234
- . 2013b, *MNRAS*, 431, 1062
- Dale, J. E., Ngoumou, J., Ercolano, B., & Bonnell, I. A. 2014, *MNRAS*, 442, 694
- Dale, J. E., Wünsch, R., Whitworth, A., & Palouš, J. 2009, *MNRAS*, 398, 1537
- Dame, T. M., Hartmann, D., & Thaddeus, P. 2001, *ApJ*, 547, 792
- Dame, T. M., Ungerechts, H., Cohen, R. S., et al. 1987, *ApJ*, 322, 706
- Davis, S. W., Jiang, Y.-F., Stone, J. M., & Murray, N. 2014, *ApJ*, 796, 107
- Davis, S. W., Stone, J. M., & Jiang, Y.-F. 2012, *ApJS*, 199, 9

- Deharveng, L., Schuller, F., Anderson, L. D., et al. 2010, *A&A*, 523, A6
- Dobbs, C. L., Krumholz, M. R., Ballesteros-Paredes, J., et al. 2014, *Protostars and Planets VI*, 3
- Draine, B. T. 2011a, *Physics of the Interstellar and Intergalactic Medium*
- . 2011b, *ApJ*, 732, 100
- Dullemond, C. P., Juhasz, A., Pohl, A., et al. 2012, RADMC-3D: A multi-purpose radiative transfer tool, *Astrophysics Source Code Library*, , , ascl:1202.015
- Dursi, L. J. 2004, *ApJ*, 606, 1039
- Elmegreen, B. G. 1983, *MNRAS*, 203, 1011
- . 2000, *ApJ*, 530, 277
- Elmegreen, B. G., & Efremov, Y. N. 1997, *ApJ*, 480, 235
- Elmegreen, B. G., & Lada, C. J. 1977, *ApJ*, 214, 725
- Elmegreen, B. G., & Scalo, J. 2004, *ARA&A*, 42, 211
- Elmergreen, B. G. 1976, *ApJ*, 205, 405
- Engargiola, G., Plambeck, R. L., Rosolowsky, E., & Blitz, L. 2003, *ApJS*, 149, 343
- Evans, II, N. J. 1991, in *Astronomical Society of the Pacific Conference Series*, Vol. 20, *Frontiers of Stellar Evolution*, ed. D. L. Lambert, 45–95
- Evans, II, N. J., Dunham, M. M., Jørgensen, J. K., et al. 2009, *ApJS*, 181, 321
- Fall, S. M., Krumholz, M. R., & Matzner, C. D. 2010, *ApJL*, 710, L142
- Federrath, C., Roman-Duval, J., Klessen, R. S., Schmidt, W., & Mac Low, M.-M. 2010, *A&A*, 512, A81
- Feldmann, R., & Gnedin, N. Y. 2011, *ApJL*, 727, L12
- Finlator, K., Özel, F., & Davé, R. 2009, *MNRAS*, 393, 1090
- Franco, J., Shore, S. N., & Tenorio-Tagle, G. 1994, *ApJ*, 436, 795
- Franco, J., Tenorio-Tagle, G., & Bodenheimer, P. 1990, *ApJ*, 349, 126
- Frank, M., Hauck, C. D., & Olbrant, E. 2012, *ArXiv e-prints*, arXiv:1208.0772
- Frieman, E. A. 1954, *ApJ*, 120, 18
- Fukui, Y., & Kawamura, A. 2010, *ARA&A*, 48, 547

- Gallagher, M. J., Leroy, A. K., Bigiel, F., et al. 2018, *ApJ*, 858, 90
- García, P., Bronfman, L., Nyman, L.-Å., Dame, T. M., & Luna, A. 2014, *ApJS*, 212, 2
- Garcia-Segura, G., & Franco, J. 1996, *ApJ*, 469, 171
- Gavagnin, E., Bleuler, A., Rosdahl, J., & Teyssier, R. 2017, *MNRAS*, 472, 4155
- Geen, S., Hennebelle, P., Tremblin, P., & Rosdahl, J. 2015a, *MNRAS*, 454, 4484
- . 2016, *MNRAS*, 463, 3129
- Geen, S., Rosdahl, J., Blaizot, J., Devriendt, J., & Slyz, A. 2015b, *MNRAS*, 448, 3248
- Geen, S., Soler, J. D., & Hennebelle, P. 2017, *MNRAS*, 471, 4844
- Gendeleev, L., & Krumholz, M. R. 2012, *ApJ*, 745, 158
- Genzel, R., Tacconi, L. J., Gracia-Carpio, J., et al. 2010, *MNRAS*, 407, 2091
- Giuliani, Jr., J. L. 1979, *ApJ*, 233, 280
- Glover, S. C. O., & Clark, P. C. 2012, *MNRAS*, 421, 9
- Goldbaum, N. J., Krumholz, M. R., Matzner, C. D., & McKee, C. F. 2011, *ApJ*, 738, 101
- Goldsworthy, F. A. 1958, *Reviews of Modern Physics*, 30, 1062
- Gong, H., & Ostriker, E. C. 2013, *ApJS*, 204, 8
- Gong, M., Ostriker, E. C., & Wolfire, M. G. 2017, *ApJ*, 843, 38
- González, M., Audit, E., & Huynh, P. 2007, *A&A*, 464, 429
- González, M., Vaytet, N., Commerçon, B., & Masson, J. 2015, *A&A*, 578, A12
- Goodwin, S. P. 1997, *MNRAS*, 284, 785
- Górski, K. M., Hivon, E., Banday, A. J., et al. 2005, *ApJ*, 622, 759
- Gratier, P., Braine, J., Rodriguez-Fernandez, N. J., et al. 2012, *A&A*, 542, A108
- Gritschneider, M., Burkert, A., Naab, T., & Walch, S. 2010, *ApJ*, 723, 971
- Gritschneider, M., Naab, T., Walch, S., Burkert, A., & Heitsch, F. 2009, *ApJL*, 694, L26

- Grudić, M. Y., Hopkins, P. F., Faucher-Giguère, C.-A., et al. 2018, MNRAS, 475, 3511
- Haffner, L. M., Dettmar, R.-J., Beckman, J. E., et al. 2009, Reviews of Modern Physics, 81, 969
- Harper-Clark, E. 2011, PhD thesis, University of Toronto (Canada)
- Harper-Clark, E., & Murray, N. 2009, ApJ, 693, 1696
- Hartigan, P., Reiter, M., Smith, N., & Bally, J. 2015, AJ, 149, 101
- Hartmann, L. 2001, AJ, 121, 1030
- Hartmann, L., Ballesteros-Paredes, J., & Bergin, E. A. 2001, ApJ, 562, 852
- Harvey-Smith, L., Madsen, G. J., & Gaensler, B. M. 2011, ApJ, 736, 83
- Haworth, T. J., & Harries, T. J. 2012, MNRAS, 420, 562
- Hayes, J. C., & Norman, M. L. 2003, ApJS, 147, 197
- Heiles, C., & Chu, Y.-H. 1980, ApJL, 235, L105
- Heiles, C., Chu, Y.-H., & Troland, T. H. 1981, ApJL, 247, L77
- Heiles, C., & Crutcher, R. 2005, in Lecture Notes in Physics, Berlin Springer Verlag, Vol. 664, Cosmic Magnetic Fields, ed. R. Wielebinski & R. Beck, 137
- Heiles, C., & Troland, T. H. 2003, ApJ, 586, 1067
- Hennebelle, P., & Iffrig, O. 2014, A&A, 570, A81
- Henney, W. J., & Arthur, S. J. 1998, AJ, 116, 322
- Henney, W. J., Arthur, S. J., de Colle, F., & Mellema, G. 2009, MNRAS, 398, 157
- Henney, W. J., Arthur, S. J., Williams, R. J. R., & Ferland, G. J. 2005, ApJ, 621, 328
- Hester, J. J., Scowen, P. A., Sankrit, R., et al. 1996, AJ, 111, 2349
- Heyer, M., & Dame, T. M. 2015, ARA&A, 53, 583
- Heyer, M., Krawczyk, C., Duval, J., & Jackson, J. M. 2009, ApJ, 699, 1092
- Heyer, M. H., & Brunt, C. M. 2004, ApJL, 615, L45
- Hillenbrand, L. A., & Hartmann, L. W. 1998, ApJ, 492, 540
- Hills, J. G. 1980, ApJ, 235, 986

- Hockney, R. W., & Eastwood, J. W. 1981, *Computer Simulation Using Particles*
- Hopkins, P. F., & Grudic, M. Y. 2018, *ArXiv e-prints*, arXiv:1803.07573
- Hopkins, P. F., Quataert, E., & Murray, N. 2011, *MNRAS*, 417, 950
- Hosokawa, T., & Inutsuka, S.-i. 2006, *ApJ*, 646, 240
- Howard, C. S., Pudritz, R. E., & Harris, W. E. 2016, *MNRAS*, 461, 2953
- . 2017, *MNRAS*, 470, 3346
- Iffrig, O., & Hennebelle, P. 2015, *A&A*, 576, A95
- Iliev, I. T., Ciardi, B., Alvarez, M. A., et al. 2006, *MNRAS*, 371, 1057
- Inoue, T., Inutsuka, S.-i., & Koyama, H. 2006, *ApJ*, 652, 1331
- Iwasaki, K., Inutsuka, S.-i., & Tsuribe, T. 2011a, *ApJ*, 733, 17
- . 2011b, *ApJ*, 733, 16
- Joung, M. K. R., & Mac Low, M.-M. 2006, *ApJ*, 653, 1266
- Kahn, F. D. 1954, *BAN*, 12, 187
- . 1969, *Physica*, 41, 172
- Kainulainen, J., Beuther, H., Henning, T., & Plume, R. 2009, *A&A*, 508, L35
- Kawamura, A., Mizuno, Y., Minamidani, T., et al. 2009, *ApJS*, 184, 1
- Kennicutt, R. C., & Evans, N. J. 2012, *ARA&A*, 50, 531
- Kennicutt, Jr., R. C. 1998, *ARA&A*, 36, 189
- Keto, E. 2002, *ApJ*, 580, 980
- . 2003, *ApJ*, 599, 1196
- . 2007, *ApJ*, 666, 976
- Kim, C.-G., Kim, W.-T., & Ostriker, E. C. 2008, *ApJ*, 681, 1148
- Kim, C.-G., & Ostriker, E. C. 2015, *ApJ*, 802, 99
- Kim, C.-G., Ostriker, E. C., & Kim, W.-T. 2013, *ApJ*, 776, 1
- Kim, C.-G., Ostriker, E. C., & Raileanu, R. 2017a, *ApJ*, 834, 25
- Kim, J.-G., & Kim, W.-T. 2013, *ApJ*, 779, 48
- . 2014, *ApJ*, 797, 135

- Kim, J.-G., Kim, W.-T., & Ostriker, E. C. 2016, *ApJ*, 819, 137
- Kim, J.-G., Kim, W.-T., Ostriker, E. C., & Skinner, M. A. 2017b, *ApJ*, 851, 93
- Kim, J.-G., Kim, W.-T., Seo, Y. M., & Hong, S. S. 2012, *ApJ*, 761, 131
- Kim, W.-T., & Stone, J. M. 2012, *ApJ*, 751, 124
- Koenig, X. P., Leisawitz, D. T., Benford, D. J., et al. 2012, *ApJ*, 744, 130
- Koepferl, C. M., Robitaille, T. P., Dale, J. E., & Biscani, F. 2017, *ApJS*, 233, 1
- Koo, B.-C., & McKee, C. F. 1992, *ApJ*, 388, 93
- Kritsuk, A. G., Norman, M. L., & Wagner, R. 2011, *ApJL*, 727, L20
- Kroupa, P., & Boily, C. M. 2002, *MNRAS*, 336, 1188
- Krumholz, M. R. 2006, *ApJL*, 641, L45
- . 2015, ArXiv e-prints, arXiv:1511.03457
- Krumholz, M. R., Dekel, A., & McKee, C. F. 2012, *ApJ*, 745, 69
- Krumholz, M. R., Fumagalli, M., da Silva, R. L., Rendahl, T., & Parra, J. 2015, *MNRAS*, 452, 1447
- Krumholz, M. R., Klein, R. I., McKee, C. F., & Bolstad, J. 2007a, *ApJ*, 667, 626
- Krumholz, M. R., & Matzner, C. D. 2009, *ApJ*, 703, 1352
- Krumholz, M. R., Matzner, C. D., & McKee, C. F. 2006, *ApJ*, 653, 361
- Krumholz, M. R., Stone, J. M., & Gardiner, T. A. 2007b, *ApJ*, 671, 518
- Krumholz, M. R., & Tan, J. C. 2007, *ApJ*, 654, 304
- Krumholz, M. R., & Thompson, T. A. 2012, *ApJ*, 760, 155
- . 2013, *MNRAS*, 434, 2329
- Krumholz, M. R., Bate, M. R., Arce, H. G., et al. 2014, *Protostars and Planets VI*, 243
- Lada, C. J., & Lada, E. A. 2003, *ARA&A*, 41, 57
- Landau, L. D., & Lifshitz, E. M. 1959, *Fluid mechanics*
- Larson, R. B. 1981, *MNRAS*, 194, 809
- Lasker, B. M. 1966, *ApJ*, 146, 471

- Lee, E. J., Miville-Deschênes, M.-A., & Murray, N. W. 2016, *ApJ*, 833, 229
- Lee, E. J., Murray, N., & Rahman, M. 2012, *ApJ*, 752, 146
- Lefloch, B., & Lazareff, B. 1994, *A&A*, 289, 559
- Leroy, A. K., Walter, F., Sandstrom, K., et al. 2013, *AJ*, 146, 19
- Leroy, A. K., Bolatto, A. D., Ostriker, E. C., et al. 2015, *ApJ*, 801, 25
- Levermore, C. D. 1984, *JQSRT*, 31, 149
- Levermore, C. D., & Pomraning, G. C. 1981, *ApJ*, 248, 321
- Lim, A. J., & Mellema, G. 2003, *A&A*, 405, 189
- Lithwick, Y., & Goldreich, P. 2001, *ApJ*, 562, 279
- Lopez, L. A., Krumholz, M. R., Bolatto, A. D., Prochaska, J. X., & Ramirez-Ruiz, E. 2011, *ApJ*, 731, 91
- Lopez, L. A., Krumholz, M. R., Bolatto, A. D., et al. 2014, *ApJ*, 795, 121
- Mac Low, M.-M., Klessen, R. S., Burkert, A., & Smith, M. D. 1998, *Physical Review Letters*, 80, 2754
- Mackey, J. 2012, *A&A*, 539, A147
- Mackey, J., & Lim, A. J. 2011, *MNRAS*, 412, 2079
- Mackey, J., Mohamed, S., Gvaramadze, V. V., et al. 2014, *Nature*, 512, 282
- Martínez-González, S., Silich, S., & Tenorio-Tagle, G. 2014, *ApJ*, 785, 164
- Mathews, W. G. 1965, *ApJ*, 142, 1120
- . 1967, *ApJ*, 147, 965
- Matzner, C. D. 2002, *ApJ*, 566, 302
- . 2007, *ApJ*, 659, 1394
- Matzner, C. D., & Jumper, P. H. 2015, *ApJ*, 815, 68
- Matzner, C. D., & McKee, C. F. 2000, *ApJ*, 545, 364
- McKee, C. F., & Cowie, L. L. 1977, *ApJ*, 215, 213
- McKee, C. F., & Ostriker, E. C. 2007, *ARA&A*, 45, 565
- McKee, C. F., & Williams, J. P. 1997, *ApJ*, 476, 144
- Medina, S.-N. X., Arthur, S. J., Henney, W. J., Mellema, G., & Gazol, A. 2014, *MNRAS*, 445, 1797

- Meidt, S. E., Hughes, A., Dobbs, C. L., et al. 2015, *ApJ*, 806, 72
- Meier, D. S., Turner, J. L., & Beck, S. C. 2002, *AJ*, 124, 877
- Mellema, G., Arthur, S. J., Henney, W. J., Iliev, I. T., & Shapiro, P. R. 2006a, *ApJ*, 647, 397
- Mellema, G., Iliev, I. T., Alvarez, M. A., & Shapiro, P. R. 2006b, *NewA*, 11, 374
- Mihalas, D. 2001, *JQSRT*, 71, 61
- Miura, R. E., Kohno, K., Tosaki, T., et al. 2012, *ApJ*, 761, 37
- Miville-Deschênes, M.-A., Murray, N., & Lee, E. J. 2017, *ApJ*, 834, 57
- Mizuta, A., Kane, J. O., Pound, M. W., et al. 2005, *ApJ*, 621, 803
- Modestov, M., Bychkov, V., Valiev, D., & Marklund, M. 2009, *PhRvE*, 80, 046403
- Molina, F. Z., Glover, S. C. O., Federrath, C., & Klessen, R. S. 2012, *MNRAS*, 423, 2680
- Mooney, T. J., & Solomon, P. M. 1988, *ApJL*, 334, L51
- Murray, N. 2011, *ApJ*, 729, 133
- Murray, N., Quataert, E., & Thompson, T. A. 2010, *ApJ*, 709, 191
- Murray, N., & Rahman, M. 2010, *ApJ*, 709, 424
- Myers, P. C., Dame, T. M., Thaddeus, P., et al. 1986, *ApJ*, 301, 398
- Naab, T., & Ostriker, J. P. 2017, *ARA&A*, 55, 59
- Nakamura, F., & Li, Z.-Y. 2014, *ApJ*, 783, 115
- Offner, S. S. R., Klein, R. I., McKee, C. F., & Krumholz, M. R. 2009, *ApJ*, 703, 131
- Oka, T., Hasegawa, T., Sato, F., et al. 2001, *ApJ*, 562, 348
- Oort, J. H., & Spitzer, Jr., L. 1955, *ApJ*, 121, 6
- Osterbrock, D. E. 1989, *Astrophysics of gaseous nebulae and active galactic nuclei*
- Ostriker, E. C., McKee, C. F., & Leroy, A. K. 2010, *ApJ*, 721, 975
- Ostriker, E. C., & Shetty, R. 2011, *ApJ*, 731, 41
- Ostriker, E. C., Stone, J. M., & Gammie, C. F. 2001, *ApJ*, 546, 980

- Park, K., Ricotti, M., Di Matteo, T., & Reynolds, C. S. 2014, *MNRAS*, 437, 2856
- Parravano, A., Hollenbach, D. J., & McKee, C. F. 2003, *ApJ*, 584, 797
- Pauldrach, A. W. A., Hoffmann, T. L., & Lennon, M. 2001, *A&A*, 375, 161
- Pellegrini, E. W., Baldwin, J. A., Ferland, G. J., Shaw, G., & Heathcote, S. 2009, *ApJ*, 693, 285
- Pellegrini, E. W., Baldwin, J. A., Brogan, C. L., et al. 2007, *ApJ*, 658, 1119
- Pereira-Santaella, M., Colina, L., García-Burillo, S., et al. 2016, *A&A*, 587, A44
- Peters, T., Banerjee, R., Klessen, R. S., et al. 2010, *ApJ*, 711, 1017
- Petrosian, V., Silk, J., & Field, G. B. 1972, *ApJL*, 177, L69
- Rahman, M., & Murray, N. 2010, *ApJ*, 719, 1104
- Rahner, D., Pellegrini, E. W., Glover, S. C. O., & Klessen, R. S. 2017, *MNRAS*, 470, 4453
- Raskutti, S. 2016, PhD thesis, Princeton University
- Raskutti, S., Ostriker, E. C., & Skinner, M. A. 2016, *ApJ*, 829, 130
- . 2017, *ApJ*, 850, 112
- Redman, M. P., Williams, R. J. R., Dyson, J. E., Hartquist, T. W., & Fernandez, B. R. 1998, *A&A*, 331, 1099
- Rho, J., & Petre, R. 1998, *ApJL*, 503, L167
- Ricotti, M. 2014, *MNRAS*, 437, 371
- Rijkhorst, E.-J., Plewa, T., Dubey, A., & Mellema, G. 2006, *A&A*, 452, 907
- Rodríguez, L. F., Gómez, Y., & Tafoya, D. 2012, *MNRAS*, 420, 279
- Rodríguez-Ramírez, J. C., Raga, A. C., Lora, V., & Cantó, J. 2016, *ApJ*, 833, 256
- Rogers, H., & Pittard, J. M. 2013, *MNRAS*, 431, 1337
- Roman-Duval, J., Jackson, J. M., Heyer, M., Rathborne, J., & Simon, R. 2010, *ApJ*, 723, 492
- Rosdahl, J., Blaizot, J., Aubert, D., Stranex, T., & Teyssier, R. 2013, *MNRAS*, 436, 2188
- Rosdahl, J., & Teyssier, R. 2015, *MNRAS*, 449, 4380

- Rosen, A. L., Krumholz, M. R., Oishi, J. S., Lee, A. T., & Klein, R. I. 2017, *Journal of Computational Physics*, 330, 924
- Rosen, A. L., Lopez, L. A., Krumholz, M. R., & Ramirez-Ruiz, E. 2014, *MNRAS*, 442, 2701
- Rosolowsky, E. 2005, *PASP*, 117, 1403
- Saaf, A. F. 1966, *ApJ*, 145, 116
- Sandford, II, M. T., Whitaker, R. W., & Klein, R. I. 1982, *ApJ*, 260, 183
- Schmidt-Voigt, M., & Koeppen, J. 1987, *A&A*, 174, 211
- Schneider, N., Bontemps, S., Girichidis, P., et al. 2015, *MNRAS*, 453, L41
- Scoville, N. Z. 2013, *Evolution of star formation and gas*, ed. J. Falcón-Barroso & J. H. Knapen, 491
- Scoville, N. Z., Polletta, M., Ewald, S., et al. 2001, *AJ*, 122, 3017
- Scoville, N. Z., Yun, M. S., Clemens, D. P., Sanders, D. B., & Waller, W. H. 1987, *ApJS*, 63, 821
- Semenov, D., Henning, T., Helling, C., Ilgner, M., & Sedlmayr, E. 2003, *A&A*, 410, 611
- Shima, K., Tasker, E. J., & Habe, A. 2017, *MNRAS*, 467, 512
- Shu, F. H. 1992, *The physics of astrophysics. Volume II: Gas dynamics*.
- Shu, F. H., Lizano, S., Galli, D., Cantó, J., & Laughlin, G. 2002, *ApJ*, 580, 969
- Skinner, M. A., & Ostriker, E. C. 2013, *ApJS*, 206, 21
- . 2015, *ApJ*, 809, 187
- Solomon, P. M., Rivolo, A. R., Barrett, J., & Yahil, A. 1987, *ApJ*, 319, 730
- Sormani, M. C., Treß, R. G., Klessen, R. S., & Glover, S. C. O. 2017, *MNRAS*, 466, 407
- Spitzer, L. 1978, *Physical processes in the interstellar medium*, doi:10.1002/9783527617722
- Spitzer, Jr., L. 1954, *ApJ*, 120, 1
- Steggles, H. G., Hoare, M. G., & Pittard, J. M. 2017, *MNRAS*, 466, 4573
- Stone, J. M., & Gardiner, T. 2009, *NewA*, 14, 139
- Stone, J. M., Gardiner, T. A., Teuben, P., Hawley, J. F., & Simon, J. B. 2008, *ApJS*, 178, 137

- Stone, J. M., Ostriker, E. C., & Gammie, C. F. 1998, *ApJL*, 508, L99
- Stone, J. M., & Zweibel, E. G. 2009, *ApJ*, 696, 233
- Strömberg, B. 1939, *ApJ*, 89, 526
- Strong, A. W., & Mattox, J. R. 1996, *A&A*, 308, L21
- Sugitani, K., Fukui, Y., Mizuni, A., & Ohashi, N. 1989, *ApJL*, 342, L87
- Sugitani, K., Fukui, Y., & Ogura, K. 1991, *ApJS*, 77, 59
- Sysoev, N. E. 1997, *Astronomy Letters*, 23, 409
- Takabe, H., Mima, K., Montierth, L., & Morse, R. L. 1985, *Physics of Fluids*, 28, 3676
- Tan, J. C., Beltrán, M. T., Caselli, P., et al. 2014, *Protostars and Planets VI*, 149
- Tan, J. C., Krumholz, M. R., & McKee, C. F. 2006, *ApJL*, 641, L121
- Tenorio-Tagle, G. 1979, *A&A*, 71, 59
- Thompson, T. A., Fabian, A. C., Quataert, E., & Murray, N. 2015, *MNRAS*, 449, 147
- Thompson, T. A., & Krumholz, M. R. 2016, *MNRAS*, 455, 334
- Tremblin, P., Audit, E., Minier, V., Schmidt, W., & Schneider, N. 2012, *A&A*, 546, A33
- Tremblin, P., Anderson, L. D., Didelon, P., et al. 2014, *A&A*, 568, A4
- Tsang, T.-H. B., & Milosavljevic, M. 2017, *ArXiv e-prints*, arXiv:1709.07539
- Turner, J. L., Beck, S. C., Benford, D. J., et al. 2015, *Nature*, 519, 331
- Turner, J. L., Consiglio, S. M., Beck, S. C., et al. 2017, *ApJ*, 846, 73
- Usero, A., Leroy, A. K., Walter, F., et al. 2015, *AJ*, 150, 115
- Vandervoort, P. O. 1962, *ApJ*, 135, 212
- Vázquez-Semadeni, E., Colín, P., Gómez, G. C., Ballesteros-Paredes, J., & Watson, A. W. 2010, *ApJ*, 715, 1302
- Vishniac, E. T. 1983, *ApJ*, 274, 152
- Vutisalchavakul, N., Evans, II, N. J., & Heyer, M. 2016, *ApJ*, 831, 73
- Walch, S., & Naab, T. 2015, *MNRAS*, 451, 2757
- Walch, S. K., Whitworth, A. P., Bisbas, T., Wünsch, R., & Hubber, D. 2012, *MNRAS*, 427, 625

- Wang, P., Li, Z.-Y., Abel, T., & Nakamura, F. 2010, *ApJ*, 709, 27
- Weaver, R., McCray, R., Castor, J., Shapiro, P., & Moore, R. 1977, *ApJ*, 218, 377
- Weidner, C., & Kroupa, P. 2006, *MNRAS*, 365, 1333
- Whalen, D., Abel, T., & Norman, M. L. 2004, *ApJ*, 610, 14
- Whalen, D. J., & Norman, M. L. 2008, *ApJ*, 672, 287
- Whitehouse, S. C., & Bate, M. R. 2006, *MNRAS*, 367, 32
- Whitworth, A. 1979, *MNRAS*, 186, 59
- Whitworth, A. P., Bhattal, A. S., Chapman, S. J., Disney, M. J., & Turner, J. A. 1994, *MNRAS*, 268, 291
- Williams, J. P., & McKee, C. F. 1997, *ApJ*, 476, 166
- Williams, R. J. R. 2002, *MNRAS*, 331, 693
- Williams, R. J. R., Bisbas, T. G., Haworth, T. J., & Mackey, J. 2018, *MNRAS*, 479, 2016
- Williams, R. J. R., Dyson, J. E., & Hartquist, T. W. 2000, *MNRAS*, 314, 315
- Wilson, B. A., Dame, T. M., Mashedier, M. R. W., & Thaddeus, P. 2005, *A&A*, 430, 523
- Wilson, R. W., Jefferts, K. B., & Penzias, A. A. 1970, *ApJL*, 161, L43
- Wise, J. H., & Abel, T. 2011, *MNRAS*, 414, 3458
- Wolfire, M. G., McKee, C. F., Hollenbach, D., & Tielens, A. G. G. M. 2003, *ApJ*, 587, 278
- Wong, T., Hughes, A., Ott, J., et al. 2011, *ApJS*, 197, 16
- Wünsch, R., Dale, J. E., Palouš, J., & Whitworth, A. P. 2010, *MNRAS*, 407, 1963
- Yeh, S. C. C., & Matzner, C. D. 2012, *ApJ*, 757, 108
- Yoda, T., Handa, T., Kohno, K., et al. 2010, *PASJ*, 62, 1277
- Yorke, H. W. 1986, *ARA&A*, 24, 49
- Zeldovich, Y. B., Barenblatt, G. I., Librovich, V. B., & Makhviladze, G. M. 1985, *The Mathematical Theory of Combustion and Explosions*
- Zuckerman, B., & Evans, II, N. J. 1974, *ApJL*, 192, L149
- Zuckerman, B., & Palmer, P. 1974, *ARA&A*, 12, 279

요약

현재 우주에서의 거의 모든 별 형성은 거대 분자운에서 일어난다. 젊고 무거운 별들은 적은 수에도 불구하고 모 분자운과 주변 성간 물질의 구조와 화학적, 역학적 성질에 지대한 영향을 미친다. 특히 무거운 별이 방출하는 자외선 복사는 주변에 따뜻한 위상의 전리 수소 영역을 형성하여 분자운의 차가운 기체를 밀어내고 침식시킨다. 자외선 복사가 분자운의 파괴에 미치는 영향은 이론가들에게 오랫동안 주목받아 왔으나, 이에 대한 정량적 이해는 아직 부족한 상황이다. 본 학위 논문에서는 다양한 별 형성 환경에서 자외선 복사 되먹임이 거대 분자운의 진화와 별 형성에 미치는 영향을 해석적 방법과 수치 모의 실험을 통해 연구하였다.

2장에서는 차가운 중성 기체와 따뜻한 전리 기체의 불연속 경계면, 즉 전리 전선에서 발생할 수 있는 작은 규모의 역학적 불안정을 연구하였다. 이를 위해 평행 평면의 자화된 전리전선에 대한 선형 안정성 분석을 수행하였다. 초기 자기장의 방향은 전선면과 평행하다고 가정하였다. 불안정의 성장률은 섭동의 파수와 상류의 차가운 기체의 전선면에 대한 상대 속도에 비례하는데, 이 결과는 화염이나 열핵반응 초신성의 연소면에서 나타나는 Darrieus-Landau 불안정과 유사하다. 자기장은 차가운 기체와 따뜻한 기체의 밀도비를 줄여주고 자기압 정도력, 장력을 발생시켜 불안정을 약화시킨다. 자기장의 세기가 충분히 강한 경우 전선면에 평행한 방향으로 진행되는 섭동은 완전히 안정화 된다. 전리전선이 무거운 별로부터 멀어지는 방향으로 가속되는 경우, 전리전선의 불안정은 Rayleigh-Taylor 불안정과 함께 나타난다.

3장에서는 구형 대칭성을 갖는 전리 수소 영역의 팽창과 이로 인한 분자운의 파괴에 대한 연구를 수행하였다. 전리 기체의 열적 압력, 성간 티끌에 작용하는 복사압, 중심 성단의 중력, 기체의 자체중력의 효과를 모두 고려한 전리 수소 영역의 팽창에 대한 준해석적 모형을 개발하였고, 모형이 예측하는 전리 수소 영역의 팽창이 수치 모의 실험의 결과와 잘 일치함을 확인하였다. 우리는 분자

운의 파괴에 필요한 최소 별 탄생 효율을 분자운의 초기 질량, 초기 면밀도의 함수로 계산하였다. 우리 은하에 존재하는 보통의 거대분자운은 10%보다 작은 별 탄생 효율로 파괴될 수 있으며, 이 때 전리 수소 영역은 주로 열적 압력에 의해 팽창한다. 이보다 큰 밀도와 큰 질량을 갖는 분자운의 파괴를 위해서는 더 높은 별 탄생 효율이 요구되며, 이 경우 전리 수소 영역은 주로 복사압에 의해 팽창한다. 전리 수소 영역의 팽창은 분자운의 자유낙하시간과 비슷한 시간 규모에서 일어나는데, 이 결과는 전리 수소 영역에 의한 분자운의 파괴가 비교적 빠르게 일어남을 시사한다.

4장에서는 난류 운동이 지배하는 거대 분자운에서의 성단 형성에 대한 3차원 수치 모형의 개발에 대해 다루었다. 우리는 점 광원에 의한 복사 전달 문제를 빠르고 정확하게 풀 수 있는 적응 광선 추적 기법을 격자기반 유체역학 코드인 *Athena*에 구현하였다. 프로세스 간에 이루어지는 광선 정보 교환을 효율적으로 수행하기 위해서 최근 제안된 병렬화 알고리즘을 개선시켜 적용하였다. 구현한 복사유체역학 알고리즘을 다양한 전리 수소 영역의 팽창 문제에 대해 시험하였다. 강-, 약-스케일링 시험을 통해 $\sim 10^3$ 개의 프로세스를 사용할 때에도 적응 광선 추적 모듈이 높은 병렬 효율을 유지함을 확인하였다. 적응 광선 추적 기법을 활용한 복사유체역학 코드의 활용가능성을 보여주기 위해 별 형성과 난류 운동의 효과를 고려한 성단의 형성에 대한 수치 모의 실험을 수행하였다. 또한 적응 광선 추적 기법과 널리 쓰이는 M_1 닫힘 방법을 통해 계산한 복사장을 직접 비교하여 후자의 경우 점광원 근방의 복사장을 정확히 기술할 수 없음을 보였다.

5장에서는 다양한 환경에서의 성단의 형성과 전리 수소 영역의 광이온화 및 복사압에 기인한 분자운의 파괴를 복사유체역학 수치 모의 실험을 통해 연구하였다. 분자운의 최종 별 탄생 효율은 분자운의 초기 면밀도가 클수록 큰 값을 갖는다. 분자운의 파괴는 무거운 별의 탄생을 시작된 후 $\sim 2\text{--}10\text{ Myr}$ 안에 이루어진다. 분자운의 초기 면밀도가 클수록 복사압은 (광이온화에 비하여) 전리 수소 영역의 역학적 진화에 중요한 역할을 담당한다. 분자운의 질량 손실을 일으키는 가장 중요한 물리적 기작은 광증발이나, 초기 질량이 작거나 초기 면밀도가 큰 분자운에서는 동적 방출에 의한 질량 손실도 무시할 수 없는 역할을 담당한다. 우리는 광증발에 의한 질량 손실률이 분자운의 크기와 성단이 단위

시간당 방출하는 이온화 광자의 개수만 의존하는 양임을 발견하였고 이 결과를 설명하는 척도 관계를 제시하였다. 분출류가 갖는 운동량은 구형 대칭성을 가정한 모형의 예측치보다 10배 가까이 작은 값을 갖는데, 이는 광자의 탈출과 기체 충돌에 의한 운동량의 상쇄 때문이다.

주요어: 전리수소영역, 불안정, 성간물질:기체운, 성간물질:운동학과 역학, 방법: 해석적, 방법:수치실험, 복사:역학, 복사 전달, 별:형성
학번: 2012-30111